Design of Catalytic Microengineered Reactors

A thesis submitted for degree of
Doctor of Philosophy
in Chemical Engineering

2002

Darren Gobby

Department of Chemical Engineering
University College London

Acknowledgements

I wish to express my thanks to my supervisors Dr. Asterios Gavriilidis and Prof. David Bogle for their advice, guidance and support during the course of this study.

I would also like to thank Dr. Panagiota Angeli, Dr. Ian Eames and Dr. Eric Fraga.

I would like to thank my family and friends for their support and encouragement.

Financial support was provided by the U.K. Engineering and Physical Sciences Research Council (EPSRC) and the Graduate School (University College London), for which I am very grateful.

Abstract

The demand for safer and more efficient chemical plants has lead the reaction engineer to consider new technologies. Process intensification steers partially towards this goal by the reduction of large inventories. Microreaction technology can be seen to be a limit of process intensification, by performing unit operations in sub mm sized domains. High specific interfacial areas and well a defined hydrodynamic environment allow precise control of an intrinsically safe operation. Microreaction technology is still an emerging discipline and a thorough understanding of the important design and operating parameters are needed to gain industrial acceptance.

The aim of this work is to understand the transport characteristics of energy and mass at this scale, in a theoretical manner, to provide the reaction engineer with some modelling tools that allow conceptual insight into the microreactor design. In addition the understanding of transport phenomena at this scale is applied to some unit operations allowing the dominant design and operating parameters to be identified. Analytical and numerical simulations have been used and it is shown that the microreactor is insensitive to the 1D velocity profile if $R > Pe > 1$ for linear and non-linear kinetics in any duct shape. Highly non-isothermal systems were shown to become near isothermal as the conductivity in the reactor wall increased, i.e. acting as a thermal shunt.

Multiphase systems were also investigated where it is shown analytically that the effect of interface curvature on reactor performance is negligible and transverse distance to the catalyst is the dominating design parameter. Two multiphase reactors were considered with different flow profiles and under some operating conditions they are shown to have equivalent performance.

In all microreactor systems studied it was shown that a high degree of conversion and isothermality could be obtained with design expressions provided to allow rapid prototyping of future microreactors.

Contents

List of Figures

List of Tables

Chapter 1

Introduction

Miniaturized microfluidic devices have been used mainly as analytical tools, which have largely evolved from manufacturing technologies developed in the semiconductor industry. Advances made in manufacturing technology allowed highly integrated systems to be developed that comprised of many components and were termed micro total analysis systems. From the work developed in the creation of these systems the huge performance benefits possible, from operating at this scale, were conceived for individual unit operations in chemical engineering. Much of the research has been in the form of exploratory work - determining the benefits of using such systems, finding out how microreactors behave and examining novel reactor configurations. Many microreactors consist of channels etched onto metal, silicon, glass or ceramic substrates via lithographic or other techniques such as EDM or laser micromachining. With the further development of microfabrication techniques it is possible to construct an integrated unit operating with integrated heaters, sensors and actuators (Hsing et al.2000). Integration allows the process of flow in microdevices not just to be pressure driven. Micropumps and microvalves are under development that incorporate a diaphragm actuated by electrostatic, piezoelectric and electromagnetic forces (Wegeng et al.1996) and provide a constant displacement on each stroke with volumetric flowrates in the order of 10-100 ml per minute.

Despite the possibility of high performance individual unit operations, immediate problems arose with regard to applying these systems to chemical engineering due to low production rates. This problem has been immediately addressed by replacing traditional scale-up principles, for process development, with a scale-out approach (parallel operation). Although scale-out is simple in concept designs are required for the inlet manifold to ensure uniform residence time distributions.

The design of microreactors will stem largely from chemical engineering, but future advances will be better achieved by interdisciplinary groups. The processing knowledge held by chemical engineers will have to be augmented with information concerning hydrodynamics and other transport phenomena at this level from other disciplines. For design, accurate simulations of the microreactors will be needed, and the applicability of the traditional macroscopic Navier-Stokes equations to microsystems has already been brought into question by several authors (Pfahler et al.1991, Peng et al.1994, Adams 1997). For flow profiles specifically in the micro regime surface effects have shown to be dominant (Gad-el-Hak 1999) and work has been done in this field by Gravesen et al.(1993) and Arkilic et al.(1997).

Microreactors need to make an impact in the industrial world and this can be achieved by enhancing the performance of existing processes or new processes with favourable operating regimes not possible with conventional reactors. In the former case many processes at present are performed under batch operation, usually stirred tank reactors. Such systems can possess unfavourable characteristics such as large hold-ups and limited transport rates due to the large reaction volume. Microreactors alleviate such problems by providing continuous operation (low hold-up) and high transport rates as a result of the inherent high specific interfacial areas. Laminar flow is an inherent feature at the microscale and diffusive transport is the main transport mechanism, and heat transfer coefficients have been reported up to a factor of 10 higher than conventional equipment (Chopey et al.1997).

An advantage, as a consequence of high transport rates, is reaction systems where there are competing reactions and residence time needs to be kept short. Residence times in microreactors become very short, 1-10 ms, (Wegeng et al.1996) and well controlled. In addition, an issue lies in the control of microreactors. Conventional reactors have response times from seconds upwards, microreactors have response times in the order of 1 ms therefore offering the possibility of tighter process control.

Microreactors can operate with process parameters (operating regimes) that are not possible in conventional systems and this has been shown by several authors when operating in the explosive regime. An example of which is the H_2/O_2 reaction using a single channel with a catalyst wire (Veser et al.2000). Conventional fixed-bed reactors for exothermic systems have often shown a high parametric sensitivity, i.e. small changes in feed can lead to large changes in the reactor temperature profile and possible runaway.

Ehrfeld et al.(2000) have considered the wider possibilities of industrial use and introduction of microreactors, and state that individual unit operation performance must be augmented with an economic analysis that includes plant start-up, chemical transport and environmental restrictions. A possible area that will need greater economic analysis is the concept of distributed manufacturing (Lerou et al.1996) where the transport of hazardous chemicals often incurs a large financial penalty. Hence the development of microreactor systems should serve to demonstrate that the transport of the reaction unit itself is more financially attractive than the storage and transport of potentially hazardous feedstocks. Dupont have produced hazardous chemicals (isocyanates) in a complete microreactor system comprising of preheaters and catalytic sections (Lerou et al.1996). A process that has been conceived as viable for such systems is the production of hydrogen cyanide via the catalytic reaction of methane and ammonia (Lerou et al.1996).

There is a need for accurate modelling of such microdevices, particularly in reference to heat, mass and momentum transfer at this scale, and a greater understanding of the reaction engineering issues involved. The modelling of such transport phenomena needs to be coupled to process development in microreactors allowing design rules for common unit operations to be established, allowing rapid prototyping, as stated by Ehrfeld et al.(2000), to occur. In light of these statements this thesis concentrates on developing robust modelling tools for fundamental microreactor transport phenomena and demonstrates the applicability of such tools to important unit operations to develop design criteria.

The thesis begins with a thorough literature survey considering the viability, fabrication and operation of microreactors, and a quantitative comparison with conventional and novel macroscopic systems. The first results chapter concentrates on the modelling of mass transfer in isothermal microreactor systems. By careful consideration of the scale, analytical solutions are presented for different kinetic schemes and geometries. These solutions are verified with numerical simulations. Such closed form solutions provide the design/reaction engineer with a clear conceptual appreciation of the dominant design and operating parameters. The second results chapter studies heat transfer in such systems. Initially the analytical results are extended into the non-isothermal regime for weakly exothermic flows (a limitation of the analytical solution), and are verified against numerical simulations. Heat integration is then considered in such systems by considering a microreactor with exothermic and endothermic reactions occurring in alternate channels using numerical simulations. Understanding the fundamental transport modelling allowed common unit operations in microreactors to be further studied with a greater emphasis placed upon conceptual design. Three unit operations are considered in separate results chapters and these are, in order, a T-mixer, methanol oxidation microreactor and two multiphase microreactors. Some results chapters contain a further literature survey that is more relevant to the design/phenomena specifically under investigation. Finally conclusions and recommended future work are given.

Chapter 2

Literature Survey

2.1 Introduction

This literature survey attempts to give an overview of the subject of microreactors. Due to the interdisciplinary nature of the field not all aspects can be covered in detail, but general concepts are introduced along with process advantages from experimental and theoretical work. Relevant work specific to any particular results section is reviewed at the beginning of that chapter.

Initially the general field of microreactors is considered, looking at viability, fabrication, operation and modelling/simulation. As a further justification for working at this scale conventional reactor systems are reviewed and quantitative comparisons made with the microreactor data available.

2.2 Origins and fabrication

The potential advantages of microreactors, based on concepts, have been quoted by many (Benson and Ponton 1993 and Lerou et al.1996). Such works speak of increased process performance, due to high specific surface area, low power consumption, inherent safety and low inventories. It was Benson and Ponton (1993) who provided one of the earliest review papers that dealt with process miniaturisation, although the emphasis was on intensification rather than microfabricated systems. Interesting analogies are drawn from the aerospace and electronics industries to the chemical industry and the concept of distributed manufacturing (point of use production) is brought into current perspective. Benson and Ponton additionally mention that many intensified unit operations already exist but, at their time of writing, had not yet gained industrial acceptance.

Lerou et al.(1996) provide a technical overview of process miniaturisation but focus on microfabricated systems. The viability of such microfabricated systems was applied to different case studies and commented upon (unlike Benson and Ponton (1993) microreactors were built and tested, therefore conclusions drawn were not purely hypothetical). An example that was chosen was the oxidation of monomethylformamide (MMF) to methyl isocyanate, a reaction which is both highly exothermic and toxic. Reaction channels were etched into silicon and packed with silver catalyst particles. Heat exchangers were also included in the unit by means of a stacking arrangement. Although the results gave conversions of around 90 % there was no particular process advantage over laboratory scale apparatus in this instance. The work did show though that a process could be effectively miniaturised for distributed production. Another example of a potential miniaturised process is the partial oxidation of methane which, although highly exothermic requires a residence time that is 75 % lower than steam reforming (Srinivasen 1997). The dimensions of microreactors could resolve any thermal management issues.

However, the physical reality of such novel systems relies on their manufacture. The fabrication methods typically used in microreactor construction have strong parentage from techniques developed in the semi-conductor industry with the result that early microreactors were often formed from silicon. Newer technologies have extended the range of materials that are available for fabrication and microengineered structures are now possible from metals, ceramics, glass and plastics. Some of the more popular microfabrication techniques are summarised in the following.

2.2.1 Photolithography and etching

This technique is one of the oldest techniques in microfabrication and involves spinning a photoresist onto a suitable substrate and patterning this resist using UV light through a chromium patterned glass mask. This resist is then formed into a protective layer, where the original material is etched using wet etching. Dry etching can also be used (plasma based techniques) which gives a structure with less undercutting.

2.2.2 Chemical vapour deposition

In this technique chemical species from a gas react on a solid surface and form a film, such films can be formed of silicon, silicon nitride and phosophosolicate glass. Typical applications for this technique are mask construction, membranes and catalyst layers. Extra energy can be imparted to the reacting gas using a plasma, this allows a lower substrate temperature.

2.2.3 Laser machining

Laser machining vaporises the material using short pulses. The technique has generated holes with aspect ratios up to 1:50. This process can also be applied to hard materials such as diamond. The process is not limited to subtractive machining, 3D structures can be realised by scanning the surface with a laser beam in the presence of reactive gases.

2.2.4 Electrodischarge machining

This technique utilises local hot spot (12,000 °C) to vaporise the substrate using an electric discharge. An electrode and substrate are immersed in a dielectric medium with a narrow gap (25 microns) between them. Upon applying a suitable potential rapid sparking occurs eroding the substrate. The surface roughness is inversely proportional to sparking frequency.

2.2.5 Glass microfabrication

Glass is a very inert material and has found favour in the chemical and pharmaceutical industry. Therefore, the fabrication of microreactors from this material is attractive for highly corrosive processes. It can be manufactured using conventional lithography using hydrogen fluoride as a wet etchant. Photoetchable glass is an alternative where upon exposure to UV light silver is formed, resulting in a crystalline structure around the silver upon appropriate heat treatment. If wet etching is employed, again using HF, the crystalline regions will etch about 20 times faster than other regions allowing structures to be formed.

2.3 Microfluidics

Fluid flow in microstructures has been reported to differ from macroscopic systems. Mathematical models to describe such behaviour vary in complexity, and there is much debate as to what scale the Navier-Stokes equations fail to be valid. Various phenomena could contribute to such observations, which are not usually significant in macroscopic flow, namely surface tension, and relative magnitude of surface roughness compared to channel dimensions. At present the flow regime is often classified by the Knudsen number (Kn); the ratio of the mean free distance a molecule travels to the system characteristic dimension. If $Kn < 0.001$ the fluid is deemed to behave as a continuum, just above this level is the slip region where the

Navier-Stokes equations have been applied but with modified slip boundary conditions. When Kn is much higher than the continuum threshold ($O(0.1)$) the fluid does not behave as a continuum (rarefaction) and is termed free molecular flow.

Friction factors (f) are commonly used to correlate flow and pressure drop, where the friction factor is dependent upon the Reynolds number and channel geometry. For laminar systems with a circular cross section the analytical result for the friction factor is $64/Re$. A number of authors have attempted to measure friction factors in microstructures with contradicting results.

Wu and Little (1983) have reported the friction factor data for trapezoidal channels and have found that for laminar and turbulent flow the friction factors were higher than in macroscopic systems. Peng et al.(1994) also report an increase in friction factor for liquid flow in rectangular channels.

In contrast to the above Choi (1991) have measured friction factors in tubes. For tubes below 100 microns the friction factor was below that of traditional analysis (Nitrogen gas). In the analysis Choi indicated that for large pressure gradients (10 MPa) a compressible flow analysis should be used for data reduction. Tuckerman (1981) additionally report that the friction factor increases with Reynolds number, but Choi (1991) found no evidence to support this, this is in agreement with Harley et al.(1995).

Pfahler (1991) also reported lower friction factors in channels from 0.5 to 50 microns than in conventional systems. Pfahler (1991) used channels from 0.5 to 50 microns and measurements of friction factor were compared with classical macroscopic correlations. Gases and liquids were used and the general trend was that the friction factor decreases as the channel size decreases (no theoretical justification given). The exception was a polar fluid which showed converse behaviour which was attributed to the electro double layer. Differences in established data and experimental results were attributed to rarefaction.

Not all authors report deviations from macroscopic models. Makihara et al.(1993) have investigated the flow of liquids in 4.5 to 50.5 micron capillary tubes, and found that measured values of flow agree with the Navier-Stokes equations.

The transition Reynolds number also has been reported to diverge from classical theory. Peng et al.(1994) found that the transition Reynolds number decreased as the channel hydraulic diameter increased, there was also some influence of the channel aspect ratio. The change in transition Reynolds number was attributed to the instabilities associated with turbulence being able to spread to the bulk of the fluid much faster than in macroscale flow. Wu and Little (1983) observed a reduced transition Reynolds number in proportion to channel surface roughness. However, Stanley et al.(1997) report an increase in transition Reynolds number for gas flows. It was reported that transition for water flow did not occur even at a Reynolds number of 10,000. The turbulence suppression has been discussed by Yu et al.(1995) which considers the effect of channel size on eddy formation, and concludes there must be a threshold size of the eddy for transition to occur.

Stanley et al.(1997) have investigated transition into the turbulent regime using heat transfer in microchannels experiments. Single phase heat transfer data showed no agreement with the macroscopic laminar Nusselt number ($Nu = 2.98$) or the turbulent macroscopic correlation (Dittus-Boelter equation) although results gave a similar gradient to the turbulent correlation (no evidence of flow transition). The Nusselt number appeared to still be a function of Reynolds and Prandtl number as in the macroscopic case. These heat transfer results are consistent with Choi et al.(1991).

Gravesen (1993) have presented a general review of microfluidics and state that determination of the Reynolds number may not adequately describe the phenomena occuring in the device. Like Harley et al.(1995) it is demonstrated that laminar high Mach number flows may be possible and it is pointed out there are no models, at the time of writing, for sonic flow in the laminar regime. Like other authors the independence of fluid viscosity with channel dimensions is also questioned.

In addition to friction factor data some authors have attempted detailed models of flow in microstructures. Arkilic and Breuer (1994) performed work on gas (He) flow in microchannels with inlet pressures ranging from 1.2 to 2.5 atm., and outlet pressures at atmospheric. A dimensionless model using the slip velocity is presented ignoring gravitational effects. It is shown that the presence of slip at the boundaries will effect the pressure distribution as well as the mass flow. Also, as the inlet to outlet pressure ratio decreases slip becomes more significant.

Beskok and Karniadakis (1994) attempted a general simulation model that took account of higher order slip effects to adequately couple the temperature jump boundary condition (analogous to fluid slip) into the governing equations. Results of the simulations showed that a developed velocity profile is reached about four channel heights downstream from a uniform inlet boundary. An interesting effect with slip flow is that the maximum velocity is not at the centreline until fully developed flow is reached.

Liu and Yu-Chong (1995) have performed experimental and numerical work on pressure distribution of gaseous flow in a microchannel. Very low pressure gradients were observed near the inlet and outlet, and these could not be explained by the slip flow model. The non-linearity of the pressure distribution depends on the type of fluid used and reaction may have an even greater effect. The numerical simulations compare well with experimental data if entrance and end effects are ignored.

Arkilic et al.(1997) presented further work in gas flow in microchannels and also emphasise the importance of compressibility at such scales. Compressibility introduces negative curvature into the pressure distribution, but such curvature is diminished as Kn is increased. The theoretical work provides an understanding of the higher gas velocities for a given pressure ratio and provides a relation between slip and Kn (via boundary conditions).

Commercial MEMS simulation packages rely heavily on fitting simulation data to experimental results by introducing empirical coefficients into the boundary conditions (van Kuilk 1999), however such coefficients have no sound theoretical basis and are likely to be system specific.

Multiphase flow

Studies of two phase flow in microchannels have concentrated on gas-liquid systems. Matsumoto and Colgate (1990) have analysed bubble movement in microchannels and show that pressure drop is inversely proportional to channel dimension and proportional to surface tension. The importance of surface tension may explain the observations by Pfahler et al.(1990); 0.5 micron channels blocked for water flow (due to air bubbles), and likewise by Stemme et al.(1990) who reported that alcohol had a flowrate three times higher than water through a 0.2 micron filter (i.e. the domination of surface tension effects).

Stanley et al.(1997) have investigated gas-liquid flows in microchannels and observe no turbulence suppression. It was claimed that a bubble-slug flow regime existed within the microchannel. Earlier work of Suo and Griffith (1964) produced a flow map, based on long bubble motion in capillaries, which supports such a claim.

Triplett et al.(1999, 1999b) have presented an experimental study of gas-liquid flow in circular and triangular tubes with hydraulic diameters in the order of 1 mm. The flow patterns reported were the same as in large scale flow, but transitions to between regimes happened at different flow conditions and velocity slip between phases was less.

Liquid-liquid systems have been investigated experimentally and theoretically. Bibby et al.(1998) model the liquid-liquid system of Shaw et al.(1998) using a commercial CFD package with interfacial mass transfer. Partition coefficients (determined from experimental data) have been included in the model. With choosing a suitable diffusion coefficient the simulations showed good agreement with experimental data. Burns and Ramshaw (1999) presented experimental flow patterns for two immiscible liquids in microchannels. It was found generally that the two phases flow in separate layers. However, it was demonstrated that the dominance of surface tension forces over gravity forces allowed the denser phase to flow over the lighter one.

2.4 Modelling

It has been stressed already that microreactors often form complete systems with actuators, sensors etc., and the modelling of fundamental transport phenomena may not describe the complete process. Therefore an understanding of the coupling between electrical, mechanical and thermal interactions is required. Numerical methods are usually employed for analysing such systems which are usually based on finite volume or finite element methods. However there are modelling difficulties with microreactor systems as the coupling of fluid flow, energy transport and chemical kinetics can give rise to a mathematical model with differing time and length scales. For conventional systems (macroscopic) it is sometimes possible to decouple the kinetics from the flow, but for microreactors, where high conversions are typically required, this may not be possible. Accounting for all variables will often lead to a stiff non-linear problem requiring large amounts of CPU time.

Hsing et al.(2000) have addressed some issues relating to scaling in microreactors, and have modelled a partial oxidation reactor that takes account of the fluid solid interactions through domain reduction. Essentially the reactor contained different solids (walls, heaters etc.) of differing vertical characteristic dimension, and the impact on the reactor performance is desired. Rather than numerically model all domains, which would require very fine grids for small solids, the concept of domain reduction was employed (Deen 1999) where the two dimensional solids are modelled as a one dimensional boundary condition. Such a reduction reduces CPU time and allows parametric studies to be performed with greater ease.

Modelling of complete systems have varied in complexity, Ernst et al.(1999) have used a commercial FEM flow code (FIDAP) to model microchannels for biomedical sensors. The simulations allowed optimised design and operating parameters to be used for fluidics and temperature. Sesterhenn et al.(1999) use a lumped model approach for modelling of complex capillary network and show good agreement with experimental data.

Integrated modelling at this scale has not been limited to MEMS and microreactor systems, valuable literature and concepts stem from other disciplines. Some interesting work in microfluidics has been applied to the medical discipline. Böhnke (1999) considers the fluid-structure coupling in the inner ear. De Wachter et al.(1999) study artificial kidneys where the dialyzer is essentially a hollow plastic tube filled with thousands of capillaries made from a semi-permeable membrane.

The Navier-Stokes equations are applied, with the Darcy equation applied across the membrane.

2.5 Applications

Initial applications of microreactors were for analytical purposes. Within the last decade the trend in microreactor research has been towards production. Much of the initial work has been experimental for new and existing processes.

2.5.1 Unit operations

For gas phase systems there are important works which demonstrate from the outset the potential of microreactor systems. An experimental paper was produced by Wei*β*meier and Hönicke (1998) where a series gas phase hydrogenation was performed using a variety of catalysts in different types of reactor. Specific surface area of the catalyst was increased by anodising the surface, allowing high space-time yields. The aim of the work was to produce the thermodynamically unstable intermediate by utilisation of the regular geometry/pores inherent in the microreactor. Internal mass transfer is discussed with reference to kinetics, and it is concluded that the diffusional limitation should be kept low. External mass transfer resistance is kept low (by reducing dead volumes), and yields of intermediate are increased. Conventional catalysts allowed, generally, 80 % conversion with a 62 % yield, whilst the microreactor gave results of 98 % conversion with 90 % yield.

Burns and Ramshaw (1999) have performed experimental (based on visual observation) and numerical work with respect to hydrodynamics and liquid-liquid extraction processes, the inherent laminar profile provides an ideal environment for such an operation. The work concerns parallel cocurrent two-phase liquid-liquid flow in a microchannel over a range of flowrates and viscosities. The two fluids used were kerosene and propanol and it was shown that buoyancy effects were negligible in these small scale regimes, as the lighter kerosene was able to flow under the denser propanol. If the viscosity ratio of these two fluids is too high then the flow is difficult to stabilise, whilst at higher flowrates droplets form due to surface energy limitations. CFD simulations showed good comparison with the simple experiments. In addition BNFL (Bibby et al.1998) have developed other liquid-liquid mixing systems and verified such work using CFD. It was shown that for a 100 micron channel complete mixing was accomplished in one second.

Jähnisch et al.(2000) have operated a micro falling film reactor (MFFR) for the direct fluorination of toluene using elemental fluorine. Traditional fluorination processes have required multistage operations, which consequently have a lower yield. Direct fluorination had previously been attempted in the gas phase but selectivities were low. Previous work in the liquid phase was shown to be very unstable with many undefined byproducts and explosions due to high heat release. In light of these operational problems microreactors were envisaged to be an ideal candidate for operation. The work performed in the MFFR showed liquid films in the order of 10 microns yielding high heat transfer and interfacial areas. In conjunction with a well controlled RTD the microreactor was able to show near constant selectivity with conversion, with higher selectivities than conventional processes. The performance benefits were mainly attributed to the high interfacial area, however an increase in temperature much above -10°C resulted in reduced selectivities due to radical formation. This is an important work as it concentrates not just on process performance but also on the possibility of new synthesis routes.

Penth (2001) concentrates on the practical hydrodynamic aspects of a possible industrial microreactor by demonstrating a design that reduces the possibility of clogging. The basic principle is that two liquid jets of reactants are introduced normal to each other and perpendicular to an inert carrier gas, which serves as coolant and transport. The reactants are transported in a very fine liquid film, which reduces the possibility of blocking and allows no reactant to remain in the reaction chamber after the reactor has ceased operation. Such a design has allowed many operating parameters to be uncoupled such as residence time and reactant flowrate. The possibility of extending this design to the production of ceramic nano-materials has been considered also by the collision of aqueous precipitation reactants.

Downstream processing of the microreactor product is another concern, although the tuning of microreactor performance should serve to minimise such processes. Nevertheless progress has been made in the preparation and characterisation of ultra-thin polymeric membranes for the separation of gases and liquids (Harre 1998).

2.5.2 New operating conditions

Veser (2001) has constructed a microreactor for high temperature oxidation (hydrogen/oxygen system; Pt catalysed). The work was based on operating the reaction medium at compositions and temperatures that are in the conventional explosive regime, yet no flames or explosions were observed over a wide range of operating conditions. In the past some authors have attributed this to the microreactor being less than the quench diameter of a particular mixture, and rapid heat transfer prevents any ignition. Through a kinetic analysis Veser has challenged these ideas and attributes the reactor stability additionally to the concept of radical quenching, where the radicals formed in the homogeneous phase meet the reactor wall (which acts as a third body) and result in a termination step despite operating in temperatures in excess of 1000°C. Veser concentrates on the point that microreactors are intrinsically safe and that the performance increase in comparison to conventional fixed bed reactors lies in the fact that there are no explosions or flames (i.e. the operating regime bounds are relaxed).

Researchers at MIT have also operated microreactors in the explosive regime, and Chopey et al.(1997) report reactions of ethane in oxygen at values up to 85 % without any explosion.

New hydrodynamic regimes have also been reported, and Hessel et al.(1998) have considered multiphase microreactors and provide concepts for phase contacting. Traditional types of multiphase reactor are compared, and it is stated that no conventional configuration can achieve both high heat and mass transfer. Dispersed phase configurations based on Taylor and hexagon flow (Hessel et al.1998) are explained along with experimental evidence for their existence. Lowe further states that coalescence can be completely avoided by employing non-dispersed methods; examples are given in the form of corrugated sheets and two channel systems connected by openings where solute is transferred through the area where phases contact, but do not mix. These configurations are similar to the work of Bibby et al.(1998).

2.5.3 Process development

As already stated microreactors have the ability to operate in conditions not possible using conventional apparatus. A well defined residence time distribution and good temperature control allow reactor performance to be tested quickly with a small amount of chemicals. Wörz et al.(2001) have used microreactors for the synthesis of vitamin precursors, where the product can combine with an intermediate to form an unwanted by-product. The reaction is highly exothermic, but the use of a microreactor suppressed any formation of a hot spot and allowed rapid quenching (enabling further processing of the unstable product). Thus, within a short amount of development time a maximum yield of 95 % was attained combined with low by-product formation.

2.5.4 Process intensification

Process intensification is the term used to describe novel designs of unit operations that have low inventories, low energy consumption and a high production to capacity ratio. A principle of process intensification is to reduce mass transfer resistances and utilse the fluidic environment to allow intrinsic reaction kinetics to determine process performance and not heat and mass transfer (Green et al.(1999)). Microreaction technology can be viewed as a limiting case of process intensification.

Hessel et al.(1999) determined experimentally the specific interface transfer area in multiphase flows using micro bubble columns and micro falling film reactors. For the micro bubble column the specific interfacial area is quoted as 15,000 m^2/m^3 and 27,000 m^2/m^3 for the micro falling film reactor. Such values are at least an order of magnitude greater than conventional contacting systems. Conventional bubble columns have specific interfacial areas in the order of 50 to 600 m^2/m^3.

2.6 Comparison with conventional catalytic reactors

It is initially envisaged that microreactor applications would focus on the fine chemical and pharmaceutical processes. Hence this section will review macro-scale technology for catalytic and multiphase catalytic processes with consideration as to how microreactors could improve process performance.

Fine chemical and pharmaceutical processes typically involve complex chemistry structures with the added constraint of very high purity. Conventional industrial processes utilised methods that concentrate on stoichiometric organic synthesis, with the offset of disposal problems caused by large amounts of byproducts (consisting mainly of organic salts). With many steps in the process the overall yield was poor, but economics allowed such inefficient processes to run.

In light of the above, many processes are favouring catalytic processes that lower by-product problems and hazardous chemical inventories, and the typical number of reaction steps for a catalytic pharmaceutical process is about eight (Mills and Chaudhari 1997). Typical configurations of such catalytic processes are liquid phase reactions with gas, liquid and/or solid phase reactants and soluble homogeneous or solid heterogeneous catalyst.

The main reaction classes include; hydrogenation, oxidation, alkylation, reductive amination, hydroxylation, isomerisation, acylation, and oxidative carbonylation. Final application areas of such processes include agrochemicals, pharmaceuticals, detergents, dyestuffs, perfumery, food products, polymers and synthetic fibres.

Although an introduction to general multiphase reactor types will be given later, batch or semi-batch reactors are often used due to low production rates; the most likely area microreactors will make an impact.

One of the most important considerations for reactor design is the control of reaction temperature, limiting reactant concentration and to understand its effect on selectivity and product quality. As such processes are multiphase the interfacial mass transfer and mixing will greatly influence the overall rate of reaction.

Another constraint on reactor design is that for pharmaceuticals the product must be of high selectivity and purity, as traditional separation techniques may not be feasible. Stereoselective conversion is often desirable, as resulting isomers often have different physical properties that aid in separation. It is also worth noting that some processes require continuous removal of products due to: detrimental effect on catalyst activity, unstable nature under reaction conditions, or thermodynamic equilibrium.

The catalyst in such processes is often expensive (high effectiveness factor is desirable), and a high efficiency of separation from the product may be a challenge (as often the product is non-volatile). Also the activity of the catalyst over many batch cycles/time on line should be considered, though it should be noted that catalysts are not normally recycled in pharmaceutical processes due to the possibility of product contamination (Mills and Chaudhari 1997).

Different types of conventional multiphase reactor will now be presented, first looking at gas-solid systems and then gas-liquid-solid systems.

It should be noted, as a practical matter, that a common use of multiphase reactors is for hydrogenations. Almost all hydrogenators work as heat transfer limited devices, hence the reaction is forced to proceed at the fastest rate possible at which the cooling system can maintain isothermal operation (Concordia 1990). Other (independent) process variables; pressure, temperature, catalyst load are set according to heat release/rate of reaction.

2.6.1 Gas-solid reactors

Plug flow reactors

Gas catalysed reactions are usually performed in a fixed bed plug flow reactor, as back mixing is undesirable due to possible adverse effects on selectivity. However under certain constraints such reactions can be performed in fluidised beds.

One of the main disadvantages of a plug flow reactor is that the heat generation is uneven, hence for a very exothermic reaction such a process might be uncontrollable. To overcome this many smaller tubes are used to enhance the surface/volume ratio; coolant runs around the outside of these tubes. As many as 20,000 tubes have been reported in an industrial PFR (Rose 1983), a schematic is shown in Fig. 2.1.

Temperature control in fixed beds is a problem as they are characterised by a low overall conductivity. If the plug flow reactor is cooled at the wall for an exothermic reaction (not adiabatic) then the centre of the reactor is hotter which sets up radial

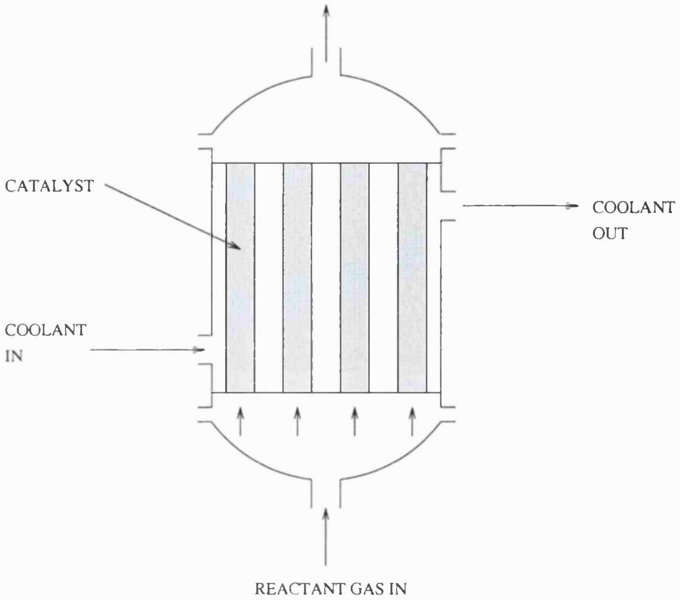

Figure 2.1: Multi-tube plug flow reactor.

gradients of heat and mass also.

For consecutive reactions (where the intermediate is required) in the PFR any by-products should be minimised by considering any diffusional limitations. Diffusional resistance (mass) is detrimental to reactor performance, as to overcome the resistance the product will have to be present at relatively high concentrations at the catalyst surface. Such a scenario will accelerate the reaction rate hence lowering selectivity.

Another general consideration is the presence of side reactions with higher activation energies. If heat generated by the exothermic reaction is not effectively removed the rate of the side reactions will be augmented, again lowering selectivity. If the reaction is only mildly exothermic then a single bed may be used; the dimensions determined by contact time and diameter to achieve plug flow.

Fluidised bed reactors

As mentioned before the fixed bed approximates plug flow, this is in contrast to the fluidised bed which has much by-passing. Hence a greater amount of catalyst may be needed for a given conversion. For higher conversion the amount of intermediate in series reaction may be depressed, hence the product should be removed as fast as possible. However there is better temperature control, therefore fluidised beds allow for the potential of near isothermal operation.

Another advantage of fluidised beds concerns the size of the catalyst particle. Fixed beds cannot use small particles due to 'clogging' and pressure drop (tube to particle diameter ratio is usually at least 10 to ensure plug flow and to prevent too

Type	Advantages	Disadvantages
Fixed bed (PFR)	Good catalyst contacting	Heat transfer limitations
Fluidised bed	Good heat transfer characteristics	Axial mixing
Monolith	High transport coefficients	Expensive to build
Gauze/wire	Good heat transfer characteristics	Poor distribution at low flow

Table 2.1: Performance characteristics of gas-solid reactors.

much channeling at the tube wall (Christoffel 1982). No such limitation exists for fluidised beds where for fast reactions (film limited) the fluidised bed allows for a more efficient use of the catalyst.

Catalyst regeneration is also easier in fluidised beds due to the fact it can be continually removed and replaced throughout the operation.

Monolithic reactors

In processes that are very exothermic non-porous/monolithic catalytic reactors are used. For such reactions the extra surface area created by a porous catalyst would make the heat transfer problem more severe (Fogler 1992). Typical dimension of the channel is about 5 mm-1 cm, whilst the length can range from 5-50 cm. Typical gas velocities are between 5-20 m/s.

Gauze/wire reactors

A gauze/wire reactor consists of a series of wire screens stacked one on top of the other, where the wire is typically made out of a platinum or a platinum-rhodium alloy. Diameter of the wires ranges between 0.004 and 0.01 cm (Fogler 1992). Coppage and London (1956) have presented heat and mass transfer data (in the form of j factors) with a Reynolds number based on hydraulic radius and interstitial velocity; $\frac{4r_H G_i}{\mu}$ where r_H is the hydraulic radius of the screen, and G_i is the mass velocity based on free flow area.

2.6.2 Multiphase reactors

The most common types of operation that involve gas, liquid and solid phases are hydrogenation, oxidation and hydration. An appropriate design and model of a three phase reactor requires the estimation of various transport (momentum,mass and heat), kinetic, and mixing parameters (Shah 1979).

Trickle/fixed bed reactor

A three phase reactor with a fixed bed of solids is usually operated by flowing liquid and gas cocurrently downward, this mode of operation defines the trickle bed reactor (favoured in the hydro-processing industry). However regardless of the flow regime, a thin liquid film exists over the solids. The relative merits of varying flow orientation will be discussed later in this section.

The trickle bed reactor has eight significant advantages (Shah 1979) which are now presented.

Firstly the catalyst is well wetted, and the reactor is usually operated under plug flow conditions (whether plug flow could be achieved in a scaled down version is a further matter that will need discussion in reference to the microreactor). However in light of the above high conversion in a single reactor configuration/design should be possible.

The liquid holdup (liquid-solid ratio) in a trickle bed reactor is small, hence the significance of homogeneous reactions are lowered.

Resistances between phases are combined, due to the 'thinness' of the liquid film (usually considered separately), as the film is very thin the interfacial resistance is lower than other types of three phase reactor.

As previously mentioned the trickle bed reactor usually operates under cocurrent downward flow conditions, hence flooding is not a problem and pressure drop is lower. Lowering the pressure drop allows for a near uniform partial pressure of the gaseous reactant (i.e. ensuring hydrogen rich conditions at the catalyst surface; starvation may cause catalyst decay).

The unit can be operated as a partially or completely vapour-phase reactor, this minimises the energy cost associated with reactant vaporisation. Also in a commercial reactor a uniform distribution of gas and liquid are achieved.

For an exothermic reaction, temperature control may be achieved by the use of 'quench' streams (usually gas) from the side of the reactor or recycling the liquid product (not possible when high conversions are required: CSTR like operation).

Shah (1979) also states some disadvantages of the trickle bed reactor. A major problem is the radial distribution of heat in large scale reactors. Localised heating can cause catalyst decay, excessive vaporisation of the liquid film, and a decrease in selectivity.

If the liquid flowrate is low then flow maldistributions may result; channelling, bypassing and incomplete catalyst wetting.

Due to pressure drop considerations the particles cannot be very small, hence intra-particle diffusion effects can be significant.

Liquid velocity (m/s)	Gas velocity (m/s)	Pressure drop (Pa)
1×10^{-03} - 2×10^{-02}	0.15 - 3	10^4 - 10^5

Table 2.2: Numerical data for industrial fixed bed reactors.

Fixed bed variants

The relative orientations of gas and liquid phases effect the overall performance of the reactor, i.e. the hydrodynamics, along with heat and mass transfer. Hence for some operations the fixed bed does not operate with cocurrent downward flow (trickle bed). For cocurrent up-flow conditions the following points should be borne in mind for design/operating parameters.

Up-flow operation gives better mixing (radial and axial), higher transfer coefficients, higher liquid holdup, better liquid distribution, better heat transfer between liquid and solid, lower concentration of solid particles and less solids plugging in relation to down-flow reaction under equivalent flow conditions. However cocurrent up-flow operation also has negative aspects; larger pressure drop, poorer conversion (axial mixing), higher degree of homogeneous reactions and more intra-particle diffusional effects. The possibility of flooding must also be considered.

Counter current flow conditions are usually favoured for gas-liquid reactions. The main function of the solids are to impart momentum transfer and promote better contact between gas and liquid. The flowrates of the fluid phases are high (near flooding), hence packing is larger to avoid excessive pressure drop.

Typical film thickness for countercurrent flow is between 0.01 and 0.1 mm under hydrodesulphurisation conditions (Satterfield 1970).

Bubble column slurry/fluidised bed reactor

In this type of reactor gas is dispersed through a deep pool of liquid containing suspended catalyst particles (Ramachandran and Chaudhari 1983). Fine catalyst particles are used in these reactors, momentum is transferred to the liquid and solid phase by movement of the gas bubbles. Typical dimensions are a height to diameter ratio of 4-10.

The reactor may be operated in batch or continuous mode (with respect to liquid), Fig. 2.2 shows a schematic of a bubble column slurry reactor.

Advantages of this type of reactor are high heat transfer due to the high liquid recirculation rate. Also, due to the absence of moving parts, maintenance and running costs are lower. A higher utilisation of the catalyst is possible as small particle sizes can be used, hence the intra-particle diffusional resistances are lowered.

Also, molecules that are easily damaged by the shear of the impeller (usually

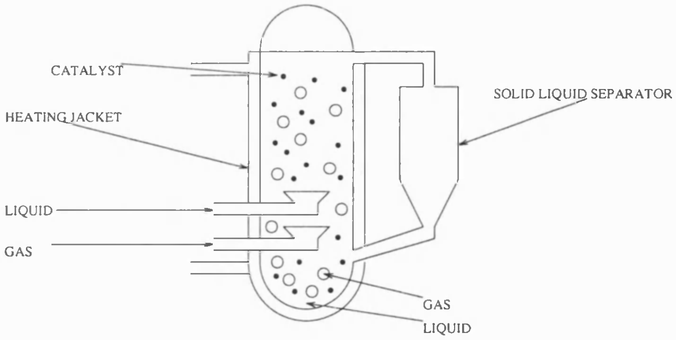

Figure 2.2: Schematic of a bubble column slurry reactor.

biological) can be used in the bubble column reactor.

However disadvantages do exist with this type of reactor, namely that there is a significant amount of back-mixing in the liquid phase which will result in poorer reactor performance. Also pressure drop should be considered if the reactant gas is only available at atmospheric pressure. A rapid decrease in specific interfacial area exists with a height exceeding the height-diameter ratio of 10, this is due to the increased rate of coalescence of gas bubbles at these higher ratios.

The common heat transfer surface is usually either a jacket or a helical coil inside the vessel. Heat transfer in a bubble column is limited due to the high film resistance present at heat transfer surfaces due to the fact that turbulence and fluid velocity are produced only by rising gas bubbles and the wakes they create. Also the vessel and coil geometry place an upper practical limit on the amount of heat transfer area that can be applied inside a vessel.

The rate of gas-liquid mass transfer is often the apparent reaction rate. It is well known that the amount of gas-liquid mass transfer depends on certain physical properties of the materials and the interfacial area available for the transfer. As the physical properties are largely determined, via the operating conditions, the interfacial area and hence the overall mass transfer coefficient, are primarily a matter of reactor geometry (Concordia 1990). The interfacial area is the sum of the surface of the gas bubbles dispersed in the reaction medium. Hence the characteristics of the bubble column reactor can be described in terms of the average bubble size they produce.

The relative orientation of phase flow is important in the bubble column reactor. If gas is introduced at the bottom of the reactor, then as the bubbles rise they will coalesce (increase in diameter) and lower the interfacial area. With downward gas flow the small bubble size is maintained over a longer reaction path, hence an increased overall gas transfer rate. Typical bubble sizes and interfacial area are presented later in this report for comparison purposes. Important parameters for design and modelling of bubble column slurry reactors are:

Reactor type	k_{La} (1/s)	$k_s \times 10^3$ (m/s)
CDC	12.0	7.0
CSTR	8.6	3.0

Table 2.3: Transport parameters for the CDC and CSTR (Lu et al.1996).

- Flow regime.
- Catalyst suspension.
- Gas holdup.
- Average bubble diameter.
- Gas-liquid mass transfer.
- Liquid-solid mass transfer.
- Heat transfer.

Correlations, by many authors, are presented in Ramachandran and Chaudhari (1983) for the previous list, however heat transfer will be elaborated upon. For exothermic reactions the inclusion of an efficient heat removal system in necessary, hence a knowledge of the heat transfer coefficient is needed. Along with the heat transfer removal methods already mentioned, heat can also be controlled by boiling a solvent or reactant which is close to the desired temperature. The bubble action provides good heat transfer, whilst the back-mixing of the liquid phase allows near isothermal operation for moderate exothermic reactions.

Novel bubble column reactors

Lu et al.(1996) have altered the hydrodynamics of the reactor to cocurrent downflow column operation (CDC), which generated a greater surface area as coalescence was retarded to a greater extent. In the conventional bubble columns, described previously, it is the gas-liquid mass transfer that is often the rate limiting step but Lu et al.(1996) showed that the contribution of such a resistance to the overall reaction rate was low in comparison to the liquid-solid mass transfer and surface reaction rate.

For a 5% loading of Pd on carbon catalyst, with water as a solvent, the transport coefficients are compared to a slurry CSTR, which is shown in Table 2.3.

Despite the fact that numerical values of the transport parameters are in the same order of magnitude as the CSTR, the main advantage of the downflow bubble reactor is that it maintains the mass transfer efficiency on scale-up. Lu et al.(1996)

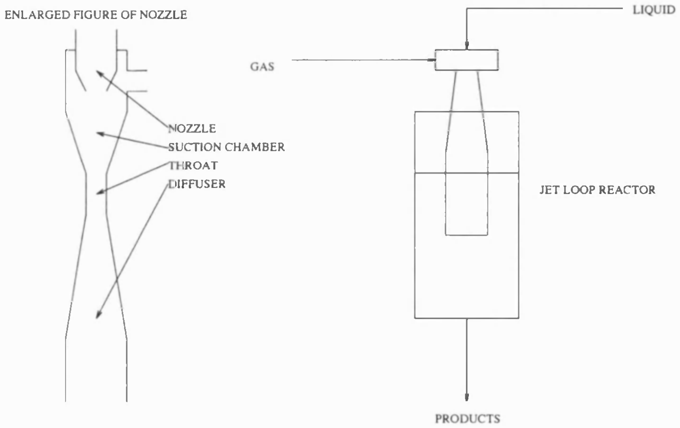

Figure 2.3: Schematic of jet loop reactor.

also show that the power input to CDC is only about 10% of a CSTR under similar reaction conditions. Hence the conclusion of the study was that the CDC could be successfully scaled-up and could be used for relatively fast reactions, unlike some bubble columns.

Jet loop reactor

The jet loop reactor is a relatively new type of reactor that is highly efficient in gas dispersion resulting in higher mass transfer rates. A schematic of the jet loop reactor is shown in Fig. 2.3.

The principle in this reactor type is the utilisation of the kinetic energy of a high velocity liquid jet to entrain the gas phase and create a fine dispersion of the two phases (Dirix and van der Wiele 1990).

The ejector discharges into the main vessel, and the liquid can be circulated through the system via an external loop. However the main ejector can be subdivided into several sections, as shown in Fig. 2.3. Initially liquid is supplied to the reactor via the nozzle and consequently gas is sucked into chamber. A mixing shock occurs in the throat (Witte 1968), causing intensive mixing of the two phases. Mass transfer then takes place in the diffuser.

The gas phase residence time is increased significantly in the jet loop reactor described previously (in comparison to jet-propelled loop reactors that have the nozzle at the bottom of the reactor) as the gas bubbles are forced to move in a direction opposite to their buoyancy.

As mentioned previously, heat transfer in reactors is an important parameter. Jet loop reactors typically incorporate shell and tube heat exchangers in an external loop. Hence the cooling capability of a jet loop reactor is more than an order of magnitude greater than a CSTR or bubble column. A high heat transfer coefficient and a very high heat transfer area, as this is external to the reactor, give the loop reactor superior performance in heat-transfer limited processes (Concordia 1990). However such looping of the liquid phase may have an adverse effect on reactor selectivity (as this serves as a form of back mixing), also jet loop reactors usually have a higher operating pressure (Concordia 1990).

Padmavathi and Remananda Rao (1991) have reported how the jet loop reactor can be applied to three phase systems and investigate the hydrodynamics with reference to the effect of solids. The apparent liquid circulation velocity and overall gas holdup increased with increasing liquid and gas flowrates and with decreasing solids loading and particle density.

Numerical parameters are presented later in this section, along with other types of reactor for comparison.

Monolith reactor

In this section the reader is encouraged to consider the monolith reactor as a scaled up version of a microreactor, although the monolith reactor has no cooling channels. Monolithic catalysts contain many small parallel passages, with the catalytic species incorporated into a thin porous oxide layer deposited on the channel wall, or into the wall itself (Edvinsson and Cybulski 1995). Traditionally the monolith reactor has been used for gas phase processes, but has now been extended to multiphase reactions. A single example of an industrial application is in hydrogenation where EKA-Nobel operates several plants in which monolith reactors are used in the hydrogenation step of the alkylantraquinone process for hydrogen peroxide production (Edvinsson and Cybulski 1995 and Irandoust et al.1989).

The flow pattern in the monolith is a series of alternate gas and liquid plugs (Taylor flow), which has good mass transfer characteristics due to the internal recirculation within the plugs and the short diffusion distance through the thin liquid film separating the bubble from the wall (Edvinsson and Cybulski 1995). The work performed on gas-liquid-solid reactions in monoliths has been compared to the trickle bed reactor (described previously) as the most common conventional reactor for three phase hydrogenations. Parameters attributed to selection of reactor are: catalyst geometry, internal and external mass transfer resistance, contact areas and pressure drop. Analysis of both types of reactor should show where trade-offs exist and indicate regions where each type has greater potential; Edvinsson and Cybulski (1995) has attempted this.

Monolithic blocks are assembled in frames that can be stacked on top of each other, and are relatively more expensive than a trickle bed reactor. This higher cost

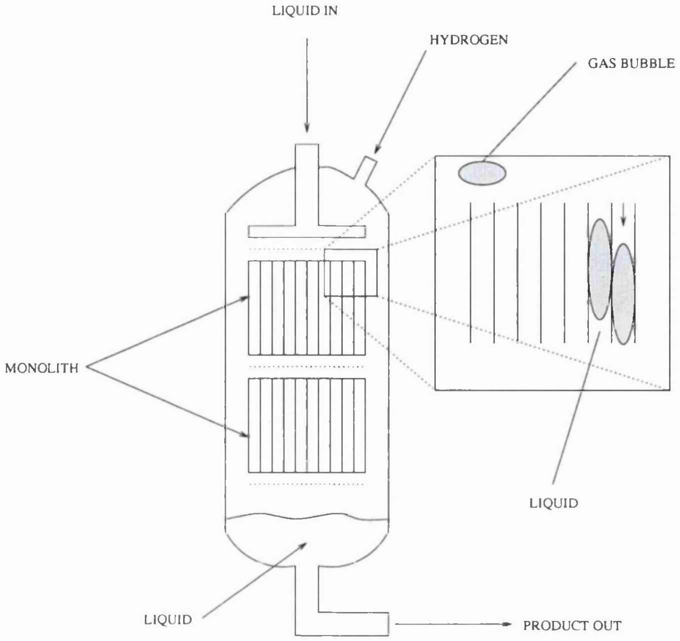

Figure 2.4: Schematic of a monolith reactor.

can be attributed to the fact that so far monolith reactors have been used for high temperature operations. However the use of monoliths can be economically justified for systems where it has an advantage, like higher yield (selectivity), increased throughput, lower running costs.

For reactions that are not mass transfer controlled (kinetic regime) then the trickle bed reactor will yield better reactor performance due to the higher load and lower cost of the catalyst. Edvinsson and Cybulski (1995) also stipulate that if selectivity is an issue (intermediate in a series reaction) then it is not immediately obvious which reactor should be used for the process.

Internal diffusion (diffusion within catalyst) length is shorter in a monolith reactor, the effective diffusion length can greatly affect the selectivity of the reaction if the reaction is mass transfer controlled. Attempts to lower the diffusion distance in the trickle bed reactor are possible by decreasing the size of the catalyst particle, but this will lead to the problems of small particles in fixed beds as mentioned previously.

A major advantage of the monolith reactor is the low pressure drop, if the reactor is operating in a down-flow mode then it is possible to balance the frictional pressure drop with the hydrostatic pressure of the liquid in the channels. An essentially zero net pressure drop provides an opportunity to operate the reactor with an internal recirculation of hydrogen with no recompression needed, hence lower running costs.

Edvinsson and Cybulski (1995) report on the catalyst types present in a monolith; incorporated and washcoat, his review of reactor performance is based upon a

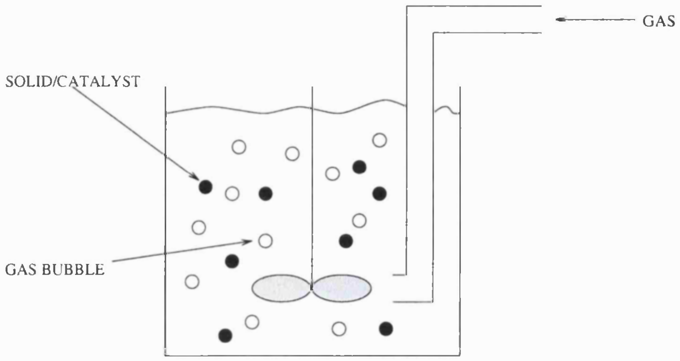

Figure 2.5: Schematic of slurry reactor.

'typical' series L-H kinetic reaction. Selectivity increases with decreasing catalyst thickness, as the external surface area decreases with increasing washcoat thickness. For traditional catalyst particles the effectiveness factor increases with thinner catalyst layers. An optimum exists for overall conversion. The monolith in this case should be compared to a catalyst particle with the same performance and other factors assessed. A point that is also highlighted is that non-uniform distribution may occur with washcoats, where all active material is in the corners: this has a negative effect.

Reaction kinetics obviously influence the choice of reactor, for fast reactions large particles are rendered unsuitable and small or shell particles must be used, although for slow reactions the trickle bed will be favoured due to the higher catalyst loads possible. Edvinsson and Cybulski (1995) give a criterion (based on reaction rate at beginning of reactor) for the choice of trickle bed or monolith reactor.

A major advantage of the monolith reactor concerns the operating cost relating to pressure drop. Large trickle bed reactors may have to have reasonably large catalyst particles to reduce pressure drop (however due to higher catalyst loadings productivity will be higher), but this also increases diffusional resistance and lowers external surface area. Selectivity is generally higher in a monolith along with insensitivity to bed depth, this will be determined by an acceptable pressure drop.

Microreactors should be compared with these monoliths (based upon characteristic dimension), as the relative performance should be greater than a standard monolith which in turn should have greater process merits than the conventional trickle bed reactor.

Slurry reactor

The slurry reactor is essentially a CSTR with solids and gas present in a bulk liquid medium, a schematic is shown in Fig. 2.5.

The slurry reactor is usually operated in batch mode, for a continuous process a fluidised bed would be used. Major advantages of the slurry reactor are the flexibility of mixing, heat recovery, and temperature control (Shah 1979). This is due to the fact that high speed mixing promotes gas dispersion and heat transfer. An inherent limitation of the system is caused by a relatively high film resistance due to low wall velocity (Concordia 1990). Fine catalyst particles can be used, which in turn minimise the intra-particle diffusion effects. However the usual limitation of a CSTR exists, namely that of poor conversion due to axial mixing. This may be overcome by reactor staging, but would ultimately result in a higher initial investment. It is also worth noting a high liquid holdup may give rise to significant homogeneous reactions and mass transfer resistances for the gaseous reactant.

Spray tower reactor

These reactors are designed for two phase systems (gas-liquid), where the liquid is atomised and enters the reactor as a fine spray at the top. Gas enters the vessel at the bottom, which has to be kept sufficiently small to permit the liquid to fall (Froment and Bischoff 1990). To achieve an efficient dispersion of the liquid the openings of the distributor must be small and the pressure high. A certain fraction of the liquid drops will hit the reactor wall and flow down as a film, whilst some coalescence will also occur with the result that interfacial area is lowered. Another effect of coalescence is that the velocity of the phase alters, hence the residence time will vary strongly with position. Mehta and Sharma (1970) have studied the overall behaviour of spray tower reactors and have provided correlations for the interfacial area and the overall mass transfer coefficient. Liquid residence times are in the order of 1 to 10 s (Perry 1998), as are the gas contact times. However back mixing can occur due to distribution of drop speed (caused by distribution of sizes of drops) and liquid striking the walls. Hence one of the design objectives for these devices is to obtain a uniform spray pattern with minimum collection at the walls.

Falling film reactor

The falling film reactor (FFR), also known as a wetted wall column, has found applications in problems where a high ratio of heat transfer to mass transfer is needed. Also pressure drop within the system is low and contact times are small. Large areas of open surface are available for heat transfer for a given rate of mass transfer in this type of equipment due to the low mass transfer rate inherent in falling film equipment.

Some typical film thicknesses, based upon a sulphonation reaction, are given in the work of Talens-Alesson (1990); such thicknesses have a range from 4.9×10^{-4} m to 8.5×10^{-4} m. Riazi et al.(1986) have discussed that the effect of gas phase heat and mass transfer resistances cannot be generally neglected in falling film apparatus. However only heat transfer at the wall will be considered for comparison purposes in this report, it is generally assumed to be greater than gas phase transfer.

Several correlations exist for heat transfer and film thickness in annular flow devices, but for comparison purposes quoted numerical values will be used. A range of film heat transfer coefficient values quoted from Ludwig (1983) for the fluid-solid heat transfer coefficient are 340-2839 W/m^2/K.

Mass transfer for liquid wetted wall columns is highly dependent upon surface conditions. If total laminar conditions prevail then transfer behaviour can be predicted by film/penetration theory. At a Reynolds number greater than 4 ripples/waves start to form resulting in surface regeneration which entails greater mass transfer.

2.6.3 Microreactors

Typical arguments for the industrial introduction of microreactors stem from broad classifications such as: inherently safe production and high heat and mass transfer rates.

Microreactors generally exploit the advantages offered by very small channels, typical characteristic dimensions are around 400 microns. Allen (1999) gives a summary of such advantages which are now presented. Small length scales have low momentum and thermal convection times and mixing is controlled by diffusion processes. However at these scales the transport limitation is not a problem, although the residence time distribution may hold the same shape as in laminar flow the actual difference in residence times may be comparable or better than near plug flow in macro-scale equipment. The high surface area to volume ratio allow surface characteristics to dominate the performance, such as catalysis and heat transfer. Small inventories give rise to low holdups and lowered exothermicity risk, along with fast response to control systems as integrated instrumentation is possible.

Table 2.4 presents data from Allen (1999) and Edvinsson and Cybulski (1995) concerning the surface area per unit volume for different types of reactor. Note that despite the monolith and the catalyst bed having similar external surface areas, the monolith benefits from having a lower pressure drop and a regular pore structure. Typical diffusion lengths for catalyst beds are 0.1 (shell) to 2.5 mm, whilst for monolithic reactors the distance is 50-150 microns. Hence as channel dimensions get smaller a higher value of the effectiveness factor (in comparison to analytical solutions for cylinders and spheres etc. (Froment and Bischoff 1990)) should result

Microchannels m^2/m^3	10^4-10^5
Catalyst bed external surface area m^2/m^3	10^2-10^3
Catalyst bed including pore area m^2/m^3	10^8-10^9
Monolith external surface area m^2/m^3	10^3

Table 2.4: Surface characteristics of some reactor types.

from a smaller value of the Thiele modulus, by virtue of a lower characteristic dimension.

The small channel advantage also alters the chemistry, Allen (1999) states that a higher precision can be obtained in the chemistry due to the high heat transfer, which can give precise control over the temperature-time history. Also excellent mixing at the molecular level gives close control over the concentration/time profile.

Heat transfer coefficients have been reported as high as 10,000 $W/m^2/K$ (liquids) and 1000 $W/m^2/K$ (gases) from PNNL (Chopey et al.1997), under boiling conditions values were reported at 35,000 $W/m^2/K$.

RTD considerations

In this section a further argument is made for the use of microreactors based on the dimensional residence time distribution. For laminar flow in long tubes/channels Levenspiel (1999) states that the dispersion model is suitable for analysis. For this section a justification will be given on the basis of long tubes, which is summarised in Froment and Bischoff (1990).

The complete convection-diffusion equation is given in (2.1), this can be compared with the one-dimensional dispersion equation.

$$\frac{\partial C}{\partial t} + 2u\left(\frac{R^2 - r^2}{R^2}\right)\frac{\partial C}{\partial z} = D\left(\frac{1}{r}\frac{\partial}{\partial r}r\frac{\partial C}{\partial r} + \frac{\partial^2 C}{\partial z^2}\right). \tag{2.1}$$

Taylor (1953) showed that an important variable of interest was the mean concentration which could be found by averaging (2.1), which eventually gives (2.2).

$$\frac{\partial \langle C \rangle}{\partial t} + u\frac{\partial \langle C \rangle}{\partial z} \sim D_a \frac{\partial^2 \langle C \rangle}{\partial z^2}. \tag{2.2}$$

Where $\langle C \rangle$ is the mean concentration and in (2.1), R is the radius of the tube, r is the radial position, u is the velocity and D is the standard diffusion coefficient. However, in (2.2) the diffusion coefficient becomes the dispersion coefficient and is given by (2.3).

$$D_a = D + \frac{1}{48}\frac{u^2 R^2}{D}. \tag{2.3}$$

A condition of the above is that the radial concentration profile is fully developed; i.e. the length to diameter ratio be sufficiently large

$$\frac{L}{d_t} > 0.04\frac{u d_t}{D}, \tag{2.4}$$

where L is the length of the tube and d_t is the diameter of the tube. The dispersion coefficient provides a sum of ordinary diffusion coupled to the effect of the velocity profile; this is what primarily causes the distribution of residence times.

The material presented previous forms an overview of the Taylor analysis that provides a theoretical justification for the Taylor dispersion model, unlike the 'Tanks in series model' where the exponent, n (number of tanks), is purely empirical. The argument for smaller dimensions is based upon (2.3), where it can be seen as the size of the channel decreases so does the dispersion coefficient. Hence as the dispersion coefficient reduces the resulting concentration profile is more like plug flow: a sharper residence time distribution. If the convection-dispersion equation is made dimensionless, where $z = (ut + r)/L$ and $\theta = t/\bar{t} = tu/L$, then the model is given by (2.5).

$$\frac{\partial C}{\partial \theta} = \left(\frac{D_a}{uL}\right)\frac{\partial^2 C}{\partial z^2} - \frac{\partial C}{\partial z}, \tag{2.5}$$

where the dimensionless group (D_a/uL) is termed the vessel dispersion number, its limits are at zero and infinity. These limits represent ideal plug flow and fully mixed flow respectively. When the dispersion number is small ($\ll 0.01$) the dimensionless residence time distribution is given by (2.6).

$$E_\theta = \frac{1}{\sqrt{4\pi\left(D_a/uL\right)}} \exp\left[-\frac{(1-\theta)^2}{4\left(D_a/uL\right)}\right]. \tag{2.6}$$

It can be seen from (2.3) to (2.6) that the distribution of the dimensionless residence time curve reduces with respect to the square of the tube radius. However in light of a design for a reaction device a set parameter will be a residence time of 1.29×10^{-2} s (chosen to reflect the methanol oxidation process in Chapter 6). Two tubes will be considered of diameters 300 microns and 5 mm. For both tubes (1 cm in length) the superficial velocity required will be

$$\frac{L}{\bar{t}} = \frac{0.01}{1.29 \times 10^{-2}} = 0.78 \quad \text{m/s}.$$

The requirement for a sharp residence time distribution stems from the trapping of an intermediate in a series reaction, or where homogeneous reactions can adversely affect selectivity at a time scale that is greater than the desired residence time. For a gas the typical diffusion coefficient is 5×10^{-6} m^2/s, therefore substituting the numbers into (2.3) (for the 300 micron tube) gives

$$D_a = 5 \times 10^{-6} + \frac{1}{48}\frac{0.78^2\left(150 \times 10^{-6}\right)^2}{5 \times 10^{-6}} = 6.2 \times 10^{-5}\text{m}^2/\text{s}.$$

From (2.6) the dimensionless residence time distribution can be plotted, this is shown in Fig. 2.6.

For a diameter of 5mm the dispersion number approaches that of mixed flow. The dimensionless RTD curve for this type of flow is shown in Fig. 2.7.

If the limits of E_θ (upper and lower) are considered for the 50 micron and 300 micron tubes, then it can be seen that the numerical bounds (dimensional time) of the distribution can be obtained by

$$\theta_{range} = \frac{t_{range}}{\bar{t}}.$$

The dimensionless limits for the two tubes are given in Table 2.5.

The desired mean residence time has already been set and hence the dimensional

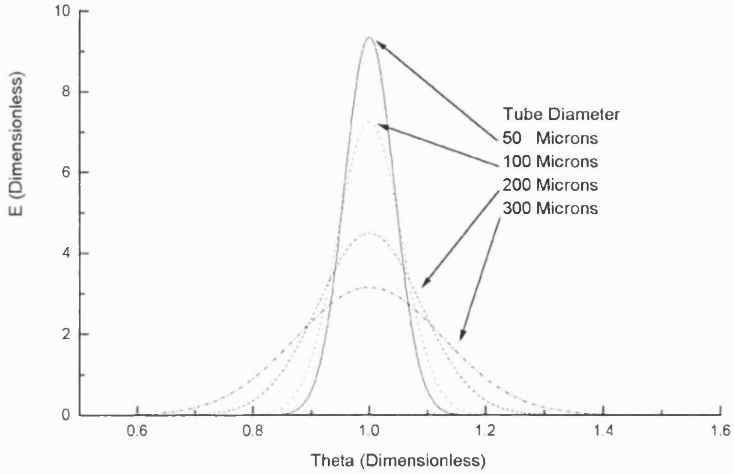

Figure 2.6: Dimensionless RTD for various tube diameters.

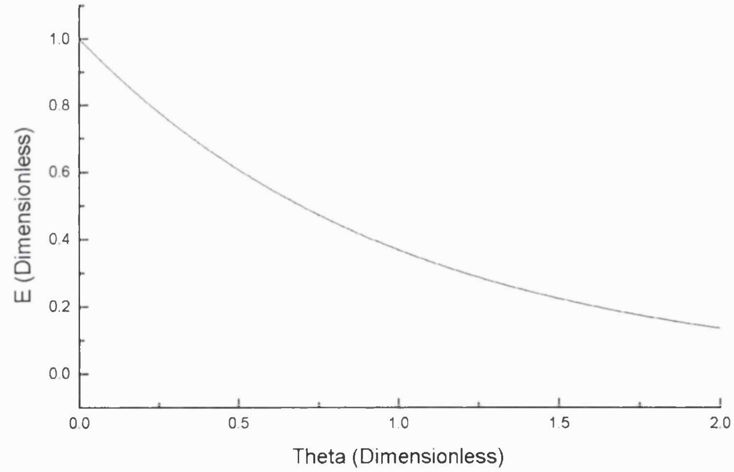

Figure 2.7: Dimensionless RTD for mixed flow conditions.

Dimensionless time	50 microns	300 microns
θ_{lower}	0.85	0.6
θ_{upper}	1.15	1.4

Table 2.5: Dimensionless bounds for 50 and 300 micron tubes.

times, for the 50 micron and 300 micron tube, are calculated as follows

$$t_{range(50\text{microns})} = 1.29 \times 10^{-02}\,(1.15 - 0.85) = 3.87 \quad \text{ms},$$

$$t_{range(300\text{microns})} = 1.29 \times 10^{-02}\,(1.4 - 0.6) = 10.32 \quad \text{ms}.$$

For the tube of 5mm the dispersion group has a value of 2, which is greater than the model above is applicable for, this corresponds to mixed flow and the range of θ is about >2.0 (Levenspiel 1999). This corresponds to a residence time range of >25.8 ms. This is over a 100 % increase in time (compared to 300 micron tube), which may be critical to a series reaction. Also note that if the tubes were a reactor and the catalyst was on the wall it is more likely that the RTD would be even further spread due to radial gradients, further research is needed to quantify such effects.

It should be noted that much shorter residence times have been reported in microreactors, PNNL has performed partial oxidation of hydrocarbons with residence times of only 1 to 10 ms. The previous theoretical justification of microreactors serves only to justify relative performance gains.

2.7 Conclusions

Tables 2.6 to 2.9[1] [2] show the relative merits of each of the main types of reactor discussed. For certain types of operation the reactor choice is obvious, and good guidelines are given in Levenspiel (1999). For fast kinetics the reaction zone is at the phase interface, hence any bulk liquid will only serve to reduce heat transfer etc. Therefore microreactors allow the bulk to be removed and allow operation in a more efficient manner. Table 2.9 shows typical bulk/film lengths of liquid for different types of reactor under 'standard' operating conditions (Concordia 1990).

In light of all the evidence presented in this literature survey a reactor is needed that can perform well for reactions that are fast, highly exothermic and may require a series intermediate as the desired product (i.e. a high selectivity with near complete isothermal operation). Microreactors have shown themselves to be an ideal candidate with heat transfer coefficients in the order of 10,000 W/m^2/K that can

---

[1] TB - Trickle Bed, FF - Falling Film, PFR - Plug Flow,
JL - Jet Loop, BC - Bubble Column, CSTR - Slurry Reactor

[2] Heat transfer areas are taken as equal for FB and BC as both use cooling jackets and sometimes have similar dimensions (for mild exothermic reactions).

achieve near isothermal operation without entering a mixed flow regime (detrimental to selectivity).

Reactor type	TB	FF	PFR(gas)	Monolith	JL	BC	CSTR(slurry)
Low film thickness	√	√		√			
Little backmixing	√	√	√	√			
Low intra p. diff.				√	√	√	√
High heat transfer		√		√	√		√
Low pressure drop	√	√		√		√	N/A
Low flowrate		√		√			√ (BATCH)
Low RTD	√		√				

Table 2.6: Merits of each type of reactor. [32], [36], [91], [99], [130]

Reactor type	Monolith	JL	BC	CSTR
Heat transfer area m^2/m^3	Adiabatic	27+external loop	~35	2.5-3.5
Heat transfer coeff. $W/m^2/K$	-	795-854	227-284	454-511
Pressure/pressure drop kPa	~zero	55E3	10E3	13.8E3
Interfacial area (G-L) m^2/m^3	1000-3000	2000-3000	600-1000	1000-1500

Table 2.7: Quantitative merits of each type of reactor. [32], [36], [90], [99]

Reactor Type	Microreactor	TB	FF
Heat transfer area m^2/m^3	10E4-10E5	~35	2.2-3.1
Heat transfer coeff. $W/m^2/K$	850-35E3	96	340-2839
Pressure/pressure drop kPa	Moderate-High	High	25-50
Interfacial area (G-L) m^2/m^3	27E3	1000-3000	2.2-3.1

Table 2.8: Quantitative merits of each type of reactor. [28], [130], [146]

Characteristic	CSTR	CSTR	BC	BC	JL	JL
Bound	Lower	Upper	Lower	Upper	Lower	Upper
Diameter(m)	0.003	0.006	0.004	0.008	0.001	0.002
Voidage	0.34	0.34	0.137	0.137	0.667	0.667

Table 2.9: Bounds of characteristic bubble sizes and void fraction for some types of reactor. [32]

Chapter 3

Modelling of Mass Transfer in Microreactors

3.1 Introduction

Prototype catalytic microreactors are costly to construct and can present manufacturing difficulties. To allow to enable rapid prototyping of these devices and optimising the performance, it is first necessary to develop models of these processes. Due to the high heat transfer coefficients in microreactors it is possible to consider isothermal operation. The governing equations are consequently the advection-diffusion mass balances for each species.

There is a large amount of literature on the solution of advection-diffusion partial differential equations (PDE's) which often are analysed by means of orthogonal eigenfunction series expansions. For single reactions the problem is analogous to heat transfer and a review of the literature is summarised in Table 3.1. A note must be made of the works by Denbigh (1951) and Cleland and Wilhelm (1956) where, in the limits of slow and fast radial diffusion, analytical results for second order homogeneous systems have been obtained. Jain (1985) have also reported results for reaction orders other than unity, but the results for zeroth and second orders were numerical although radial velocities were included in the analysis. A common feature of all works in Table 3.1 is that axial diffusion is neglected and this is a reasonable assumption if the transport in the reactor is convection dominated. Table 3.2 shows works by authors that have included the axial dispersion term.

Few industrially important processes have reaction systems that occur as a single step process. A much more important class of problems are the parallel and series reaction schemes, as shown in Fig. 3.1. The methods reported in Tables 3.1 and 3.2 have considered the evaluation of reactant conversion, but for multiple

Author	Kinetics	Flow profile	Duct shape	Method
Denbigh (1951)	HO2	L	Tube	RTD
Baron et al.(1952)	HE1	P	Tube	E
Cleland and Wilhelm (1956)	HO1, HO2	L, P	Tube	N
Katz (1959)	HE1	L, P, PL	Tube	IT
Lauwerier (1959)	HO1	L	Tube	E
Lupa and Dranoff (1966)	HE1	L	Annulus	E
Solomon and Hudson (1967)	HE1, HO1	L	Tube	E
Colton et al.(1971)	HE1	L	Plate	E
Homsy and Strohman (1971)	HO1	L, PL	Tube	E
Ogren (1975)	HE1, HO1	L	Tube	E
Nigam et al.(1982)	HE1, HO1	L	Tube	GLT
Jain et al.(1985)	HO0, HO1, HO2	L, WI	Tube	N

Table 3.1: Studies for single reactions in regular geometries. Legend: HOx - homogeneous reactions of order x, HEx - heterogeneous reactions of order x, L - Newtonian flow profile, P - plug flow profile, PL - power law fluid, WI - wall injection, T - turbulent, RTD - residence time distribution, E - eigenvalue expansion, N - numerical with analytical solution in some limit, IT - integral transform, LT - Laplace transform, GLT - Galerkin method on Laplace transform, FFT - Finite Fourier transform.

Author	Kinetics	Flow profile	Duct shape	Method
Walker (1961)	HE1, HO1	L	Tube	E
Hsu (1965)	HO1	L	Tube	E
Dang and Steinberg (1980)	HE1, HO1	L	Tube	E
Apelblat (1982)	HE1, HO1	L	Tube	LT
Dang (1983)	HE1, HO1	L	Tube	E
Balakotaiah et al.(2000)	HE1	L	Tube	E

Table 3.2: Studies for single reactions with axial diffusion, legends as in Table 3.1.

Author	Kinetics	Flow profile	Duct shape	Method
Hudson (1965)	HE1	L	Tube	E
Lyczkowski et al.(1971)	HE1	L, T	Tube/plate	E
Huang and Varma (1980)	HE1	P	Tube	FFT
Dang (1984)	HE1	P	Tube	E
Lawal (1996)	HE1, HO1	PL	Tube/plate	E
Levien and Levenspiel (1999)	HO1	PL	Tube	RTD

Table 3.3: Studies for multiple reactions, legends as in Table 3.1.

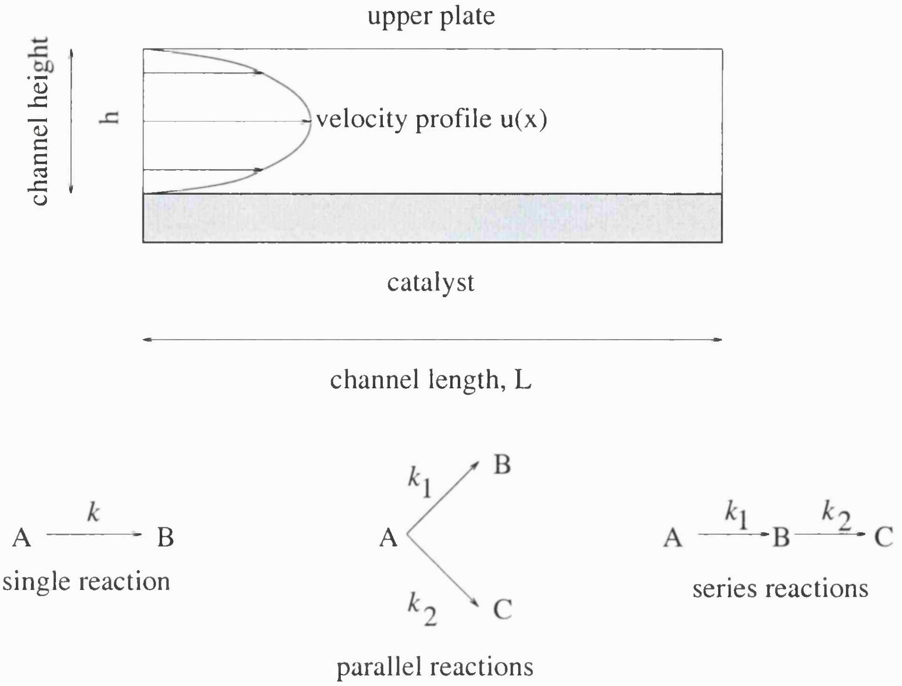

Figure 3.1: Schematic showing the problem and notation used. The reaction systems considered are also shown.

reaction systems a high selectivity and/or high yield is desirable. Knowledge of the performance indices will allow the reaction engineer to quickly establish design and operating parameters, therefore, models are required that also give information about the product distribution; such works are cited in Table 3.3 for multiple reactions.

Most of the above analysis requires the use of eigenvalue expansions, which require many eigenvalues and terms that can be efficiently obtained only by use of a computer. Such long expressions do not easily give insight into the dominant parameters, and hence shorter solutions are sought. In the current literature for multiple reactions the results are for first order kinetics which makes their use limited. In addition, microreactors do not necessarily conform to the shape of a tube or perfect rectangle due to the fabrication techniques used. Isotropic etching methods tend to fabricate rectangular channels with rounded corners, whilst anisotropic etching gives rise to trapezoidal cross sections (cf. Madou 1997). In light of this a method that easily extends to arbitrary duct geometries would give a better insight into reactor performance. The current study attempts to address the issues by developing solutions applicable to linear and non-linear kinetics, multiple reactions and arbitrary geometries.

A one-dimensional model is developed in §3.2 by averaging the advection-diffusion equation describing the evolution of transverse concentration of chemical components. The new model permits the key physical parameters, which control reactor performance and the concentration of by-products to be identified via closed form expressions. To illustrate how the method of solution may be applied to microchannel flows a parallel plate geometry is first considered with a single reaction. The analysis is extended to first order parallel and series reactions in §3.3 and 3.4. In the limit of $Da \ll 1$ the method can be adapted to yield solutions for second order single, parallel and series reactions in §3.5. All solutions are tested against full numerical simulations. Arbitrary shaped ducts are examined in §3.6 and the main conclusions are drawn in §3.7.

3.2 Vertically-averaged description: single first order reaction

This section describes the formulation and analytical solution of the mathematical model. Initially a physical description and defining equations along with assumptions are introduced. The method of solution (vertically-averaged formulation) for the simple case of a single first-order reaction is then presented followed by a description of numerical simulations to consider entrance effects.

3.2.1 Physical description and defining equations

The mathematical model is based on laminar incompressible microscale flow between two parallel plates, where a heterogeneous catalytic reaction occurs only on the lower plate (Fig. 3.1). When the dimensions of the microscale channel h are comparable to the mean free path of the gas molecules λ, the mean flow deviates from Stokes viscous flow (cf. Batchelor 1967) because the no-slip condition imposed on the rigid walls is not strictly applicable (Schaaf and Chambre 1961). The effect of wall slip on the flow is characterised by the Knudsen number ($Kn = \lambda/h$), which represents the ratio of the mean free path of the gas to the channel width. When the Knudsen number is small ($Kn \leq 10^{-3}$), slip effects are negligible and Stokes flow applies. When the Knudsen number is large ($Kn \geq 10$), a continuum description is no longer applicable and the gas flow is described by molecular simulation. Beskok and Karniadakis (1999) proposed a model of laminar flow between parallel plates which included the slip effects at the wall, parameterised in terms of the Knudsen number and a slip coefficient (which represents the fraction molecules undergoing diffuse reflection at the boundary). The flow profile was validated against Monte

Carlo simulations and experimental data and is given by

$$\frac{v(x)}{U} = \frac{-\left(\frac{x}{h}\right)^2 + \left(\frac{x}{h}\right) + \frac{Kn}{1-bKn}}{\frac{1}{6} + \frac{Kn}{1-bKn}}, \tag{3.1}$$

where U is average velocity between the plates, x is the distance from the lower wall and b is the slip coefficient. In a parallel plate geometry, the pressure drop is not sufficient to cause the Knudsen number to vary with axial distance and the flow profile is invariant with axial position. When $Kn \gg 1$ the velocity profile approaches a flat shape and hence the reactor resembles a plug flow reactor (PFR). Therefore, even though slip flow is rarely encountered in microreactors, the use of (3.1) allows us to study the effect of velocity profile ranging from laminar to plug.

The concentration of the reactant, c_a, is described by the advection-diffusion equation

$$v(x)\frac{\partial c_a}{\partial z} = D\left(\frac{\partial^2 c_a}{\partial x^2} + \frac{\partial^2 c_a}{\partial z^2}\right), \tag{3.2}$$

where D is molecular diffusivity. Modelling assumptions applied are constant fluid properties, isothermality, no volume change and dilute reacting solution.

The flux conditions at the upper and lower wall are expressed by

$$\frac{\partial c_a\left(h,z\right)}{\partial x} = 0, \qquad D\frac{\partial c_a\left(0,z\right)}{\partial x} = kc_a\left(0,z\right), \tag{3.3}$$

respectively, where k is the first order reaction rate constant. The concentration of the reactant entering the channel is $c_a\left(x,0\right) = c_a(0)$. The equations are reduced to dimensionless form by introducing the following dimensionless groups (Dankwerts boundary conditions are not used as axial diffusion is negligible)

$$\eta = \tfrac{x}{h}, \quad \zeta = \tfrac{z}{L}, \quad \theta_a = \tfrac{c_a}{c_a(0)}, \quad Pe = \tfrac{Uh}{D}, \quad \Psi = \tfrac{Kn}{1-bKn}, R = \tfrac{L}{h}, u = \tfrac{v}{U}.$$

The governing equation (3.2) reduces to

$$\frac{Pe}{R}u(\eta)\frac{\partial\theta_a}{\partial\zeta} = \frac{\partial^2\theta_a}{\partial\eta^2} + \frac{1}{R^2}\frac{\partial^2\theta_a}{\partial\zeta^2}, \quad \text{where} \quad u(\eta) = \frac{\eta - \eta^2 + \Psi}{\frac{1}{6} + \Psi}. \tag{3.4}$$

When $Pe \gg 1$ axial diffusion can be neglected. Therefore (3.4) can be further simplified to

$$\frac{Pe}{R}u(\eta)\frac{\partial\theta_a}{\partial\zeta} = \frac{\partial^2\theta_a}{\partial\eta^2}. \tag{3.5}$$

The boundary conditions are transformed to

$$\theta_a(\eta, 0) = 1, \quad \frac{\partial\theta_a(1,\zeta)}{\partial\eta} = 0, \quad \frac{\partial\theta_a(0,\zeta)}{\partial\eta} = Da\theta_a(0,\zeta), \tag{3.6}$$

where Da, defined as $Da = kh/D$, is the Damköhler number which characterises the ratio of diffusive to reactive timescales.

3.2.2 Vertically-averaged solution

The above equations, are simplified by considering the reactant concentration averaged across the channel, $\overline{\theta_a}$, where

$$\overline{\theta_a}(\zeta) = \int_0^1 \theta_a(\eta,\zeta)\,\mathrm{d}\eta, \tag{3.7}$$

varies with downstream position. In this case a separable solution of the form $\theta_a(\zeta,\eta) = \overline{\theta_a}(\zeta)f_a(\eta)$ can be assumed. The solution method employed in the following is essentially equivalent to the eigenvalue method proposed and applied by previous researchers (cf. Walker 1961).

For microreactors a key variable that controls reactor performance is Pe/R, which is typically of $O(0.01 - 1)$ (cf. Kursawe et al.1999, Walter and Liauw 1999 and Hsing et al.2000). Under these conditions only the first term in the eigenvalue expansion is important (cf. Walker 1961), and it is this term we seek in the formulation proposed. It is worth noting that $Pe/R = \tau_{dt}/\tau_c$, is the ratio of transverse diffusive to advective timescales. Thus, the inequality $Pe/R \ll 1$ is equivalent to $\tau_{dt} \ll \tau_c$. The linear boundary conditions on the upper and lower walls require f_a to satisfy,

$$\frac{\mathrm{d}f_a}{\mathrm{d}\eta} = 0, \quad \eta = 1, \quad \text{and} \quad \frac{\mathrm{d}f_a}{\mathrm{d}\eta} = Daf_a, \quad \eta = 0, \tag{3.8}$$

and the integral constraint

$$\int_0^1 f_a(\eta)\mathrm{d}\eta = 1, \tag{3.9}$$

which arises from (3.7). Substituting $\theta_a(\zeta,\eta) = f_a(\eta)\overline{\theta_a}(\zeta)$ into (3.5) and separating the variables shows that

$$\frac{\mathrm{d}\overline{\theta_a}}{\mathrm{d}\zeta} = -\lambda_a\overline{\theta_a}, \tag{3.10}$$

and

$$-\frac{\lambda_a Pe}{R}\left(\frac{\eta-\eta^2+\Psi}{\frac{1}{6}+\Psi}\right) f_a = \frac{\mathrm{d}^2 f_a}{\mathrm{d}\eta^2}, \tag{3.11}$$

where λ_a is a concentration decay constant. Integrating (3.10) and applying the entrance condition $\overline{\theta_a}(0) = 1$, gives

$$\overline{\theta_a} = \exp(-\lambda_a\zeta). \tag{3.12}$$

The above equation is first solved for $\Psi \gg 1$, which corresponds to large Knudsen number under which plug flow transports the reactant along the channel. When Ψ is large, the transverse concentration profile of A satisfies

$$-\frac{\lambda_a Pe}{R} f_a = \frac{\mathrm{d}^2 f_a}{\mathrm{d}\eta^2}. \tag{3.13}$$

The general solution to the harmonic equation is $f_a(\eta) = A\cos(\alpha\eta) + B\sin(\alpha\eta)$, with $\alpha = \sqrt{\lambda_a Pe/R}$, where A, B and λ_a need to be determined. Imposing the flux conditions which are satisfied on the walls yields a relationship between A, B and λ_a: $B\alpha = ADa$ and $-A\sin\alpha + B\cos\alpha = 0$. The decay rate λ_a is determined from $\alpha\tan\alpha = Da$;

$$\sqrt{\frac{\lambda_a Pe}{R}}\tan\left(\sqrt{\frac{\lambda_a Pe}{R}}\right) = Da. \tag{3.14}$$

In the limits of slow and fast reactions corresponding respectively to $Da \ll 1$ and

$Da \gg 1$, the decay rate of A can be determined from

$$\frac{\lambda_a Pe}{R} = \begin{cases} 3\left(\frac{Da}{2}+1\right) - \sqrt{\left(\frac{9Da^2}{4}+3Da+9\right)}, & Da < 2.0, \\ \left(\frac{\pi Da}{2(Da+1)}\right)^2, & Da > 2.0. \end{cases} \tag{3.15}$$

The asymptotic limit for low Damköhler numbers is determined by

$$\begin{aligned}
&\frac{\alpha\sin(\alpha)}{\cos(\alpha)} = Da, \\
&\alpha\left(\alpha - \frac{\alpha^3}{6} + \ldots\right) = Da\cos(\alpha), \\
&\alpha\left(\alpha - \frac{\alpha^3}{6} + \ldots\right) = Da\left(1 - \frac{\alpha^2}{2} + \ldots\right), \\
&\alpha^2 - \frac{\alpha^4}{6} = Da - \frac{\alpha^2}{2}Da, \\
&\alpha^4 - 6\left(Da/2+1\right)\alpha^2 + 6Da = 0, \\
&\alpha^2 = \frac{6\left(Da/2+1\right) \pm \sqrt{36(Da/2+1)^2 - 24Da}}{2}, \\
&\alpha^2 = 3(Da/2+1) \pm \sqrt{9(Da/2+1)^2 - 6Da}, \\
&\alpha^2 = 3(Da/2+1) - \sqrt{(9Da^2/4) + 3Da + 9},
\end{aligned}$$

where the upper limit (high Da) is a result of the function tan tending to ∞ as the decay group (α) approaches $2/\pi$. In the limiting case of $Da \gg 1$, the decay constant tends to

$$\lambda_a \to \left(\frac{\pi}{2}\right)^2 \frac{R}{Pe} \tag{3.16}$$

and the conversion of A

$$\left(X = 1 - \overline{\theta_a}\right) \tag{3.17}$$

tends to $1 - \exp\left(-\left(\frac{\pi}{2}\right)^2 \frac{R}{Pe}\right)$. Thus, even in the limit $Da \to \infty$ (or more specifically for $Da > O(10)$), the conversion of A is not complete as the reactor begins to operate in the mass transfer limited regime (some packets of fluid cannot reach catalyst) whilst convective transport still removes reactant from the system. This can also

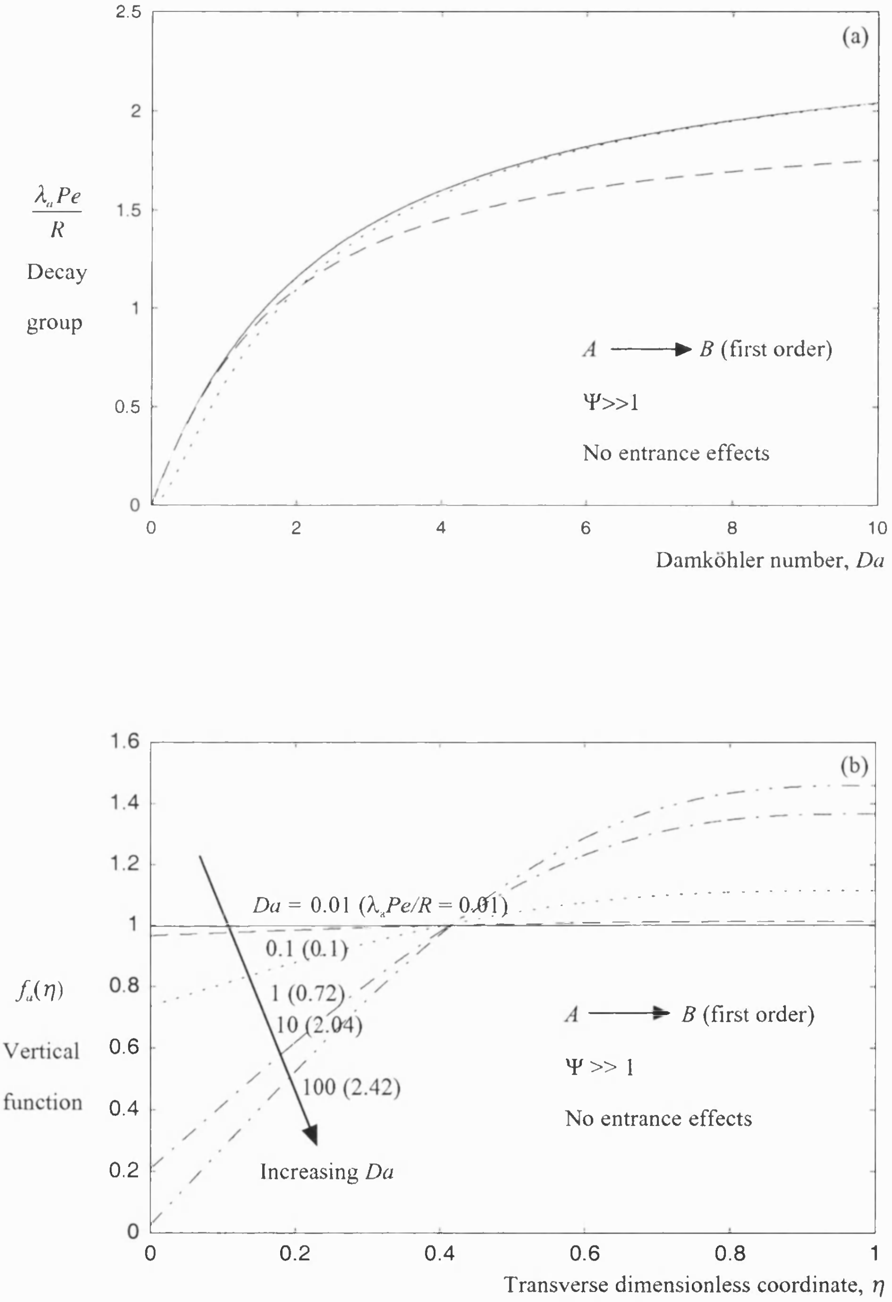

Figure 3.2: (a) Decay group for component A, calculated analytically from the vertically-averaged solution (3.14) for the limit $\Psi \gg 1$ as a function of Da (full curve). (b) Vertical function profiles for $Da = 0.01$, 0.1, 1, 1.0, 100 ($\Psi \gg 1$).

be seen from (3.15) where the decay group reaches a threshold with increasing Da. However when $Pe/R \to 0$, complete conversion can be achieved. Figure 3.2 (a) shows a comparison between the decay group ($Pe\lambda_a/R$) calculated according to (3.14) for $\Psi \gg 1$ and the asymptotic expansions (3.15), which indicate that the asymptotic expansions predict the decay group to within 5 %. The general solution of (3.13) yields an explicit function of the vertical function, this requires the coefficient A to be determined which is accomplished by the integral constraint (3.9),

$$\begin{aligned}
f &= A\left[\cos(\alpha\eta) + \frac{Da}{\alpha}\sin(\alpha\eta)\right], \\
1 &= A\left[\frac{\sin(\alpha\eta)}{\alpha} - \frac{Da}{\alpha^2}\cos(\alpha\eta)\right]_0^1, \\
1 &= A\left[\frac{\sin(\alpha)}{\alpha} - \frac{Da}{\alpha^2}\cos(\alpha) + \frac{Da}{\alpha^2}\right], \\
A &= \frac{\alpha^2}{Da},
\end{aligned}$$

and the vertical function is

$$f_a(\eta) = \frac{\alpha^2}{Da}\left(\cos\alpha\eta + \frac{Da}{\alpha}\sin\alpha\eta\right). \tag{3.18}$$

Figure 3.2 (b) shows the vertical function f_a as a function of η and provides an appreciation of how the transverse concentration profile varies with Da for $\Psi \gg 1$. It is worth noting that each curve corresponds to a unique value of the decay group $\alpha = \lambda_a Pe/R$ and hence represents an infinite number of λ_a, Pe and R combinations.

The above analytical results are restricted by the condition that $\Psi \gg 1$. A numerical scheme was developed to calculate the vertically-averaged solutions for an arbitrary value of Ψ in order to ascertain the impact of the velocity profile on the decay group. The decay constant λ_a was determined by integrating f_a from the lower wall to the upper wall and searching for a unique value of λ_a for which the function satisfies both boundary conditions (3.8) and the integral constraint (3.9). Since the differential equation (3.11) and the boundary conditions (3.8) are linear in f_a, an initial value of f_a can be prescribed at the lower wall and then integrated in the transverse direction using a shooting method. The choice of f_a is arbitrary as the solution is linear and the result normalised according to the integral constraint.

In Fig. 3.3, numerical results showing the variation of the decay group with Ψ are presented for different values of the Damköhler number. Note that as Ψ

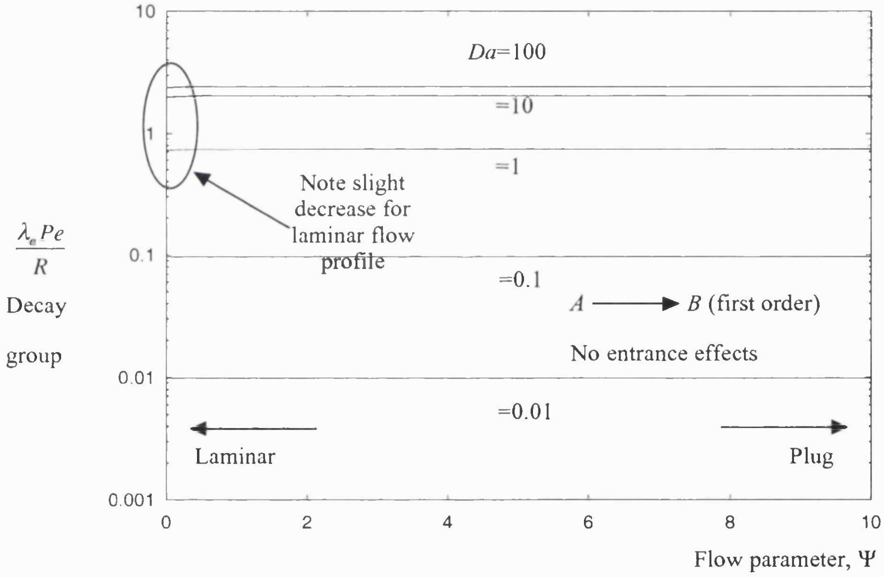

Figure 3.3: Variation of the decay group with Ψ for different *Da* numbers.

increases, the velocity near the wall increases and the velocity profile tends to become more plug. The change in the decay group as the velocity profile changes from laminar to plug flow is typically less than 1%. Therefore, the analytical solutions developed for plug flow (3.15) are essentially independent of the velocity profile. Similar observations have been made by Balakotaiah et al.2000 who demonstrate that in the limit of $Da \ll 1$, $Pe/R \ll 1$ the behaviour of a catalytically coated channel is identical to that of a homogeneous PFR. In the limit of $Da \gg 1$ the reactor operates in the mass transfer controlled regime and can additionally be interpreted as a homogeneous advection-reaction problem with a rate constant related to transverse diffusion time. This can be seen from (3.15) where a threshold for the decay rate exists as Da becomes large.

3.2.3 Entrance length considerations

The vertically-averaged solutions indicate that the concentration profile is ultimately determined by the ratio $\lambda_a Pe/R$ and Da, and is weakly dependent on Ψ. However, the vertically-averaged solution method is not able to account for entrance effects which arise from the fact that the concentration of A is uniform at the channel entrance cross section (i.e. a Dirichlet boundary condition). To determine the ability of the analytical solutions to describe the reactant concentration, a full numerical code was written (Appendix A.3) to solve the governing equation (3.5) and determine the influence of entrance effects on the downstream development of the concentration profile. The parabolic advection-diffusion (3.5) equation along with boundary conditions (3.6) was solved numerically using a finite difference scheme with explicit stepping in the axial direction and a mesh size sufficiently small to ensure convergence.

The time taken for reactant to diffuse from the upper wall to the lower wall is $O(h^2/D)$, and in this time a parcel of fluid has been advected a distance $O(Uh^2/D)$. In order that entrance effects are negligible, this distance must be smaller than the length of the channel L, which necessarily requires $Uh^2/D \ll L$ or $Pe/R \ll 1$. After solving (3.5) the vertical function f_a is calculated from $f_a(\eta, \zeta) = \theta_a(\eta, \zeta)/\overline{\theta_a}(\zeta)$. This function provides an appreciation of how transverse concentration profiles change and is plotted in Fig. 3.4 (a) at downstream positions $\zeta = 0.05, 0.1, 0.15$ when $Pe/R = 1.0$, $Da = 5.0$ and $\Psi = 0.0$; the vertically-averaged solution is plotted as a solid line. The figure shows that convergence to the vertically-averaged solution is good, even through the condition Pe/R being small is not strictly true. The second plot, Fig. 3.4 (b), demonstrates the development of the vertical function when $\Psi = 10$, and a comparison with the plot for $\Psi = 0.0$ shows a negligible effect of the velocity profile on the vertical function. These results indicate that the vertical function closely follows the vertically-averaged solution and this agreement increases with downstream distance.

3.3 First order parallel reactions

The scheme for the parallel reaction is shown in Fig. 3.1. The concentration of components A, B and C are c_a, c_b and c_c respectively. The reactants are advected by the same mean flow and their diffusive spreading are characterised by the same Peclet number. The concentration of the components are normalised by the entrance concentration of A, to yield θ_a, θ_b and θ_c. The entrance condition is therefore $\theta_a = 1$ and $\theta_b = \theta_c = 0$ at $\zeta = 0$. The rate constants of A to B and A to C are k_1 and k_2 respectively, and are characterised by Damköhler numbers $Da_1 = k_1 h/D$ and $Da_2 = k_2 h/D$. On the surface of the catalyst, the boundary conditions satisfied by the reactant concentration are

$$\frac{\partial \theta_a}{\partial \eta} = (Da_1 + Da_2)\theta_a, \qquad \frac{\partial \theta_b}{\partial \eta} = -Da_1\theta_a, \qquad \frac{\partial \theta_c}{\partial \eta} = -Da_2\theta_a, \tag{3.19}$$

which describes the conversion of A to both B and C. The concentration of B and C are determined from the concentration of A. Seeking solutions which vary linearly with the concentration of A and satisfy the entrance condition $\theta_b = \theta_a = 0$ at $\zeta = 0$, the concentration of B and C are determined to be

$$\theta_b(\zeta,\eta) = \frac{Da_1}{Da_1 + Da_2}(1 - \theta_a(\eta,\zeta)), \qquad \theta_c(\zeta,\eta) = \frac{Da_2}{Da_1 + Da_2}(1 - \theta_a(\eta,\zeta)), \tag{3.20}$$

where θ_a is determined from the solution of (3.5), satisfying boundary conditions (3.6). It can be seen (3.20) satisfy all relevant conditions from the following; lower boundary condition

$$\begin{aligned}
\left.\frac{\partial \theta_b}{\partial \eta}\right|_{\eta=0} &= -\frac{Da_1}{Da_1 + Da_2}\frac{\partial \theta_a}{\partial \eta}, \\
\left.\frac{\partial \theta_b}{\partial \eta}\right|_{\eta=0} &= -\frac{Da_1}{Da_1 + Da_2}(Da_1 + Da_2)\theta_a, \\
\left.\frac{\partial \theta_b}{\partial \eta}\right|_{\eta=0} &= -Da_1\theta_a,
\end{aligned}$$

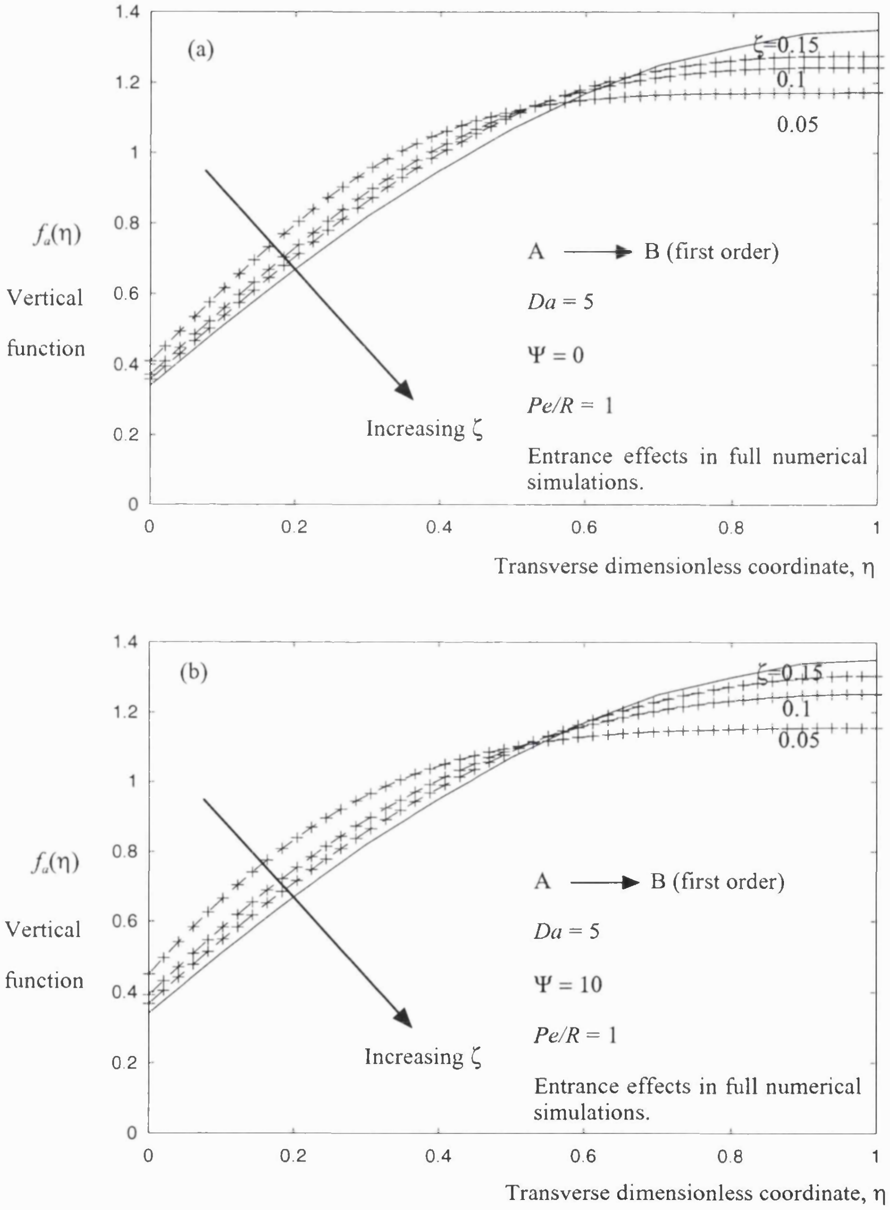

Figure 3.4: Vertical function profiles of reactant A at three positions downstream from the inlet for $Pe/R = 1$ and $Da = 5.0$ obtained from the full numerical simulations, (a) for parabolic flow and (b) for plug flow. The analytical vertical function is shown as a solid line.

upper boundary condition

$$\begin{aligned}\left.\frac{\partial \theta_b}{\partial \eta}\right|_{\eta=1} &= -\frac{Da_1}{Da_1+Da_2}\left.\frac{\partial \theta_a}{\partial \eta}\right|_{\eta=1},\\ \left.\frac{\partial \theta_b}{\partial \eta}\right|_{\eta=1} &= 0.\end{aligned}$$

In addition, it can also be seen that by direct substitution of (3.20) that the governing equation and inlet conditions are satisfied. The equation for θ_c is derived in the same way. When B is the desired product, the ratio of the reactant concentration $\overline{\theta_b}(1)$ to the conversion of A $(1-\overline{\theta_a}(1))$ is a key parameter to determine, which in this system is a constant.

In common with all systems involving parallel reactions, the distribution of products is based on kinetics only. Equation (3.20) clearly shows a linear dependence of B and C on conversion with the gradient determined by the Damköhler numbers. Due to the explicit linear result, no optimum is possible and no further discussion is deemed necessary as reactor performance is governed by kinetics.

3.4 First order series reactions

For series reactions the governing equations are similar to (3.5). For the sake of simplicity it is assumed that diffusivities of all components are identical, resulting in the same Pe number for all components. On the surface of the catalyst ($\eta = 0$), the boundary conditions satisfied by the concentration of the reactants are

$$\frac{\partial \theta_a}{\partial \eta} = Da_1\theta_a, \quad \frac{\partial \theta_b}{\partial \eta} = Da_2\theta_b - Da_1\theta_a, \quad \frac{\partial \theta_c}{\partial \eta} = -Da_2\theta_b, \tag{3.21}$$

with Damköhler numbers $Da_1 = k_1h/D$ and $Da_2 = k_2h/D$. The advection-diffusion equations and boundary conditions are linear in θ_a, θ_b and θ_c. To simplify the solution a dummy variable $\tilde{\theta}_b$ is introduced along with a decay constant $\tilde{\lambda}_b$ according to

$$\theta_b(\eta,\zeta) = a\theta_a(\eta,\zeta) + \tilde{\theta}_b(\eta,\zeta). \tag{3.22}$$

This allows the problem to be reformulated so that one solves for θ_a and $\tilde{\theta}_b$. Reformulation in this way allows the boundary condition for $\tilde{\theta}_b$ to have the same form as θ_a

$$\frac{\partial \tilde{\theta}_b}{\partial \eta} = Da_2 \tilde{\theta}_b, \tag{3.23}$$

and hence $\tilde{\lambda}_b$ can be determined in an identical manner, i.e. from (3.13).

The constants in (3.22) can be determined by the series boundary condition (3.21) for θ_b

$$\frac{\partial \theta_b}{\partial \eta} = a\frac{\partial \theta_a}{\partial \eta} + \frac{\partial \tilde{\theta}_b}{\partial \eta} = (Da_2 a - Da_1)\theta_a + Da_2 \tilde{\theta}_b. \tag{3.24}$$

The constant a needs to be determined, this can be done by substituting the boundary condition at the catalyst for component A and equating the coefficients of θ_a terms in (3.24) yielding

$$a = \frac{Da_1}{Da_2 - Da_1}. \tag{3.25}$$

Therefore the concentration of B is calculated from

$$\theta_b(\eta, \zeta) = \frac{Da_1}{Da_2 - Da_1}\theta_a(\eta, \zeta) + \tilde{\theta}_b(\eta, \zeta). \tag{3.26}$$

The dummy concentration variable $\tilde{\theta}_b$ satisfies the advection-diffusion equation, since it is a linear combination of θ_a and $\tilde{\theta}_b$. In addition, $\tilde{\theta}_b$ must satisfy

$$\frac{\partial \tilde{\theta}_b}{\partial \eta} = Da_2 \tilde{\theta}_b, \quad \eta = 0, \tag{3.27}$$

in order that the lower boundary condition (3.21) for θ_a and θ_b is satisfied. The initial condition for the dummy variable is $\tilde{\theta}_b = Da_1/(Da_1 - Da_2)$ at $\zeta = 0$, so that $\theta_b = 0$ at the reactor inlet. It can easily be seen that $\tilde{\theta}_b$ satisfies the same equation as θ_a for the single reaction case, the only difference being the Damköhler number which is now Da_2. Hence $\tilde{\lambda}_b$ can now be determined from (3.14).

The vertically-averaged solution for $\tilde{\theta}_b$ is determined in the same separable form as θ_a and the axial component is

$$\overline{\tilde{\theta}_b}(\zeta) = \frac{Da_1}{Da_1 - Da_2} \exp(-\tilde{\lambda_b}\zeta). \tag{3.28}$$

The axial concentration profile of $\overline{\theta_b}$ is

$$\overline{\theta_b}(\zeta) = \frac{Da_1}{Da_1 - Da_2} \left(\exp(-\tilde{\lambda_b}\zeta) - \exp(-\lambda_a\zeta) \right). \tag{3.29}$$

When $Da_1/Da_2 = 1$, the concentration of B is determined from (3.29)) by taking the limit of the right hand side of (3.29) under identical timescales, i.e. $Da_1 = Da_2$ and $\lambda_a = \tilde{\lambda_b}$. Thus, the differential operator can now be introduced (where $\lambda = \mathrm{fn}(Da)$)

$$\frac{\exp\left(-\mathrm{fn}\left(Da_2\right)\right) - \exp\left(-\mathrm{fn}\left(Da_1\right)\right)}{Da_1 - Da_2} \longrightarrow -\frac{\mathrm{d}\exp\left(-\mathrm{fn}\left(Da_1\right)\right)}{\mathrm{d}Da_1}, \tag{3.30}$$

$$-\frac{\mathrm{d}\exp\left(-\lambda_a\right)}{\mathrm{d}Da_1} = \frac{\mathrm{d}\lambda_a}{\mathrm{d}Da_1} \exp\left(-\lambda_a\right), \tag{3.31}$$

from (3.14)

$$\begin{aligned} \frac{\mathrm{d}\lambda_a}{\mathrm{d}Da_1} &= \left[\frac{1}{2}\sqrt{\frac{Pe}{R}} \frac{1}{\sqrt{\lambda_a}} \tan\left(\sqrt{\frac{\lambda_a Pe}{R}}\right) \right. \\ &+ \left. \sqrt{\frac{\lambda_a Pe}{R}} \frac{1}{2} \left[\frac{Pe}{R} \frac{1}{\sqrt{\lambda_a}} \sec^2\left(\sqrt{\frac{\lambda_a Pe}{R}}\right) \right] \right], \end{aligned} \tag{3.32}$$

$$\begin{aligned} \frac{\mathrm{d}\lambda_a}{\mathrm{d}Da_1} &= \left[\frac{1}{2}\sqrt{\frac{Pe}{R}} \frac{1}{\sqrt{\lambda_a}} \tan\left(\sqrt{\frac{\lambda_a Pe}{R}}\right) \right. \\ &+ \left. \sqrt{\frac{\lambda_a Pe}{R}} \frac{1}{2\lambda_a} \left[\sqrt{\frac{\lambda_a Pe}{R}} \tan^2\left(\sqrt{\frac{\lambda_a Pe}{R}}\right) + \sqrt{\frac{Pe\lambda_a}{R}} \right] \right], \end{aligned} \tag{3.33}$$

multiply top and bottom by λ_a

$$\begin{aligned}\lambda_a\frac{\mathrm{d}\lambda_a}{\mathrm{d}Da_1} &= \frac{1}{2}\left[\sqrt{\frac{Pe\lambda_a}{R}}\tan\left(\sqrt{\frac{Pe\lambda_a}{R}}\right)\right. \\ &+ \left.\sqrt{\frac{Pe\lambda_a}{R}}\left[\sqrt{\frac{Pe\lambda_a}{R}}\tan^2\left(\sqrt{\frac{Pe\lambda_a}{R}}\right)+\sqrt{\frac{Pe\lambda_a}{R}}\right]\right], \qquad (3.34)\end{aligned}$$

and substitution of (3.14) into (3.34) yields

$$\begin{aligned}\overline{\theta_b}(\zeta) &= Da_1\exp(-\lambda_a)\frac{\mathrm{d}\lambda_a}{\mathrm{d}Da_1} \\ &= \frac{1}{2}(\lambda_a Da_1)\left(Da_1 + Da_1^2 + (\lambda_a Pe/R)\right)\exp(-\lambda_a). \qquad (3.35)\end{aligned}$$

When Da_1, $Da_2 \gg 1$, the limiting values of the decay rates λ_a and $\tilde{\lambda}_b$ are determined from (3.14). In the limit of large Da_1, the conversion of A is never 100 % and tends to (3.17). Expanding (3.29) in increasing powers of $1/Da_1$ and $1/Da_2$, the exit concentration of B is determined to be

$$\overline{\theta_b}(1) = \frac{Da_1}{Da_1 - Da_2}\left(\exp\left(-\frac{\pi^2 R}{4Pe}\left(1 - \frac{2}{Da_2} + O(1/Da_2^2)\right)\right)\right)$$

When Da_1, $Da_2 \ll 1$ or $\gg 1$, the limiting values of the decay rates λ_a and $\tilde{\lambda}_b$ are determined from (3.15). In the limit of large Da_1, the conversion of A is never complete, whilst in the limit of large Da_2, the concentration of B tends to zero because it is converted rapidly into C.

Figures 3.5 (a, b) show the variation of concentration of intermediate B with conversion of A at the reactor outlet. Conversion was increased by increasing Da, keeping for each curve a specified Da_1/Da_2 ratio. The different curves represent different ratios of Da_1/Da_2. Comparison between the full numerical solutions (diamonds) describing transport by a parabolic velocity profile and the vertically-averaged solution for $\Psi = 0$ indicate good agreement when $Pe/R = 0.1$. Good agreement is also achieved with the analytical vertically-averaged solution for $\Psi = 10$, indicating the weak dependence of the exit concentrations of A, B and C on the flow profile when $Pe/R \ll 1$. As mentioned before, entrance effects become important when $Pe/R \gg 1$. However, Da_1 can also influence the magnitude of entrance effects, especially in the range $Pe/R \geq 1$. High Da_1 will create significant concentration gradients at the entrance, which cannot be effectively accounted for in the vertically-averaged solution. As shown in Fig. 3.5 (b), where $Pe/R = 1$ the discrepancy

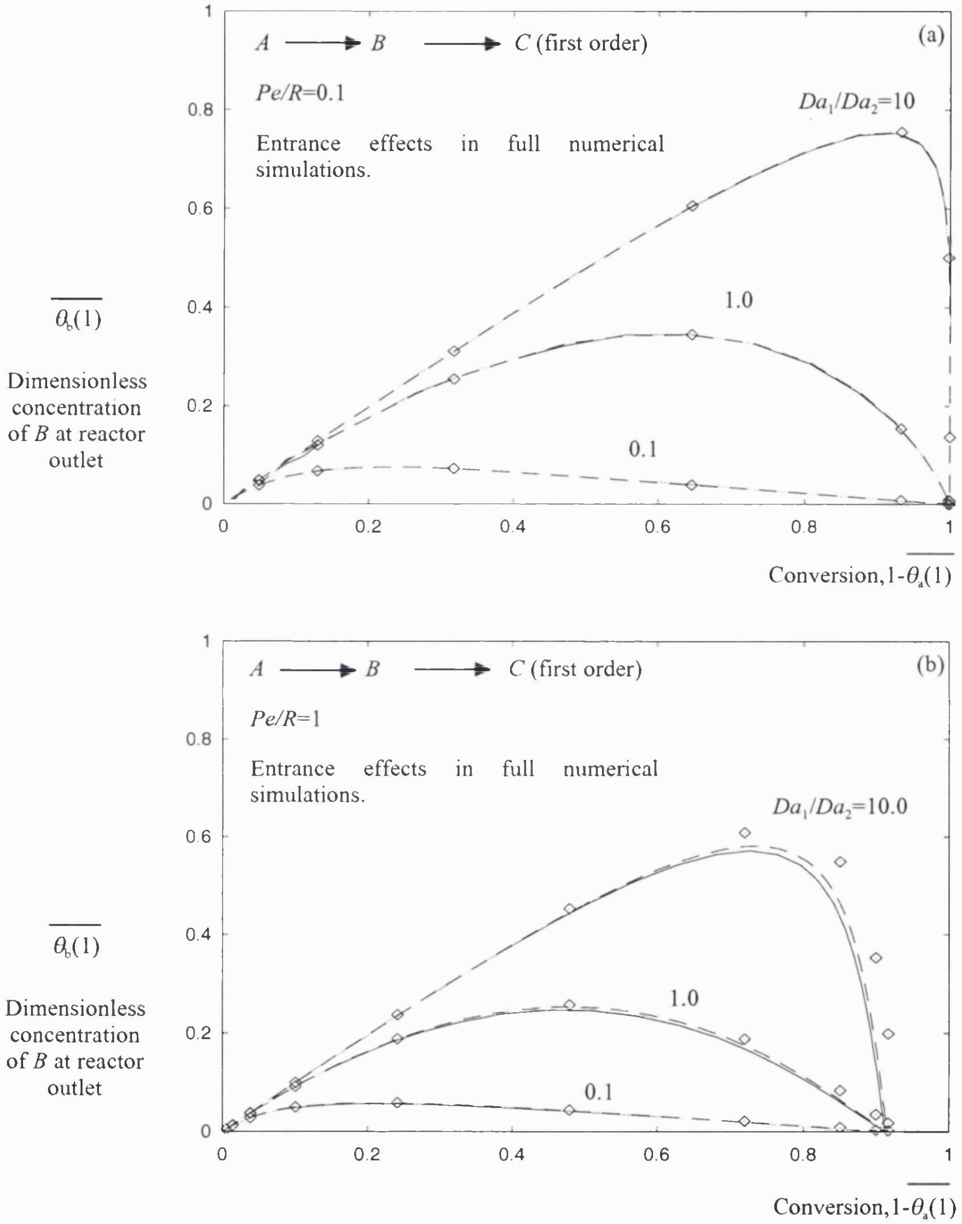

Figure 3.5: Variation of outlet reactor concentration of intermediate product B with conversion of A for varying Da_1/Da_2 ratios, (a) $Pe/R = 0.1$ (b) $Pe/R = 1$. Full numerical simulations are indicated by the diamonds, whilst vertically averaged formulations for $\Psi = 0$ and $\Psi = 10$ are shown by the solid and dashed lines respectively.

between numerical and vertically averaged formulations is significant at large conversions, which are obtained at high Da_1. This is reflected on the under-estimation of outlet concentration of B. Comparing Figs. 3.5 (a) and 3.5 (b) it is seen that the higher intermediate product concentrations are obtained for $Pe/R = 0.1$, where $\tau_{dt} \ll \tau_c$ as explained before. It is worth noting that the $\overline{\theta_b}(1)$ vs $1 - \overline{\theta_a}(1)$ dependence obtained in Fig. 3.5 (a) is practically the same as one would obtain in a homogeneous PFR (cf. Levien and Levenspiel (1999)). Finally, when $Pe/R = 1$, i.e. when $\tau_{dt} \simeq \tau_c$, 100% conversion cannot be achieved as shown in Fig. 3.5 (b).

3.5 Extension to second order reactions for small Damköhler numbers

The vertically-averaged formulation developed in §3.2, is now applied to gain insight into the non-linear case of second order reactions. This problem is complicated by the mass flux condition on the surface of the catalyst which is no longer proportional to reactant concentration, rendering the solution nonlinear. As before, $Pe/R \ll 1$ and under this condition the vertically-averaged reactant concentration is weakly dependent on the velocity profile; and hence plug flow is assumed. In the limit $Da \ll 1$ the method developed in §3.2 can be adapted to yield closed form expressions for second order catalytic reactions. The advection-diffusion equation for the plug flow system is

$$\frac{Pe}{R}\frac{\partial \theta_a}{\partial \zeta} = \frac{\partial^2 \theta_a}{\partial \eta^2}, \tag{3.36}$$

and the associated boundary conditions are

$$\frac{\partial \theta_a(0,\zeta)}{\partial \eta} = Da_1 \theta_a^2(0,\zeta), \qquad \frac{\partial \theta_a(1,\zeta)}{\partial \eta} = 0. \tag{3.37}$$

The change of θ_a across the channel width is $O(Da_1\theta_a^2)$, so that in the limit of $Da_1 \ll 1$, the difference between the wall concentration of reactant A and the vertically averaged concentration $\overline{\theta_a}$ is negligible. Under this approximation, the vertically averaged concentration profile along the channel is determined by integrating (3.36), applying the flux condition on the walls, to give

$$\frac{Pe}{R}\frac{\mathrm{d}\overline{\theta_a}(\zeta)}{\mathrm{d}\zeta} = -Da_1 \overline{\theta_a}^2(\zeta). \tag{3.38}$$

	Reaction type		
	Single	Parallel	Series
$\frac{\partial\theta_a(0,\zeta)}{\partial\eta}$	$Da\theta_a^2$	$Da_1\theta_a^2 + Da_2\theta_a$	$Da_1\theta_a^2$
$\frac{\partial\theta_b(0,\zeta)}{\partial\eta}$	$-Da\theta_a^2$	$-Da_1\theta_a^2$	$Da_2\theta_b - Da_1\theta_a^2$
$\overline{\theta_a}(\zeta)$	$\frac{1}{1+\frac{RDa\zeta}{Pe}}$	$\frac{Da_2}{(Da_1+Da_2)\exp(Da_2R\zeta/Pe)-Da_1}$	$\frac{1}{1+\frac{RDa_1\zeta}{Pe}}$
$\overline{\theta_b}(\zeta)$	$1-\overline{\theta_a}(\zeta)$	$1 - \frac{Da_2}{Da_1}\ln\left(\frac{(Da_1+Da_2)-Da_1\exp\left(\frac{-Da_2R\zeta}{Pe}\right)}{Da_2}\right) - \left(\frac{Da_2}{(Da_1+Da_2)\exp\left(\frac{Da_2R\zeta}{Pe}\right)-Da_1}\right)$	$\frac{Da_1}{Da_2}\exp\left(-\frac{Da_2R\zeta}{Pe}\right)\int_0^{\frac{zPe}{RDa_2}}\left(\frac{\exp(z)}{\left(1+z\left(\frac{Da_1}{Da_2}\right)\right)^2}\right)\mathrm{d}z$

Table 3.4: Summary of analytical results describing first and second order single, parallel and series reactions occuring in a parallel plate reactor for $Da \ll 1$ and $Pe/R \ll 1$.

Integrating and applying the inlet condition $\theta_a(0) = 1$, we have

$$\overline{\theta_a}(\zeta) = \frac{1}{1+\frac{RDa\zeta}{Pe}}. \tag{3.39}$$

Figure 3.6 shows a comparison between the full numerical solution and the analytical expression (3.39) for the concentration of A for varying Pe/R ratios and Damköhler numbers. It can be seen that good agreement between analytical and numerical solutions is obtained for small Damköhler numbers ($Da = 0.02$) even when $Pe/R = O(1)$. However, for Damköhler numbers greater than about 0.5 there is a discrepancy between (3.39) and the full numerical simulation. The above procedure has been extended to parallel and series systems (derivations shown in §3.5.1 and 3.5.2 respectively); the analytical solutions are presented in Fig. 3.7 (for parallel systems) and Fig 3.8 (for series systems) and Table 3.4. Comparisons with numerical solutions demonstrated good agreement.

3.5.1 Second order parallel reactions

The reaction scheme for second order parallel reactions is (at the catalyst, $\eta = 0$)

$$\frac{\partial\theta_a}{\partial\eta} = Da_1\theta_a^2 + Da_2\theta_a, \qquad \frac{\partial\theta_b}{\partial\eta} = -Da_1\theta_a^2, \qquad \frac{\partial\theta_c}{\partial\eta} = -Da_2\theta_a, \tag{3.40}$$

hence the reaction is second order for component B and first order for component C. Vertically averaging the advection-diffusion equation we obtain

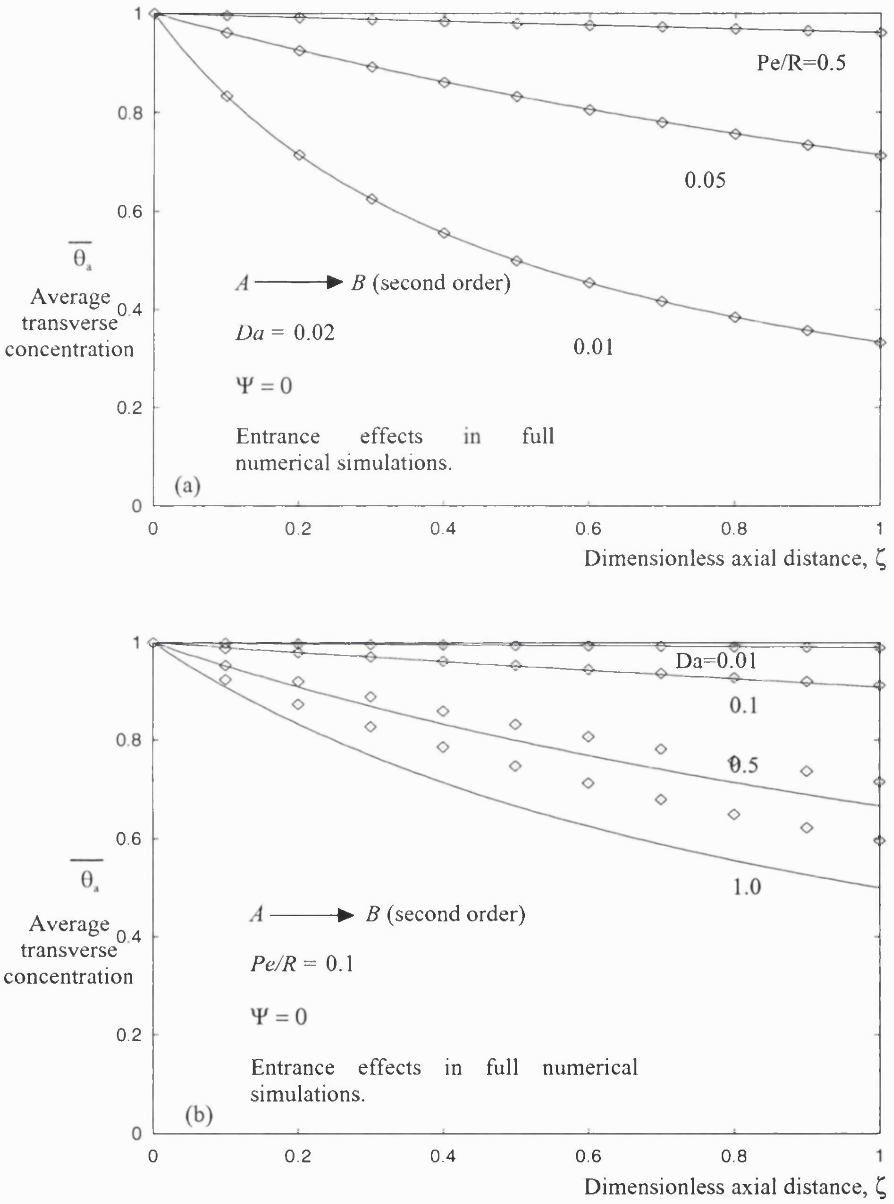

Figure 3.6: Axial concentration profiles for a second order reaction. Diamonds represent full numerical simulations whilst lines correspond to the analytical solution (3.39), for (a) $Da = 0.02$ at different Pe/R ratios and (b) $Pe/R = 1$ at different Da numbers.

$$\frac{Pe}{R}\frac{\mathrm{d}\overline{\theta_a}}{\mathrm{d}\zeta} = -Da_1\overline{\theta_a}^2 - Da_2\overline{\theta_a}, \tag{3.41}$$

which, upon integration, yields

$$\overline{\theta_a}(\zeta) = \frac{Da_2}{(Da_1 + Da_2)\exp\left(\frac{Da_2 R\zeta}{Pe}\right) - Da_1}. \tag{3.42}$$

Therefore, the vertically-averaged concentration of B is

$$\begin{aligned}\overline{\theta_b} = \frac{RDa}{Pe}\int_0^\zeta \overline{\theta_a}^2 \mathrm{d}\zeta &= 1 - \frac{Da_2}{Da_1}\ln\left(\frac{(Da_1 + Da_2) - Da_1\exp(-Da_2\zeta R/Pe)}{Da_2}\right) \\ &- \frac{Da_2}{(Da_1 + Da_2)\exp(Da_2 R\zeta/Pe) - Da_1}. \end{aligned} \tag{3.43}$$

A plot of (3.43) is shown in Fig. 3.7 for different Damköhler number ratios. The reactant (A) axial profiles give trends as expected. However, it is interesting to note the axial profiles of the product B. Despite the difference in magnitudes of the Damköhler number the exit concentration of B changes relatively little. This can be attributed to the dominating effect of the first order reaction for high Damköhler numbers limiting the amount of B that can be produced, and the overall lower rate the second order reaction rate at low Damköhler numbers when the ratio of Damköhler numbers favours product B.

3.5.2 Second order series reactions

The reaction scheme for second series reactions is (at the catalyst, $\eta = 0$)

$$\frac{\partial\theta_a}{\partial\eta} = Da_1\theta_a^2, \qquad \frac{\partial\theta_b}{\partial\eta} = Da_2\theta_b - Da_1\theta_a^2, \qquad \frac{\partial\theta_c}{\partial\eta} = -Da_2\theta_b, \tag{3.44}$$

hence the reaction is second order for the first step, and first order for the second step. The boundary condition can be vertically averaged to yield

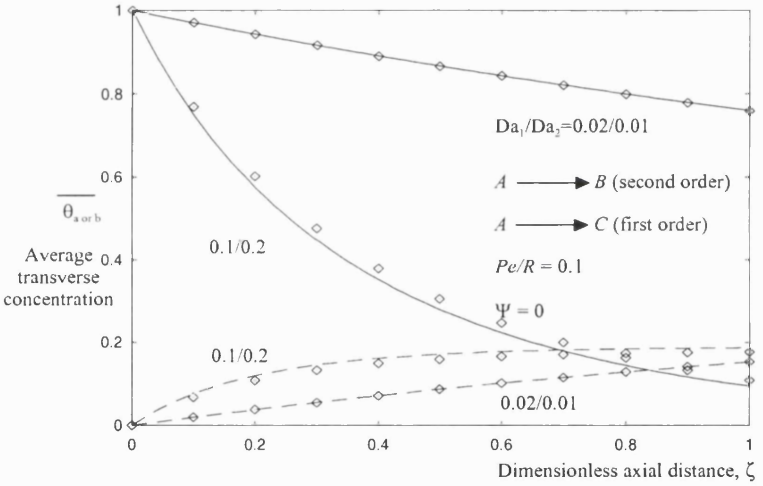

Figure 3.7: Axial concentration profiles for parallel reactions, for reactant A (solid line), product B (dashed line) for varying Da ratios with $Pe/R = 0.1$. Points represent full numerical simulations (entrance effects included).

$$\frac{\mathrm{d}\overline{\theta_b}}{\mathrm{d}\zeta} = -\frac{R}{Pe}Da_2\overline{\theta_b} + \frac{R}{Pe}Da_1\overline{\theta_a}^2, \tag{3.45}$$

using an integrating factor ($\exp(RDa_2\zeta/Pe)$) gives a simpler O.D.E. to be solved

$$\frac{\mathrm{d}}{\mathrm{d}\zeta}\left(\overline{\theta_b}\exp(RDa_2\zeta/Pe)\right) = \frac{RDa_1}{Pe}\overline{\theta_a}^2\exp(RDa_2\zeta/Pe). \tag{3.46}$$

Integrating yields

$$\overline{\theta_b} = \exp(-RDa_2\zeta/Pe)\int_0^{\zeta}\frac{RDa_1}{Pe}\overline{\theta_a}^2\exp(RDa_2\zeta/Pe)\mathrm{d}\zeta, \tag{3.47}$$

and letting $z = RDa_2\zeta/Pe$ and substituting (3.39) gives

$$\overline{\theta_b}(\zeta) = \frac{Da_1}{Da_2}\exp(-RDa_2\zeta/Pe)\int_0^{zPe/RDa_2}\left(\frac{\exp(z)}{\left(1 + z\left(\frac{Da_1}{Da_2}\right)\right)^2}\right)\mathrm{d}z. \tag{3.48}$$

A plot of (3.48) is shown in Fig. 3.8, this plot shows trends similar to the first order system with the exception that the maximum values of the intermediate product B are reduced and these peaks occur at a lower conversions.

3.6 Extension to arbitrary shaped ducts

As we have shown, when $Pe/R \ll 1$, the reactive processes are weakly dependent on the flow field. We shall show that under these conditions the influence of duct geometry may be straightforwardly introduced into the analytical solutions developed previously.

In the most general form, the transport of chemical species by plug flow is described by the advection-diffusion equation

$$\nabla^2\theta_a = \frac{Pe}{R}\frac{\partial\theta_a}{\partial\zeta}, \tag{3.49}$$

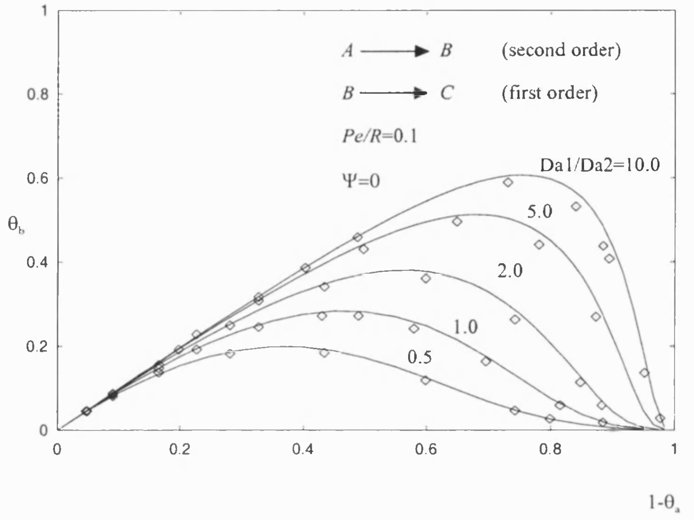

Figure 3.8: Concentration of product B as a function of conversion of A (series system) for varying ratios of Da number at $Pe/R = 0.1$. Points represent full numerical simulations.

where $\nabla^2\theta_a$ is the Laplacian of transverse gradients of concentration. The transverse dimensions are made dimensionless by the hydraulic diameter (d) and hence the aspect ratio is $R = L/d$.

In the simplest case of a first order reaction, a flux condition is imposed on the surface of the duct and this condition is expressed in vectorial form as

$$\nabla\theta_a \cdot \hat{\mathbf{n}} = Da\theta_a. \tag{3.50}$$

Seeking a separable solution (where ξ is the second transverse coordinate),

$$\theta_a = \overline{\theta_a}(\zeta) f_a(\eta, \xi), \tag{3.51}$$

reduces the system of equations to

$$\nabla^2 f_a = -\frac{\lambda_a Pe}{R} f_a, \quad \nabla f_a \cdot \hat{\mathbf{n}} = Da f_a. \tag{3.52}$$

The decay rate λ_a is thus determined by the calculation of a single eigenvalue for (3.52). Once λ_a is determined, the variation of the vertically-averaged concentration is then obtained by (3.12). These considerations also extend to multiple reactions occuring in parallel and series, where the solution (3.26) applies when λ_a and $\tilde{\lambda}_b$ are determined from (3.52) with $Da = Da_1$ and $Da = Da_2$ respectively.

In most cases, determination of the decay constant, λ_a, is achieved numerically (except for large or small Damköhler numbers). However, there are two important examples when λ_a may be calculated analytically: circular and rectangular ducts. The case of a circular duct was studied by Walker (1961) where his approach is essentially generalised in this chapter. For the case of a circular duct, (3.52) reduces to

$$\frac{1}{r}\frac{\mathrm{d}}{\mathrm{d}r}\left(r\frac{\mathrm{d}f_a}{\mathrm{d}r}\right) = -\frac{\lambda_a Pe}{R} f_a. \tag{3.53}$$

This is a particular form of Bessel's equation and hence has the solution $f_a \propto J_0\left(\sqrt{(\lambda_a Pe/R)}\, r\right)$. Substituting f_a into the boundary condition yields the following equation, which is used to determine λ_a

$$\sqrt{\frac{\lambda_a Pe}{R}} J_1\left(\sqrt{\frac{\lambda_a Pe}{R}}\right) = Da J_0\left(\sqrt{\frac{\lambda_a Pe}{R}}\right). \tag{3.54}$$

Asymptotic expressions for the decay group may be calculated in the limit of large and small Da see also (Fig. 3.9). Knowing that, for small Da,

$$\alpha\frac{J_1(\alpha r)}{J_0(\alpha r)} = Da, \tag{3.55}$$

and substituting the following first order expansions of the zero and first order Bessel functions (for low Da)

$$\begin{aligned} J_0(\alpha) &\to 1.0, \\ J_1(\alpha) &\to \frac{1}{2}\alpha, \end{aligned} \tag{3.56}$$

yields

$$\alpha = \sqrt{2Da} \quad : \quad Da \ll 1. \tag{3.57}$$

Conversely for $Da \gg 1$ a higher order expansion of the Bessel functions gives

$$\alpha \frac{\left[\frac{\alpha r}{2} - \frac{1}{2}\left(\frac{\alpha r}{2}\right)^3\right]}{1 - \frac{1}{2}\left(\frac{\alpha r}{2}\right)^2} = Da, \tag{3.58}$$

which can be rearranged into

$$\frac{\alpha^2}{2} - \frac{\alpha^4}{16} = Da - \frac{Da\alpha^2}{4}, \tag{3.59}$$

as $Da \to \infty$ the RHS of (3.59) becomes zero and $\alpha \to \alpha_0$, where α_0 is the root of the zeroth order Bessel function. For values near the root the zeroth order Bessel function can be expressed as

$$J_0(\alpha) = J_0(\alpha_0) + (\alpha - \alpha_0)J_0'(\alpha_0), \tag{3.60}$$

substituting this into (3.55), inverting and rearranging gives

$$\alpha = 2.2 - \frac{2.2}{Da} \quad : \quad Da \gg 1. \tag{3.61}$$

In Fig. 3.9 the decay group obtained after solving (3.54) is shown as a function of Da along with first order asymptotic expansions of (3.54) in the limits of $Da \gg$ and $Da \ll 1$.

For the case of a rectangular duct of height 1 and width γ the vertical function is assumed to take the separable form ($f_a = XY$). Thus (3.52) becomes

$$\frac{X''}{X} + \frac{Y''}{Y} = \frac{-\lambda_a Pe}{R}, \tag{3.62}$$

where

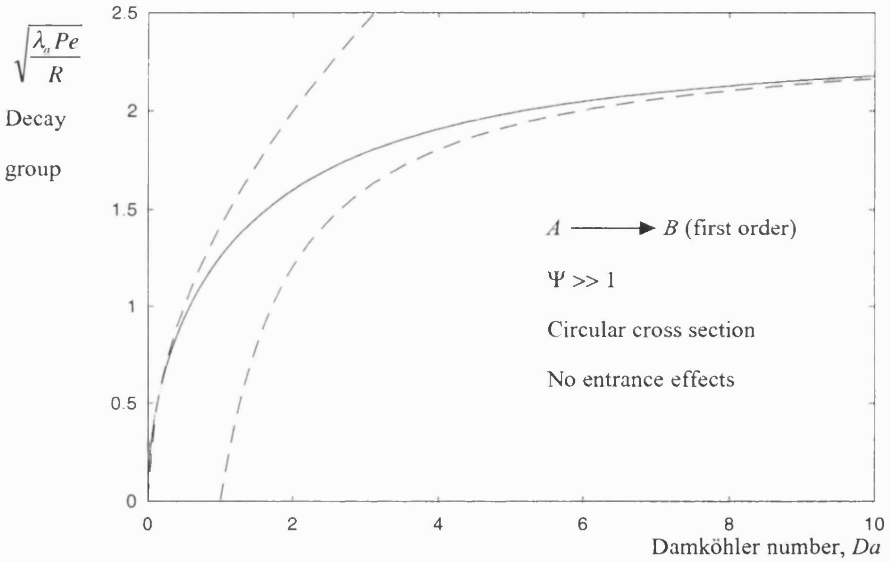

Figure 3.9: The decay group of component A, calculated analytically from the similarity solution (for the limit $\Psi \gg 1$) is shown for a duct of circular cross section as a function of Da (full curve). For comparison 1st order asymptotic expansions for the decay rate (obtained in the limit of $Da \ll 1$ and $Da \gg 1$) are plotted as dashed curves.

$$X'' = \frac{\partial^2 X}{\partial \eta^2}, \quad Y'' = \frac{\partial^2 Y}{\partial \xi^2}. \tag{3.63}$$

Further, substitution of $X'' = -\alpha^2 X$ and $Y'' = -\beta^2 Y$, into (3.62) gives

$$\alpha^2 + \beta^2 = \frac{\lambda_a Pe}{R}. \tag{3.64}$$

For first order reactions, utilising the boundary conditions on all surfaces, α and β can be determined from

$$\tan\alpha\left[\alpha - \frac{Da^2}{\alpha}\right] = 2Da, \quad \gamma\tan\beta\left[\beta - \frac{Da^2}{\beta}\right] = 2Da. \tag{3.65}$$

The decay constants (α and β) in this case are determined by (3.57) and (3.61).

In general the calculation of the decay constant requires numerical solution of (3.52). However there are practical limits, such as when $Da \ll 1$, when analytical expressions may be calculated. Integrating (3.49) over the cross section of the duct A and applying Green's theorem gives

$$\frac{Pe}{R}\frac{\partial \overline{\theta_a}}{\partial \zeta} = \frac{1}{A}\int \nabla^2 \theta_a \mathrm{d}A = -\frac{Da}{A}\oint \theta_a \mathrm{d}S, \tag{3.66}$$

where S is the perimeter of the tube. When $Da \ll 1$, the difference between the concentration at the wall and the depth-average concentration is negligible so that

$$\oint \theta_a \mathrm{d}S = \overline{\theta_a} S. \tag{3.67}$$

Thus, the decay group, using (3.10), (3.66) and (3.67), is

$$\frac{\lambda_a Pe}{R} = \frac{DaS}{A}. \tag{3.68}$$

Referring to the example of a circular tube, the decay constant $\lambda_a \to 2DaR/Pe$ is recovered for $Da \ll 1$; for the case of a rectangular duct the decay constant is $\lambda_a \to 2Da\left(1 + \frac{1}{\gamma}\right) R/Pe$. It can be seen that the rectangular solution approaches that of a parallel plate, when $\gamma \to \infty$, by comparing the decay constant for a rectangular duct with (3.15).

The extension of the analytical method to arbitrary duct geometries has been demonstrated for first order reactions by multiplying the Damköhler number by the geometrical factor S/A. Specifically the method has been shown for circular and rectangular ducts. The method is also applicable to other reaction orders (for $Da \ll 1$) by the same modification of the Damköhler number. Therefore the effect of duct geometry may be simply incorporated into the analytical solutions already presented previously.

3.7 Conclusions

In catalytic wall microreactors, where transverse diffusion is fast and axial diffusion can be neglected, the advection-diffusion equation for a first order reaction can be solved analytically since the problem reduces to the solution of a single eigenvalue problem. The vertically-averaged formulation is first illustrated for the case of laminar flow in a parallel plate catalytic microreactor and the analytical results are tested against full numerical simulations of the governing equations. It is shown that axial and radial concentration profiles are essentially not affected by the velocity profile. The primary conclusion from this work is that under the conditions considered ($1 \ll Pe \ll R$) the transverse transport of reactants is fast and the advection-diffusion equations may be replaced by a one-dimensional vertically-averaged formulation; a homogeneous formulation of the equation set. This method can also be extended to second-order kinetics, multiple reactions and ducts of arbitrary cross section when the Damköhler number is small. The cases considered illustrate its wide applicability. Reduction of the dimension of the problem (from three spatial variables to one), makes this technique a useful tool for rapid evaluation of microreactor performance without residing to computationally demanding methods such as computational fluid dynamics which require grid generation and significant computing time.

Nomenclature

Roman symbols

Symbol	Assignment	Unit
A	area of duct	m^2
A, B, C	chemical components	-
b	slip coefficient	-
c	concentration	mol/m^3
d	hydraulic diameter (S/A)	m
D	molecular diffusivity	m^2/s
f	vertical function	-
h	reactor height	m
J_0	Bessel function of the first kind (zero order)	-
J_1	Bessel function of the first kind (first order)	-
k	reaction rate constant	m/s
Kn	Knudsen number	-
L	reactor length	m
Pe	Peclet number	-
r	dimensionless radial coordinate	-
R	aspect ratio, L/h	-
S	perimeter of duct	m
u	dimensionless velocity	-
U	mean velocity	m/s
v	velocity	m/s
x	vertical coordinate	m
z	axial coordinate	m

Greek symbols

Symbol	Assignment	Unit
θ	dimensionless concentration wrt. $c_a(0)$	-
$\tilde{\theta}_b$	dummy dimensionless concentration of B	-
$\overline{\theta}$	mean axial dimensionless concentration	-
λ_a	decay constant	-
λ	mean free path of gas molecules	m
ζ	dimensionless axial distance	-
η	dimensionless transverse distance	-
ξ	dimensionless transverse distance	-
Ψ	flow parameter $Kn/(1-bKn)$	-
α	decay group, $\sqrt{\lambda_a Pe/R}$	-
β	decay group	-
γ	dimensionless width (rect. duct)	-
τ_c	characteristic convection time	s
τ_{dt}	characteristic transverse diffusion time	s
τ_{da}	characteristic axial diffusion time	s

Subscripts

Symbol	Assignment
a	component A
b	component B
c	component C

Chapter 4

Modelling of Heat Transfer in Microreactors

4.1 Introduction

The previous chapter developed analytical techniques for the prediction of mass transfer in microreactors. The initial section in this chapter (§4.2) adapts these methods for combined heat and mass transfer in a single channel to yield fundamental insights into non-isothermal transport phenomena at this scale.

The potential for efficient energy management at this scale yields the introduction of a new type of catalytic reactor in §4.3. In this reactor the concept of coupling an endothermic and exothermic reaction is implemented. Such a reactor consists of a series of catalytically coated plates with an endothermic and exothermic reaction occuring in alternate channels. Heat is transferred between channels by conduction through the channel wall. Results are given for this reactor for first order kinetics in both channels, showing the potential for isothermal operation. The reactor operation is then demonstrated for a more realistic set of reactions where the reversible endothermic ethane dehydrogenation reaction is considered in one channel, whilst in the other the exothermic propane combustion reaction takes place.

4.2 Single channel reactor

In order to investigate non-isothermal flows in catalytic microreactors, where heat is produced on the catalyst by an exothermic reaction, a single channel is examined first with an identical geometry to the reactor studied in Chapter 3. An analytical solution is sought and techniques similar to the isothermal reactor with non-linear kinetics in Chapter 3 are utilised.

The mathematical model is based on laminar incompressible microscale flow between two parallel plates, where a heterogeneous first order catalytic reaction only occurs on the lower plate (A → B). Modelling assumptions applied are constant fluid properties, no volume change and dilute reacting solution. As $Pe_m \gg 1$, axial diffusion can be neglected and the dimensionless mass balance for species A is

$$\frac{Pe_m}{R} u(\eta) \frac{\partial \theta_a}{\partial \zeta} = \frac{\partial^2 \theta_a}{\partial \eta^2}, \tag{4.1}$$

where $u(\eta)$ is the velocity profile, θ_a the dimensionless concentration, ζ and η are the dimensionless axial and vertical coordinates respectively, $Pe_m = Uh/D$ and $R = L/h$ (aspect ratio). The mass flux boundary condition at the catalyst is

$$\frac{\partial \theta_a (0,\zeta)}{\partial \eta} = Da \exp\left(\gamma \left(\frac{y}{y+1}\right)\right) \theta_a (0,\zeta), \tag{4.2}$$

where $y = T/(T - T_0)$, $\gamma = E_a/RT_0$ and the Damköhler number is defined as $Da = A \exp(-\gamma)\, h/D$. This equation is solved in conjunction with the energy equation, which takes on a similar form

$$\frac{Pe_e}{R} u(\eta) \frac{\partial y}{\partial \zeta} = \frac{\partial^2 y}{\partial \eta^2}, \tag{4.3}$$

where $Pe_e = U\rho c_p h/k$, with the inlet condition

$$y(\eta, 0) = 1. \tag{4.4}$$

The boundary conditions for the energy balance are an adiabatic boundary condition on the top wall with energy flux on the bottom wall due to the reaction exotherm

$$\frac{\partial y (1,\zeta)}{\partial \eta} = 0, \quad \frac{\partial y (0,\zeta)}{\partial \eta} = -\frac{\beta Da}{Le} \exp\left(\gamma \left(\frac{y}{y+1}\right)\right) \theta_a (0,\zeta), \tag{4.5}$$

where $Le = k/\rho c_p D$ and $\beta = (-\Delta H) c_0/\rho c_p T_0$. The above system of equations constitute a highly non-linear problem. We explore briefly how the limiting case of a weakly exothermic reaction, corresponding to $\beta \ll 1$, may be obtained analytically. Using an averaging method, as in Chapter 3 for second order reactions, the vertically-averaged analytical solution for weakly exothermic flow is

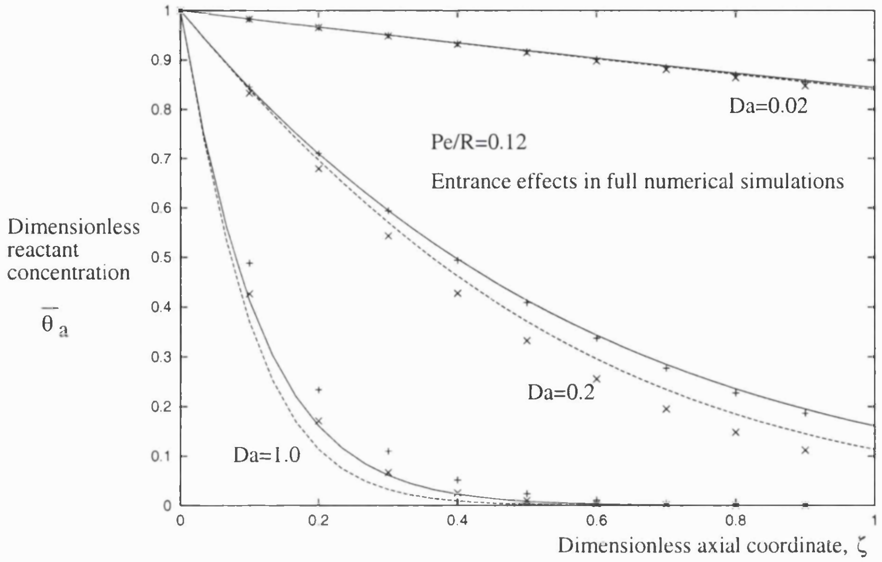

Figure 4.1: Dimensionless axial reactant profiles for different Damköhler and β numbers; + and × correspond to full numerical solutions for β 0.1 and 0.3 respectively, solid and dashed lines correspond to analytical solutions for β 0.1 and 0.3 respectively.

$$\overline{\theta_a}(\zeta) = \frac{\left(1+\frac{\gamma\beta Pe_m}{2LePe_e}\right)\exp\left(-\frac{Da\zeta RA}{Pe_m}\right)}{1+\frac{\gamma\beta}{2LePe_e}\exp\left(-\frac{Da\zeta RA}{Pe_m}\right)}, \tag{4.6}$$

where $A = 1 + (\gamma\beta Pe_m/(2LePe_e))$. Figure 4.1 shows these average profiles of reactant for different β and Damköhler numbers. As expected the higher the β and Damköhler number the higher the reactant conversion. A comparison is made in Fig. 4.1 with full numerical simulations, which are displayed as discrete points. It can be seen that there is reasonable agreement for $Da < 0.2$ and $\beta < 0.1$. The discrepancies observed are partly due to the formulation of the analytical solution, which involves a binomial expansion in terms of β and Damköhler number of the exponential terms in (4.5).

For the higher Damköhler number of 1 in Fig. 4.1 it can be seen that although the profiles are not well matched the axial position corresponding to near complete conversion (ca. $\zeta = 0.7$) is successfully predicted by both solutions.

4.3 Coupled plate reactor

The coupled plate reactor consists of channels with exothermic and endothermic reactions occuring in alternate channels. Heat is transferred between the phases

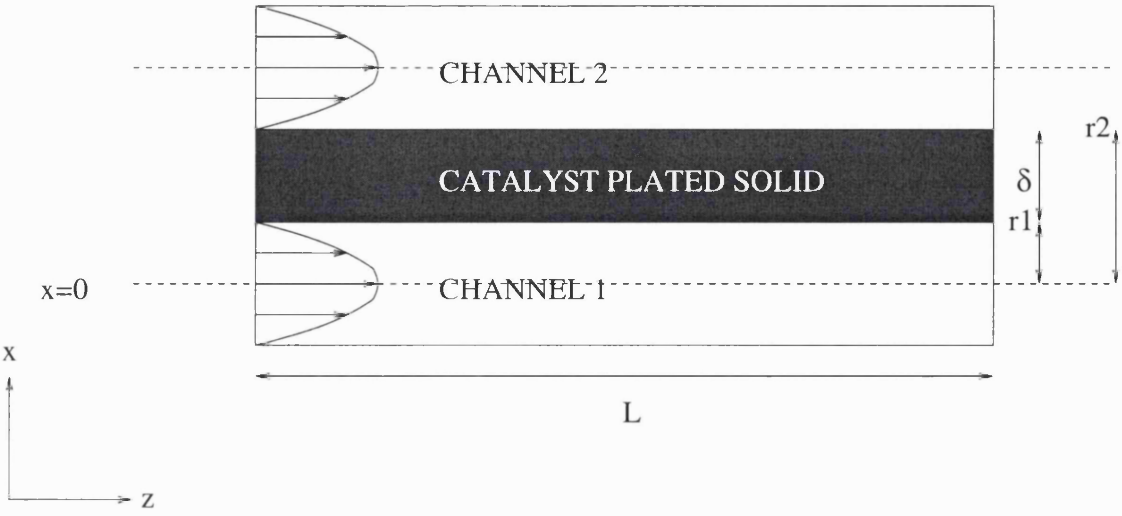

Figure 4.2: Schematic of coupled plate reactor.

through a solid channel wall. Correct choice of operating and design parameters will yield potential for isothermal operation.

4.3.1 Reactor configuration and model

The reactor consists of an array of parallel rectangular plates (see Fig. 4.2). On the surface of each plate a thin layer of catalyst is deposited. Each alternate channel is coated with the same catalyst, depending on the type of reaction occuring. Such a configuration allows only one type of reaction to take place in each channel; i.e. endothermic or exothermic. Overall adiabatic conditions are assumed, hence it suffices to examine the behaviour of a reactor segment, confined by the dotted lines in Fig. 4.2. The plates are considered to be infinitely wide so that a 2D model can be implemented.

4.3.2 2D model formulation

A two-dimensional model is developed to determine the concentration field of the reacting species and the temperature distribution in the reactor. The thickness of the catalyst layer is assumed negligible, with an effectiveness factor of 1, and hence only the mass and energy balances in the two gas phases and the solid phase are considered. Interaction between adjacent phases is implemented through the boundary conditions posed.

In the development of the model the following simplifying assumptions have been adopted: steady-state operation (for first two sections), one dimensional incompressible fluid flow, negligible pressure drop, no homogeneous reactions, and fully developed flow at reactor inlet, while radiation from solid phase is neglected.

The dimensional form of the modelling equations are first given followed by the dimensionless forms, for clarity only the mass and energy balances for channel 1 are given; the equations for both channels are identical.

4.3.3 Dimensional form of model

Channel 1 - mass equation

$$u_{1x}\frac{\partial c_1}{\partial z} = D_1\left[\frac{\partial^2 c_1}{\partial x^2} + \frac{\partial^2 c_1}{\partial z^2}\right], \tag{4.7}$$

where u_{1x} is the laminar parabolic velocity profile,

$$\frac{u_{1x}}{U} = \frac{\left(\frac{x}{2r_1}\right) - \left(\frac{x}{2r_1}\right)^2 + C}{\frac{1}{6} + C}, \tag{4.8}$$

c_1 is the species concentration, C is a constant for slip effects $(Kn/(1-bKn))$ and D_1 is the molecular diffusivity. Subject to the following boundary conditions

$$c_1\left(x,0\right) = c_{10}, \tag{4.9}$$

$$\frac{\partial c_1\left(0,z\right)}{\partial x} = 0, \tag{4.10}$$

$$\frac{\partial c_1\left(r_1,z\right)}{\partial x} = \frac{-r_{1(rxn)}}{D_1} = \frac{-A\exp\left(\frac{-E_a}{RT}\right)c_1(r_1,z)}{D_1}, \quad \text{wall reaction,} \tag{4.11}$$

$$\frac{\partial c_1\left(x,L\right)}{\partial z} = 0, \tag{4.12}$$

Channel 1 - heat equation

$$u_{1x}\frac{\partial T_1}{\partial z} = \frac{k_1}{\rho_1 c_{p1}}\left[\frac{\partial^2 T_1}{\partial x^2} + \frac{\partial^2 T_1}{\partial z^2}\right]. \tag{4.13}$$

Subject to the following boundary conditions

$$T_1(x,0) = T_{10}, \tag{4.14}$$

$$\frac{\partial T_1(0,z)}{\partial x} = 0, \tag{4.15}$$

$$\frac{\partial T_1(r_1,z)}{\partial x} = \frac{1}{k_1}\left[r_{1(rxn)}(-\Delta H_1) + k_s \left.\frac{\partial T_s}{\partial x}\right|_{r_1}\right], \tag{4.16}$$

$$\frac{\partial T_1(x,L)}{\partial z} = 0, \tag{4.17}$$

Solid phase

$$k_s\left(\frac{\partial^2 T_s}{\partial z^2} + \frac{\partial^2 T_s}{\partial x^2}\right) = 0. \tag{4.18}$$

Adiabatic boundary conditions are applied at the axial ends of the solid, whilst to satisfy temperature continuity at the gas solid interfaces the following boundary conditions are applied

$$\begin{aligned} T_s(r_1,z) &= T_1(r_1,z), \\ T_s(r_2,z) &= T_2(r_2,z). \end{aligned} \tag{4.19}$$

4.3.4 Dimensionless form of model

The following dimensionless spatial and transient coordinates are introduced

$$\zeta = \tfrac{z}{L}, \quad \eta = \tfrac{x}{2r_1}, \quad \eta_s = \tfrac{x-r_1}{\delta}, \quad \varphi = \left(\tfrac{r_1+\delta}{r_2} + 1\right) - \tfrac{x}{r_2}. \tag{4.20}$$

$$R_1 = \tfrac{L}{r_1}, \quad R_2 = \tfrac{L}{r_2}, \quad R_w = \tfrac{L}{\delta}. \tag{4.21}$$

$$\theta = \tfrac{c}{c_0}, \quad y = \tfrac{T}{T_0}, \quad T_r = \tfrac{T_{20}}{T_{10}}, \quad Pe_m = \tfrac{UL}{D}, \quad Pe_h = \tfrac{U\rho c_p L}{k}. \tag{4.22}$$

where $\omega = D$ or α.

Channel 1 - mass equation

$$U_1 \left[\frac{\eta - \eta^2 + C}{\frac{1}{6} + C}\right] \frac{c_{10}}{L} \frac{\partial \theta_1}{\partial \zeta} = D_1 \left[\frac{c_{10}}{r_1^2} \frac{\partial^2 \theta_1}{\partial \eta^2} + \frac{c_{10}}{L^2} \frac{\partial^2 \theta_1}{\partial \zeta}\right], \tag{4.23}$$

$$U_1 \left[\frac{\eta - \eta^2 + C}{\frac{1}{6} + C}\right] \frac{1}{L} \frac{\partial \theta_1}{\partial \zeta} = D_1 \left[\frac{1}{r_1^2} \frac{\partial^2 \theta_1}{\partial \eta^2} + \frac{1}{L^2} \frac{\partial^2 \theta_1}{\partial \zeta^2}\right], \tag{4.24}$$

$$U_1 \left[\frac{\eta - \eta^2 + C}{\frac{1}{6} + C}\right] L \frac{\partial \theta_1}{\partial \zeta} = D_1 \left[\frac{L^2}{r_1^2} \frac{\partial^2 \theta_1}{\partial \eta^2} + \frac{\partial^2 \theta_1}{\partial \zeta^2}\right], \tag{4.25}$$

$$Pe_{m1} \left[\frac{\eta - \eta^2 + C}{\frac{1}{6} + C}\right] \frac{\partial \theta_1}{\partial \zeta} = \left[R_1^2 \frac{\partial^2 \theta_1}{\partial \eta^2} + \frac{\partial^2 \theta_1}{\partial \zeta^2}\right]. \tag{4.26}$$

Subject to the following boundary conditions

$$\theta_1\left(\eta,0\right)=1, \tag{4.27}$$

$$\frac{\partial\theta_1\left(0,\zeta\right)}{\partial\eta}=0, \tag{4.28}$$

$$\frac{\partial\theta_1\left(0.5,\zeta\right)}{\partial\eta}=-\frac{Da_1}{R_1}\exp\left(\gamma_1\left(\frac{y_1(0.5,\zeta)-1}{y_1(0.5,\zeta)}\right)\right)\theta_1(0.5,\zeta), \tag{4.29}$$

$$\frac{\partial\theta_1\left(\eta,1\right)}{\partial\zeta}=0, \tag{4.30}$$

where $Da = LA\exp\left(\frac{-E_a}{RT_0}\right)/D$.

Channel 1 - heat equation

$$U_1\left[\frac{\eta-\eta^2+C}{\frac{1}{6}+C}\right]\frac{T_{10}}{L}\frac{\partial y_1}{\partial\zeta}=\frac{k_1}{\rho_1 c_{p1}}\left[\frac{T_{10}}{r_1^2}\frac{\partial^2 y_1}{\partial\eta^2}+\frac{T_{10}}{L^2}\frac{\partial^2 y_1}{\partial\zeta^2}\right], \tag{4.31}$$

$$U_1\left[\frac{\eta-\eta^2+C}{\frac{1}{6}+C}\right]\frac{1}{L}\frac{\partial y_1}{\partial\zeta}=\alpha_1\left[\frac{1}{r_1^2}\frac{\partial^2 y_1}{\partial\eta^2}+\frac{1}{L^2}\frac{\partial^2 y_1}{\partial\zeta^2}\right], \tag{4.32}$$

$$Pe_{h1}\left[\frac{\eta-\eta^2+C}{\frac{1}{6}+C}\right]\frac{\partial y_1}{\partial\zeta}=\left[R_1^2\frac{\partial^2 y_1}{\partial\eta^2}+\frac{\partial^2 y_1}{\partial\zeta^2}\right]. \tag{4.33}$$

Subject to the following boundary conditions

$$y_1\left(\eta,0\right)=1, \tag{4.34}$$

$$\frac{\partial y_1(0,\zeta)}{\partial \eta} = 0, \tag{4.35}$$

$$\frac{\partial y_1(0.5,\zeta)}{\partial \eta} = \frac{\beta Da}{LeR_1} \exp\left(\gamma_1 \left(\frac{y_1(0.5,\zeta)-1}{y_1(0.5,\zeta)}\right)\right) \theta_1(0.5,\zeta) + \kappa_1 \left.\frac{\partial y_s}{\partial \eta}\right|_{r_1}, \tag{4.36}$$

$$\frac{\partial y_1(\eta,1)}{\partial \eta} = 0, \tag{4.37}$$

Solid phase

$$\frac{\partial^2 y_s}{\partial \zeta^2} + R_w \frac{\partial^2 y_s}{\partial \eta^2} = 0. \tag{4.38}$$

Subject to the following boundary conditions

$$\begin{aligned} y_s(0,\zeta) &= y_1(0.5,\zeta), \\ y_s(1,\zeta) &= y_2(1,\zeta). \end{aligned} \tag{4.39}$$

4.3.5 Summary of dimensionless forms

The following governing equations describe channel 1 and the solid phase of the coupled reactor

$$Pe_{m1}\left[\frac{\eta-\eta^2+C}{\frac{1}{6}+C}\right]\frac{\partial \theta_1}{\partial \zeta} = \left[R_1^2 \frac{\partial^2 \theta_1}{\partial \eta^2} + \frac{\partial^2 \theta_1}{\partial \zeta^2}\right], \tag{4.40}$$

$$Pe_{h1}\left[\frac{\eta-\eta^2+C}{\frac{1}{6}+C}\right]\frac{\partial y_1}{\partial \zeta} = \left[R_1^2 \frac{\partial^2 y_1}{\partial \eta^2} + \frac{\partial^2 y_1}{\partial \zeta^2}\right], \tag{4.41}$$

$$\frac{\partial^2 y_s}{\partial \zeta^2} + R_w \frac{\partial^2 y_s}{\partial \eta^2} = 0. \tag{4.42}$$

The governing equations for channel 2 are identical to channel 1, except the variable η is replaced by φ.

4.3.6 Reaction systems

The initial set of simulations performed considers reactions with identical physicochemical parameters but with equal and opposite heats of reaction. Furthermore first order kinetics are assumed. Such a general system is studied in order to isolate the effect of reactor design parameters on its performance. The second set of simulations concern a case where in channel 1 the endothermic reversible ethane dehydrogenation reaction occurs, and in channel 2 the exothermic propane combustion reaction takes place.

Ethane can react over a palladium catalyst to produce ethylene and hydrogen

$$C_2H_6 \longrightarrow C_2H_4 + H_2. \tag{4.43}$$

The reaction is highly endothermic. Intrinsic kinetics determined by Gobina et al.(1995) are used for the simulations

$$r_{C_2H_6} = k_1 \left[P_{C_2H_6} - \frac{P_{C_2H_4} P_{H_2}}{K_e} \right]. \tag{4.44}$$

The equilibrium conversion of ethane, for the dehydrogenation reaction at 660K is only 1%. Since the reaction is endothermic and reversible both the equilibrium constant and the conversion increase with elevating temperature. Thus, to achieve appreciable conversion it is imperative to operate the reaction at a high temperature, i.e. maintain the temperature at the highest allowable value. Hence an operating temperature of 1100K was selected for a feed comprising of ethane and nitrogen (50 vol%). Note that at this high temperature homogeneous reactions and catalyst coking also occur and radiative heat transport should be considered, but these effects are not considered here because our analysis is focussed on the effects of coupling catalytic endothermic and exothermic reactions.

Propane reacts with oxygen on a platinum-rhodium monolith catalyst according to the following stoichiometric equation

$$C_3H_8 + 5O_2 \longrightarrow 3CO_2 + 4H_2O. \tag{4.45}$$

Bennet et al.(1991) report a first order rate equation for propane oxidation in an excess of oxygen

$$r_{C_3H_8} = k_2 C_{C_3H_8}. \tag{4.46}$$

Parameters varied include Damkohler numbers, residence times and channel gap (keeping solid width the same). In the first set of calculations, Da and Pe were varied only in channel 2. In the second set, Da and Pe were varied in channel 1 only, while channel gap and inlet temperatures were kept the same in both channels. In all cases, variations have been expressed as percentages with 100% value assigned to the base case.

4.4 Results and discussion for the coupled plate reactor

This section gives results of the model presented in Section 4.3.1. The first section considers simplified first order kinetics, whilst the second section considers a more realistic dehydrogenation/combustion system. For these two sections the model assumes no slip of the fluid at the wall (i.e. no Kn effects) and physical properties that vary according to

$$\rho = \rho_0 \left(\frac{T}{T_0}\right)^{-1}, \quad D = D_0 \left(\frac{T}{T_0}\right)^{1.75}, \quad k = k_0 \left(\frac{T}{T_0}\right)^{0.75}. \tag{4.47}$$

The third sections considers a transient coupled reactor where first order kinetics are used to investigate characteristic scales of such a device.

4.4.1 First order reactions

The parameters used for the first order kinetics calculations (base case) are shown in Table 4.1.

When the physicochemical parameters of both reaction systems are identical, (except the sign of the heat of reaction), the heat generation and removal rates

Parameter	Value
Pe	1500
Le	1.77
Da	27.7
β	± 0.167
R	0.0025
R_w	0.0050
θ_0	0.5

Table 4.1: Dimensionless parameters used for first order reaction system.

are the same at each axial position. This results in isothermal behaviour. As shown in Fig. 4.3, the axial temperature profile is flat and conversion in both channels is the same. It must be noted that radial gradients for temperature and concentration were insignificant for all simulations performed. For this reason the profiles shown, correspond to gas and solid phases, unless otherwise stated. Figure 4.4 shows the dimensionless temperature profile along the reactor length for $Da_1 = 27.7$, $Da_2 = 125$ and $\beta_1 = -0.167$. Four curves are presented with differing β_2 numbers. If the lower extreme is considered first ($\beta = 0.037$), it can be seen that the temperature decreases monotonically along the reactor. This is due to the fact that the heat produced by the exothermic reaction is not sufficient to satisfy the heat required by the endothermic reaction. For the upper extreme, ($\beta = 0.3$) the opposite occurs. Heat generated by the exothermic reaction is not compensated fully by the endothermic one, resulting in a temperature increase. At $\zeta = 0.2$ the exothermic reaction has nearly gone to completion while the endothermic one does not reach completion even at the end of the reactor. The maxima observed in Fig. 4.4 is due to the higher Da in the exothermic/combustion channel. This maximum exists even when the heat generated is lower than what is required by the endothermic reaction, as is the case for $\beta_2 = 0.077$.

Figure 4.5 shows the dimensionless axial temperature profile where $\beta_1 = -0.167$, $\beta_2 = 0.3$ and $Da_1 = 27.7$. In this case, the heat of the exothermic reaction is greater than that of the endothermic one. For the lower Da_2 (15.4) the rate of exothermic reaction is initially slower and does not reach completion, while the endothermic reaction does. The combination of a higher β and lower Da in channel 2 as compared to channel 1 gives rise to this characteristic 'S' shape curve. As Da_2 increases the exothermic reaction becomes faster and reaches completion at a point closer to the reaction entrance. This explains the temperature peak, which in real terms corresponds to a temperature increase of approximately 110K. Further calculations have also confirmed that significantly different β and Da numbers between channels give rise to non-isothermal behaviour.

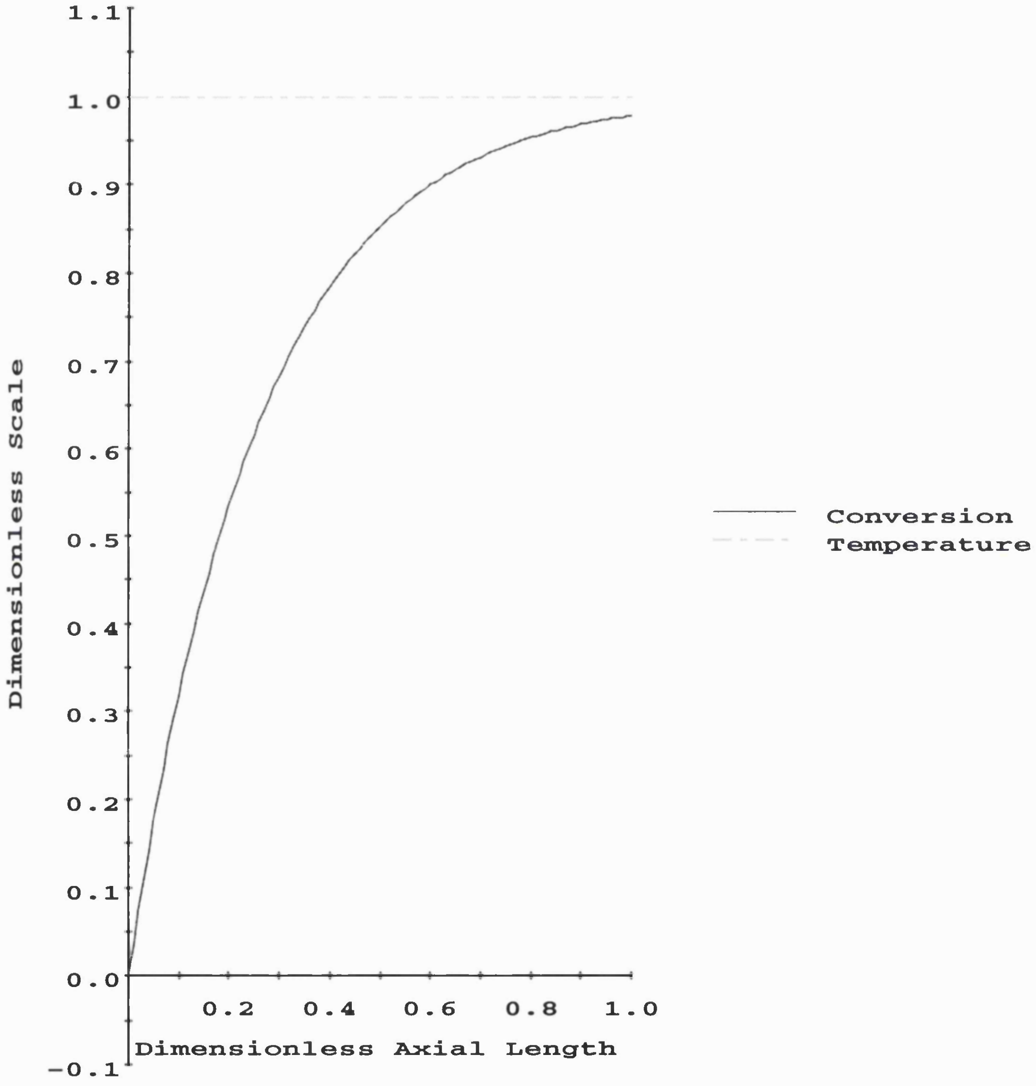

Figure 4.3: Plot of conversion and temperature vs dimensionless axial length for first order base case.

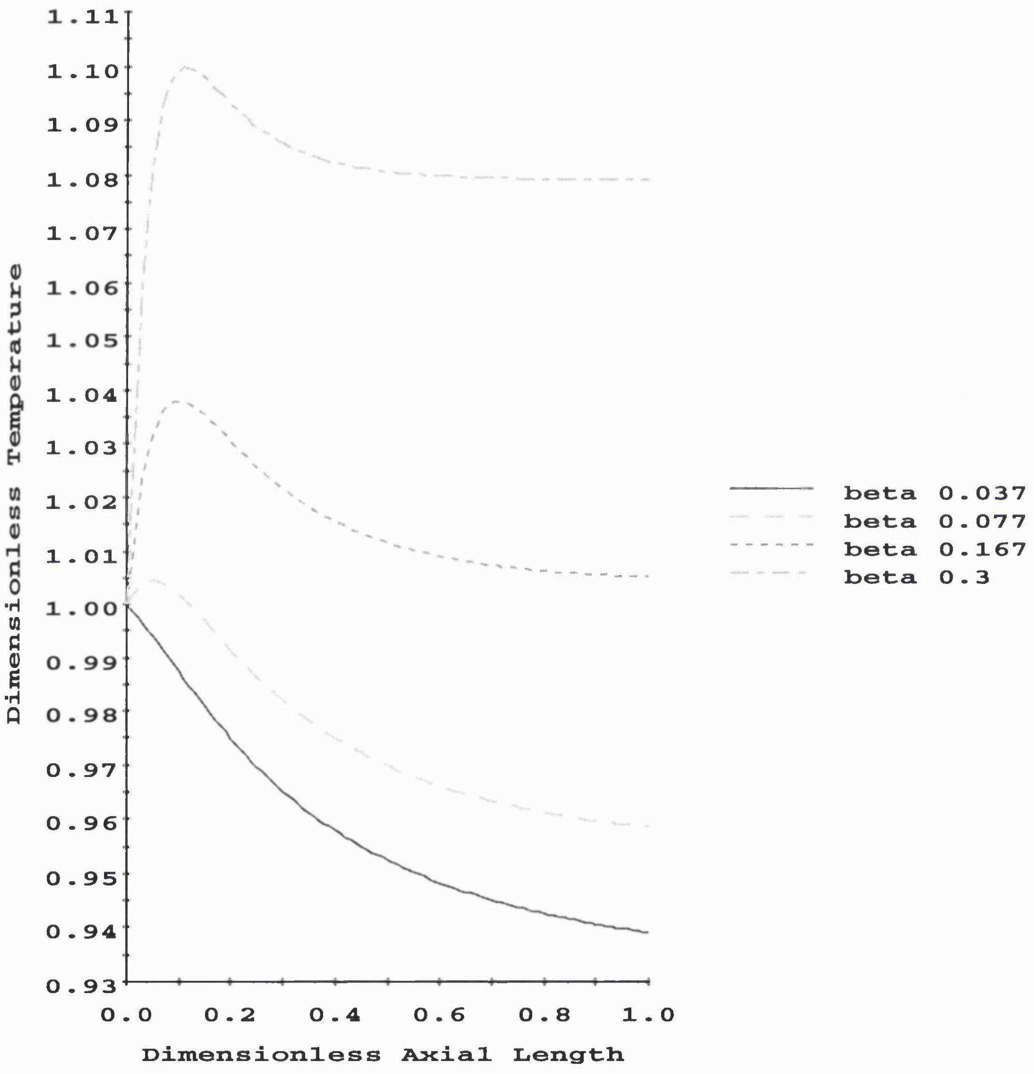

Figure 4.4: Axial temperature profiles for varying β_2 numbers.

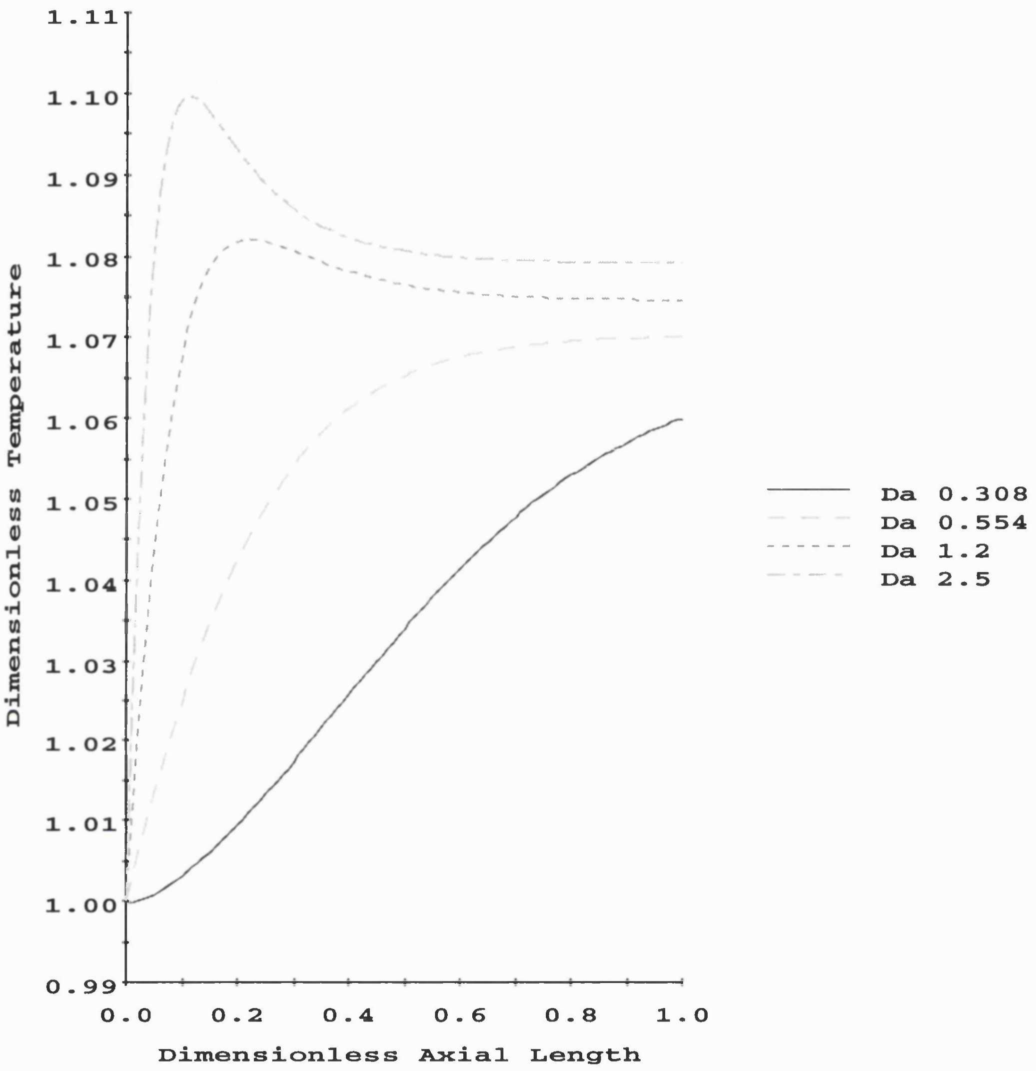

Figure 4.5: Axial temperature profiles for varying Da_2 numbers.

4.4.2 Dehydrogenation/combustion reactions

The parameters used for the dehydrogenation/combustion calculations (base case) are shown in Table 4.2.

Figure 4.6 shows the 'base-case' results for the dehydrogenation/combustion system. It can be seen that, under the conditions considered, the endothermic reaction in channel 1 reaches a conversion of 68%, which is close to the equilibrium value. The combustion reaction in channel 2 reaches 100% conversion at a dimensionless axial

Parameter	Channel 1	Channel 2
Pe	49.75	382.5
Le	1.77	1.77
Da	0.3375	13.85
β	-2.07	0.167
R	0.0025	0.0025
R_w	0.005	0.005

Table 4.2: Dimensionless parameters used for the dehydrogenation/combustion system.

length of approximately 0.4. The latter as well as the peak in temperature profile are due to the fact that the combustion reaction is faster than the dehydrogenation reaction.

Figure 4.7 shows the axial temperature profiles when Da_1 is varied (to simulate the change of catalyst loading for dehydrogenation).

As expected the temperature peak is increased when a lower catalyst loading is used in channel 1. A more subtle trend observed is that as Da_1 decreases the temperature peak moves further down the reactor.

Figure 4.8 shows the effects of residence time, through altering the Pe number in channel 1, on the reactor performance. For the base case, the residence time in channel 1 is 500 ms, whilst in channel 2 it is 63 ms. Conversion profile in the combustion channel is hardly affected. This indicates that the amount of heat generated remains constant. However, conversion for the endothermic reaction, at higher Pe numbers, decreases significantly and the outlet temperature falls. Since, Pe number increase is related to a decrease in residence time, a lower conversion is to be expected. Note that in spite of a lower conversion, a larger amount of heat is consumed by the endothermic reaction.

The effect of wall conductivity is considered by varying the value of κ. For values of κ between 10 and 500, which would be typical of a ceramic or metal microreactor, no significant effect was observed. The value of κ was artificially lowered to 0.1 and the results are shown in Fig. 4.9.

Until now the results presented, have shown a single wall temperature in a channel because the difference in channel wall temperatures was very small. This is due to efficient radial heat transfer inherent in microreactors. Altering the conductivity to such a low level provides a high heat transfer resistance hence a noticeable radial temperature gradient appears in the solid. Note, that even though radial gradients were not observed for typical microreactor systems, axial gradients can develop as demonstrated for example in Fig. 4.7.

Figures 4.10 and 4.11 show the effect of channel size on axial temperature and

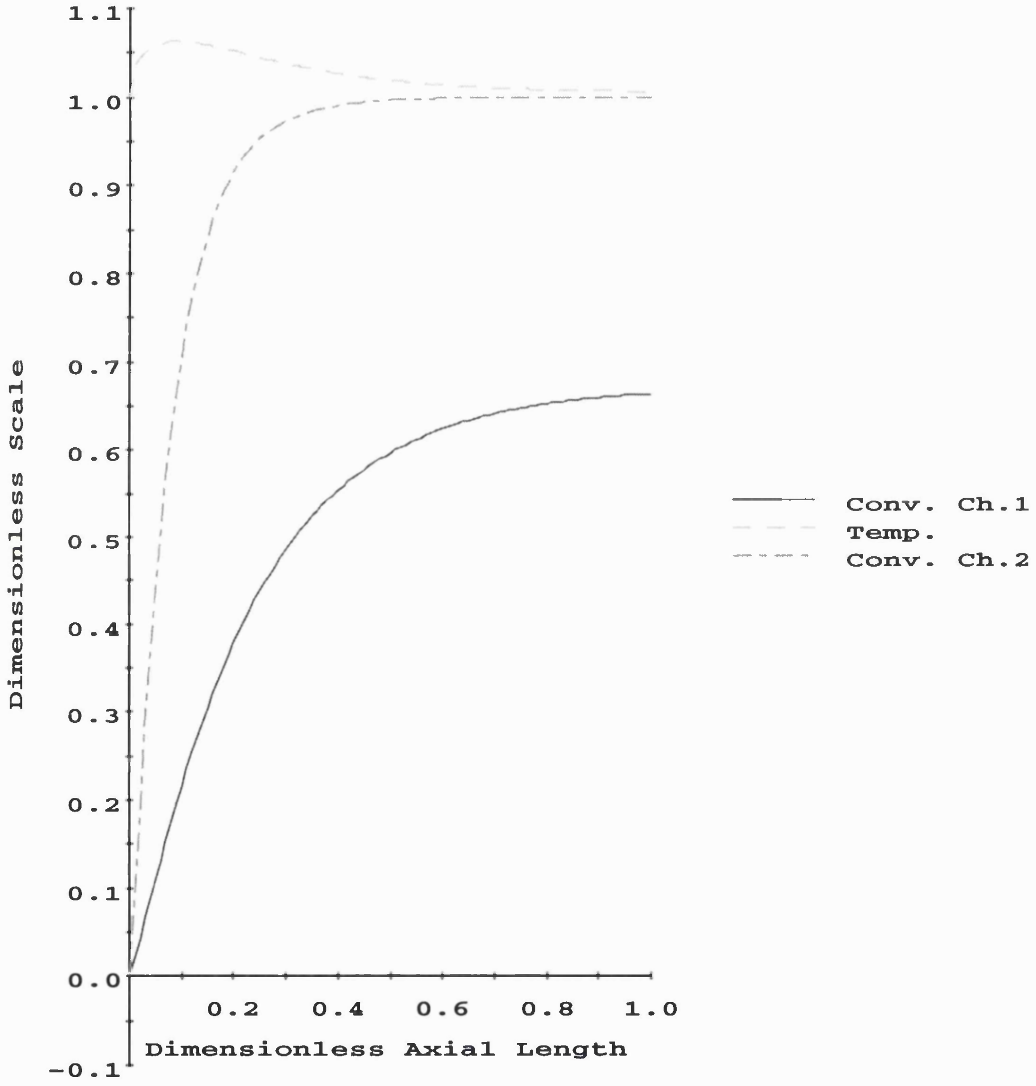

Figure 4.6: Conversion in channels 1 and 2 and temperature profiles for dehydrogenation/combustion base case.

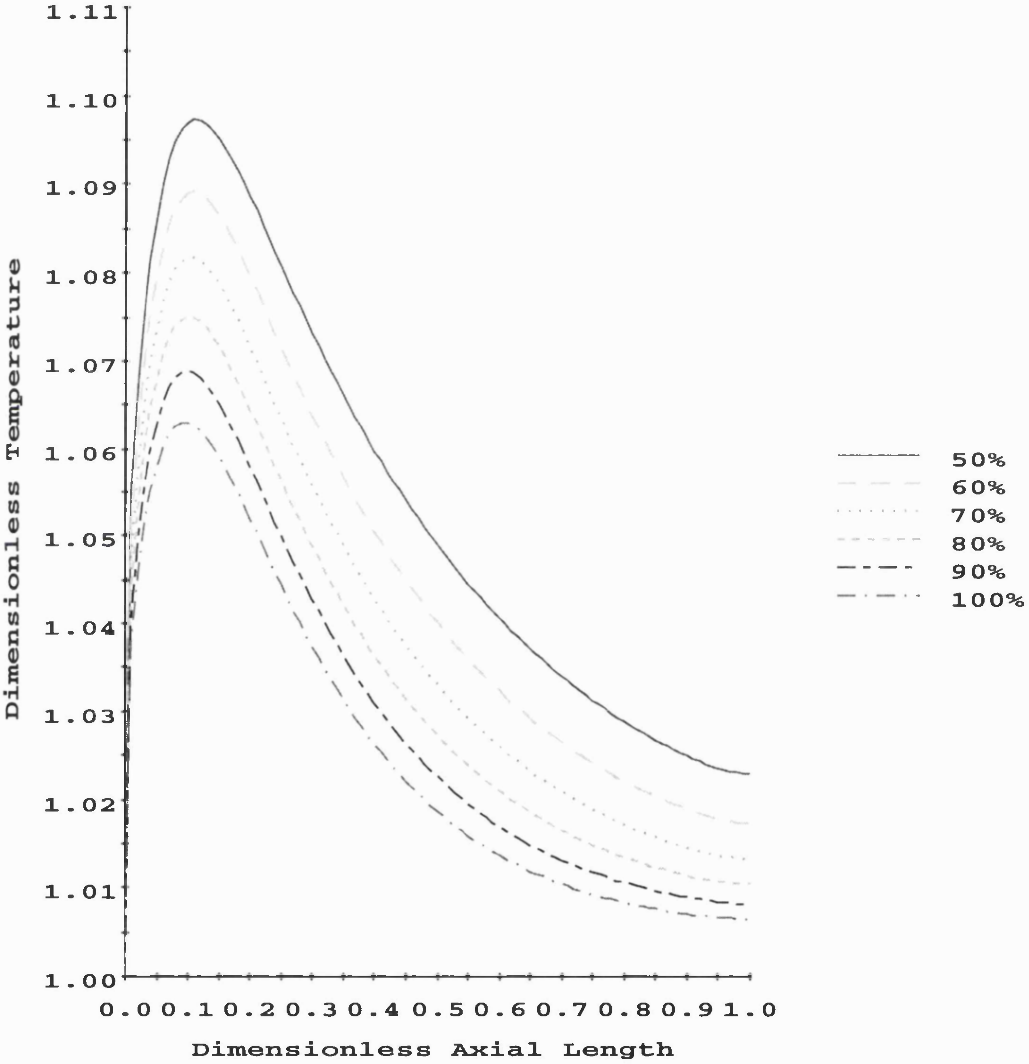

Figure 4.7: Temperature profiles for varying Da_1 numbers. Da_1 is expressed as a percentage of the base case.

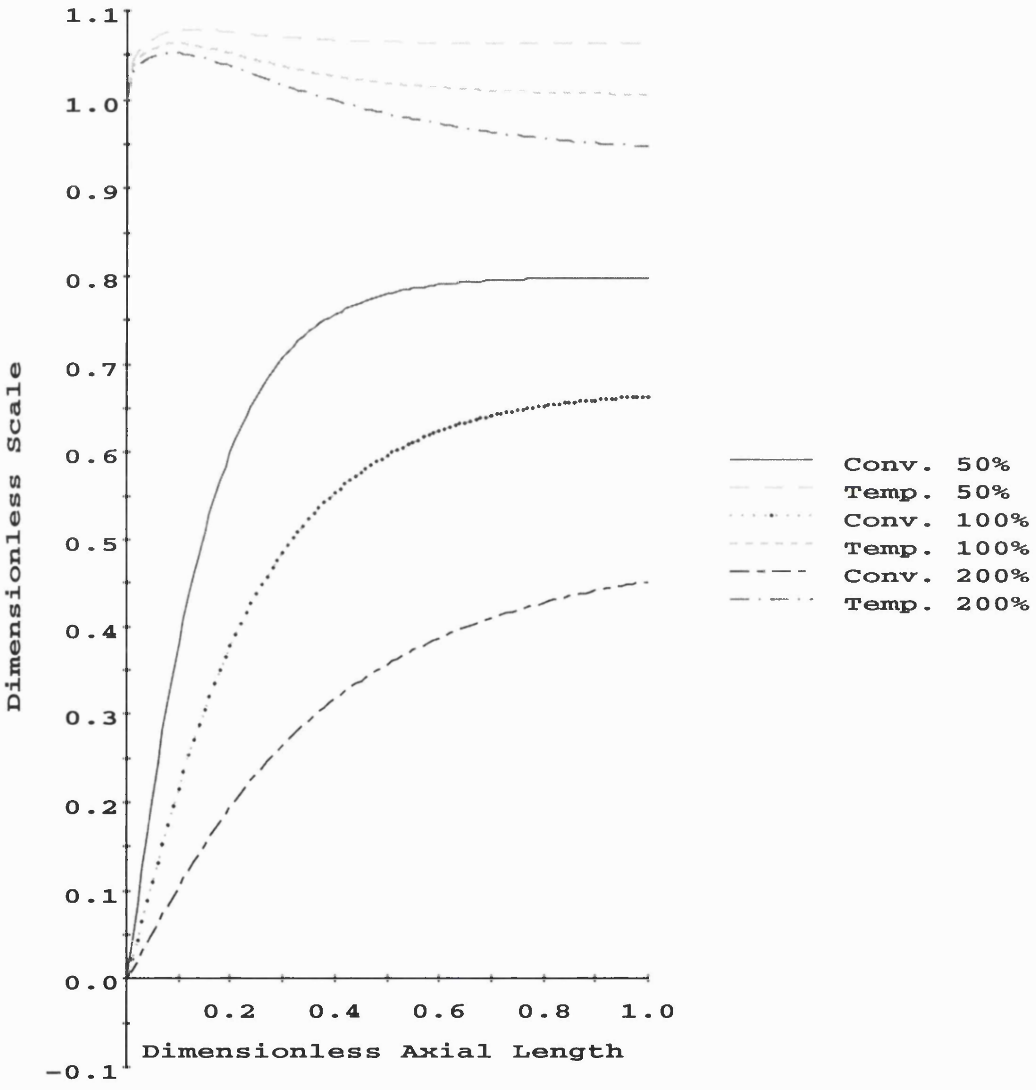

Figure 4.8: Conversion in channel 1 and temperatures for varying Pe numbers. Pe_1 is expressed as a percentage of the base case.

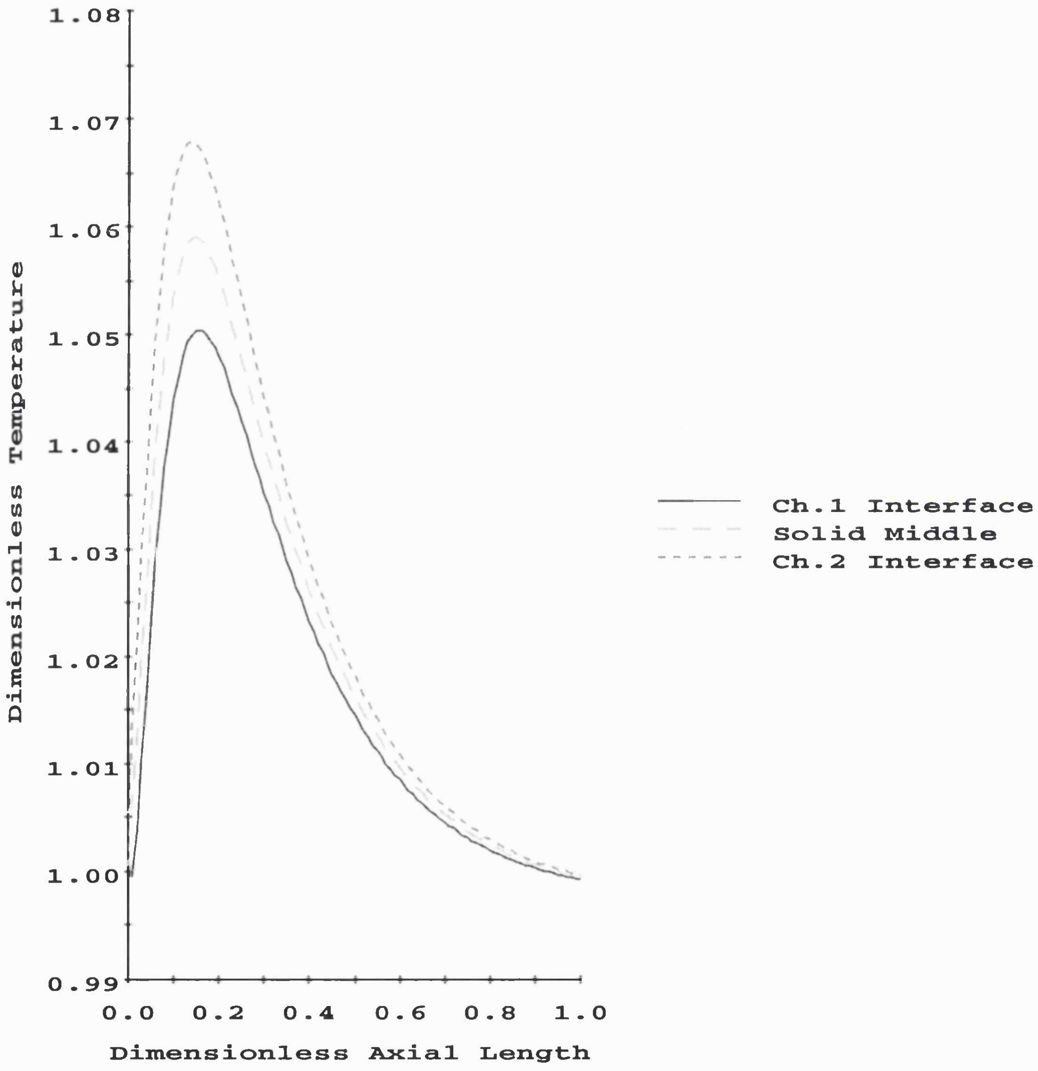

Figure 4.9: Axial temperature profiles at different radial positions.

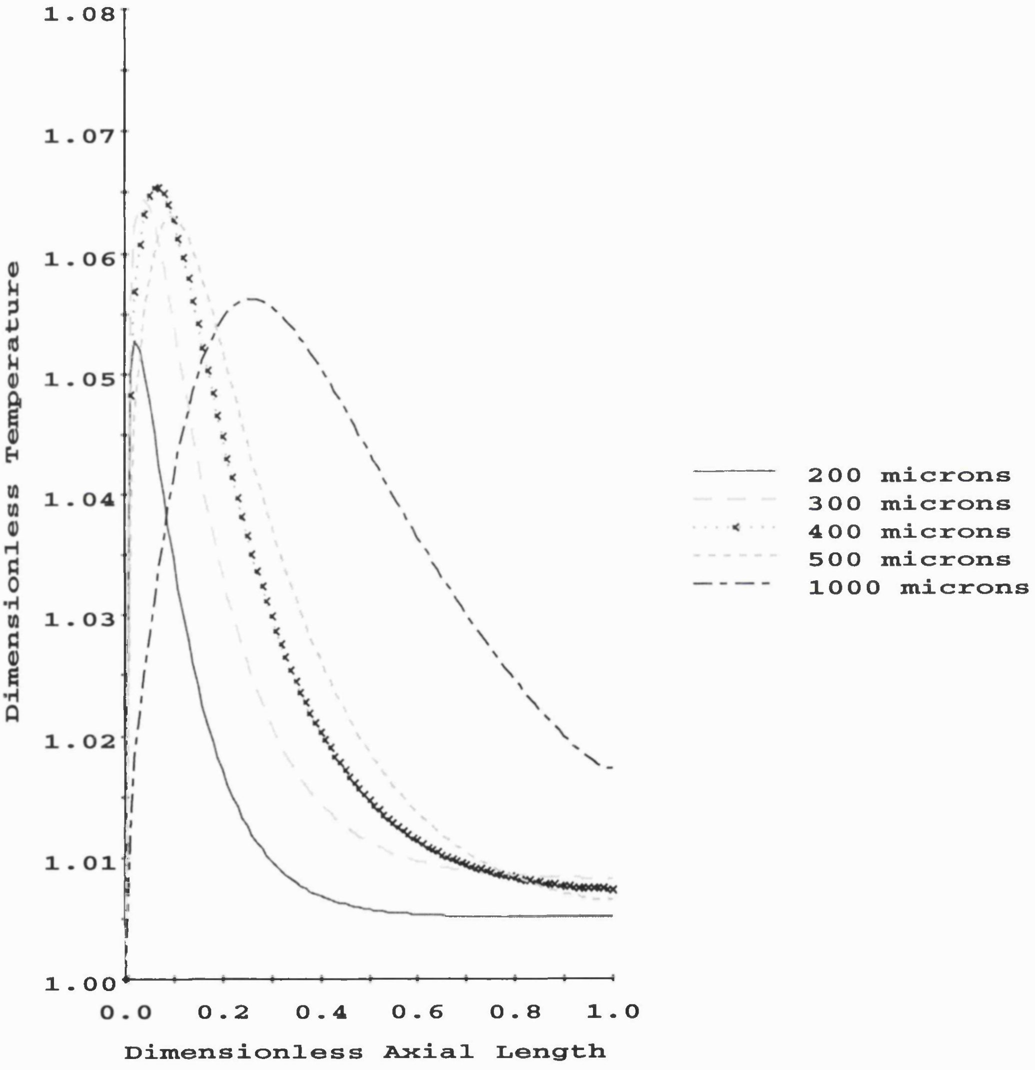

Figure 4.10: Axial temperature profiles for varying channel size.

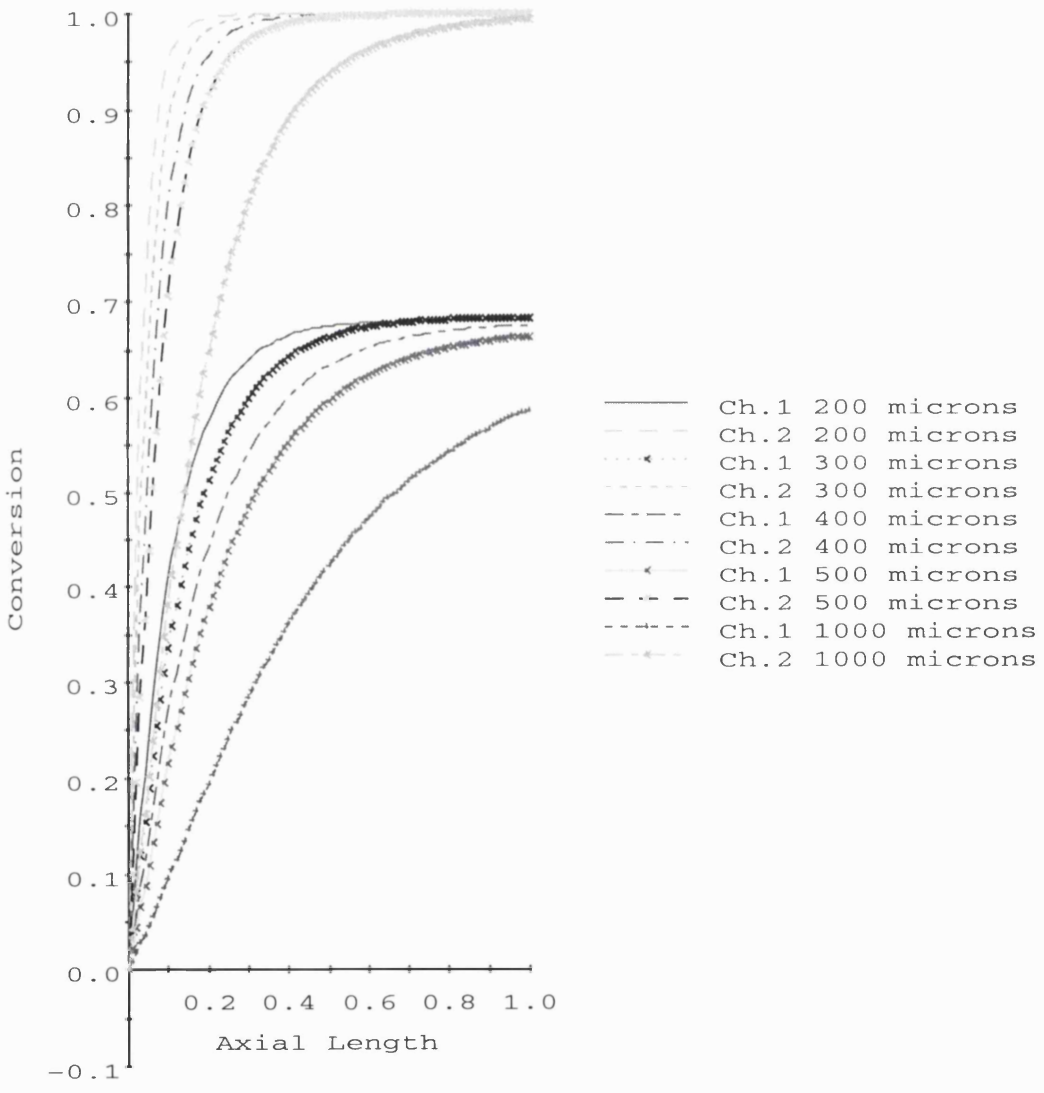

Figure 4.11: Conversion profiles in channels 1 and 2 for varying channel size.

conversion profiles. For these calculations the sizes of both channels were equal, and Peclet numbers were kept constant (see Table 4.2), hence inlet flowrates increase with channel size. A maximum peak temperature is observed for a channel size of 400 microns. This is due to the interaction between radial diffusive and axial convective mass transfer. At small channel sizes, radial diffusive mass transfer is so efficient that it allows the additional reactant, entering the channel, to reach the catalyst and react. Beyond 400 microns, radial diffusive resistance becomes more significant , and slows down both reactions. In particular, at 1000 microns the full reactor length is required to achieve complete conversion for the combustion, while the dehydrogenation does not reach equilibrium, as shown in Fig. 4.11. The sharper conversion profiles obtained at a smaller channel size, give rise to corresponding sharper temperature peaks in Fig. 4.10. These results indicate that there is an optimum channel size, below which there is insufficient use of catalyst and above which insufficient reactant conversion is obtained. Further improvements may be possible by allowing the two channel sizes to differ.

It is worth noting that the activation energies were artificially altered in the simulations which exhibited a high degree of non-isothermality. Temperature and conversion profiles did not change appreciably, indicating an insensitivity of reactor performance with respect to these parameters.

4.5 Conclusions

In catalytic wall microreactors, where transverse diffusion is fast and axial diffusion can be neglected, the governing equations can be vertically-averaged to yield axial profiles for weakly non-isothermal systems. Reduction of the dimension of the problem, makes this technique a useful tool for rapid evaluation of microreactor performance without residing to computationally demanding numerical methods such as computational fluid dynamics, which require grid generation and significant computing time. In addition, a theoretical study of a catalytic microreactor that combines the thermal effects of an exothermic and endothermic reaction was carried out. The two reactions take place on alternate catalytically coated microchannels. Two cases were considered, first order reactions and a dehydrogenation/combustion reaction system. Isothermal behaviour is achieved when heat generation and removal rates are similar. Different heats of reaction, reaction kinetics, catalyst loadings, inlet concentrations or inlet flowrates between the two reactions can lead to differences in heat generation and removal rates and result in non-uniform axial temperature profiles. Radial temperature and concentration profiles though, were found to be insignificant for realistic values of operating and physicochemical parameters. Calculations with varying channel size indicated that optimal values exist for efficient reactor operation.

This chapter concludes the results chapters that consider the fundamental transport characteristics in microreactors. Mass and heat transfer have been evaluated and suitable expressions developed that allow rapid prototyping in a conceptual manner. The remainder of the results chapters in this thesis use the transport phenomena identified in this, and the previous chapter, as an aid to more advanced unit operation design.

Nomenclature

Roman symbols

Symbol	Assignment	Unit
A	pre-exponential factor	m/s
b	slip coefficient	-
c	concentration	mol/m^3
c_0	inlet concentration	mol/m^3
c_p	specific heat capacity	J/kg/K
D	diffusivity	m^2/s
Da	Damköhler number	-
E_a	activation energy	J/mol
f_a	vertical function	-
h	channel height	m
ΔH	heat of reaction	J/mol
k	thermal conductivity or reaction rate constant	W/m/K m/s
Kn	Knudsen number	-
L	reactor length	m
Le	Lewis number	-
Pe_e	energy Peclet number	-
Pe_m	mass Peclet number	-
R	aspect ratio (L/h) or ideal gas constant	-
T	temperature	K
T_o	inlet temperature	K
u	fluid velocity	m/s
U	bulk fluid velocity	m/s
y	dimensionless temperature	-

Greek symbols

Symbol	Assignment	Unit
α	decay group	-
β	heat of reaction group	-
η	dimensionless transverse coordinate	-
γ	activation energy group (set at 5.0)	-
κ_1	dimensionless ratio $(k_s r_1/k_1\delta)$	-
λ_a	decay constant	-
ρ	density	kg/m^3
θ_a	dimensionless reactant concentration	-
ζ	dimensionless axial coordinate	-

Subscripts

Symbol	Assignment
0	inlet conditions
1	channel 1 (endothermic)
2	channel 2 (exothermic)
a	species a
b	species b
e	equilibrium
s	solid
w	wall

Chapter 5

Mixing Characteristics of T-type Microfluidic Mixers

5.1 Introduction

Fast reactions taking place in conventional reactors may be constrained by relatively slow mass and/or heat transfer (Mills and Chaudhari (1997)). They include oxidations, hydrogenations and nitrations, as well as other single or multiphase reactions. They can be performed more efficiently in microreactors due to their enhanced heat and mass transfer properties. Various researchers have already demonstrated the improved performance of microreactors for oxidations Hsing et al.(2000), Franz et al.(1998), Tonkovich et al.(1998), hydrogenations Weiβmeier and Hönicke (1998) and nitrations Burns and Ramshaw (2000). Higher conversion and selectivity were obtained, and this was due to the fact that heat and mass transport was fast, even though the reactors operated in the laminar flow regime, because of the small diffusional distances inside the microchannels.

Many micromixers employ the same principle of minimising diffusional distances to induce fast mixing between fluid streams. Löwe et al.(2000) have reviewed various types of micromixers including the mixing tee configuration (Hsing et al.(2000)), where two gas streams are able to diffuse at the inlet of a T junction before subsequent processing. Such a configuration is also applicable to liquids as demonstrated by Bökenkamp et al.(1998) who achieved better mixing in turbulent flow conditions. Bessoth et al.(1999) have used a mixer based on multi lamination of two liquid streams and achieved 95% mixing within 15 ms. Ehrfeld et al.(1999) have also characterised single and array micromixers and compared them to conventional macroscopic systems.

The Fourier number,

$$Fo = \frac{D_{ab}t}{D_h^2}, \tag{5.1}$$

originating from transient diffusive heat and mass transfer (Bird et al.(1960)), relates the progress of diffusive transport processes to various geometries and has been commonly employed for determining mixing time (Bibby et al.(1998)). For a typical gas diffusivity, $D_{ab} \sim 10^{-5}$ m^{2}s^{-1}, if substantial to complete mixing is required ($0.1 < Fo < 1$) within 100 ms then a characteristic dimension of 100×10^{-6} m to 316×10^{-6} m is required.

In this work the focus is on a mixer design which will precede a catalytic microreactor to be used for methanol-oxidation on a silver catalyst. This reaction has a residence time of the order of 10 ms (McKetta) and as such is a good candidate as a model reaction for microreactors. The mixer is based on a T type configuration as shown in Fig. 5.1. The two gases enter the top branches of the T and mix by diffusion at the T junction and lower section. Computational Fluid Dynamics (CFD) simulations are employed to determine the mixing length for various design and operating variables. Comparison with the simpler Fo analysis is finally presented.

5.2 Theory

5.2.1 Mathematical model of the T reactor

The equations used to describe the system are the continuity, Navier-Stokes (pressure and velocity) and the species convection-diffusion equations. Derivations and details of the equations can be found in Bird et al.(1960), and their dimensionless forms are shown in (5.2) to (5.4) respectively.

$$\nabla.\mathbf{v} = 0, \tag{5.2}$$

$$\frac{D\mathbf{v}^*}{Dt^*} = -\nabla^* p^* + \frac{1}{Re}\nabla^{*2}\mathbf{v}^*, \tag{5.3}$$

$$\frac{Dx_a^*}{Dt^*} = \frac{1}{Re.Sc}\nabla^{*2}x_a^*. \tag{5.4}$$

where

$$Re = \frac{\rho u d}{\mu},$$
$$Sc = \frac{\mu}{\rho D_{ab}}.$$

A physical description can be assigned to the above dimensionless groups. The Reynolds number (Re) characterises the ratio of inertial to viscous forces. The product of the Schmidt number (Sc) (≈ 0.8 for gases) and Reynolds number (Re) describes the ratio of mass transport by convection to that by diffusion. This product is termed the Peclet number (Pe) and is given by (ud/D_{ab}). Convection dominates the transfer process for a Peclet number greater than 2 (Versteeg and Malalasekera (1996)).

All physical properties are determined by the gas kinetic theory and JANNAF databases (CFDRC). The diffusivity value for the binary gas mixture (methanol and oxygen) is 2.78×10^{-5} $\mathrm{m^2s^{-1}}$. In all cases studied the flow is laminar, while adiabatic conditions are applied at domain boundaries. Compressibility and slip effects are taken into account (though in most cases they are negligible). The inlet temperature of both fluids are specified at 400K. Unless otherwise stated all simulations were performed in 3D.

Simulations were performed using CFD-ACE^{TM} by CFDRC and IBM XLF FORTRAN 90 on an IBM RS6000. Body fitted structured grids were used and the total number of cells was approximately 17 000 in all cases. The SIMPLEC method was implemented for pressure-velocity coupling and all spatial discretisations were performed using the second order UPWIND method.

5.2.2 Mixing characteristics

The two gases, methanol and oxygen, are used to investigate the mixing characteristics of the T mixer. The flowrates used are chosen to give residence times appropriate for the methanol oxidation reactor which follows the mixer.

In order to evaluate the mixing efficiency the mixing length needs to be known.

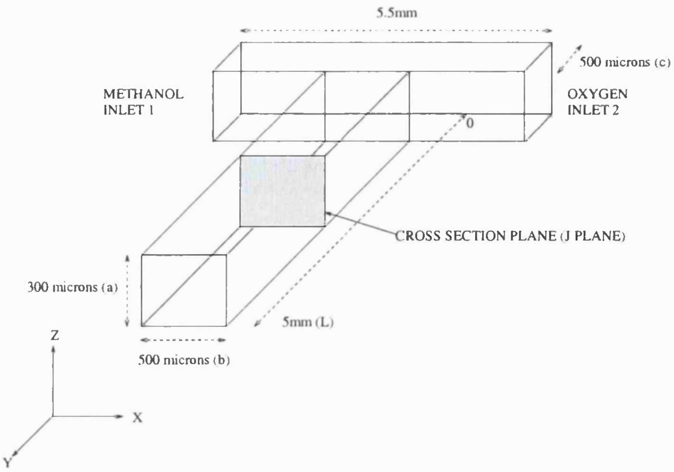

Figure 5.1: Schematic of T mixer.

A combination of two gases is considered completely mixed when the equilibrium composition (ω_∞) is reached. Since in practice this may require long mixing lengths, we define that complete mixing is achieved when all locations in a cross section deviate by no more than ±1% from the equilibrium composition. In other words, mixing in considered complete when:

$$\omega_{lower} \leq \omega \leq \omega_{upper}, \tag{5.5}$$

where

$$\begin{aligned} \omega_{lower} &= \omega_\infty - \frac{1}{100}\omega_\infty, & (5.6) \\ \omega_{upper} &= \omega_\infty + \frac{1}{100}\omega_\infty. & (5.7) \end{aligned}$$

A FORTRAN algorithm, incorporated into the CFD code, allowed the completely mixed position to be established. The algorithm searches along the T mixer starting from the top of the junction and examining each 'J' plane in turn (see Fig. 5.1). The mixing length corresponds to the first 'J' plane (from top of junction) that satisfies the complete mixing criterion:

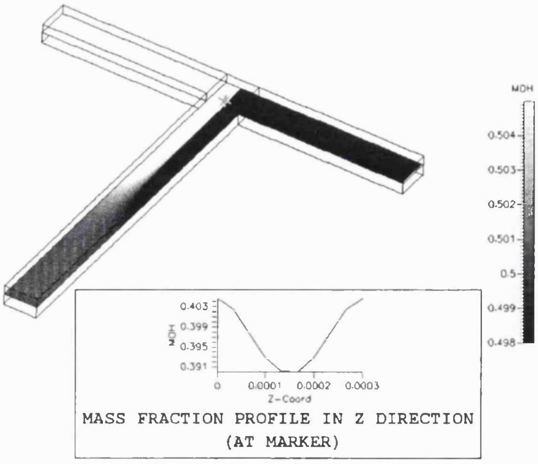

Figure 5.2: Methanol mass fraction contours in base case mixer ($Pe = 8.08$).

$$\omega_\infty - \frac{\omega_\infty}{100} \leq \omega\left(x, y^*, z\right) \leq \omega_\infty + \frac{\omega_\infty}{100}, \tag{5.8}$$

where starting at $y = 0$, find minimum y (y^*) such that (5.8) is satisfied $\forall x, z$.

Unless stated otherwise all mixing lengths are reported from the uppermost point (i.e. y = 0) in the mixer, and methanol always enters at the left inlet.

5.3 Results and discussion

5.3.1 Base case

The dimensions for the base case are those shown in Fig. 5.1. Velocities of both fluids are 0.3 m/s corresponding to a Peclet number of 8.08 (based on hydraulic diameter) in the centre channel. Inlet velocity profiles are flat whilst the lengths of the side branches are sufficient to allow the velocity profiles to develop. The base case has a mixing length of 2.83 mm and an average pressure drop (over the whole of the mixer) of 14.6 Pa. The mass fraction profiles of the two fluids are shown in Fig. 5.2. All other simulations are variations of this base case.

5.3.2 Fluid velocity variation

Simulations were performed for inlet gas velocities equal in each stream varying from 1.0 $\times 10^{-3}$ to 0.5 m/s (Pe range from 0.027 to 13.49). Figure 5.3 shows the

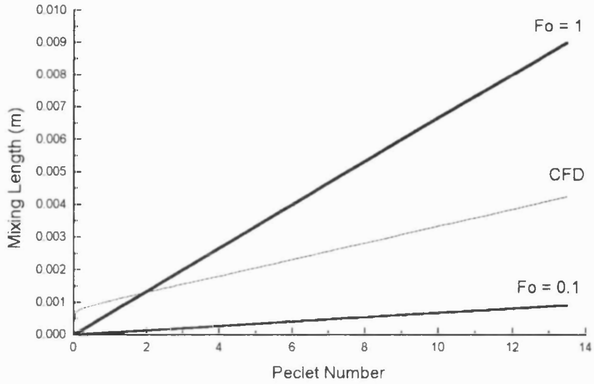

Figure 5.3: Mixing length vs Peclet number. *Fo* indicate mixing lengths obtained from Fourier numbers.

variation of mixing length as a function of outlet Peclet number. Pressure drops across the mixer are small and vary from 0.011 to 24.8 Pa.

At small *Pe*, diffusion dominates over convection and mixing occurs largely within the T junction. As *Pe* increases a significant amount of mixing takes place in the centre channel and a progressively larger mixing length is required. The dependence of mixing length on *Pe* number is linear for most of the *Pe* range. Only at the limit of small *Pe* a sharp decrease of mixing length is observed and this can be attributed to the fact that substantial mixing occurs in the T junction, where the interface available for diffusion between the two streams is being formed.

5.3.3 Aspect ratio variation - constant width

For the T mixer the aspect ratio is defined as a/b (see Fig. 5.1). The same aspect ratio applies to both inlet branches and the centre channel. The base case aspect ratio is 0.6. For all simulations in this section the width (b) is kept constant at 500 microns and the inlet flowrates at 0.3 m/s ($Pe = 8.08$). Fig. 5.4 shows the effect of aspect ratio on mixing length. It can be seen that a minimum exists at an aspect ratio of about 0.8, while after a value of about 1.5 the mixing length becomes independent of the aspect ratio. Pressure drops range from 5.0 to 336.0 Pa.

At low aspect ratios (low values of a) Fig. 5.4 shows that as aspect ratio increases the mixing length decreases. This can be attributed to the effect of horizontal wall shear at these small dimensions. Methanol has a lower viscosity than oxygen (1.3 and 2.56×10^{-5} kg-m/s^2 respectively) and hence develops its velocity profile earlier than oxygen past the T junction. The methanol stream is moving faster than the

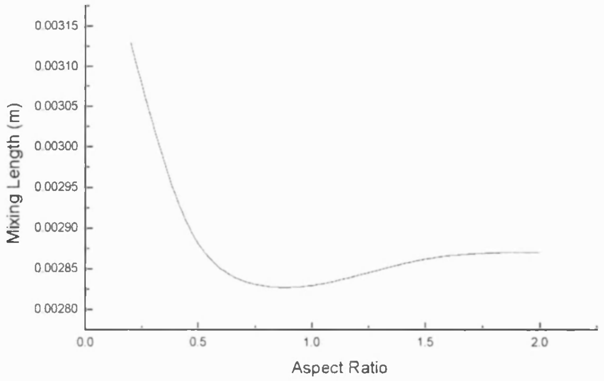

Figure 5.4: Mixing length vs aspect ratio for b = 500 microns.

oxygen one at the entrance of the centre channel (see Fig. 5.5). The different residence times of the two fluids at this part do not favour mixing by diffusion in the x direction. Eventually the flow pattern is developed downstream. As the aspect ratio increases the effect of horizontal wall shear decreases which leads to symmetrical velocity profiles achieved closer to the entrance of the centre channel, and hence better mixing.

Above an aspect ratio of about 0.45, diffusion in the z direction in the junction starts to become important. The simulations showed that concentration gradients start existing along z also (see insert in Fig. 5.2) due to different residence times of fluid elements in the z direction. This would counteract the previous effect (above an aspect ratio of 1) and lead to an increase in mixing length. As the aspect ratio further increases, z velocities begin to develop (their formation was suppressed at low aspect ratios). Such velocities tend to eliminate differences in velocity along z. The mixing length reaches a limiting value for aspect ratios above 1.5. At these high hydraulic diameters wall shear is no longer significant and both streams have similar symmetrical velocities at the core of the channel. Diffusion will mainly depend on the distance b and will be unaffected by further increases in the aspect ratio.

A 2D solution was also performed ($b = 500$ microns, $a = \infty$), and it was initially expected that the 2D solution would represent the limit of the upper aspect ratio (due to infinite approximation in the z direction). However the 2D results yielded a mixing length which is lower than any of the 3D simulations (2.46×10^{-3} m compared to 2.83×10^{-3} m respectively). This is attributed to the 2D simulation not considering velocity and concentration gradients in the z direction. As a result all fluid elements in the z direction have identical residence times.

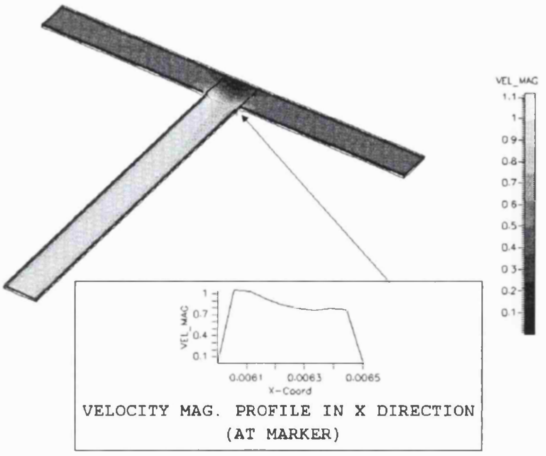

Figure 5.5: Velocity magnitude contours in a 0.1 aspect ratio mixer.

It should be noted that at aspect ratios below 0.2 slip effects are more pronounced and give similar velocity profiles as those reported in Kavepour et al.(1997) (flatter profile - reduced core velocity). Although slip effects result in a reduction of the core velocity, mixing lengths still increased with decreasing aspect ratio, indicating that at these small hydraulic diameters viscous effects dominate over slip effects.

5.3.4 Aspect ratio variation - constant hydraulic diameter

The base case T mixer has a constant cross sectional area throughout the centre channel. The hydraulic diameter ($d = 2ab/(a + b)$) for this channel is 375 microns. Figure 5.6 shows the effect on mixing length of various aspect ratios whilst keeping the hydraulic diameter constant. For this range of aspect ratio the pressure drop varied from 9.0 (low aspect ratio) to 28.9 Pa (high aspect ratio). Average inlet velocity (0.3 m/s) and inlet channel widths (500 microns) are also kept constant. It is dimension b (x direction) that is the important parameter for mixing as this is the dimension where the largest concentration gradients exist initially.

As the aspect ratio increases and b reduces, the diffusion distance in the x axis and consequently the mixing length reduce. At the same time, distance a increases and concentration profiles appear in the z direction due to velocity gradients in the z direction. Above an aspect ratio of 1 diffusion in the z direction reduces slightly the mixing efficiency. It is reasonable to assume that the mixing length at sufficiently high aspect ratios would reach a constant value.

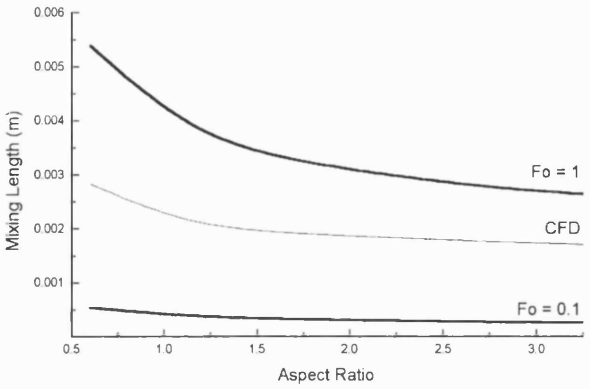

Figure 5.6: Mixing length vs aspect ratio for d = 375 microns. Fo indicate mixing lengths obtained from Fourier numbers.

Mixing angle	Pressure drop (Pa)	Mixing length ($\times 10^{-3}$m)
$+45^o$	3.54	2.03
$+30^o$	3.57	1.93
$+20^o$	3.59	1.93
0^o	3.64	1.96
-20^o	3.68	1.97
-45^o	3.71	2.12
-65^o	3.76	2.25

Table 5.1: Simulation results for different mixing angles.

5.3.5 Mixing angle variation

Simulations were performed to investigate whether the mixing angle has an effect on mixing length and pressure drop. Inlet channel widths are 500 microns and the inlet velocity of each stream is 0.3 m/s. The mixing angle is defined as the angle between the inlet channel and the horizontal. Hence the T mixers discussed so far have a mixing angle of 0^o. All simulations for this section are in 2D due to excessive CPU time required for 3D simulations. Although mixing lengths and pressure drops may be slightly different between 2D and 3D simulations the trends are expected to be the same.

Results for different mixing angles are shown in Table 5.1, where the mixing length is measured from the top of the centre channel. The mixing length varies from 1.93×10^{-3} m to 2.25×10^{-3} m, which is small, especially if one considers that the junction length (δ) ranges from 4.57×10^{-4} m to 9.57×10^{-4} m. Furthermore the pressure drop is small and varies from 3.57 to 3.76 Pa.

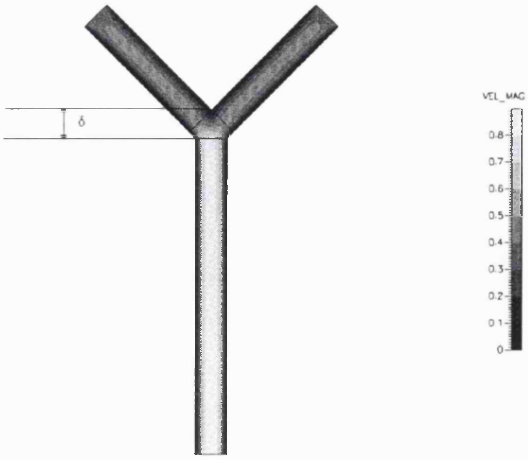

Figure 5.7: Velocity magnitude contours in a mixer with a 45^o mixing angle and 0.3 m/s inlet velocities.

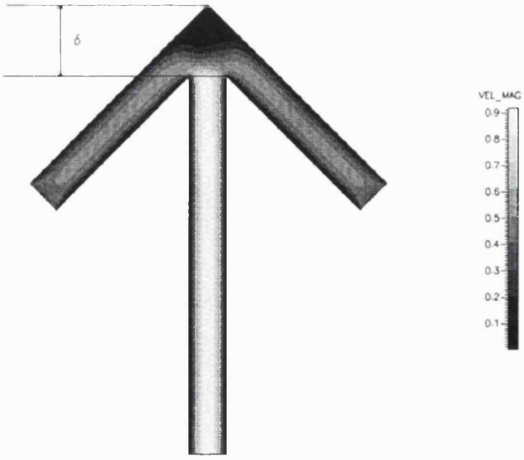

Figure 5.8: Velocity magnitude contours in a mixer with a -45^o mixing angle and 0.3 m/s inlet velocities.

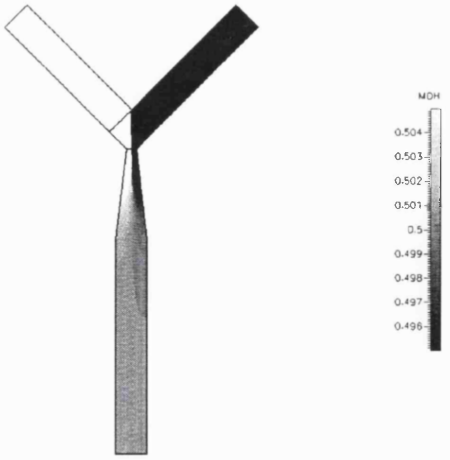

Figure 5.9: Methanol mass fraction contours in a 160 micron throttle at inlet velocities of 0.3 m/s.

Hence for the range of parameters studied, mixing angle has only a marginal effect on mixing length. However, negative mixing angles create stagnant zones, whilst positive ones don't, as shown in Figs. 5.7 and 5.8. In addition, alteration of mixing angle allows a reduction of the footprint area, hence a more efficient use of material and space.

5.3.6 Throttle T mixer

A method to decrease the diffusional distance required for mixing, apart from using a thinner centre channel, is to introduce an orifice immediately after the T junction. However, this will introduce relatively large pressure drops. An alternative is to utilise a Venturi type configuration, which enables some degree of pressure recovery (Coulson and Richardson (1993)). Simulations were performed for a mixing angle of 45^o, while the centre channel wall has an angle of 7^o from the y-axis. A schematic of the throttle mixer can be seen in Fig. 5.9, where methanol contours are shown for a 160 micron throttle with a channel width of 500 microns.

A comparison was made between 2D and 3D (a = 300 microns) simulations for a throttle of 160 microns, each gas having an inlet velocity of 0.3 m/s. The results (Table 5.2) show that the pressure drops in the 3D geometry are higher than the 2D case. This is attributed to the higher shear stresses present in the 3D case, where the throttle is confined by four walls. The mixing length is slightly smaller for the 2D simulations, which was also observed in the base case (section 5.3.3). Since the mixing length is of primary interest, subsequent simulations in the throttle mixer

Dimension	Pressure drop (Pa)	Mixing length ($\times 10^{-3}$m)
2D	8.965	1.41
3D	23.247	1.54

Table 5.2: Comparison of 2D and 3D simulations for a 160 micron throttle.

were performed in the 2D geometry.

Throttle size

The throttle size was varied between 10 and 500 microns, while the inlet gas velocities were kept constant at 0.3 m/s; the results are shown in Fig. 5.10. All mixing lengths correspond to the distance from the top of the centre channel.

The model used in the solution domain can accommodate microscale effects. It is based on the model of Kavepour et al.(1997) which uses the Knudsen number (Kn) to evaluate the degree of fluid slip at the channel walls.

$$Kn = \frac{\lambda}{D_h} = \sqrt{\frac{\pi\gamma}{2}}\frac{Ma}{Re}, \tag{5.9}$$

where Ma is the Mach number and has a value of 0.1 for the smallest throttle size. Mixing length increases monotonically with throttle size as shown in Fig. 5.10. As the size of the throttle decreases the diffusional distance decreases, hence better mixing is achieved although increased velocity at the throttle means that gases are there for a shorter time. The curve in Fig. 5.10 shows a slight sigmoidal trend with points of inflexion at about 100 and 300 microns. Below 10 microns the flow is in the slip regime (Kavepour et al.(1997)).

The inflexion point at 300 microns can be attributed to the change in the velocity profile in x direction at the throttle. For large throttle sizes above 300 microns the simulations showed that the velocity profile is not symmetric with larger velocity gradients along x for the methanol than for oxygen (due to the effect of shear stresses; see also §5.3.3). This asymmetry in the velocity profile does not favour mixing. Therefore mixing becomes more efficient for throttle sizes below 300 microns (i.e. the gradient of the curve in Fig. 5.10 is greater below 300 microns).

Below the second inflexion point at 100 microns mixing becomes less efficient with a decrease in throttle size. Beyond this point, the core velocity at the throttle increases sharply; this affects the residence time and consequently mixing at the throttle.

Pressure drops varied from 3.54 Pa to 1631 Pa for the largest and smallest throttle

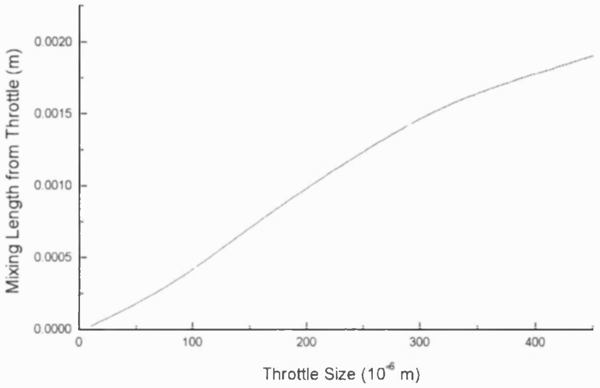

Figure 5.10: Mixing length vs throttle size (microns).

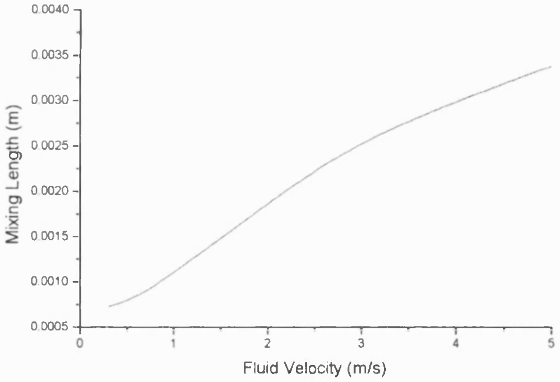

Figure 5.11: Mixing length vs fluid velocity at inlet channels (10 micron throttle).

sizes respectively.

Inlet velocities

Simulations with different inlet velocities (equal for each inlet channel) were also performed in the throttle mixer. For the geometric configuration used, i.e. 45^o mixing angle, the only throttle that could mix completely the reactants up to inlet velocities of 5 m/s (within the base centre channel) is the 10 micron throttle, which is used for the simulations in this section. A plot of mixing length against fluid inlet velocity is shown in Fig. 5.11. For these conditions the pressure drop ranges from 1632 Pa to 125 $\times 10^3$ Pa.

Figure 5.12: Methanol mass fraction contours a 10 micron throttle mixer at inlet velocities of 5 m/s.

There are two points of inflexion in Fig. 5.11. The inflexion at low velocities corresponds to the core fluid in the throttle moving at higher velocity. The other inflexion point, at high velocities, is where recirculation patterns appear just after the throttle. These can be seen in Fig. 5.12 where methanol mass fraction contours are plotted for inlet velocities of 5 m/s. These recirculation patterns keep fluid elements for a longer period in some areas of the centre channel, which results in a smaller increase of mixing length with fluid velocity.

5.4 Fourier number considerations

As mentioned earlier Bibby et al.(1998) have used the Fourier number to determine required mixing dimensions or time. However, the applicability of the Fourier number to convective systems must be addressed. The time variable in a purely diffusive system is real time, but in a convective system is space-time. The space-time (τ) is defined as

$$\tau = \frac{V}{\nu}, \tag{5.10}$$

where V is volume of the system, and ν is the volumetric flowrate. As previously stated mixing can be regarded as substantially complete if the Fourier number is in the region 0.1 to 1. Therefore the Fourier expression (5.1) can be rearranged to give a value for mixing time. The latter when multiplied by the average channel velocity gives the corresponding mixing length. This is compared with the CFD simulations in Figs. 5.3 and 5.6. The characteristic dimension used in the Fourier number is b as this represents the physical length the gas must diffuse to achieve uniform composition. It must be pointed out that use of the channel hydraulic diameter as the characteristic dimension would render the Fourier number invariant with aspect ratio.

It can be seen from Fig. 5.3 that the predictions based on the Fourier number provide reasonable upper and lower limits for the mixing lengths except at low values of Peclet number. In this case the CFD solution provides a greater mixing length than the Fourier predictions. This demonstrates that at low flowrates the flow pattern greatly affects the diffusive mixing. Convective flow is not captured in the Fourier number predictions and they underestimate the required mixing lengths. It is interesting to note that the intersection of the CFD and $Fo(1.0)$ solution appears at a Peclet number of approximately 2, where mass transport by convection begins to dominate.

In Fig. 5.6 the Fourier number predictions also provide reasonable limits for the mixing length as aspect ratio is altered. In fact the mixing length determined by CFD is approximately the average of the mixing lengths for $Fo = 0.1$ and $Fo = 1$, for the whole range of aspect ratios.

Applying the Fourier predictions to the throttle mixers can give useful limits but should be used with caution. A suitable characteristic length needs to be determined, whilst other effects such as compressibility and recirculating flow patterns cannot be captured in the calculations.

5.5 Conclusions

The mixing characteristics of T-type micromixers with constant and varying diameter channels, for gases of different viscosity, operating in the laminar flow regime were studied through CFD simulations. The effect of various operating and design parameters on the effectiveness of mixing was investigated. Shorter mixing lengths were obtained for low inlet flowrates. Mixing length showed a weak nonmonotonic dependence on aspect ratio (for constant channel width), while it decreased with aspect ratio (for constant hydraulic diameter). At small channel dimensions wall shear can play a significant role, while at larger ones concentration gradients and velocities along the z direction appear. These effects are not captured in 2-D simulations, which predict shorter mixing lengths and pressure drops than 3-D. The fact that the two fluids have different viscosities gives rise to non-symmetrical velocity profiles towards the centre channel entrance. The angle between the inlet channels seems to have little effect on the mixing length or pressure drop and hence it provides a convenient design parameter that can be used to minimise mixer footprint area. Mixing length can be reduced by using throttle mixers, where the dimension of the centre channel is varying. Small throttle sizes resulted in faster mixing, but at the expense of high pressure drop. The mixing lengths from the CFD simulations were compared with those from Fourier number predictions, which can be used for rapid determination of required channel dimensions. It was concluded that the Fourier number provides reasonable limits ($0.1 < Fo < 1$) especially for high flowrates, where mixing mainly takes place in the centre channel.

Nomenclature

Symbol	Assignment	Unit
a	channel height	m
b	centre channel width	m
c	inlet channel width	m
d	hydraulic diameter	m
D_{ab}	diffusion coefficient of a in b	m^2/s
D_h	characteristic dimension	m
Fo	Fourier number	-
Kn	Knudsen number	-
Ma	Mach number	-
p	pressure	Pa
Pe	Peclet number for centre channel	-
Re	Reynolds number	-
Sc	Schmidt number	-
t	time	s
u	mean velocity	m/s
$\mathbf{v}$	velocity vector	m/s
V	volume	m^3
x	mole fraction	-
y	vertical length	-
δ	junction depth	m
γ	specific heat ratio (c_p/c_v)	
λ	mean free path of gas	m
μ	viscosity	Pa·s
ν	volumetric flowrate	m^3/s
ρ	density	kg/m^3
τ	space-time	s
ω	mass fraction	-

Superscript	Assignment
$*$	dimensionless form of variable

Subscript	Assignment
a	species a
b	species b

Chapter 6

Catalytic Methanol Oxidation

6.1 Introduction

In previous Chapters it has been well demonstrated that microreactors offer high rates of heat and mass transfer. Highly exothermic gaseous reactions are ideal applications where microreactors can be applied. Many exothermic reactions of this nature are typically rate limited in industry by the maximum heat removal duty available in the reactor. With the high heat transfer rates inherent in microreactors these systems reduce the potential of temperature/reaction runaway. In addition the dimensions of most microreactors are smaller than the quench distance (characteristic minimum distance through which a flame in a stationary gas mixture can propagate - typically in the order of a few hundred microns (Potter (1960)) for many mixtures, hence different operating regimes can be explored that cannot be achieved in conventional reactors. Such benefits manifest, overall, as a safer design and product yield limitations in conventional operating regimes can be overcome. In light of this, oxidation reaction systems are a natural candidate for further investigation. In addition to high heat release many oxidation reactions produce important intermediates. For the reaction system studied, methanol oxidation, the desired product is the intermediate, formaldehyde. Formaldehyde can undergo further oxidation to carbon dioxide and water at high temperature, hence residence time and temperature control are critical parameters.

This Chapter concentrates on detailed analysis of a catalytic methanol oxidation reactor that has already been fabricated. Through the use of rigorous simulations a framework is developed that can improve the operation of the current reactor and designs of future units.

In §6.2 a description of the existing methanol oxidation microreactor, fabricated at University College London, is given. A general purpose CFD-FORTRAN (combination of commercial software and adaption routines) code is validated for methane combustion in §6.3 which is later adapted for methanol oxidation and used for verification. Methanol oxidation kinetics are validated in §6.4 using an adiabatic PFR (Plug Flow Reactor) model and industrial data. Such kinetic data is used in the finite difference/volume (FDV) model for the existing methanol oxidation microreactor. The FDV model is developed in FORTRAN and is written based upon the transport characteristics identified in Chapters 3 and 4. It is intended as an alternative to traditional CFD methods, and for selected cases comparisons are made between the two in §6.6. The equations of the FDV model are presented in §6.5 along with the solution method. A thorough investigation of the methanol oxidation reactor is presented in §6.6 and a conclusion is given in §6.7.

6.2 Physical description

A microreactor has been fabricated at University College London for methanol oxidation. An image of the reactor is shown in Fig. 6.1 and an end elevation schematic is shown in Fig. 6.2. The reactor was fabricated in silicon by wet etching with KOH. Gases enter the reactor through two inlet ports where meandering channels form the pre-heat section. A 'T' section allows the two gases to mix and proceed to the centre channel where catalyst is deposited on the bottom surface. Due to the wet etching method employed (isotropic etching) the channel is of a trapezoidal shape. The unit is sealed with a glass cap and the complete reactor is then fitted to a stainless steel heating block. For the modelling work in this Chapter only the reaction section is considered. In addition it is also assumed that the gases are perfectly mixed at the entrance to the centre channel, and that due to the void spaces surrounding the centre channel a 2D simulation can be employed. This is due to the fact that the void spaces serve as an adiabatic boundary condition and the amount of silicon forming the channel walls is too small to serve as a heat sink. Transverse gradients of energy and mass (vertical) have already been considered in Chapters 3 and 4.

The length of the complete unit is 63 mm with a width of 25 mm. The centre channel is approximately 300 microns high by 600 microns wide with a length of 20 mm.

6.3 Verification of FORTRAN kinetics model

A model has been developed in FORTRAN to interface with the commercial code CFDRC to allow heterogeneous surface/catalytic reactions to be modelled of

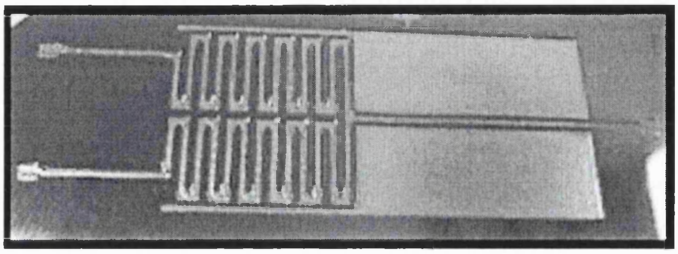

Figure 6.1: Image of the methanol oxidation microreactor.

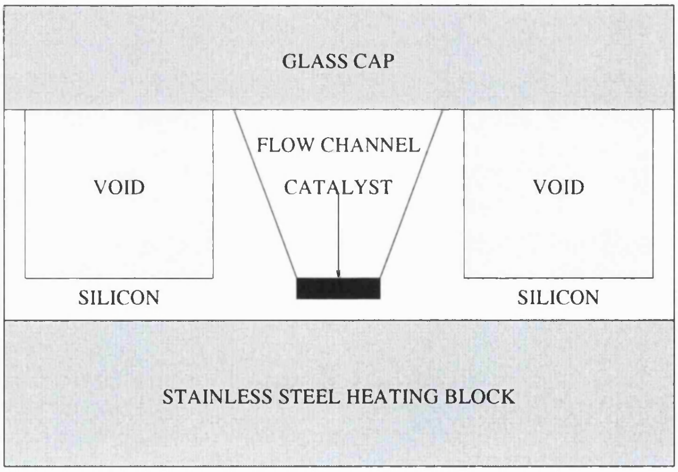

Figure 6.2: End elevation of the reacting channel (not to scale).

arbitrary kinetics.

This model will be validated by modelling a hybrid combustor for catalytic methane combustion. Research into catalytic combustion is active as it is a promising method for the simultaneous reduction of NO_x, CO, and unburnt hydrocarbons emissions from gas turbines (Groppi et al.(1995)). Catalytic combustion allows low fuel concentrations as the catalyst lowers the ignition temperature.

Many combustor configurations exist, but all have the catalytic process in a monolith due to pressure drop minimisation. Groppi et al.(1995) describe the following phenomena occurring in the monolith:

1. Heterogeneous reactions at the catalyst wall and homogeneous reactions in the gas phase.
2. Heat, mass, and momentum transfer by convection and diffusion in the gas phase and at the gas-solid interface.
3. Mass diffusion in the catalyst pores.
4. Heat transfer by conduction and radiation in the solid.

A high degree of coupling exists between the previous phenomena due to the intense thermal effects associated with the heat of combustion.

6.3.1 Monolith model

This section will describe the two models that are being compared, equations and assumptions will be given where necessary. The monolith is assumed to be a cylinder once the catalyst has been deposited.

Groppi's model

Groppi's most detailed model considers the temperature dependence of the gas properties and includes momentum, continuity, species, and enthalpy balances. Physical properties have been approximated with power law relationships and the ideal gas equation of state has been used. The monolith is assumed to be a cylinder and symmetry is assumed as the centreline. Hence the governing equations for continuity, momentum (in the axial direction), enthalpy and fuel are

$$\frac{\partial \rho u}{\partial z} + \frac{1}{r}\frac{\partial \rho v r}{\partial r} = 0, \tag{6.1}$$

$$\rho \left(u \frac{\partial u}{\partial z} + v \frac{\partial u}{\partial r} \right) = - \frac{\mathrm{d}P}{\mathrm{d}z} + \frac{1}{r} \frac{\partial}{\partial r} \left(\mu r \frac{\partial u}{\partial r} \right), \tag{6.2}$$

$$\rho c_p \left(u \frac{\partial T}{\partial z} + v \frac{\partial T}{\partial r} \right) = \frac{1}{r} \frac{\partial}{\partial r} \left(k_t r \frac{\partial T}{\partial r} \right), \tag{6.3}$$

$$\rho \left(u \frac{\partial m_f}{\partial z} + v \frac{\partial m_f}{\partial r} \right) = \frac{1}{r} \frac{\partial}{\partial r} \left(D_f \rho r \frac{\partial m_f}{\partial r} \right). \tag{6.4}$$

CFD model

The governing equations in the commercial CFD code are the Navier-Stokes (Appendix C) and Stefan-Maxwell equations along with physical property routines described in detail in §6.5.3.

Assumptions in both models

The following assumptions are included in both models:

1. Steady-state conditions.
2. Heterogeneous reaction at the catalytic wall with irreversible first order kinetics in the fuel concentration and zeroth order in the oxygen concentration.
3. Intra-porous diffusion effects have been accounted for by the effectiveness factor approach for an isothermal catalyst. The validity of this hypothesis has been verified by Smith (1977) by *a posteriori* calculation of temperature gradients in the catalyst depth. A γ-Al_2O_3 washcoat was assumed, with dispersed noble metal catalyst, and typical parameters are given in Table 6.1.
4. Heat transfer by conduction and radiation have been neglected, it is assumed that a single monolith channel operates adiabatically. Also the effect of homogeneous reactions was shown to have little effect by Groppi et al.(1995).

Additional equations

This section concentrates on the boundary conditions applied to the model. The surface reaction is a boundary condition but to incorporate into the CFD code it has

Thickness of active catalyst layer	δ=20μm
Pore radius	r_p=100Å
Void fraction	ε_p=0.5

Table 6.1: Characteristics of γ-Al_2O_3 washcoat.

to be derived as a spatial array of discretised source terms (Patankar (1980)). Symmetry conditions are applied at the channel axis, whilst other boundary conditions are listed in the following sections.

Inlet conditions ($\forall$r)

$$\begin{aligned} T(0) &= T_0, \\ m_f(0) &= m_{f0}, \\ p\,(0) &= p_0, \\ v(0) &= 0, \\ u(0) &= u_0. \end{aligned}$$

Wall conditions (r=R)

$$\begin{aligned} \rho D_f \frac{\partial m_f}{\partial r} &= -\eta K_c \delta \rho m_f, \\ k_{tg}\frac{\partial T}{\partial r} &= -\Delta H_R \eta K_c \delta \frac{\rho m_f}{M_f}, \\ u(r) &= 0, \\ v(r) &= 0, \end{aligned}$$

where η is the effectiveness factor and is given by

$$\eta = \frac{\tanh\theta}{\theta}, \tag{6.5}$$

and θ is the Thiele modulus and is given by

$$\theta = \delta\sqrt{\frac{K_c}{D_{eff}}}. \tag{6.6}$$

Stoichiometry

$$\mathrm{CH_4 + 2O_2 \longrightarrow CO_2 + 2H_2O}.$$

6.3.2 Comparison of models

Table 6.2 shows the operating conditions and geometric parameters in the catalytic combustors.

Inlet gas temperature	723 K
Molar fraction of fuel at inlet	2%
Pressure	10 atm
Inlet planar velocity	11.98 m/s
Diameter of channel	1.2 mm
Channel length	10 mm
Activation energy	90.17 kJ/mol
Intrinsic rate constant	175 1/s

Table 6.2: Operating and geometric parameters used in calculations.

Fig. 6.3 shows the wall temperature profile in the CFD model, whilst Groppi's wall temperate profile is shown as points on the same figure, (both simulations have a pre-exponential factor of 175 1/s). It can clearly be seen that good profile agreement exists between the two models especially at the temperature shock at the beginning of the reactor. Differences in temperature values are attributed to the calculation of heat of reaction. In Groppi's model an explicit value is specified whilst in the CFD-FORTRAN model a value is calculated from a thermochemical database.

6.4 Validation of methanol oxidation kinetics

Methanol oxidation is the process used to manufacture formaldehyde. Commercial processes use methanol and air as feed stocks and use a silver or metal oxide catalyst. It is the silver catalyst process that will be used to compare a microreactor with a conventional fixed bed reactor.

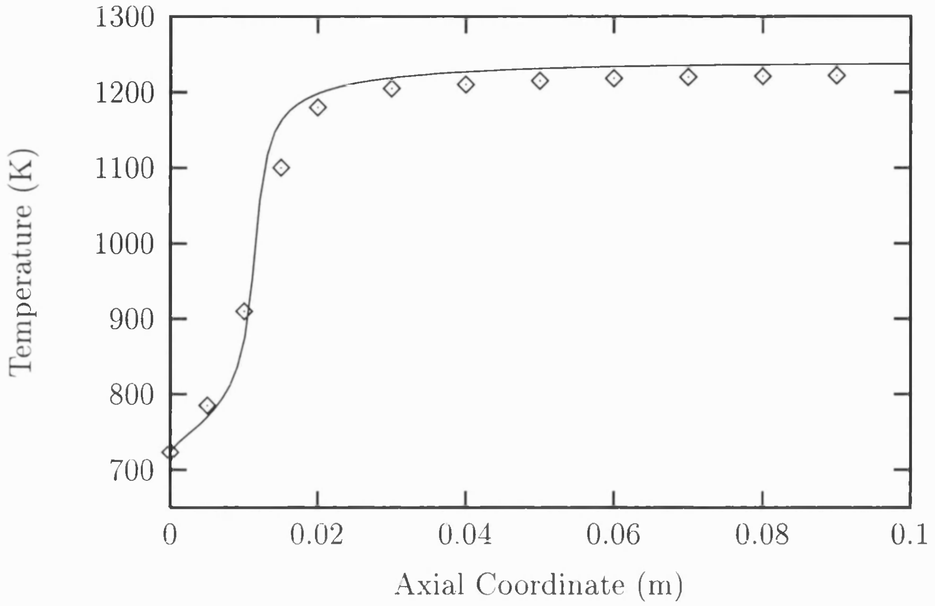

Figure 6.3: Comparison of wall temperature profiles for catalytic combustion. The CFD-FORTRAN model is shown in solid lines whilst Groppi's results are shown as points.

This section introduces the industrial silver catalyst process and provides kinetic data and mechanisms from various literature sources. The kinetic data is used in a PFR (Plug Flow Reactor) model and compared to the data of the industrial process.

6.4.1 Methanol - rich oxidation

Main reactions and catalyst

The mixture for the silver catalyst process is rich in methanol to stay above the flammability limit of the gas at atmospheric pressure. A methanol-air mixture (about 50:50 mol ratio) just above atmospheric pressure is passed through a fixed thin catalyst bed of silver particles (0.5 to 3 mm in size). The exit temperature is around 650°C and the residence time is about 0.04 s or less (Fischer patent (1973) and Bayer patent (1977)). Methanol conversion is typically 65 - 70% per pass. In this process the methanol is oxidised and dehydrogenated to formaldehyde by the following principle reactions

$$\begin{aligned} CH_3OH + \frac{1}{2}O_2 &\longrightarrow CH_2O + H_2O \qquad \Delta H_{298K}\,(-156 \text{ kJ/mol})\,, && (6.7)\\ CH_3OH &\longrightarrow CH_2O + H_2 \qquad \Delta H_{298K}\,(+85 \text{ kJ/mol})\,. && (6.8) \end{aligned}$$

Between 50 and 60% of the formaldehyde formed is via the exothermic reaction (the net result of the two is a reaction exotherm). Assuming each reaction contributes 50% to formaldehyde production then the endothermic and exothermic reactions can be combined to yield

$$CH_3OH + \frac{1}{4}O_2 \longrightarrow CH_2O + \frac{1}{2}H_2O + \frac{1}{2}H_2 \qquad \Delta H_{298\mathrm{K}}\,(-35.5\ \mathrm{kJ/mol})\,. \qquad (6.9)$$

Industrial process

A feed mixture is generated by sparging air into a pool of heated methanol (which must be free of iron carbonyls and sulphur compounds), and combining the vapour with steam. The steam acts as thermal ballast for reaction control. This mixture then passes through a further superheater (exit temperature approximately 200°C) and then to the reactor containing the catalyst. Within the reactor (after the catalyst) the product is rapidly cooled in a steam generator and water cooled in a heat exchanger and fed to the bottom of an absorption tower. The majority of the methanol, water, and formaldehyde is condensed in the bottom (water cooled) section of the tower. The remaining methanol and formaldehyde are recovered from the tail gas in the top of the absorber by countercurrent contact with clean process water. The absorber bottoms go to a distillation tower where methanol is recovered for recycle to the reactor. Bottoms product from the distillation column consists of an aqueous solution of formaldehyde which is then sent to an anion exchange unit Kirk-Othmer (1999).

Reaction kinetics

A literature search yielded no kinetic data in the temperature range of the industrial process, probably due to the high degree of mass transfer limitation. However some studies have provided kinetics and suggested mechanisms at lower temperatures. Robb and Harriott (1974) propose a Langmuir-Hinshelwood mechanism whilst Bhattacharyya et al.(1971) suggest an Eley-Rideal mechanism. Despite the different mechanisms suggested a common element between the two works is that it is oxygen that is adsorbed primarily on the catalyst surface whilst other species may be adsorbed on top of a layer of adsorbed oxygen.

The kinetics of Bhattacharyya et al.(1971) are used for this study as it is possible to extend them into a higher temperature regime. Hence a major assumption of the model is that the mechanism is still valid at the higher temperatures of the industrial process. The rate equation given by Bhattacharyya et al.(1971) has been derived on the basis of a steady-state adsorption model (Eley-Rideal).

$$r = \frac{2k_o k_m p_{o_2}^{\frac{1}{2}} p_m}{k_m p_m + 2k_o p_{o_2}^{\frac{1}{2}}}. \tag{6.10}$$

Rate constant data from Bhattacharyya et al.(1971) are shown in Table 6.3.

	k_o (mol/(s.kg$_{cat}$.Pa$^{0.5}$)	k_m (mol/(s.kg$_{cat}$.Pa)
264°C	1.52×10^{-3}	2.05×10^{-1}
281°C	2.83×10^{-3}	2.90×10^{-1}
290°C	5.00×10^{-3}	4.01×10^{-1}
E_a	95×10^{3}	62.7×10^{3}

Table 6.3: Values of k_o and k_m at different temperatures and activation energies from Bhattacharyya et al.(1971).

The expressions for k_o and k_m are given by the standard exponential form

$$k = A\exp\left(\frac{-E_a}{RT}\right), \tag{6.11}$$

where A is the pre-exponential factor and is used as an adjustable parameter in extrapolating kinetic data to higher temperature regimes.

The kinetics given previously (6.10) adequately describe the consumption of the reactant gas; methanol. However, the kinetics do not give a quantitative insight into the rate of product formation and consumption via other reaction routes. A comprehensive mechanism is given in Held and Dryer (1998), but the most significant side reaction, as identified by Robb and Harriott (1974) and Chauval et al.(1973), is the partial oxidation of formaldehyde to CO_2. Little information is available on this series reaction but Allen (1964) and Robb and Harriott (1974) have suggested an activation energy based upon a reduced silver catalyst (172 kJ/mol). Chauval et al.(1973) have reported that formaldehyde remains stable below 573K and Robb and Harriott (1974), along with Allen (1964), have further suggested that this can be modelled as a first order process. Hence the pre-exponential factor has been chosen as 5.0×10^{13} m/s to give formaldehyde yields within the industrial range 86-90% based on methanol (Lowenheim and Moran (1975)).

$$\begin{aligned} CH_2O + O_2 &\longrightarrow CO_2 + H_2O, & (6.12)\\ r_{ch_2o/co_2} &= A\exp\left(\frac{-172\times10^3}{RT}\right) C_{ch_2o}. & (6.13) \end{aligned}$$

Therefore a semi-realistic mechanism is introduced for methanol oxidation in a microreactor. Although some parameters have been extrapolated a reasonable evaluation of reactor performance for methanol oxidation by stoichiometric reactions (6.9) and (6.12) along with reaction kinetics (6.10) and (6.13). It should be noted that the series reaction is only included in the FDV model in this chapter, the CFD and PFR models only consider a single reaction.

6.4.2 Validation of reaction kinetics

Due to the extrapolation of the reaction kinetics it is prudent to test them against the reported data for the industrial process. Not only will this serve as a validation of the kinetic model but it will allow relative performances of the conventional adiabatic reactor and the microreactor to be assessed. The kinetics given by Bhattacharyya et al.(1971) account for the methanol consumed that produces formaldehyde, hydrogen and water, the series reaction is not modelled in the adiabatic PFR.

To verify the kinetics (6.9) and (6.10) will be modelled in an adiabatic PFR. The adiabatic temperature rise and the space-time will be compared for a methanol conversion of 85%. The main uncertainty of the kinetic model is the pre-exponential factors in the kinetic rate constants (6.10), although the order of magnitude is known from Wachs and Madix (1978) where similar expressions have been developed. Values used for the pre-exponentional factors in the PFR model are 2.9×10^{13} mol/(s.kg$_{cat}$.Pa$^{0.5}$) (k_o) and 5.0×10^{13} mol/(s.kg$_{cat}$.Pa) (k_m). It is also assumed there is negligible pressure drop over the catalyst bed, which is typically 1.8 to 2.1 m in diameter and 0.01 to 0.025 m in depth (Kirk-Othmer (1999), Ullman's (1987)). Typical feed of methanol is 3700 kg/h (Kirk-Othmer (1999)) which corresponds to a volumetric flowrate (at inlet temperature $\simeq$ 150°C (Kirk-Othmer (1999)) of 1.3 m^3/s. The weight of catalyst required for given conversion in a PFR is given by

$$W = F_{\mathrm{m}0} \int_{0}^{0.85} \frac{\mathrm{d}X}{-r}. \tag{6.14}$$

From Satterfield (1991) a 50:50 mol ratio of air to methanol is passed to the reactor. Therefore the fractional change of moles in the reactor (ε) can be given as

$$\varepsilon = y_{\mathrm{m}0}\delta = 0.5 \times +(0.75) = +0.375. \tag{6.15}$$

Species	Symbol	Initial	Change	Remaining	Concentration
CH_3OH	A	F_{AO}	$-F_{AO}X$	$F_A = F_{AO}(1-X)$	$\frac{C_{AO}(1-X)}{1+0.375X}\left(\frac{T_O}{T}\right)$
O_2	B	$\theta_B F_{AO}$	$-\frac{F_{AO}X}{4}$	$F_B = F_{AO}\left(\theta_B - \frac{X}{4}\right)$	$\frac{C_{AO}\left(\theta_B-\frac{X}{4}\right)}{1+0.375X}\left(\frac{T_O}{T}\right)$
CH_2O	C	$\theta_C F_{AO}$	$F_{AO}X$	$F_C = F_{AO}X$	$\frac{C_{AO}X}{1+0.375X}\left(\frac{T_O}{T}\right)$
H_2	D	$\theta_D F_{AO}$	$\frac{F_{AO}X}{2}$	$F_D = \frac{F_{AO}X}{2}$	$\frac{C_{AO}\frac{X}{2}}{1+0.375X}\left(\frac{T_O}{T}\right)$
H_2O	E	$\theta_E F_{AO}$	$\frac{F_{AO}X}{2}$	$F_E = \frac{F_{AO}X}{2}$	$\frac{C_{AO}\frac{X}{2}}{1+0.375X}\left(\frac{T_O}{T}\right)$
N_2	I	$\theta_I F_{AO}$	0	$F_I = \theta_I F_{AO}$	$\frac{C_{AO}\theta_I}{1+0.375X}\left(\frac{T_O}{T}\right)$
Total	-	F_{TO}	$\delta F_{AO}X$	$F_{TO} + \delta F_{AO}X$	-

Table 6.4: Stoichiometric table of methanol oxidation reaction.

The stoichiometric table for the system is shown in Table 6.4. The partial pressures of each species can be obtained from the ideal gas law

$$p_i = C_i RT. \tag{6.16}$$

If the above are combined the reaction rate (6.10) can be expressed as a function of conversion and temperature

$$r = \frac{2k_o k_m \left(\frac{C_{AO}\left(\theta_B - \frac{X}{4}\right)}{1+0.375X} RT_O\right)^{\frac{1}{2}} \left(\frac{C_{AO}(1-X)}{1+0.375X} RT_O\right)}{\left(k_m \left(\frac{C_{AO}(1-X)}{1+0.375X} RT_O\right)\right) + \left(2k_o \left(\frac{C_{AO}\left(\theta_B - \frac{X}{4}\right)}{1+0.375X} RT_O\right)^{\frac{1}{2}}\right)}. \tag{6.17}$$

To obtain reaction rate as a function of conversion the energy balance must be solved, which for an adiabatic PFR is

$$X\left[-\Delta H_R(T)\right] = \int_{T_O}^{T} \sum \theta_i c_{pi} \mathrm{d}T, \tag{6.18}$$

$$X = \frac{\sum \theta_i \overline{c_{pi}} (T - T_O)}{-\left[\Delta H_R(T_R) + \Delta\widehat{c_p}(T - T_R)\right]}, \tag{6.19}$$

where $\Delta H_R(T_R)$ = -35.5 kJ/mol, (from lumping (6.7) and T_R = 298 K) and the mean specific heat capacities, with inlet conditions, of the species are given in Table 6.5, which gives $\Delta\widehat{c_p}$ as -0.725 J/(mol.K). Equation (6.19) can be re-arranged to give

Species	c_{pi} (J/mol/K)	θ_i
CH_3OH	84.50	1.0
O_2	33.81	0.25
CH_2O	57.45	0.0
H_2	31.16	0.0
H_2O	38.39	0.4
N_2	30.0	0.75

Table 6.5: Mean specific heats (c_{pi}) [40] at bulk catalyst operating temperature of 680 K and composition at inlet of each species.

Reactor parameter/variable	Value
F_{m0} (mol/s)	18.34
X	0.85
Catalyst weight (kg)	276.0
Packed reactor volume (m^3)	0.05
Volumetric flowrate (m^3/s)	1.290
Space-time (s)	0.038
Inlet temp. (K)	437.00
Outlet temp. (K)	679.593
Temp. rise (K)	242.593

Table 6.6: Results from adiabatic PFR program.

temperature as a function of conversion (Fogler (1992)).

$$T = \frac{X\left[-\Delta H_R\left(T_R\right)\right] + \sum \theta_i \overline{c_{pi}} T_O + X \Delta \widehat{c_p} T_R}{\sum \theta_i \overline{c_{pi}} + X \Delta \widehat{c_p}}. \tag{6.20}$$

The reaction rate is now known as a function of conversion, hence (6.14) can be integrated to give the catalyst weight required. The void fraction can be estimated by the correlation of Haughey and Beveridge (1969), which gives the void fraction as 0.45 resulting in a bed density of 5500 kg/m^3, based on a catalyst diameter of 1 mm. Knowing the catalyst weight and void fraction allows the reactor volume (V) (with catalyst) to be evaluated. The initial reactant concentration and flowrate along with the reactor volume allow the space-time to be calculated according to

$$\tau_{\mathrm{pfr}} = \frac{V C_{\mathrm{m0}}}{F_{\mathrm{m0}}}. \tag{6.21}$$

The results from the FORTRAN 90 PFR program are shown in Table 6.6, and give flowrates, reactor dimension and temperatures for the adiabatic PFR, some design and operating parameters are compared directly in Table 6.7. All parameters used in the PFR model are shown in Appendix D.

Parameter	Industrial value/range [26] [79] [89] [138]	Calculated value
τ_{pfr}	0.01 – 0.04	0.038
Volume	0.025 – 0.087	0.050
Adiabatic temp. rise	150 – 500	242
Catalyst pellet diameter	0.5 to 3.0 mm	1 mm

Table 6.7: Comparison of industrial parameters with adiabatic PFR parameters.

6.4.3 Solution method

Equation (6.14) was integrated using the IMSL routine QDAG, which is based on a globally adaptive scheme to minimise error of all sub-intervals. All FORTRAN 90 codes are shown in Appendix E.

6.4.4 Summary of validation

It can be seen that space-times, catalyst bed volume and adiabatic temperature rise shown in Table 6.7 compares well to the industrial process, hence these kinetics will be used in the microreactor simulations.

6.5 FDV Model

CFD modelling can allow detailed modelling of the methanol oxidation reactor, however the CPU time can be excessive due to solving the Navier-Stokes equations in addition to the species and energy equations. An alternative model is the finite difference/volume (FDV) model, that does not solve for the velocity profile, this is given explicitly from the work by Beskok and Karniadakis (1999), (4.8). From earlier work, in heat and mass transfer, it is concluded that in a typical microreactor dimensions and operating conditions ($Pe/R \ll 1$) (see Table 6.8) the velocity profile has negligible effect on reactor performance. The FDV model is written in FORTRAN 90 coupled to IMSL libraries (linear solvers). The mass and energy equations are solved in dimensionless form and appropriately coupled by a sequential solution method. The mass and energy equations are presented in turn followed by the solution method used in the simulation.

6.5.1 Mass equations

The mass equations are modelled as a parabolic PDE in a parallel plate where axial diffusion has been neglected, and this is solved by an explicit method for each species. Equations are solved on a mass fraction basis to account for volume change

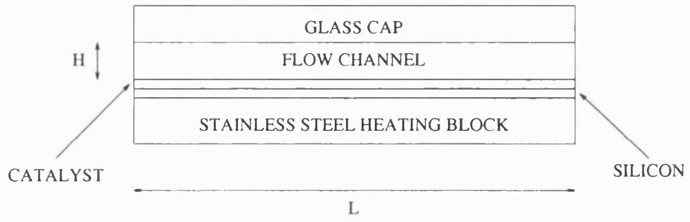

Figure 6.4: Schematic of the solution domain for the methanol oxidation reactor (not to scale).

and the methanol reaction is modelled as a simultaneous series system according to the following

$$\begin{aligned} CH_3OH + \frac{1}{4}O_2 &\rightarrow CH_2O + \frac{1}{2}H_2O + \frac{1}{2}H_2, & (6.22)\\ CH_2O + O_2 &\rightarrow CO_2 + H_2O, & (6.23) \end{aligned}$$

where the reaction rates for methanol oxidation and formaldehyde oxidation are given by (6.10) and (6.13) respectively (constants used are given in Appendix D). The dimensional equation describing transport in the reactor for each species is given by the following advection-diffusion equation (where $u(x)$ is the velocity profile as given in Beskok and Karniadakis (1999))

$$D\frac{\partial^2 Y_i}{\partial x^2} - u(x)\frac{\partial Y_i}{\partial z} = 0, \qquad (6.24)$$

with the following boundary conditions (where r_i is now on a surface area of catalyst basis)

$$\begin{aligned} Y_i\big|_{(0,x)} &= Y_{i0}, & (6.25)\\ \frac{\rho D_i}{M_i}\frac{\partial Y_i}{\partial x}\bigg|_{(z,0)} &= r_i, & (6.26)\\ \frac{\rho D_i}{M_i}\frac{\partial Y_i}{\partial x}\bigg|_{(z,H)} &= 0. & (6.27) \end{aligned}$$

Introducing the following variables reduces the equation to its dimensionless form

$$\eta = \tfrac{x}{H} \quad \zeta = \tfrac{z}{L} \quad Pe = \tfrac{uH}{D_i} \quad R = \tfrac{L}{H} \quad \Psi = \tfrac{Kn}{1-bKn}.$$

$$\frac{\partial^2 Y_i}{\partial \eta^2} - v(\eta)\frac{Pe}{R}\frac{\partial Y_i}{\partial \zeta} = 0, \tag{6.28}$$

and

$$Y_i\big|_{(0,\eta)} = Y_{i0}, \tag{6.29}$$

$$\left.\frac{\rho D_i}{hM_i}\frac{\partial Y_i}{\partial \eta}\right|_{(\zeta,0)} = r_i, \tag{6.30}$$

$$\left.\frac{\rho D_i}{hM_i}\frac{\partial Y_i}{\partial \eta}\right|_{(\zeta,1)} = 0. \tag{6.31}$$

6.5.2 Energy equation

This section is presented in two parts, initially the rationale and simplification of the boundary conditions is shown (reduction in dimensionality) for a generic solid. The governing equations are then presented with the simplified boundary conditions for the methanol oxidation reactor.

Reduced boundary conditions

The microreactor has a variety of solid domains (silver catalyst, silicon, stainless steel and glass) of different characteristic dimensions. Modelling domains of different characteristic dimensions requires a fine grid (especially at domain interfaces) hence CPU time and memory requirements can be excessive. However such different domain scales can be exploited in the context of domain reduction (Deen (1998)). The idea in this section is to combine the solid domains into a single boundary condition (i.e. to reduce a 2D domain into a 1D boundary condition). A theoretical justification can be established using the Biot number, which is used to characterise the ratio of solid to fluid resistance for heat transfer. The Biot number is defined as

$$Bi = \frac{h_{solid}L'}{k_{solid}},$$

where h is the natural convection heat transfer coefficient, k is the thermal conductivity of the solid and L' is the thickness of the solid in the vertical (x) dimension. If the characteristic length in any dimension is small in comparison to other lengths then the temperature in that dimension can be deemed constant if $Bi \ll 1$, this can be shown by considering the convective boundary condition at the edge of the solid domain. The convective boundary condition at the edge domain of the solids (where L' is the vertical thickness of the solid exposed to the surroundings) can be expressed as

$$\frac{\partial T}{\partial x}\left(z, L'\right) = -\frac{h_{solid}}{k_{solid}}\left[T\left(z, L'\right) - T_{\infty}\right], \tag{6.32}$$

where T_{∞} is the ambient temperature of the surroundings. If (6.32) is simplified by approximating the derivative, then (after rearrangement) the following is obtained

$$\frac{T\left(z, 0\right) - T\left(z, L'\right)}{T\left(z, L'\right) - T_{\infty}} \sim \frac{h_{solid}L'}{k_{solid}} = Bi. \tag{6.33}$$

Thus it can be seen that if Bi (typically $O\left(5 \times 10^{-3} - 0.2\right)$ in the catalytic methanol oxidation reactor) is small then the difference in vertical temperatures, in the solid, is also small. Therefore the solid temperature distribution can be represented as

$$\overline{T}\left(z\right) = \frac{\int\limits_{x_1}^{x_2} T\left(x, z\right) \mathrm{d}x}{x_2 - x_1}, \tag{6.34}$$

and the heat conduction equation for conduction in the solid is (where S is a general source term)

$$k\nabla^2 T + S = 0. \tag{6.35}$$

If (6.35) is integrated over the thickness of the solid, and rearranged, the following flux equation is obtained (where $\overline{T}$ is the averaged temperature over x)

$$k\frac{\partial T}{\partial x}\bigg|_{x2} = k\frac{\partial T}{\partial x}\bigg|_{x1} - k\frac{\partial^2 \overline{T}}{\partial z^2}L' - \overline{S}L'. \tag{6.36}$$

From (6.36) it can be seen that the boundary condition allows for axial conduction whilst maintaining a flux in the vertical direction.

Governing equations and boundary conditions

The energy equation is solved by an elliptic finite-volume method with first order UPWIND differencing (boundary value problem) due to axial conduction in the boundary conditions. In the following the dimensional and dimensionless forms of the energy equation are shown, along with boundary conditions. The dimensional governing PDE for energy (in a parallel plate) is given by

$$\frac{k}{\rho c_p}\frac{\partial^2 T}{\partial x^2} - u(x)\frac{\partial T}{\partial z} = 0,$$

if the following variables are introduced

$$\theta = \tfrac{T}{T_0} \quad \eta = \tfrac{x}{H} \quad \zeta = \tfrac{z}{L} \quad v(\eta) = \tfrac{u(x)}{U} \quad R = \tfrac{L}{H} \quad Pe = \tfrac{U\rho c_p H}{k},$$

the governing equation becomes

$$\frac{\partial^2 \theta}{\partial \eta^2} - \frac{v(\eta)Pe}{R}\frac{\partial \theta}{\partial \zeta} = 0. \tag{6.37}$$

By applying (6.36) to the glass domain it is possible to obtain a boundary condition for the top surface of the gas domain

$$k\,\frac{\partial T}{\partial x}\bigg|_{gas\ top} = k_{glass}\,\frac{\partial T}{\partial x}\bigg|_{glass\ bottom} = k_{glass}\left(\frac{\partial^2 \overline{T}}{\partial z^2}\right)L'_{glass} - h_{top}\left(\overline{T} - T_\infty\right), \tag{6.38}$$

by introducing the following variables

$$\eta = \tfrac{x}{L} \quad \zeta = \tfrac{z}{L} \quad Bi_{top} = \tfrac{h_{top}L}{k_{glass}} \quad R_{top} = \tfrac{L'_{glass}}{L},$$

the boundary condition for the top surface becomes

$$\frac{\partial \theta}{\partial \eta} = R_{top} \left(\frac{\partial^2 \overline{\theta}}{\partial \zeta^2} \right) - Bi_{top} \left(\overline{\theta} - \theta_\infty \right).$$

The bottom boundary condition consists of a thin layer of silver, silicon and steel, each of the solid domains can be vertically-averaged to yield expressions similar to (6.36). As the heat flux in the vertical dimension must be the same in each solid phase then the axial conduction terms can be added yielding a single boundary condition representing the different solid phases. The boundary condition for the composite bottom solid is (where Q is a volumetric heat source)

$$\begin{aligned} k_{silver} \frac{\partial T}{\partial x} &= -\left(\frac{\partial^2 \overline{T}}{\partial z^2} \right) \left(k_{silver} L'_{silver} + k_{silicon} L'_{silicon} + k_{ss} L'_{ss} \right) + h_{bottom} \left(\overline{T} - T_\infty \right) \\ &- QL_{ss} - r_i \Delta H, \end{aligned} \tag{6.39}$$

again, introducing the following variables

$$\eta = \tfrac{x}{L} \quad Bi_{bot} = \tfrac{h_{bottom} L}{k_{silver}} \qquad R_{silver} = \tfrac{L'_{silver}}{L} \quad R_{silicon} = \tfrac{L'_{silicon}}{L} \quad R_{ss} = \tfrac{L'_{ss}}{L}$$

$$K_{silicon} = \tfrac{k_{silicon}}{k_{silver}} \quad K_{ss} = \tfrac{k_{ss}}{k_{silver}} \quad K_{silver} = \tfrac{k_{silver}}{k_{silver}} = 1,$$

the boundary condition for the bottom surface becomes

$$\begin{aligned} \frac{\partial \theta}{\partial \eta} &= -\left(\frac{\partial^2 \overline{\theta}}{\partial \zeta^2} \right) \left(K_{silver} R_{silver} + K_{silicon} R_{silicon} + K_{ss} R_{ss} \right) + Bi_{bot} \left(\overline{\theta} - \theta_\infty \right) \\ &- \frac{QL'_{ss} L}{k_{silver} T_0} - \frac{r_i \Delta H L}{k_{silver} T_0}. \end{aligned} \tag{6.40}$$

A Dirichlet boundary condition for temperature is applied at the reactor inlet, whilst a zero derivative Neumann condition is applied at the reactor outlet. It should be emphasised at this point that the solid boundary conditions only serve to model the axial conduction along the boundary.

External heat convection

The reactor is assumed to be exposed to the ambient surroundings, natural convection effects are included on all external horizontal planes. The following correlations are used for the heat transfer coefficient, h (W/m^2/K), for upward and downward facing horizontal planes (Coulson et al. 1993)

$$h_{top} = 1.31(\Delta T/L)^{0.25} \qquad \text{(upward)},$$
$$h_{bottom} = 0.59(\Delta T/L)^{0.25} \qquad \text{(downward)}.$$

In using these heat transfer correlations it is assumed that buoyancy effects give rise only to streamline convection conditions. The characteristic length, L, is taken to be the mean length of the solid side, and ΔT is the mean temperature difference in Kelvins.

6.5.3 Physical properties

In this section the procedures to calculate the physical properties of the gases are presented. Each physical property is treated in a separate subsection and all molecular weights refer to the fluid molecular weight, given as

$$M_{mix} = \frac{1}{\sum_{i=1}^{Nspecies} \frac{Y_i}{M_i}}.$$

Density

Density of the gas mixture is computed by the ideal gas law

$$\rho = \frac{pM_{mix}}{RT}.$$

Viscosity

Viscosity of the gas mixture is computed by the semi-empirical Wilke formations, given as

$$\mu_{mix} = \frac{\sum_{i=1}^{Nspecies} (X_i \mu_i)}{\sum_{j=1}^{Nspecies} (X_j \varphi_{ij})},$$

where

$$\begin{aligned}\mu_i &= 2.6693\times10^{-6}\frac{\sqrt{M_iT}}{\sigma_i^2\Omega_\mu},\\ \varphi_{ij} &= \frac{1}{\sqrt{8}}\left(1+\frac{M_i}{M_j}\right)^{-1/2}\left[1+\left(\frac{\mu_i}{\mu_j}\right)^{1/2}\left(\frac{M_i}{M_j}\right)\right]^2.\end{aligned}$$

and σ and Ω are the Leonard-Jones collision diameter and collision integral respectively.

Specific heat capacity

Specific heat capacities for individual gas species are calculated from the CHEMKIN thermochemical database (Kee et al.(1986)). The specific heat for the gas mixture is given as

$$c_{p(mix)} = \sum_{i=1}^{Nspecies} Y_i c_{pi}.$$

Thermal conductivity

Almost all gases, over a wide range of temperature, have a Prandtl (Pr) number of 0.7. Therefore the thermal conductivity of the gas mixture is computed according to

$$k_{mix} = \frac{\mu_{mix}}{c_{p(mix)}Pr}.$$

Mass diffusion

The mass flux is computed through the Fickian diffusion model

$$j_i = -\rho D_i \nabla Y_i,$$

where D_i is the diffusion coefficient for species i and is given by

$$D_i = \frac{1 - X_i}{\left(\sum_{j=1}^{Nspecies} \frac{X_j}{D_{ij}} \right)_{j \neq i}},$$

where

$$D_{ij} = 1.8583 \times 10^{-2} \frac{\sqrt{T^3 \frac{1}{M_i} + \frac{1}{M_j}}}{p\sigma_{ij}^2 \Omega_D},$$

and

$$\sigma_{ij} = \frac{1}{2} (\sigma_i + \sigma_j),$$

where σ and Ω have the same meaning as before.

In the FDV model such methods are only evaluated at the inlet, any temperature changes at a cell are reflected in the physical properties by the following relationships

$$D_i = D_{i0} \left(\frac{T}{T_0} \right)^{1.5} \quad U = U_0 \left(\frac{T}{T_0} \right)^{1} \quad \mu = \mu_0 \left(\frac{T}{T_0} \right)^{0.7} \quad k = k_0 \left(\frac{T}{T_0} \right)^{0.7} \quad \rho = \rho_0 \left(\frac{T}{T_0} \right)^{-1}.$$

6.5.4 Solution method

The mathematical model, (6.28), (6.37) and associated boundary conditions, describing the catalytic methanol reactor are a coupled set of partial differential equations (PDE's). A sequential method is employed in the model where each equation (energy and mass) is solved for its dominant variable, keeping all other variables constant, for that iteration. Iteration continues between both equations until convergence of the coupled system satisfies tolerance criteria. The solution of each equation (energy and mass) are described in the following.

Mass equation

The mass equation can be modelled as an initial value problem, and hence an explicit solver is used. Although explicit parabolic solvers have a low memory requirement they can become unstable. Hence the rules of Carnahan et al.(1969) have been used to give grid sizes that ensure stability.

Energy equation

Due to axial conduction boundary conditions the domain of the energy equation is closed and must be solved as a boundary value problem. Discretising the energy equation (in the sequential method) results in a set of linear algebraic equations with a banded coefficient matrix. As the coefficient matrix is sparse and banded special solution techniques can be used that reduce the number of FLOPS (floating point operations) and memory.

IMSL routines have been used in the FORTRAN 90 model to solve the resulting linear algebraic system. Initially routine DLFCRB is called which performs an *LU* decomposition of the coefficient matrix and estimates condition number (ratio of the largest to smallest element in the matrix diagonal). If the condition number is sufficiently small then routine DLFIRB is called with iterative refinement performed on the solution vector. Such an algorithm seems complex, but the basis is more clearly explained in the following (Press et al.1996). Assume that linear equation set is

$$\mathbf{A} \cdot \mathbf{x} = \mathbf{b}. \tag{6.41}$$

However the solution vector $\mathbf{x}$ is unknown with any degree of accuracy. If $\delta\mathbf{x}$ is the unknown error then the slightly wrong solution is $\mathbf{x} + \delta\mathbf{x}$ which also effects the right hand side, yielding

$$\mathbf{A} \cdot (\mathbf{x} + \delta\mathbf{x}) = \mathbf{b} + \delta\mathbf{b}. \tag{6.42}$$

If (6.41) is subtracted from (6.42) then

$$\mathbf{A} \cdot \delta\mathbf{x} = \delta\mathbf{b}. \tag{6.43}$$

Equation (6.42) can be solved for $\delta\mathbf{b}$. If this is substituted into (6.43) then

$$\mathbf{A} \cdot \delta\mathbf{x} = \mathbf{A} \cdot (\mathbf{x} + \delta\mathbf{x}) - \mathbf{b}. \tag{6.44}$$

Parameter	Value
Channel height	300 microns
Channel width	600 microns
Channel length	20 mm
Stainless steel height	5 mm
Glass cap height	3 mm
Bottom silicon height	200 microns
Catalyst height	0.1 microns
k_{ss}	23.0 W/m/K
k_{glass}	1.45 W/m/K
$k_{silicon}$	2.2 W/m/K
k_{silver}	429.0 W/m/K

Table 6.8: Design parameters of the methanol oxidation microreactor.

In (6.44) the right hand side is known, thus only the error $\delta\mathbf{x}$ needs to be calculated. This can be subtracted from the original wrong solution to get an improved solution. Increased performance benefits arise if the original solution was obtained by *LU* decomposition, this is due to the fact that the *LU* decomposed form of $\mathbf{A}$ already exists and all that is needed is to compute the right hand side and back substitute.

6.6 Catalytic methanol oxidation

The reactor built at UCL has dimensions and other design parameters as shown in Table 6.8. In this section the reactor is first operated adiabatically in §6.6.1 and compared with in the adiabatic PFR model in §6.4.2. An isothermal comparison is made in §6.6.2 to further ascertain the importance of reactor model and physical property temperature dependence. In §6.6.3 the heat transfer characteristics of the reactor are investigated for various design and operating parameters with non-reacting flow. Such an investigation allows a more intuitive analysis of the more complex reacting flow cases that follow. With the design parameters given in Table 6.8 the reactor is also assigned a 'base case' set of operating parameters, reactor performance under these conditions is investigated in §6.6.4. Operating and design parameters are investigated in §6.6.5 and §6.6.6 respectively, conclusions are drawn in §6.7.

6.6.1 Model verification (adiabatic operation)

In order to ascertain the accuracy of the model a comparison is made against the adiabatic PFR model (which has already been validated against industrial data) for complete conversion. For this to be possible all solid thermal conductivities and

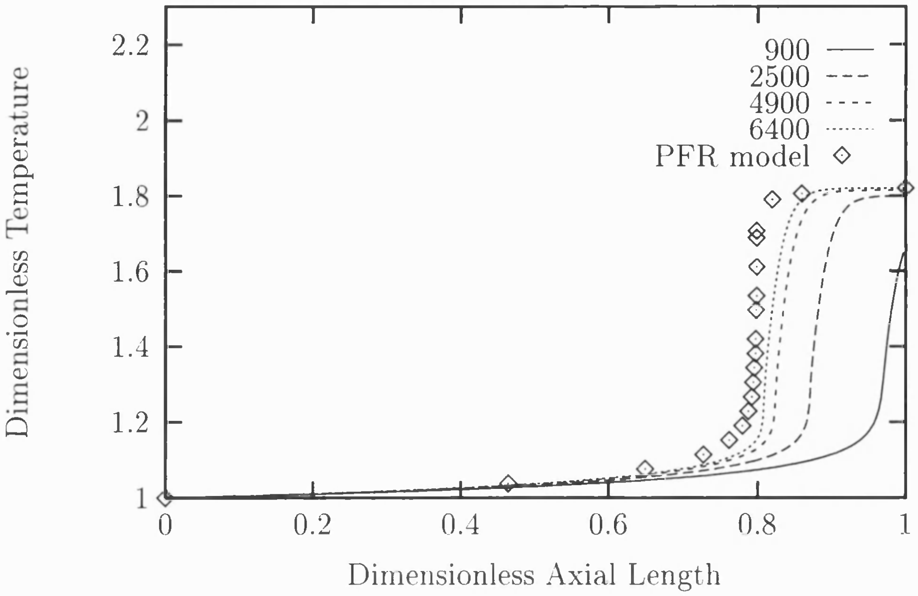

Figure 6.5: Axial temperature profiles in the adiabatic FDV model and the PFR model, the FDV model is shown as lines (styled according to the number of grid points used in the simulation) and the adiabatic PFR model is shown as discrete points.

heat transfer coefficients are set to zero. The reactor is 0.02 m long and 300 × 10^{-6} m high, all operating parameters are identical to the adiabatic PFR in §6.4.2. This results in the following inlet energy and mass Peclet numbers

$$\begin{aligned} Pe_e &= \frac{0.51 \times 0.872 \times 1100 \times 300 \times 10^{-6}}{3.8 \times 10^{-3}} = 3.87, \\ Pe_m &= \frac{0.51 \times 300 \times 10^{-6}}{3 \times 10^{-5}} = 5.10. \end{aligned}$$

A decrease in grid size, corresponding to an increase in the number of grid points, will allow the residual error to approach to the asymptotic limit of zero. However such accuracy is offset by the increase in CPU time, hence the grid is refined until the difference in outlet temperatures, between successive simulations, is less than 2.0%. Figure 6.5 shows the axial temperature profiles given by the FDV (for different grid sizes) and PFR model. It can be seen that there is good agreement in the prediction of the temperature shock. In Fig. 6.5 a difference in the temperature profiles is observed. This can be attributed to different models being used, and §6.6.2 addresses this issue.

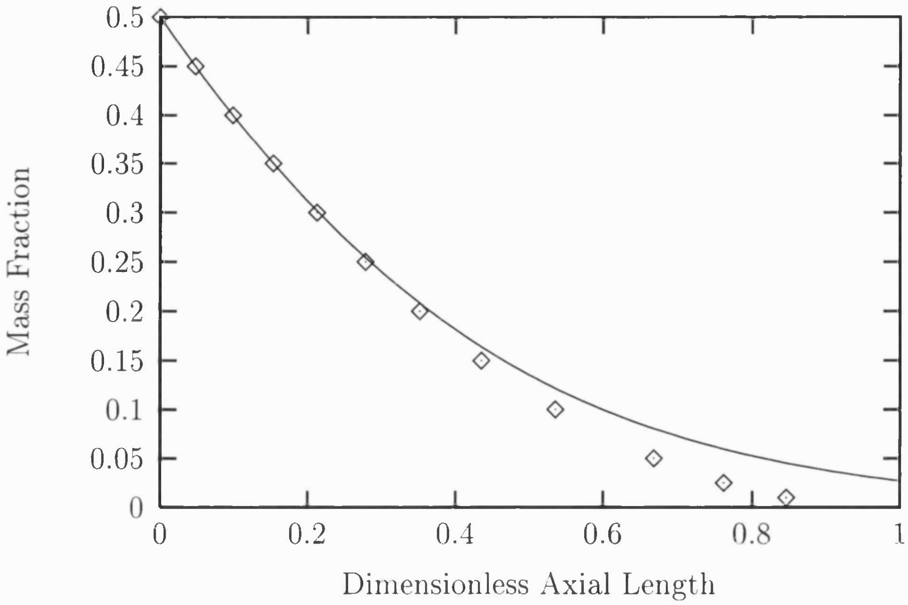

Figure 6.6: Comparison of methanol mass fraction profiles for isothermal operation (423 K) in the microreactor (line) and PFR (points), both reactors are 1 m in length.

6.6.2 Model verification (isothermal operation)

In light that the reactor operates with a low Pe/R ratio (approximately 0.1) it is expected that the microreactor solution would approach the adiabatic PFR solution but not be identical. In addition the microreactor model accounts for the physical property temperature dependence and therefore the influence of this modelling discrepancy needs to be evaluated. Fig. 6.6 shows the comparison of reactant (methanol) axial profiles in a 1 m reactor operating at 423 K. It can be seen that the PFR has a slightly higher performance than the microreactor (due to distribution of fluid residence times), such a difference in axial profiles can explain the different axial positions of the temperature shock in Fig. 6.5 and the influence of physical properties temperature dependence, when $Pe/R \ll 1$, is deemed to be small.

6.6.3 Non-reacting flow

To aid understanding the transport mechanisms in the microreactor non-reacting flow simulations will initially be presented. In this section a pure oxygen feed stream is introduced into the reactor and the effects of conductivity/thickness of solids, heater power and flowrate are shown. Table 6.8 shows the relevant parameters of the physical device and all simulations are based on a deviation from these parameters. Average temperatures are presented, and are calculated according to

$$\overline{T} = \frac{\int_A T \mathrm{d}A}{\int_A \mathrm{d}A}. \tag{6.45}$$

Unless otherwise stated the base Peclet numbers for energy and mass are 30.0 and 50.0 respectively (roughly an order of magnitude higher than for adiabatic operation).

Conductivity/thickness of solids

In this section the effect of axial conduction, caused by the solids, is investigated. Thicknesses of all materials are scaled by a constant factor to represent an increase or decrease in solid material. By applying a constant factor to all the solids the ratio of thickness between each solid material does not change (i.e. 0 is for no solids and 1 is the base case). The thickness of all solids from the original reactor are given in Table 6.8.

Axial average temperature profiles are shown in Fig. 6.7. It can be seen that axial conduction gives a sharper temperature gradient at the reactor inlet with a higher degree of isothermality throughout the majority of the reactor. Such differences will be augmented with highly exothermic reaction chemistry. With the solids acting as a thermal shunt hot spot formation can be reduced as the shunt smooths out the temperature profile.

Heater power

In the non-reacting flow simulations there has been no power input from the stainless steel heating block. However the following results show how the addition of further heat may increase isothermality. Average axial temperature profiles are shown in Fig. 6.8 with power density (W/m^3) as the adjustable parameter. As the heater power is increased the magnitude of the negative axial temperature gradients, at the beginning of the reactor, are reduced. Hence isothermality may be achieved with relative ease due to axial conduction at the fluid boundary. If the increase in heater power is high enough then positive axial temperature gradients will result at the beginning of the reactor, and hence an elevated temperature profile results throughout the remainder of the channel. From these results it can be seen that downstream reactor temperature is strongly influenced by conditions at the reactor inlet, such dependence is augmented by axial conduction due to the solids at the fluid boundaries.

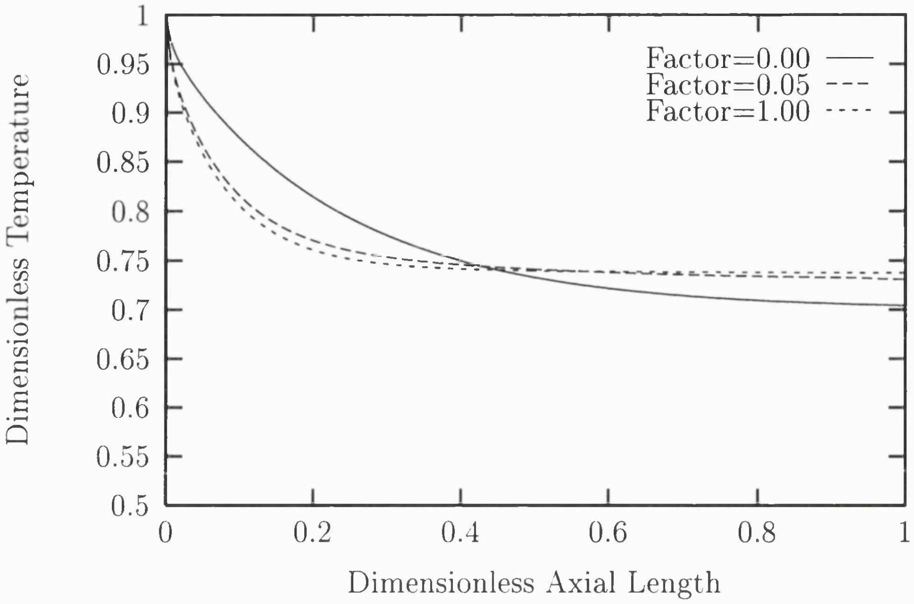

Figure 6.7: Average axial temperature profiles for different solid thickness scaling factors for Pe_e of 30.0 and Pe_m of 50.0.

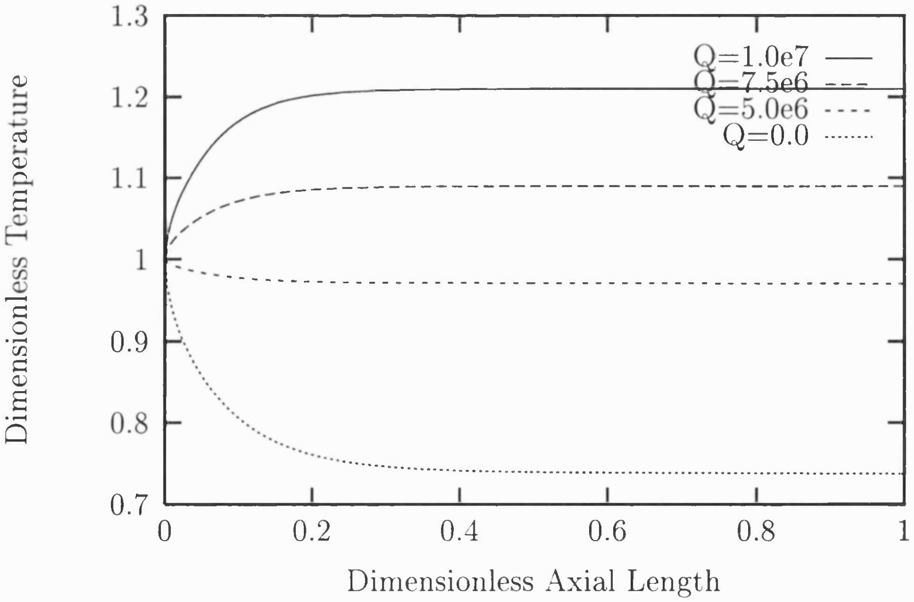

Figure 6.8: Average axial temperature profiles for different power densities for Pe_e of 30.0 and Pe_m of 50.0, other parameters are set according to Table 6.8.

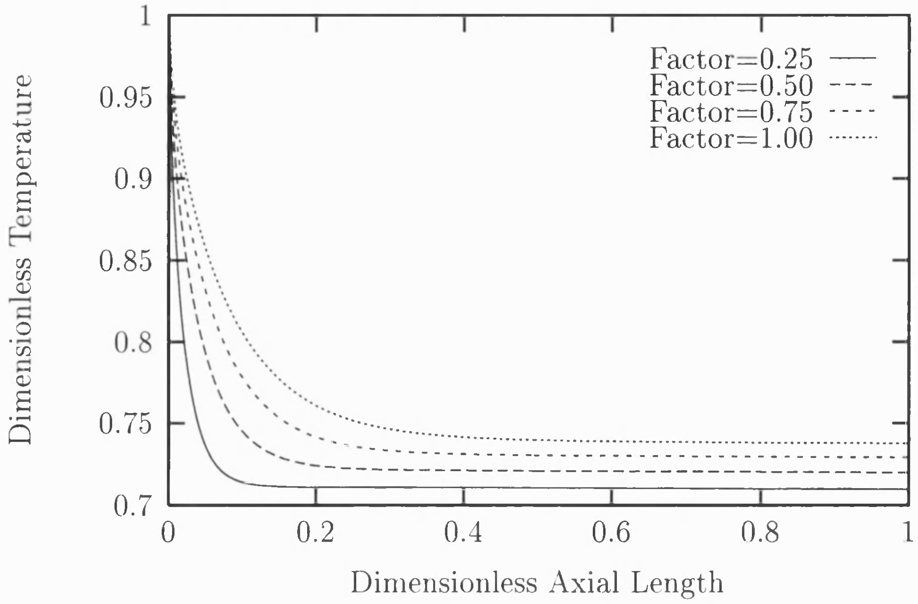

Figure 6.9: Average axial dimensionless temperature profiles for different flowrates (factors of base Peclet number) with no heater power, other parameters are set according to Table 6.8.

Flowrate

In this section the flowrate is varied for the fabricated reactor, as specified in Table 6.8. Variations of flowrate a represented by factors of the base Peclet numbers (Pe_e of 30.0 and Pe_m of 50.0) for no heat input (Fig. 6.9) and heat input with a power density of 7.5×10^6 W/m^3 (Fig. 6.10). It can clearly be seen in these figures that regardless of flowrate axial conduction is smoothing the temperature profile. The axial temperature gradients are lowest for the higher fluid velocities, this is expected as the fluid elements have less time to attain energy by diffusion in the transverse direction. Note that in the Fig. 6.10 the axial temperature profile has a slight negative gradient, especially towards the end of the reactor, indicating that the effect of natural convection starts to dominate over the process of axial conduction.

6.6.4 Base case simulations

In this section the methanol oxidation microreactor operates with design variables as given in Table 6.8. In addition, the operating parameters are given in Table 6.9. Performing a reference simulation will allow the effects of design and operating parameters to be clearly established in future sections.

Figure 6.11 shows the average axial temperature profile in the reactor, and the axial temperature profiles at the catalyst and at the top of the flow section in the

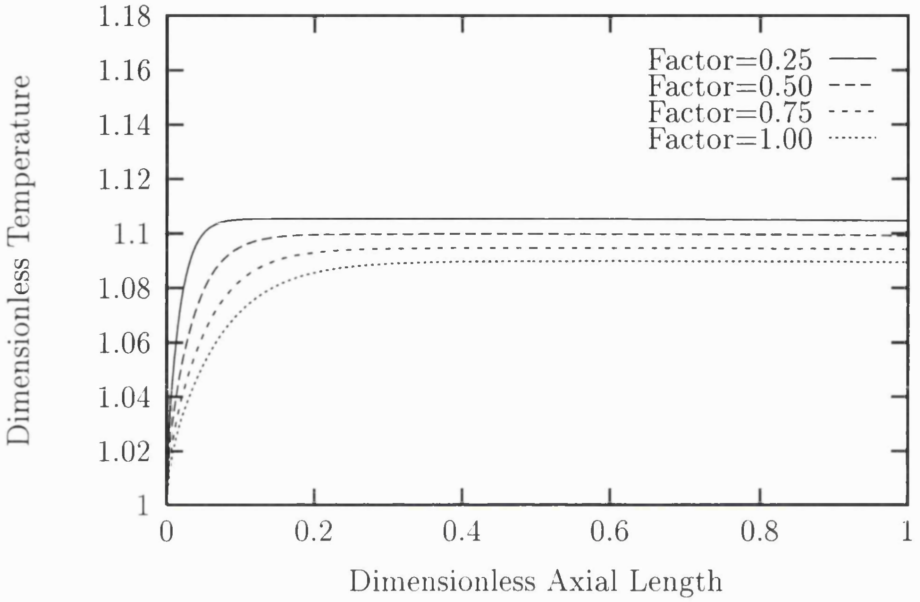

Figure 6.10: Average axial dimensionless temperature profiles for different flowrates (factors of base Peclet number) with a power density of 7.5×10^6 W/m^3.

Parameter	Value
Peclet number (energy)	3.87
Peclet number (mass)	5.10
Inlet temperature	423 K
Ambient temperature	298 K
Power density (heating block)	5.5×10^6 W/m^3
Inlet mass fraction methanol	0.5
Inlet mass fraction oxygen	0.125
Inlet mass fraction nitrogen	0.375

Table 6.9: Operating parameters of the methanol oxidation microreactor.

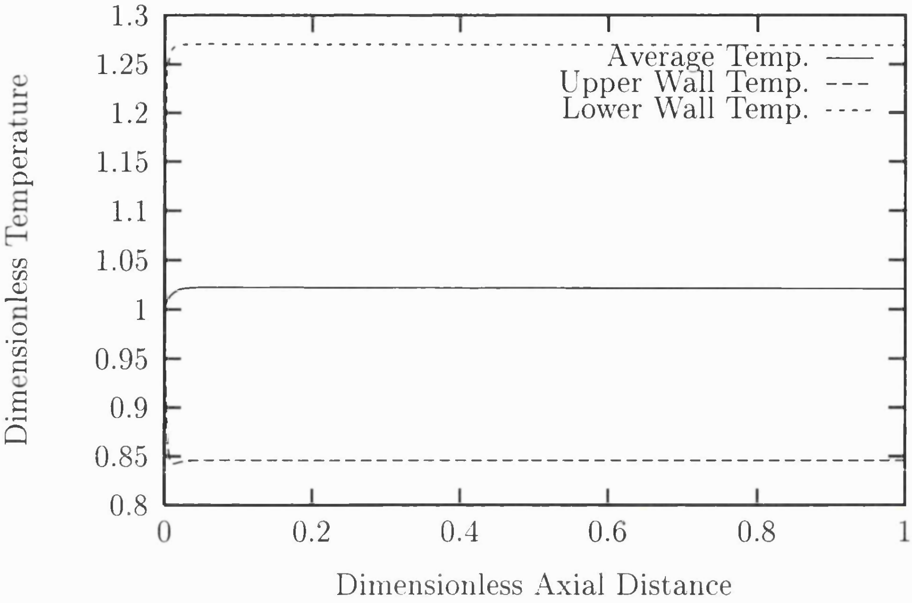

Figure 6.11: Average, catalytic and top wall axial dimensionless temperature profile in the methanol oxidation microreactor for base case parameters.

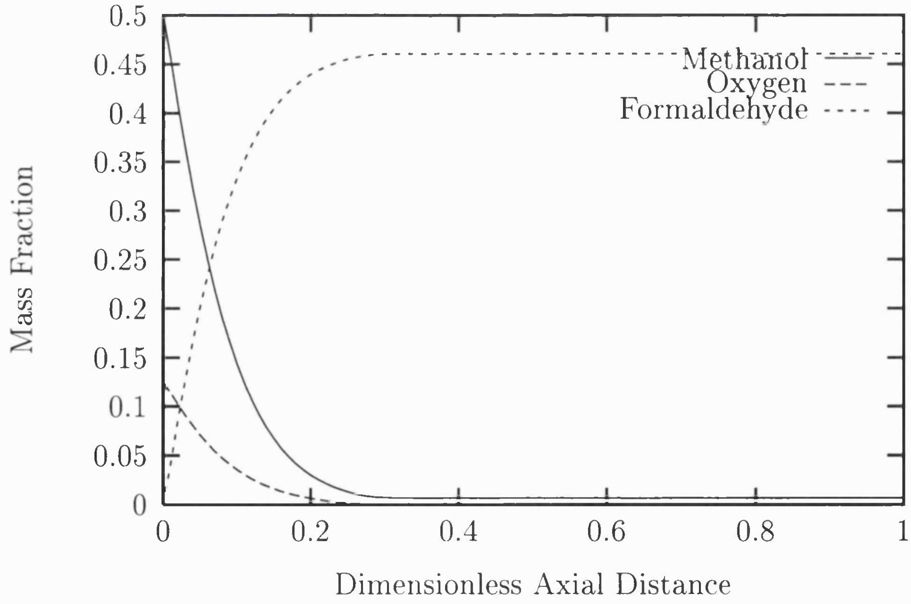

Figure 6.12: Average axial mass fraction profiles for methanol, oxygen and formaldehyde in the methanol oxidation microreactor for base case parameters.

Simulation	Pe_m	Pe_e
Base case	5.10	3.87
Run 1	10.20	7.74
Run 2	40.80	30.96
Run 3	500.00	377.30
Run 4	650.00	492.40

Table 6.10: Peclet numbers for different simulation runs.

reactor. It can clearly be seen in Fig. 6.11 that significant transverse temperature gradients exist in the methanol oxidation microreactor, in contrast to adiabatic operation. However, the effect of the solids acting as a thermal shunt still smoothes out the axial temperature profile except at the entrance of the reactor. At the entrance there is backward axial heat transmission along the solids and, due to high heat transfer coefficients in microreactors, rapid heat transfer takes place resulting in a sharp axial temperature gradient.

Figure 6.12 shows axial mass fraction profiles of methanol, oxygen and formaldehyde. It can be seen that under these operating conditions complete conversion of methanol is not achieved as reactants are fed to the reactor in stoichiometric proportions for the the partial oxidation reaction (6.9) and further oxygen is consumed in the formaldehyde oxidation before all methanol is reacted. If the formaldehyde oxidation (6.12) was not present then a sharper axial positive gradient of formaldehyde would result until reaching a mass fraction value of 0.5, corresponding to complete conversion of methanol.

6.6.5 Operating parameter considerations

In this section the effect of operating parameters on reactor performance are investigated; initially flowrate of reactants (by inlet Peclet numbers) is shown followed by inlet temperature, inlet composition and power density in the heating block.

Flowrate - Peclet numbers

In this section the effect of flowrate on reactor performance is investigated. The base case Peclet numbers are multiplied by identical factors and the simulations performed are shown in Table 6.10.

Figure 6.13 shows the average axial methanol mass fraction profiles in the methanol oxidation reactor. The profiles exhibit typical isothermal exponential trends at lower flowrates (base case, run 1 and run 2). At higher flowrates it can be seen that inflexion points in the profiles occur near the entrance of the reactor, similar trends are observed for adiabatic design and operating parameters. Such trends are attributed

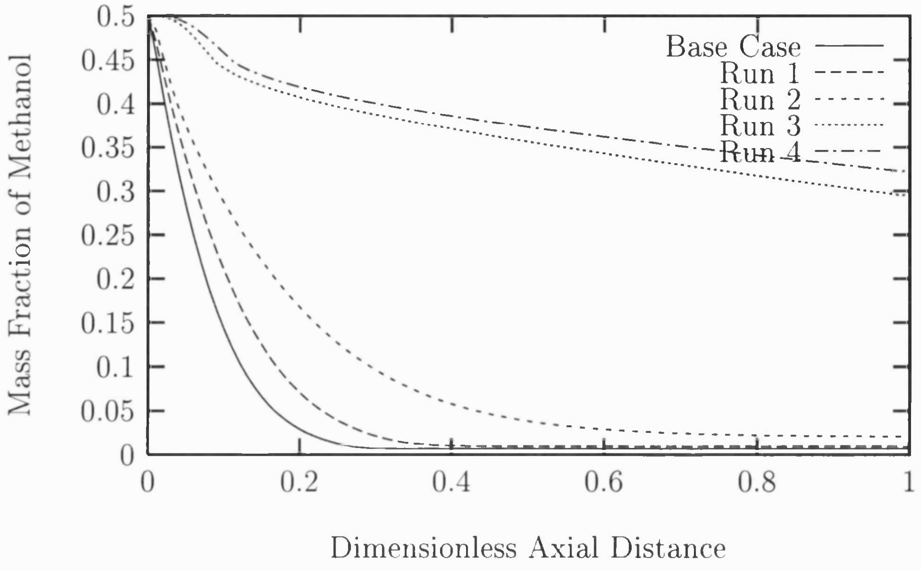

Figure 6.13: Average axial methanol mass fraction profiles in the methanol oxidation microreactor for different flowrates.

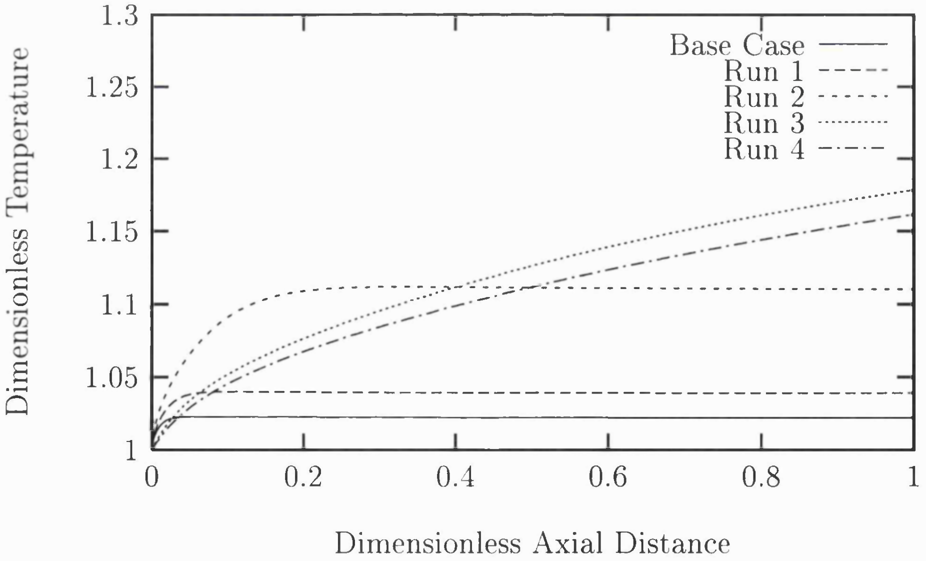

Figure 6.14: Average axial dimensionless temperature profiles in the methanol oxidation microreactor for different flowrates.

to non-isothermal effects in the reactor which can be seen in Fig. 6.14, where backward axial wall conduction is not dominating over the convective process to heat the gas at that point.

Figure 6.14 shows the average axial temperature profiles in the methanol oxidation microreactor. The results show that the temperature profiles are flat (except at

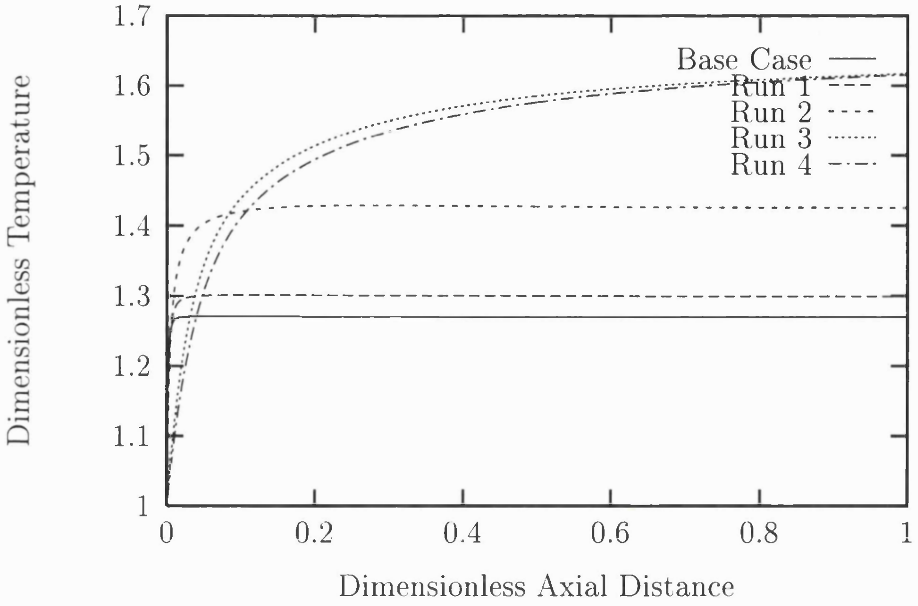

Figure 6.15: Axial dimensionless temperature profiles at the catalyst in the methanol oxidation microreactor for different flowrates.

the entrance) for the base case, run 1 and run 2, as a consequence of the conducting solids acting as a thermal shunt. As the flowrate is increased the average temperature rises in the reactor, this is expected as the point of near complete conversion moves further downstream, hence more reactant is converted resulting in higher heat release. The maximum temperature reaches a plateau with increasing flowrate as the point of near complete conversion will move far enough downstream that it occurs past the exit of the reactor. At the point where near complete conversion occurs at the exit of the reactor any increase in flowrate will reduce the total amount of reactant converted resulting in a lower temperature profile, this can be seen by examining runs 3 and 4 in Fig. 6.14. Note that the gradients near the entrance are sharper than the mass fraction gradients, again this is due to axial conduction.

A better insight into reactor performance can be gained by considering the temperature profiles at the catalyst surface. Figure 6.15 shows the axial dimensionless temperature profiles at the catalyst surface. It can be seen that a high degree of isothermality exists when $Pe/R < 1$. Due to high heat transfer coefficients, microreactors have often shown potential for isothermal behaviour, hence aiding in selectivity. However in the case of the methanol oxidation microreactor only isothermality at the catalyst surface is important (neglecting possible homogeneous reactions) and isothermality is aided by axial conduction in the boundary solids. It can be seen from Fig. 6.15 that a careful selection of flowrate and power applied to the heating block allows precise control of temperature at the catalyst surface.

Simulation	Inlet temperature	Pe_m	Pe_e
Base case	423 K	5.10	3.87
Run 1	350 K	5.61	4.42
Run 2	530 K	4.56	3.30

Table 6.11: Inlet temperatures for different simulation runs and modified inlet Peclet numbers.

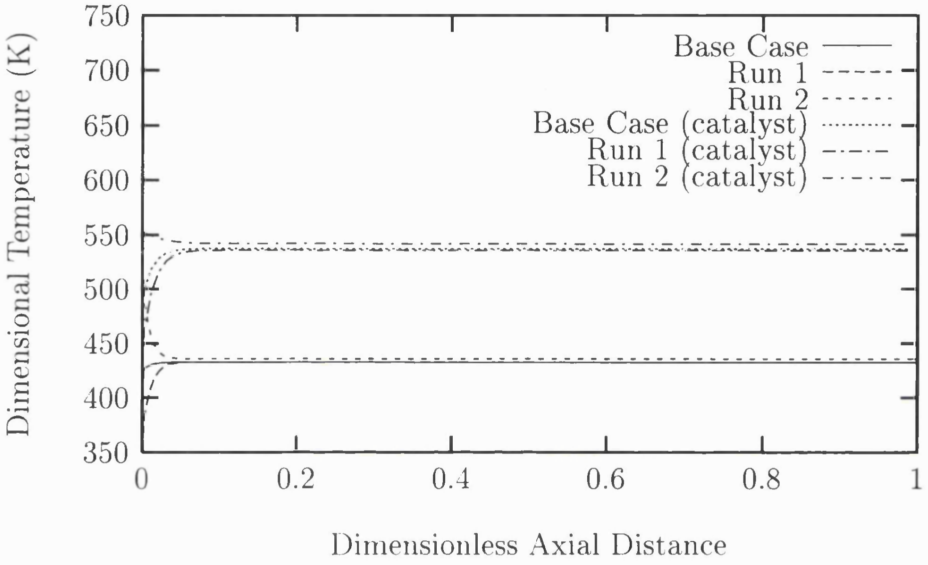

Figure 6.16: Average and catalyst axial dimensional temperature profiles for different inlet temperatures.

Inlet temperature

In this section the effect of inlet temperature on reactor performance is investigated, in the base case simulations the reactants were assumed to be heated to 423 K (roughly equivalent to the industrial process). Table 6.11 shows the simulations performed and modified inlet Peclet numbers (due physical property temperature dependence), and the results are shown in Figs. 6.16 and 6.17.

Figure 6.16 shows the effect of inlet temperature upon bulk and catalyst temperature in the reactor. It can be seen that a good degree of isothermality is achieved with inlet temperature having little effect on the bulk or catalyst temperature. This is reflected in Fig. 6.17 where the isothermality yields mass fraction profiles of methanol of roughly exponential trend. It should be noted that a slight point of inflexion exists in run 1 at the inlet where there is a sharp increase in temperature. This is in contrast to run 2 where there is a sharp negative temperature gradient, this can be attributed to natural convection processes starting to dominate the heat transfer in this region. Such inlet effects result in different mass fraction profiles as

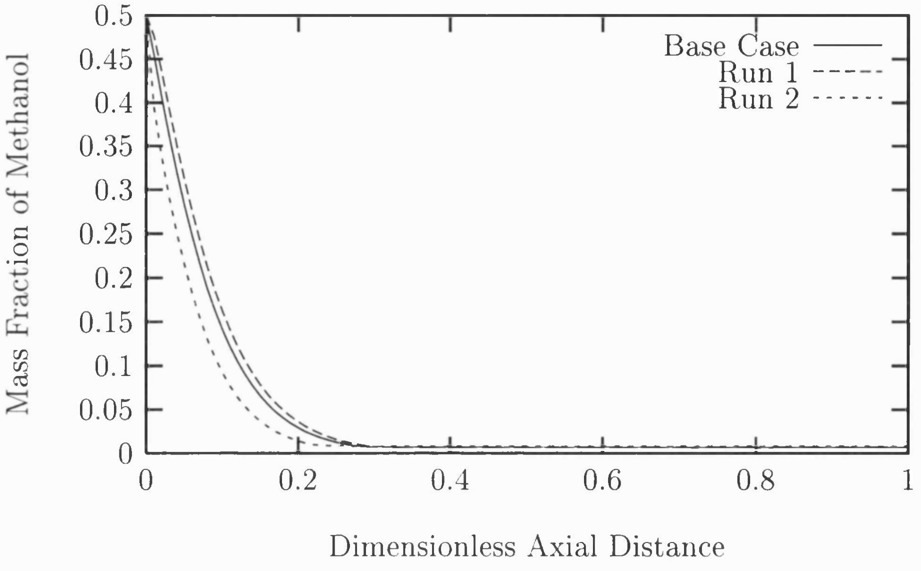

Figure 6.17: Average axial methanol mass fraction profiles for different inlet temperatures.

Simulation	Power density (W/m^3)	CH_3OH	O_2	N_2
Base case	5.5×10^6	0.500	0.125	0.375
Run 1	6.4×10^6	0.500	0.125	0.375
Run 2	5.5×10^6	0.500	0.500	0.000
Run 3	6.4×10^6	0.500	0.500	0.000

Table 6.12: Mass fraction inlet compositions for different simulation runs.

a higher amount of conversion occurs at the reactor inlet in run 2 than either the base case or run 1 as the temperature is higher.

Inlet composition and power density

In this section the effect of inlet composition on reactor performance is investigated. The industrial process required additional steam at the reactor inlet to serve as a thermal ballast to reduce excessive temperature rises, however the efficient heat transfer in microreactors does not justify such an addition and hence will be investigated no further. In addition the reactant composition at the reactor inlet was governed by flammability limits. As the methanol oxidation microreactor characteristic diameter is below the quench diameter of methanol-oxygen mixtures, no such operating constraint regarding feed composition need be considered. Table 6.12 shows the inlet compositions performed. The Peclet numbers were kept identical to the base case as their difference with change of composition was negligible.

Figure 6.18 shows the average axial dimensionless temperature profile for differ-

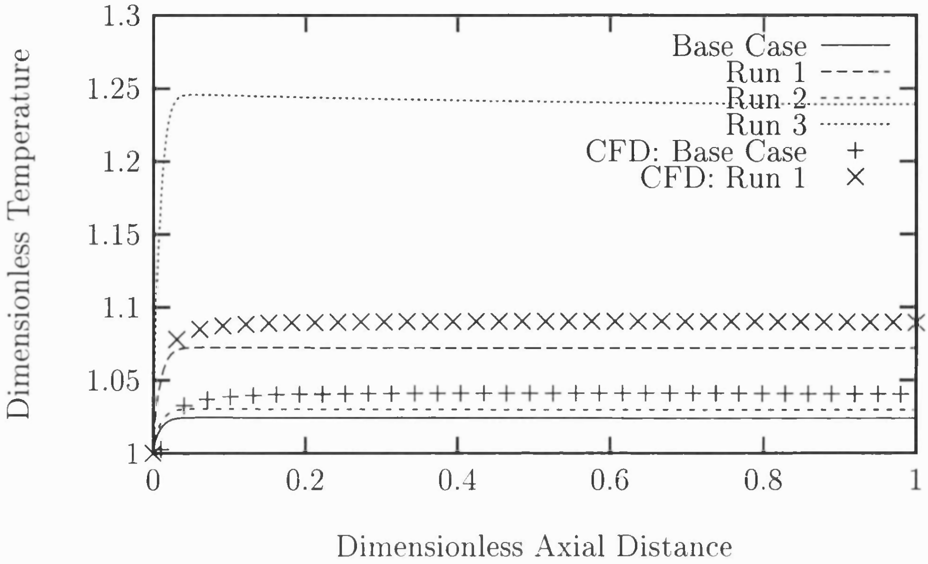

Figure 6.18: Average axial dimensionless temperature profiles for different inlet compositions and power densities. Runs using a CFD solution are also shown for comparison.

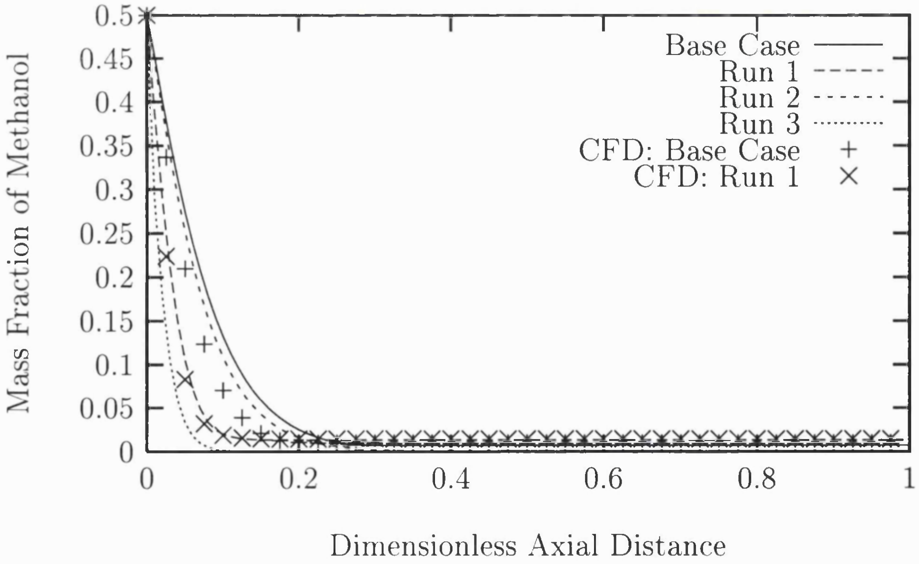

Figure 6.19: Average axial mass fraction profiles of methanol for different inlet compositions and power densities. Runs using a CFD solution are also shown for comparison.

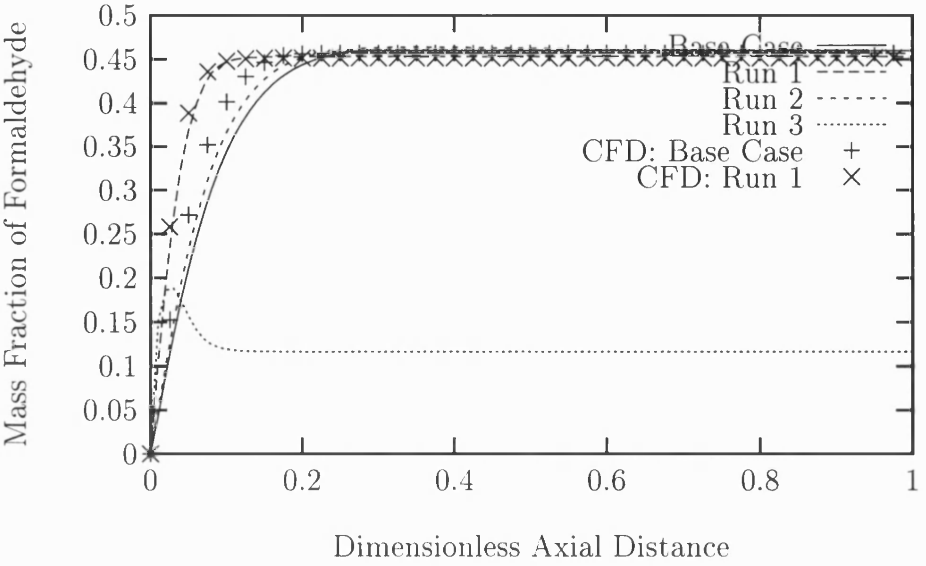

Figure 6.20: Average axial mass fraction profiles of formaldehyde for different inlet compositions and power densities. Runs using a CFD solution are also shown for comparison.

ent compositions and power densities. It can be seen in run 3 that the temperature attained in the reactor is much higher than the other runs (although a good degree of isothermality is still obtained in the reactor). This is attributed to the series reaction (oxidation of formaldehyde) occuring and higher heat generation; as more reactants flow through the reactor in a given time. Although the series reaction has a high activation energy it also has a high heat of reaction; hence a small conversion of formaldehyde will result in a high heat release. Higher formaldehyde conversion can be seen by considering the mass fraction profiles of methanol and formaldehyde shown in Figs. 6.19 and 6.20 respectively. Figure 6.19 shows the average axial mass fraction of methanol, it can be seen that altering the feed composition to oxygen instead of air does not significantly effect the axial profile, except that complete conversion is now possible as there is an excess of oxygen (i.e. no competition from series reaction for oxygen). Increasing the power input to the reactor results in sharper profiles as shown in runs 1 and 3. Figure 6.20 shows the average mass fraction of formaldehyde. It can be seen that an excess of oxygen at the base case power density does not significantly effect the yield of formaldehyde due to the large activation energy of the series reaction, although there is a slight improvement in reactor performance as the excess of oxygen enhances the methanol oxidation reaction rate. At the increased power setting the activation energy barrier of the series reaction is overcome and formaldehyde oxidation can proceed at a significant rate.

This can be seen in run 3 where formaldehyde is converted until a dimensionless axial distance of 0.1 where all oxygen has been consumed.

Figure 6.18 shows the temperature profiles calculated with the modified CFD code, where the Navier-Stokes equations are solved implicitly, for verification purposes. The axial profiles of temperature are similar but there are small differences in the actual values of dimensionless temperature. Such differences are attributed to the intrinsic calculation of thermodynamic properties in the CFD code, which are hidden from the user. However, as the trends are similar it is deemed that the FDV model is sufficiently accurate for this study. Figures 6.19 and 6.20 show the profiles of methanol and formaldehyde respectively, these have slightly sharper axial gradients due to the higher temperature predicted by the CFD model.

It is worth noting that the FDV model CPU time and memory requirements are an order of magnitude less than the CFD code, the weak dependence of reactor performance on flow field greatly reducing the equation set.

6.6.6 Design parameter considerations

In this section the effect of design parameters on reactor performance is investigated; initially reactor channel height is first considered followed by the conductivity of construction materials.

Channel height

In this section the effect of channel height on reactor performance is investigated (keeping U constant). Altering the channel height also alters the Peclet numbers for mass and energy, Table 6.13 shows the parameters used in each simulation, runs 8 to 12 concentrate in the profile transition range (300 - 400 microns) which is explained later in the text.

Figure 6.21 shows the average axial methanol mass fraction profiles in the reactor for different channel heights. The plots show generally that as reactor height increases, i.e. the transverse distance for reactants to diffuse, the reactor performance is reduced in terms of conversion. However there are some important points to note in this plot; when the channel height is reduced to 100 microns the thickness of the solids (and heat capacity) is much greater than the fluid, hence reactants are rapidly cooled (Figs. 6.25 and 6.26) resulting in lower conversion due to low reaction rate. In Fig. 6.21 it can be seen that the initial rate of conversion of methanol in the 500 micron channel is faster than the 300 micron channel despite achieving a lower conversion. At 500 microns the the temperature is higher but this also accelerates the series reaction to a smaller extent. As the channel height further increases the

Simulation	Height (m)	Pe_m	Pe_e	Pe_m/R
Base case	300×10^{-6}	5.10	3.87	0.0765
Run 1	100×10^{-6}	1.70	1.29	8.5×10^{-3}
Run 2	500×10^{-6}	8.50	6.45	0.2125
Run 3	750×10^{-6}	12.75	9.68	0.4781
Run 4	900×10^{-6}	15.30	11.61	0.6885
Run 5	1100×10^{-6}	18.70	14.19	1.0290
Run 6	1300×10^{-6}	22.10	16.77	1.4370
Run 7	2000×10^{-6}	34.00	25.80	3.4000
Run 8	330×10^{-6}	5.61	4.26	0.0926
Run 9	350×10^{-6}	5.95	4.52	0.1041
Run 10	360×10^{-6}	6.12	4.64	0.1102
Run 11	370×10^{-6}	6.29	4.77	0.1164
Run 12	390×10^{-6}	6.63	5.03	0.1293

Table 6.13: Channel height and Peclet numbers for different simulation runs.

effect of temperature on methanol conversion is reduced as the series reaction begins to dominate oxygen consumption. This is reflected in the formaldehyde mass fraction profiles in Fig. 6.22. Additionally it can be seen that near the entrance region that there are slight points of inflexion in the methanol mass fraction profiles as the channel height increases. Initially these were attributed to oscillations in the explicit parabolic solver (and further grid refinement was investigated) but eventually it was seen that such inflexions were true phenomena of the reactor. Figures 6.23 and 6.24 show the methanol mass fraction profile at the catalyst surface, it can be seen that in the height region between 300 and 400 microns there is depletion of methanol developing at the inlet to the catalyst surface which is gradually recovered downstream. As the reactor height increases (i.e. conversion is less) the amount of methanol at the catalyst surface downstream from the depletion point increases. In light of the methanol profiles at the catalyst surface it can be seen why there is a point of inflexion at the surface, which is augmented with channel height but reaching a threshold value as $Pe_m/R \rightarrow O(1)$. Such behaviour can be explained by considering the transverse profiles at different axial distances along the reactor. Figures 6.27, 6.28 and 6.29 shows the transverse mass fraction profiles of methanol at different axial positions for channel heights of 300, 750 and 1100 microns respectively. At 300 microns, where $Pe_m/R \ll 1$ the transverse mass fraction profiles are roughly uniform and approach increased uniformity with downstream axial distance. Figure 6.28 shows the transverse mass fraction profiles of methanol at the same axial positions but for a reactor channel height of 750 microns. It can be seen that significant transverse gradients exist at the inlet of the reactor with near depletion of methanol at the catalyst surface which is also the case in Fig.

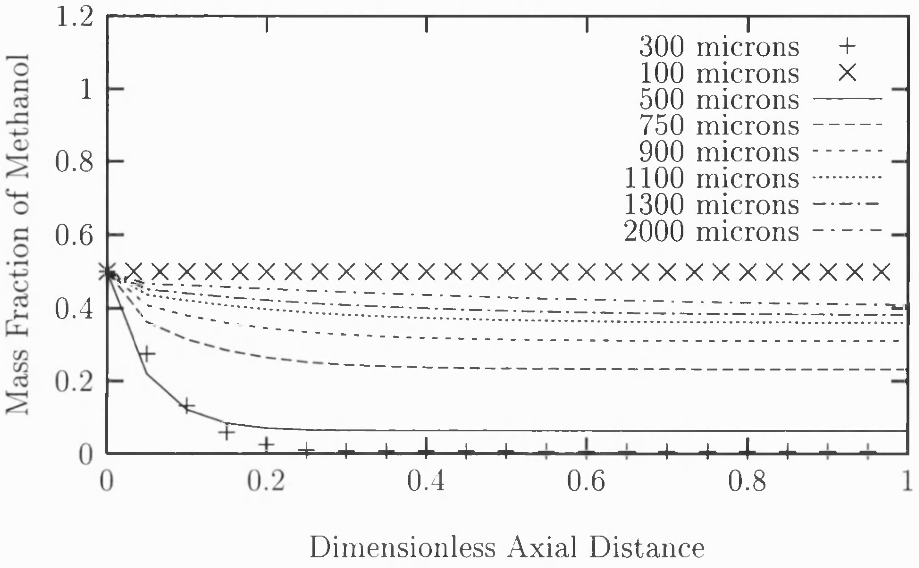

Figure 6.21: Average axial methanol mass fraction profiles for different channel heights.

6.29, such transverse profiles start to occur as $Pe/R \rightarrow O(1)$. Recovery of methanol concentration at the catalyst seems to reach a higher level in Fig. 6.29 for the same dimensionless axial positions, but conversion in this reactor is lower so there is a decrease in reactor performance. In considering the transverse profiles at high channel heights an important point to note is that as the transverse mass fraction profiles develop (i.e. far enough downstream) the difference in mass fraction between the catalyst and the top of the channel is about 0.1.

Although the phenomena of non-monotonic mass fraction profiles in the reactor have been explained in terms of transverse mass fraction profiles it is important to attribute a physical reasoning to the development of these transverse profiles with increasing channel height. As the channel height increases there is depletion of reactants at the catalyst surface and diffusional transport at approximately 423 K cannot replenish reactants within the space-time at the inlet section due to $Pe/R \rightarrow O(1)$. At the inlet of the reactor high Peclet numbers advect the reactant faster than the diffusive mechanisms. Also conversion will be worse with increasing channel height as at $Pe/R \rightarrow O(1)$ velocity profiles become important and there is a distribution of residence times which reduces reactor performance. Further downstream the heat of reaction increases the temperature so transverse diffusive transport of reactants can replenish the catalyst surface, the reactor now operates with small transverse gradients.

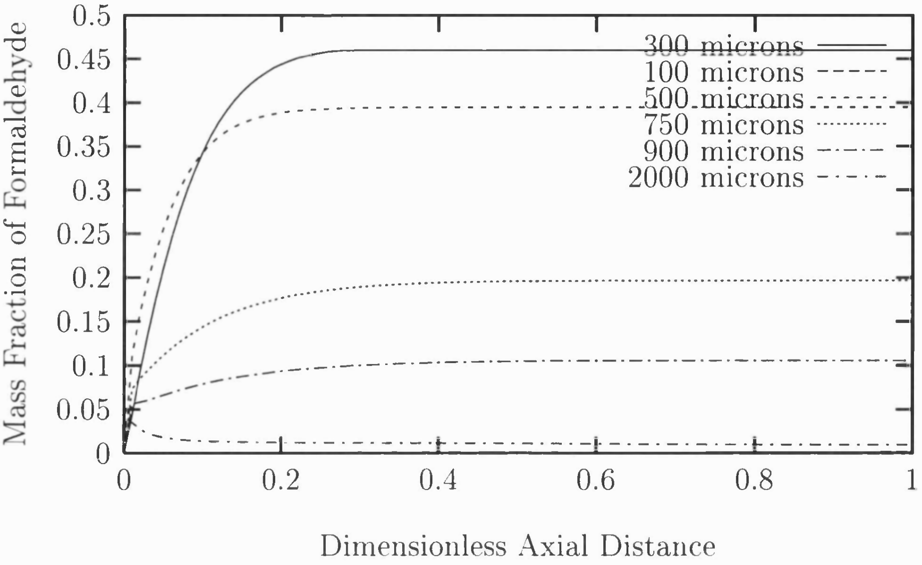

Figure 6.22: Average axial formaldehyde mass fraction profiles for different channel heights.

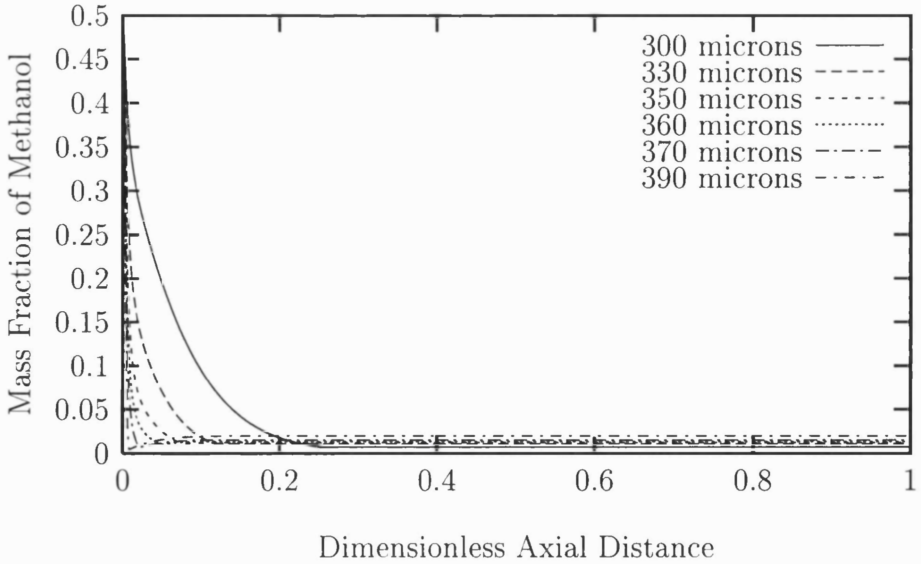

Figure 6.23: Catalytic axial methanol mass fraction profiles for channel heights between 300 and 390 microns.

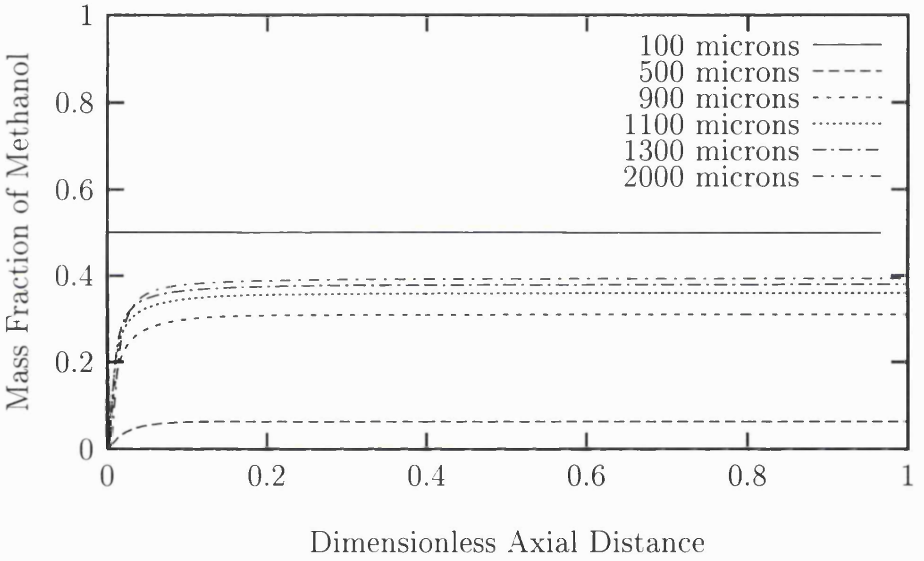

Figure 6.24: Catalytic axial methanol mass fraction profiles for different channel heights.

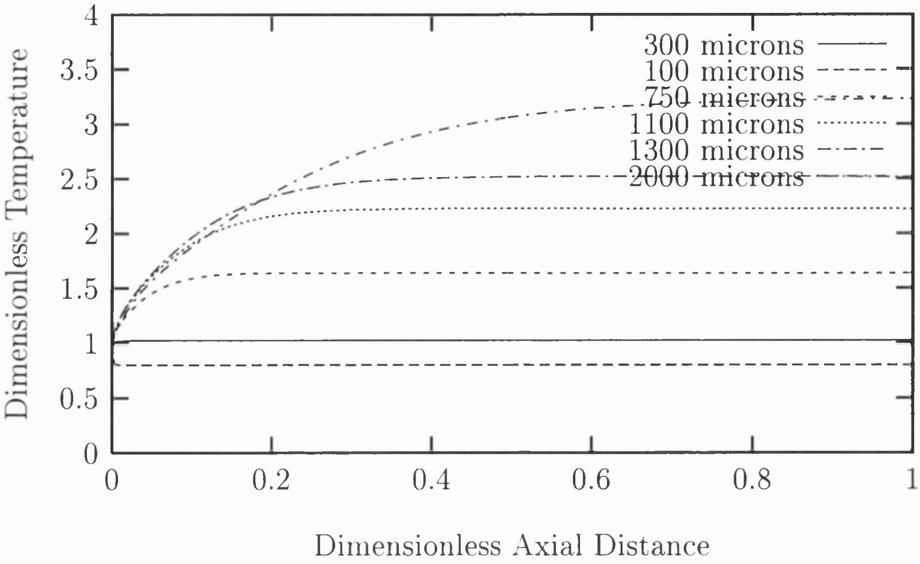

Figure 6.25: Average axial dimensionless temperature profiles for different channel heights.

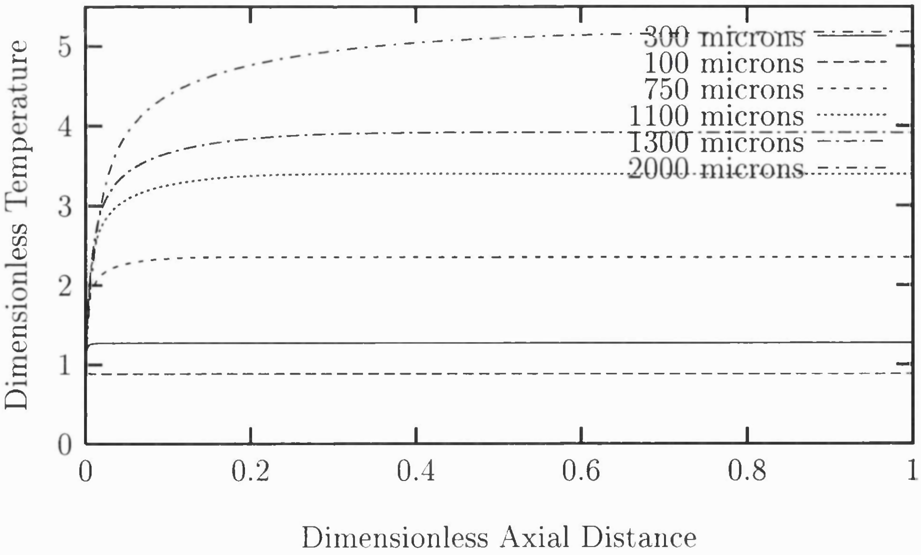

Figure 6.26: Catalytic axial dimensionless temperature profiles for different channel heights.

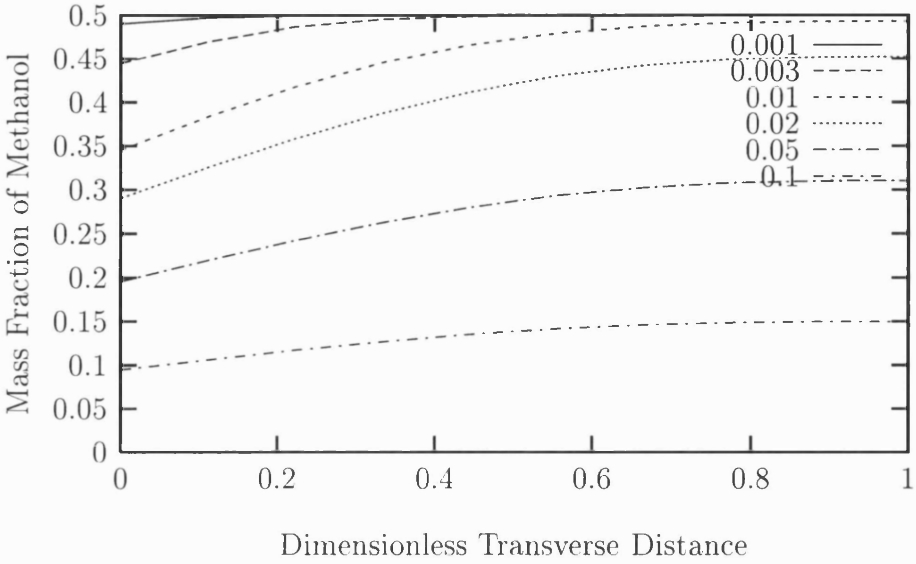

Figure 6.27: Transverse methanol mass fraction profiles at different dimensionless axial distances for a channel height of 300 microns (base case).

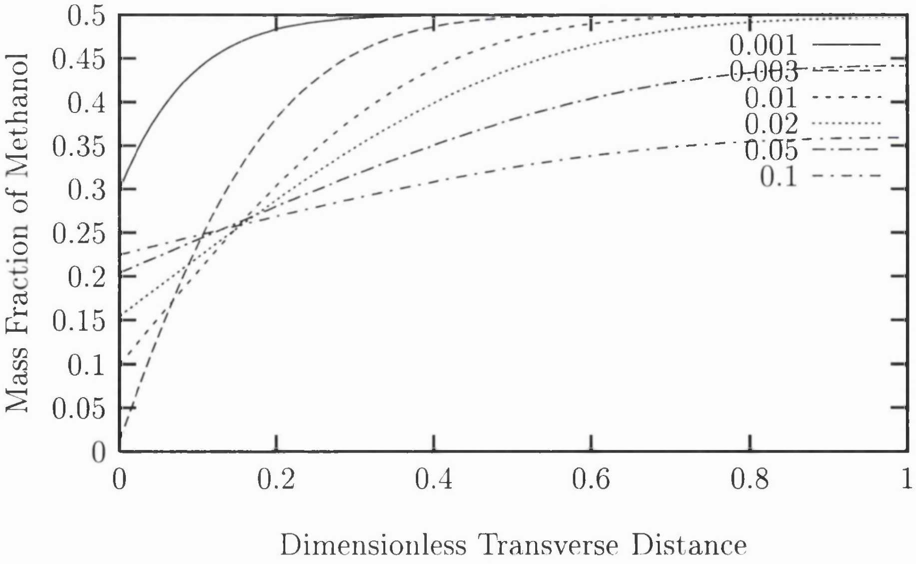

Figure 6.28: Transverse methanol mass fraction profiles for different dimensionless axial distances for a channel height of 750 microns.

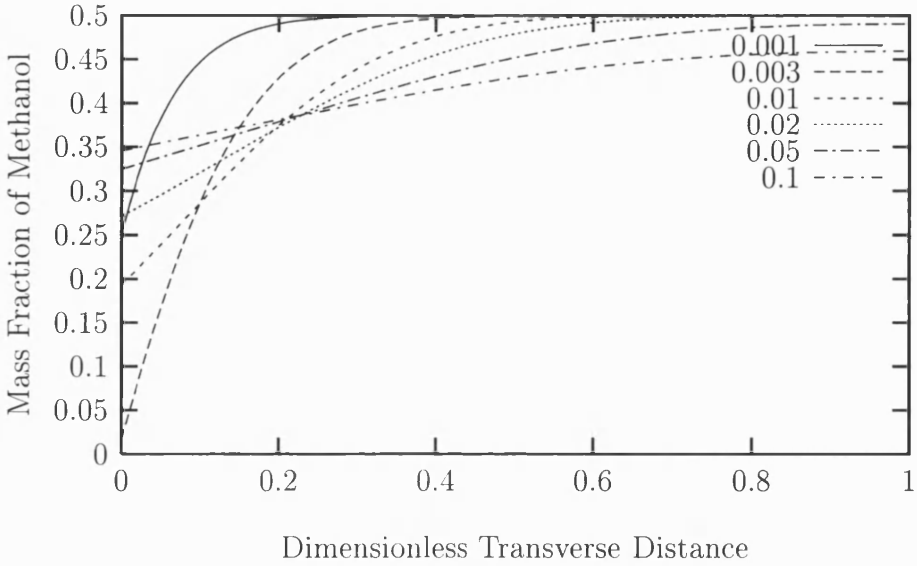

Figure 6.29: Transverse methanol mass fraction profiles for different dimensionless axial distances for a channel height of 1100 microns.

It should be noted that in Figs. 6.25 and 6.26 excessive temperature rises occur within the reactor as the channel height increases beyond 1mm. At these channel heights the combustion reaction proceeds at an appreciable rate, as the heat in the system cannot be removed as efficiently as at lower channel heights. The higher activation energy of the combustion reaction is overcome and most of the methanol is reacted to carbon dioxide and water (Figs: 6.30 and 6.31). The high temperatures are attributed to the heat of reaction of formaldehyde combustion -524.9 kJ/mol, which is an order of magnitude higher than the methanol partial oxidation reaction (-35.5 kJ/mol). Thermal feedback then occurs to the entrance of the reactor through the conducting solid walls further increasing the rate of the combustion reaction upstream. However, to verify the model fixed temperature wall boundary conditions were applied at the channel walls (i.e. no thermal feedback and no volumetric heat source) for a channel height of 2mm. The temperature set at the boundary walls was chosen to be similar to the base case temperatures at the catalyst surface. Figures 6.32 and 6.33 show mass fraction and temperature axial profiles respectively. It can be seen that the temperature in the reactor is kept relatively low and monotonically approaches the boundary value temperatures with increasing axial distance. In addition, it can be seen there is a negligible amount of formaldehyde depletion, in contrast to Fig. 6.22, indicating a low series rate of reaction.

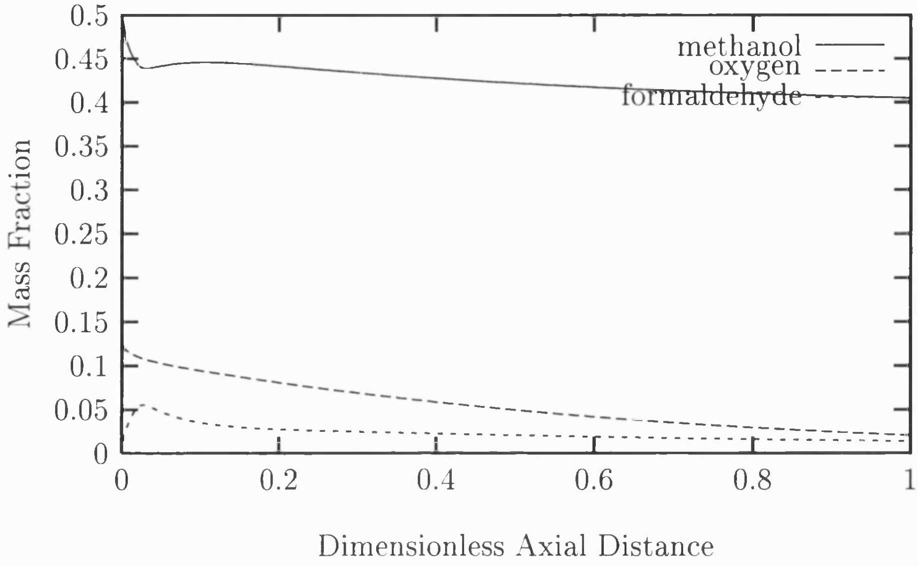

Figure 6.30: Average axial mass fraction profiles for methanol, oxygen and formaldehyde for a channel height of 2000 microns.

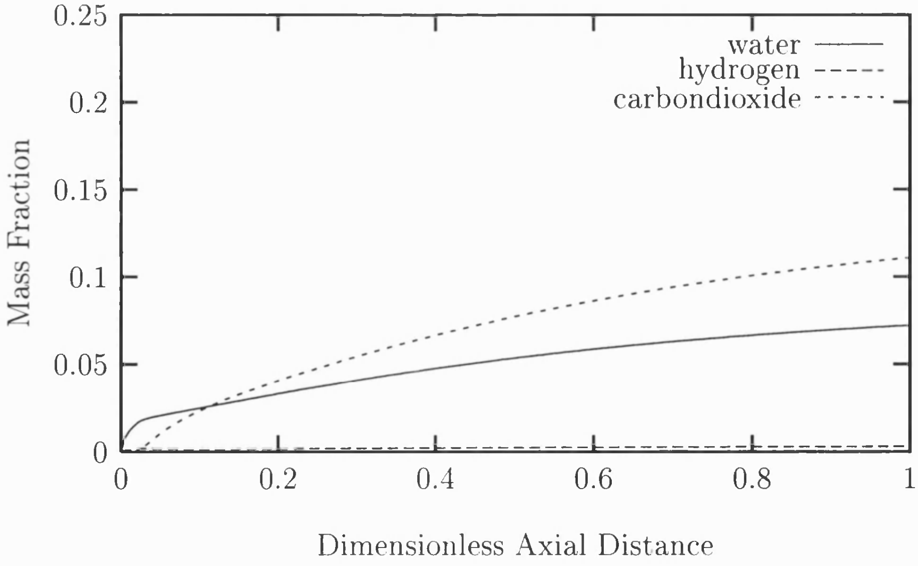

Figure 6.31: Average axial mass fraction profiles for water, hydrogen and carbon dioxide for a channel height of 2000 microns.

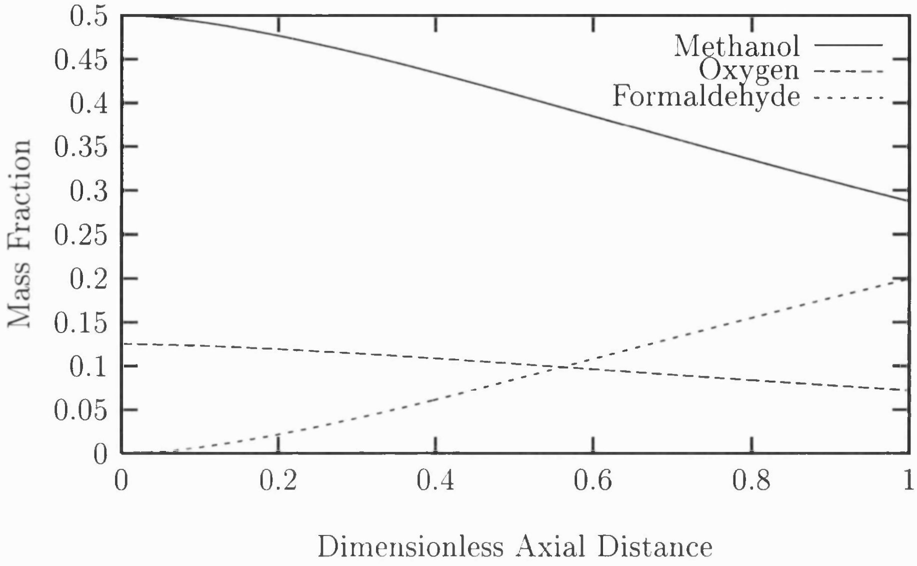

Figure 6.32: Average axial mass fraction profiles for methanol, oxygen and formaldehyde for a channel height of 2000 microns with fixed temperature wall boundary conditions ($\theta = 1.27$).

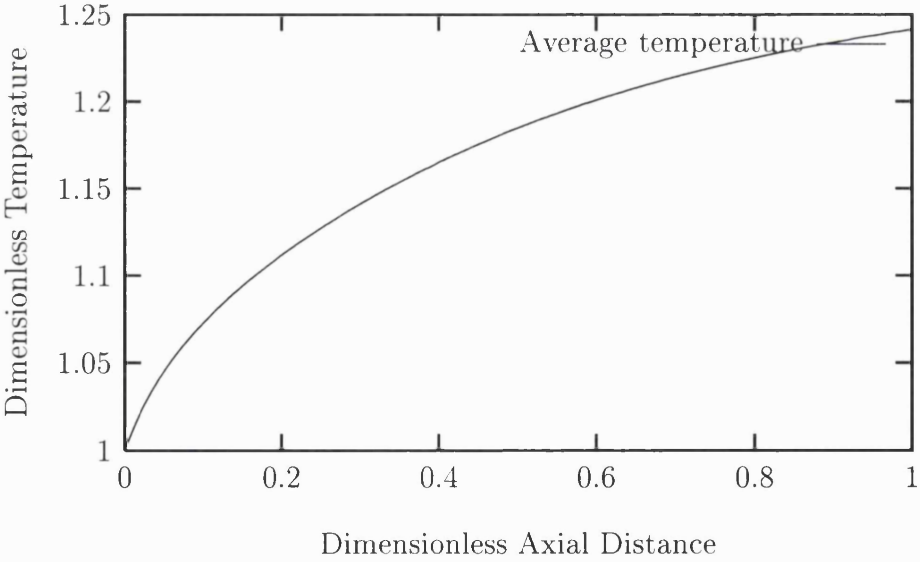

Figure 6.33: Average axial temperature profile for a channel height of 2000 microns with fixed temperature wall boundary conditions ($\theta = 1.27$).

Solid effects

In this section the effect of the solids (reactor construction materials) on reactor performance is investigated (keeping channel height constant). Two parameters could be varied, conductivity and thickness, but they are not independent. It can be seen from (6.36) that the axial second derivative is linearly multiplied by conductivity and thickness hence only the height of the solids will be altered as this is a physically more reasonable adjustable parameter. In altering the height of the solids all materials are scaled by an identical factor (with the exception of the catalyst) hence the ratio between solids is kept constant. In order to maintain a constant heat flux to the reactor the power density in the heating block is adjusted accordingly.

The effect of solids thickness has already been shown in §6.6.3 by Fig. 6.7 where it could be seen that axial conduction in the solids yields a more isothermal profile even for very low solid heights. Such effects are expected to be augmented when reaction occurs and Fig. 6.34 shows the average axial dimensionless temperature profiles for different solid heights. Figure 6.34 shows the general trend that as the thickness of the solids is reduced then there is a departure from isothermality in the reactor and a sharp axial temperature gradient (hot spot) occurs near the inlet and the temperature is lower at the outlet. Such effects can be attributed to ignition of the reaction near the inlet as heat cannot be conducted away by the solids easily but only by convection of the flowing reacting gas (which has a lower heat capacity). At very low solid thickness heat transfer downstream is due to natural convection and power by the heating block. Natural convection initially dominates the process but eventually both transport mechanisms reach equilibrium; hence the gas is not cooled to the ambient temperature. As the thickness of the solids is increased then a greater amount of heat can be conducted through the boundary solids (higher degree of isothermality). This is shown in the plot by reduced axial gradients and higher exit temperatures. It should be noted that increasing the thickness of solids much above the base case simulation had little effect on the axial temperature profiles, this can be seen in Fig. 6.34 and is reflected in the axial mass fraction profiles of methanol and formaldehyde, shown in Figs. 6.35 and 6.36 respectively. The mass fraction profiles show initial axial gradients as expected (i.e. the lower the thickness of solids the lower the axial gradient - typical for a fixed bed), however the end conversion was lower for high temperature operation. This phenomenon is attributed to the hot spot at the inlet of the reactor allowing the series reaction to proceed at a high enough rate to consume oxygen, which lowers the conversion of methanol.

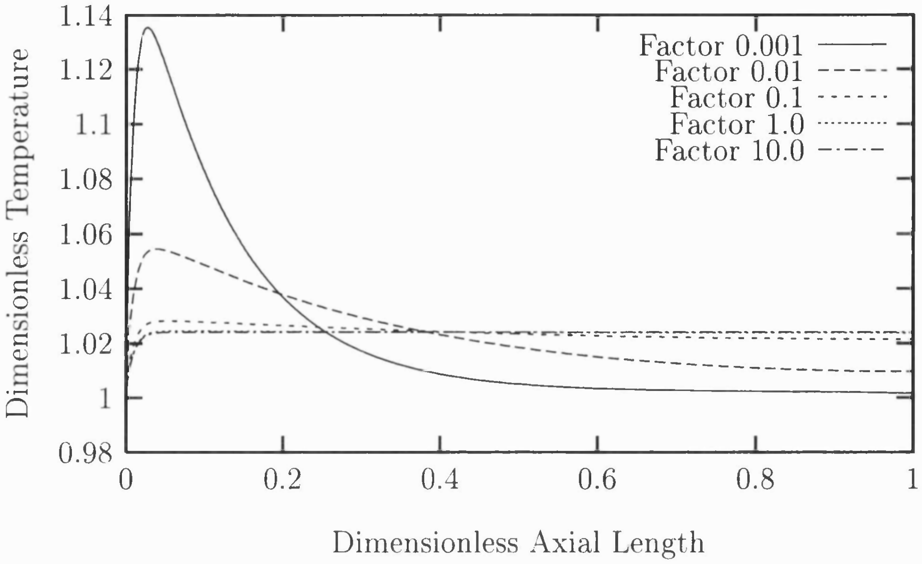

Figure 6.34: Average axial dimensionless temperature profiles for different solid heights (shown as factors of base case).

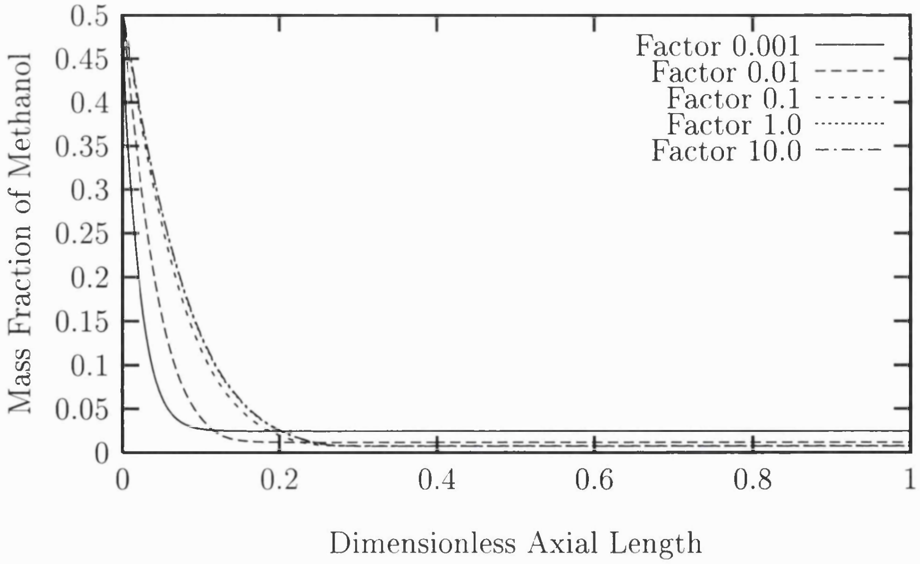

Figure 6.35: Average axial methanol mass fraction profiles for different solid heights (shown as factors of base case).

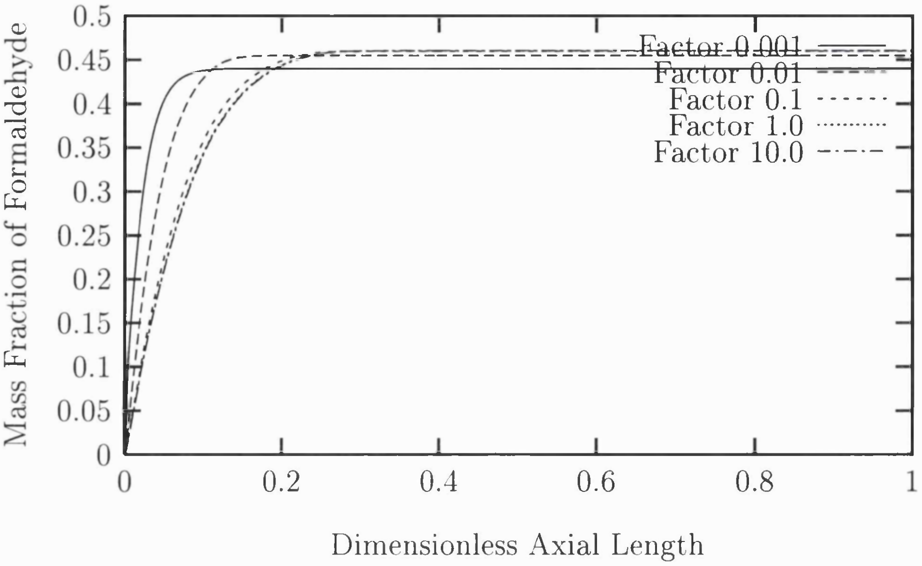

Figure 6.36: Average axial formaldehyde mass fraction profiles for different solid heights (shown as factors of base case).

6.7 Conclusions

Methanol oxidation in a catalytic wall microreactor has been shown through the use of simulations. The kinetics used are validated against a standard adiabatic PFR model with high conversion. Such kinetics are incorporated into a FDV model of the microreactor and compared under adiabatic operation. Non-reacting flow simulations were first considered for a pure oxygen feed stream, this showed that with conduction in the solid boundaries a good degree of isothermality could be achieved by careful selection of flowrate and heater power. With reaction it was shown that a high degree of isothermality can be obtained over the catalyst surface for Pe up to a value of about 4.

Operating parameters were investigated and it was found that inlet temperature had a small impact on reactor performance, whilst if an methanol-oxygen mixture was used (in contrast to methanol-air) with a too higher power density then yield of formaldehyde was reduced due to excess oxygen and high enough temperatures to overcome activation energy of the series reaction.

In addition to operating parameters being investigated of the existing reactor the design parameters were also considered. The most significant design parameter was the channel height. If the channel height was very low the heat transfer was too efficient and the reaction rate was low leading to small conversions. A transition region was shown to exist between 300 and 400 microns where depletion of reactants at the catalyst surface near the inlet exists. Above 500 microns $Pe/R \to O(1)$ and the transverse distance for methanol to diffuse becomes too great within the reactor space-time. Such arguments were clearly shown for the isothermal case in Chapter 3. In addition with an increased channel height the removal of heat is not so efficient resulting in an enhanced rate of series reaction (which gives high temperatures due to a high heat of reaction) resulting in the lowering of the yield of formaldehyde. The thickness of the solids fabricating the reactor was also investigated (this was shown to be analogous to the conductivity) and was shown to act as a thermal shunt, hence maintaining an isothermal profile. Such isothermality is reduced with a lowering of solid height, but a threshold was shown to exist above the base case parameters.

In light of the above it can be concluded that the most important combination of design and operating parameters are channel height, flowrate and heater power. These parameters are not totally independent from the results shown but a clear guideline for good reactor performance is that $Pe/R \ll 1$. Thus, this criterion apparently holds for both isothermal and highly non-isothermal reactor systems.

Operating at this scale demonstrates the high degree of isothermality that can be achieved in such exothermic systems. In addition feed composition operating bounds are relaxed to allow mixtures to be used that would be considered explosive in conventional apparatus. Along with demonstrating the reactor performance benefits a solution technique has been used that allows a large reduction in CPU time in comparison to CFD based techniques and an easier implementation of design variable variation (solid thickness etc.). The solution method employed showed an order of magnitude reduction in CPU time, memory requirements and yielded similar results.

Nomenclature

Roman symbols

Symbol	Assignment	Unit
A	pre-exponential factor	m/s
c_{pi}	specific heat capacity of species	J/mol/K
C_i	concentration	mol/m^3
D	diffusivity	m^2/s
E_a	activation energy	J/mol
F	molar flowrate	mol/s
h	heat transfer coefficient	W/m^2/K
ΔH	heat of reaction	J/mol
j	mass flux	kg/m^2/s
k/K_c	first-order reaction rate constant	1/s
k	thermal conductivity	W/m/K
k	specific reaction rate constant	mol/(s.kg_{cat}.Pa)
k	Boltzmann constant	1.38×10^{-23} J/K
L	length	m
M_f	relative molecular mass	kg/kmol
p	pressure	Pa
Q	volumetric source term	W/m^3
r/r	reaction rate (solid catalyst)	mol/(kg.s)
r_p	pore radius	m
r_{x}	reaction rate (species x)	$\mathrm{mol_x}$/(hr.min) or mol_x/(m^2s)
R	ideal gas constant (8.314)	J/mol/K
T	absolute temperature	K
T_∞	ambient temperature	K
u	axial velocity	m/s
V	volume	m^3
W	catalyst weight	kg
X	conversion	-
y	mole fraction	-

Greek symbols

Symbol	Assignment	Unit
δ	mole change per mole of reactant/catalyst thickness	-/m
ϵ	ratio of mole change in stoichiometry to total moles in feed	-
ϵ_p	void fraction	-
η	effectiveness factor	-
ν_i	stoichiometric coefficient for species i	-
ρ	density	kg/m^3
ϕ	dependent variable	-
$\emptyset$	ratio of moles entering (i) to a	-
τ	space-time	s
θ	Thiele-modulus	-
υ	transverse velocity	m/s

Subscripts

Symbol	Assignment
ch_2o	formaldehyde
co_2	carbon dioxide
cstr	continuous slurry tank reactor
eff	effectiveness factor
f	fuel
i	ideal/species index
m	methanol
o/o_2	oxygen
0	initial state
pfr	plug flow reactor
R	reference
tg	wall catalyst

Chapter 7

Multiphase Microreactors

7.1 Introduction

All reactor systems considered so far have considered single phase processes. In light of the transport characteristics identified in Chapter 3 for these systems it is a natural progression to consider multiphase systems. Experimental multiphase microreactors have already been reported previously and require accurate modelling for an optimum design.

A large number of industrial applications involve multiphase systems, and fluid flow in microchannels has been found to diverge from what is expected in classical theory (Peng et al.(1994)). In multiphase systems there is the added difficulty of how the phases are brought into contact. Research in large scale channels has shown that a variety of flow regimes can be established depending on the properties of the two fluids, the geometry of the channel and the flowrates. In microchannels the different flow patterns which can form have not been fully established yet, but initial findings in gas-liquid systems suggest regimes such as bubbly and stratified flow can exist (Stanley et al.(1997), Shaw et al.(1998)). Liquid-liquid extractors have also been used with the two phases in direct contact (Robins et al.(1997), Shaw et al.(1998)).

In order to provide a theoretical study on multiphase systems a template reaction case has to be considered; nitrobenzene reduction. The reaction and kinetics are given in §7.2. This reaction is used in two types of multiphase microreactor; a horizontal porous contact microreactor (HPCM) given in §7.3 and a micro falling film reactor (MFFR) given in §7.4. Results for the two reactors are given in §7.5 and conclusions in §7.6.

The HPCM brings the two phases together via a diffusion barrier, such as a porous wall, where the gas diffuses into the liquid phase without forming bubbles. A 2D numerical solution is obtained using a commercial CFD code.

The MFFR contains thin liquid films flowing in microchannels by gravity forces, and the study uses the analytical techniques developed in Chapter 3 to evaluate the effects of interface curvature on the reactor performance. The problem is defined in 3D and solved numerically using an explicit form of the 3D velocity profile for a Newtonian fluid.

Results for both the HPCM and MFFR are presented for various design and operating parameters and the performance benefits of each are compared.

The advantages of these two types of reactor is that the phases do not need separation after reaction, in addition the well defined contact area makes such reactors suitable for kinetic measurements.

7.2 Nitrobenzene reduction

An industrially important reaction is used to determine the behaviour of multiphase microreactors; the reduction of nitrobenzene to aniline. Aniline is an important chemical in the manufacture of dyes and antioxidants (Wisniak and Klien, 1984). The overall stoichiometric equation is

$$\mathrm{C_6H_5NO_2} + 3\mathrm{H_2} \rightarrow \mathrm{C_6H_5NH_2} + 2\mathrm{H_2O} \quad (-\Delta H = 490\mathrm{kJ/mol})\,, \tag{7.1}$$

via the intermediate stage of phenyl-hydroxylamine. A common catalyst used is 5 % Pd/C, which will be the catalyst assumed in this investigation.

The mechanism of nitrobenzene reduction is not well understood, however the reaction has been observed to be first order with respect to hydrogen and zeroth order with respect to nitrobenzene (Turek et al.1986) using a 5 % Pd/C catalyst. Turek et al.(1986) have calculated the reaction rates, based on the surface area of catalyst, and have determined the activation energy as 53, 250 J/mol. The reaction rate (mol/m^2/s) is given by

$$r = kc_{\mathrm{H_2}}, \tag{7.2}$$

where

$$k = 3.217 \times 10^6 \exp\left(-\frac{53,250}{RT}\right). \tag{7.3}$$

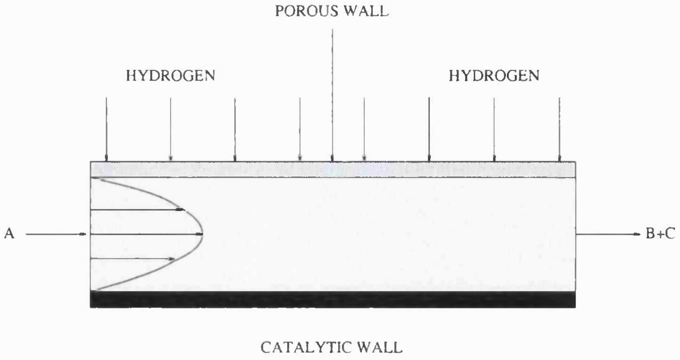

Figure 7.1: Schematic of the HPCM.

Parameter	Base Case Value
H_2 saturation concentration, c_{sat}	60 mol/m^3
Nitrobenzene inlet concentration, $c_{\text{NB}_{(\text{inlet})}}$	406.5 mol/m^3
Channel height, d	100 μm
Diffusion coefficient, D	2.8×10^{-9} m^2/s
Channel length, L	0.02 m
Reaction rate constant, k	2.5×10^{-3} m/s
Operating temperature, T	305 K
Reaction mixture velocity, U	0.01 m/s

Table 7.1: Parameters used in the base case simulation.

7.3 Horizontal porous contact microreactor (HPCM)

In this section the reduction of nitrobenzene is studied in a parallel plate reactor with separated feed using a commercial CFD code modified with FORTRAN subroutines to model the hydrogenation reaction and the diffusive hydrogen boundary condition at the upper surface of the domain. A schematic of the reactor is shown in Fig. (7.1). Parametric studies are shown in order to investigate the effect of channel height, reaction mixture velocity, diffusion coefficient and reaction rate constant on the concentration profiles and reactant conversion.

The gas and liquid phases are brought into contact through a porous diffusing wall, whilst catalyst was deposited on the opposite wall. Concentration of nitrobenzene at the inlet was 5 wt%. Density and viscosity of the reaction mixture were kept constant during the simulations and isothermality was assumed. The reactor length was set at 0.02 m and the base case parameters used are shown in Table 7.1.

7.3.1 Dimensional model

The governing equation for all species is

$$u\frac{\partial c}{\partial z} = D\left[\frac{\partial^2 c}{\partial x^2} + \frac{\partial^2 c}{\partial z^2}\right], \tag{7.4}$$

where u is the velocity profile obtained by solving the Navier-Stokes equations in Appendix C. The boundary conditions applied for nitrobenzene are

$$\begin{aligned}
c_{\mathrm{NB}}\big|_{z=0} &= c_{\mathrm{NB}_{(\mathrm{inlet})}},\\
\left.\frac{\partial c_{\mathrm{NB}}}{\partial y}\right|_{x=2Y} &= 0,\\
\left.\frac{\partial c_{\mathrm{NB}}}{\partial y}\right|_{x=0} &= 0,\\
\left.\frac{\partial c_{\mathrm{NB}}}{\partial x}\right|_{x=d} &= 0,\\
\left.\frac{\partial c_{\mathrm{NB}}}{\partial x}\right|_{x=0} &= kc_{\mathrm{H}_2}.
\end{aligned} \tag{7.5}$$

The boundary conditions for hydrogen are

$$\begin{aligned}
c_{\mathrm{H}_2}\big|_{z=0} &= 0,\\
\left.\frac{\partial c_{\mathrm{H}_2}}{\partial y}\right|_{x=2Y} &= 0,\\
\left.\frac{\partial c_{\mathrm{H}_2}}{\partial y}\right|_{x=0} &= 0,\\
c_{\mathrm{H}_2}\big|_{x=d} &= c_{\mathrm{sat}},\\
\left.\frac{\partial c_{\mathrm{H}_2}}{\partial x}\right|_{x=0} &= 3kc_{\mathrm{H}_2}.
\end{aligned} \tag{7.6}$$

The density of the reaction mixture is set at 1000 kg/m^3 and the viscosity at 4.5×10^{-5} kg/m/s.

7.4 Micro falling film reactor (MFFR)

Traditional falling film towers are typically associated with processes such as absorption, humidification and reaction. The main characteristic of this unit operation is the motion of thin layers of liquid over wetted surfaces under the action of gravity. Experimentally the MFFR has been reported to generate films as thin

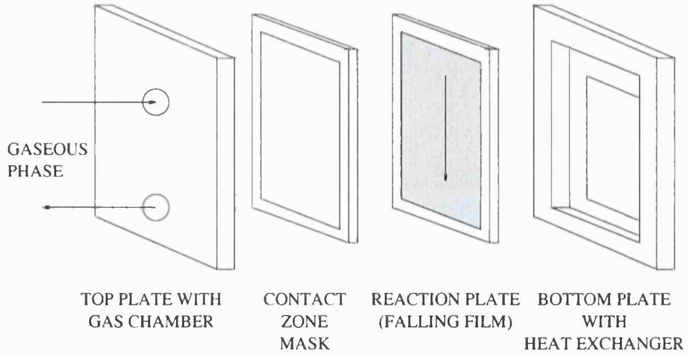

Figure 7.2: Schematic of MFFR structure.

as 25 microns, corresponding to specific interfacial areas of about 20,000 m^2/m^3, exceeding conventional apparatus by at least an order of magnitude.

The MFFR consists of a reaction plate (open channels that contain the film with catalyst on the bottom), a housing with an integrated micro heat exchanger and a transparent plate for inspection. The housing and reaction plate are made of high alloy stainless steel. The system is gas tight up to 10 bar, and the reaction plate consists of 64 channels of a width of 300 microns by a depth of 100 microns. Such an arrangement can handle liquid flows up to 50 ml/h. A schematic of the reactor construction components is shown in Fig. 7.2. The liquid reactant is distributed into many substreams at the top of the reaction plate. Each substream enters a reaction channel through a single orifice and flows downward as a film to a withdrawal zone at the bottom.

The solution domain of the MFFR differs from the HPCM in that the liquid phase is unconfined and has a curved phase interface. In the limit of low Damköhler numbers the 3D analytical solution for arbitrary geometries, developed in Chapter 3, can be applied to the hydrogen equations. This allows the effect of the shape of interface upon reactor performance to be investigated.

The dimensionless parameters (Da and S_c) required to represent nitrobenzene reduction are too high for the analytical solution to be valid, hence 3D numerical solutions are used. Conversion has been defined as

$$X = \frac{c_{\mathrm{NB}}(L) - c_{\mathrm{NB}}(0)}{c_{\mathrm{NB}}(0)} \times 100. \tag{7.7}$$

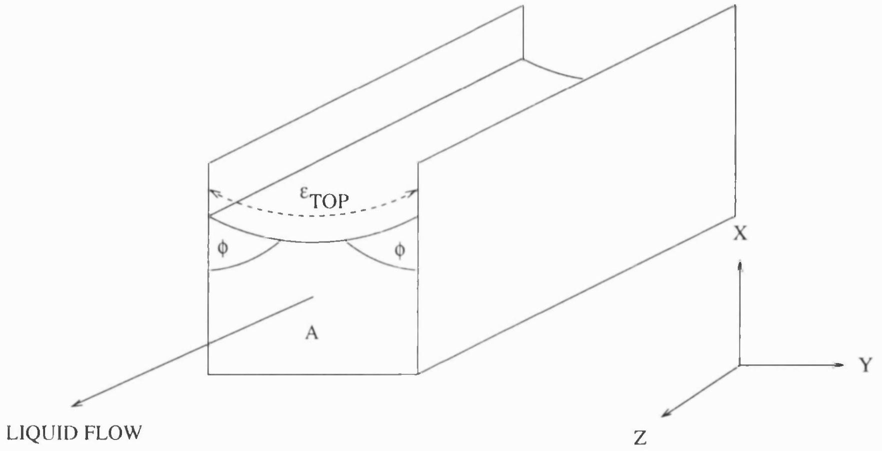

Figure 7.3: Coordinate directions in the MFFR, all dimensionless coordinates are scaled from 0 to 1.

7.4.1 Dimensionless model

To simplify the modelling and analysis only one channel is considered, in addition other modelling assumptions have been made:

- liquid film is isothermal (due to heat exchanger and high heat transfer coefficient) at 305 K,
- liquid film height is given by $\delta = \sqrt{3\mu U/\rho g}$ (Cooper et al.1934),
- mean liquid film interface/height is constant in the axial direction,
- velocity distribution is assumed to be plug (from arguments given in Chapter 3) for the analytical solution, see Table 7.3,
- physical properties are constant,
- reacting solution is dilute,
- gas phase has negligible effect on liquid hydrodynamics,
- no evaporation of liquid phase,
- mass transfer at the interface keeps liquid at the top of the reactor at its saturation limit with respect to hydrogen.

If only the liquid domain is considered then the reactor performance can be determined by the solution of the advection-diffusion equation for hydrogen; component B. From the work developed in Chapter 3 the dimensionless equation for all species can be given as

$$\frac{Pe}{R}\frac{\partial \theta}{\partial \zeta} = \frac{\partial^2 \theta}{\partial \eta^2} + \frac{\partial^2 \theta}{\partial \varepsilon^2}, \tag{7.8}$$

where

$$\zeta = \frac{z}{L} \quad \eta = \frac{x}{\delta} \quad \varepsilon = \frac{y}{2Y} \quad \theta_{\mathrm{NB}} = \frac{c_{\mathrm{NB}}}{c_{\mathrm{NB(inlet)}}} \quad \theta_{\mathrm{H_2}} = \frac{c_{\mathrm{H_2}}}{c_{\mathrm{sat}}}. \tag{7.9}$$

The boundary conditions for nitrobenzene are

$$\left.\frac{\partial \theta_{\mathrm{NB}}}{\partial \eta}\right|_{\eta=0} = 3Da\theta_{\mathrm{H_2}}\left(\frac{c_{\mathrm{sat}}}{c_{\mathrm{NB(inlet)}}}\right), \tag{7.10}$$

$$\left.\frac{\partial \theta_{\mathrm{NB}}}{\partial \eta}\right|_{\eta=1} = 0, \tag{7.11}$$

$$\left.\frac{\partial \theta_{\mathrm{NB}}}{\partial \varepsilon}\right|_{\varepsilon=0} = 0, \tag{7.12}$$

$$\left.\frac{\partial \theta_{\mathrm{NB}}}{\partial \varepsilon}\right|_{\varepsilon=1} = 0, \tag{7.13}$$

$$\theta_{\mathrm{NB}}(\zeta = 0) = 1. \tag{7.14}$$

The boundary conditions for hydrogen are

$$\left.\frac{\partial \theta_{\mathrm{H_2}}}{\partial \eta}\right|_{\eta=0} = 3Da\theta_{\mathrm{H_2}}, \tag{7.15}$$

$$\left.\frac{\partial \theta_{\mathrm{H_2}}}{\partial \varepsilon}\right|_{\varepsilon=0} = 0, \tag{7.16}$$

$$\left.\frac{\partial \theta_{\mathrm{H_2}}}{\partial \varepsilon}\right|_{\varepsilon=1} = 0, \tag{7.17}$$

$$\theta_{\mathrm{H_2}}(\eta = 1) = 1, \tag{7.18}$$

$$\theta_{\mathrm{H_2}}(\zeta = 0) = 0. \tag{7.19}$$

7.4.2 Interface curvature

The shape of the interface in the rectangular microchannel is expected to influence reactor performance. Olim (2000) has presented a simple method for determining the interface shape (Appendix G). Olim formulated the problem by considering a potential energy balance in the liquid due to body forces and surface tension at the phase interface. Such a formulation results in a second order O.D.E. with an adjustable parameter (λ). This forms a 1D minimisation problem in terms of λ where it is assumed that the shape of the interface is determined by the minimum potential energy subject to the constraint of conserving the volume of liquid.

For analytical modelling the required information needed for model closure is the liquid contact angle with the channel solid. In the paper of Olim (2000) the Bond number is an additional parameter, however at this scale surface tension forces dominate and the Bond (Bo) number is negligible.

Table 7.2 gives the interface curvature information for several contact angles of liquid with the solid wall. The cross sectional arc length of the interface is given (ε_{top}) and the area underneath the interface is integrated to ensure that liquid volume is conserved.

Angle (rad) ϕ	Angle (deg) ϕ	ε_{top}	A
0.349	20.0	5.21	1.0
0.698	40.0	3.83	1.0
1.047	60.0	2.45	1.0
1.396	80.0	1.27	1.0
1.570	90.0	1.0	1.0

Table 7.2: Table of interface lengths and flow areas for different contact angles, ε_{top} and A are dimensionless.

7.4.3 Analytical solution at low fluxes

From Chapter 3 the equations are integrated over the cross section of the liquid domain. Equation 7.18 has been replaced by

$$\frac{\partial \theta_{\mathrm{H}_2}}{\partial \eta} = S_c(1 - \theta_{\mathrm{H}_2}), \qquad (7.20)$$

to allow a Dirichlet condition to be applied in the analytical solution. If the value assigned to the source coefficient, S_c, represents a timescale larger than Da an effective Dirichlet condition of 1 will be applied at the interface surface.

$$\begin{aligned}\frac{Pe}{R}\frac{\partial\overline{\theta_{\mathrm{H}_2}}}{\partial\zeta} &= \int\int_A \frac{\partial^2\theta_{\mathrm{H}_2}}{\partial\eta^2} = -\oint \frac{\partial\theta_{\mathrm{H}_2}}{\partial\eta}\mathrm{d}S, &(7.21)\\ &= -3Da\overline{\theta_{\mathrm{H}_2}} + S_c(1-\overline{\theta_{\mathrm{H}_2}})\varepsilon_{\mathrm{top}}. &(7.22)\end{aligned}$$

Equation 7.22 can be rewritten as

$$\frac{\partial\overline{\theta_{\mathrm{H}_2}}}{\partial\zeta} + B\overline{\theta_{\mathrm{H}_2}} = C, \tag{7.23}$$

where

$$B = (3Da + S_c\varepsilon_{\mathrm{top}})\frac{R}{Pe}, \qquad C = S_c\varepsilon_{\mathrm{top}}\frac{R}{Pe}. \tag{7.24}$$

The solution of (7.23) requires the use of an integrating factor, viz.

$$\exp^{\int B\mathrm{d}\zeta} = \exp^{B\zeta}, \tag{7.25}$$

therefore

$$\begin{aligned}\exp^{B\zeta}\frac{\mathrm{d}\overline{\theta_{\mathrm{H}_2}}}{\mathrm{d}\zeta} + B\overline{\theta_{\mathrm{H}_2}}\exp^{B\zeta} &= C\exp^{B\zeta}, &(7.26)\\ \frac{\mathrm{d}}{\mathrm{d}\zeta}\left(\overline{\theta_{\mathrm{H}_2}}\exp^{B\zeta}\right) &= C\exp^{B\zeta}. &(7.27)\end{aligned}$$

Integrating both sides with respect to ζ gives (where D is an integration constant)

$$\begin{aligned}\overline{\theta_{\mathrm{H}_2}}\exp^{B\zeta} &= \frac{C\exp^{B\zeta}}{B} + D, &(7.28)\\ \overline{\theta_{\mathrm{H}_2}}(\zeta) &= \frac{C}{B} + D\exp^{-B\zeta}. &(7.29)\end{aligned}$$

Using the axial initial condition for θ_b gives

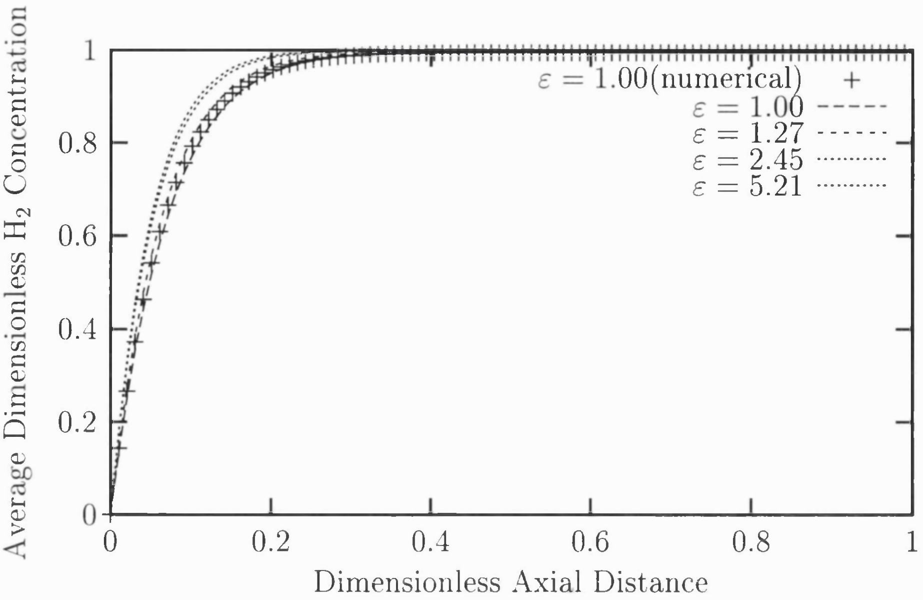

Figure 7.4: Axial profiles of mean hydrogen concentration in the reactor for different cross sectional interface lengths, $Pe/R = 0.1$ and $Da = 0.01$, $Pe = 50$, $R = 500$, $S_c = 2.5$.

$$D = -\frac{C}{B}, \tag{7.30}$$

therefore the final expression for the mean concentration of hydrogen in the reactor is

$$\overline{\theta_{\mathrm{H}_2}} = \left(\frac{S_c\varepsilon_{\mathrm{top}}}{Da + S_c\varepsilon_{\mathrm{top}}}\right) - \left(\frac{S_c\varepsilon_{\mathrm{top}}}{Da + S_c\varepsilon_{\mathrm{top}}}\right)\exp\left(-\left(Da + S_c\varepsilon_{\mathrm{top}}\right)(R/Pe)\zeta\right). \tag{7.31}$$

From (7.31) it can be seen that as S_c becomes large, and S_c/Da is large (necessary for an effective Dirichlet condition of hydrogen at the top surface), the reactor will saturate with hydrogen an $\varepsilon_{\mathrm{top}}$ will have little effect. Knowing that the interface curvature has little effect on reactor performance allows the numerical simulations to be simplified by using a Cartesian grid (which will be used for the MFFR simulations). Figure 7.4 shows a comparison with numerical data (using a Dirichlet condition for hydrogen at the top surface) for the different interface lengths as given in Table 7.2. It can be seen that the effect of the interface curvature is small and that the analytical result is in good agreement with the numerical simulation.

7.4.4 Numerical modelling

An analytical solution is available for the velocity profile in a 3D duct with a free slip boundary applied to a flat phase interface (H.4). This is incorporated into a numerical solution of the governing advection-diffusion P.D.E. for hydrogen. The derivation is shown in Appendix H.

The MFFR has been solved in dimensionless form and the values assigned to the dimensionless groups in the base case have been chosen to reflect the conditions in the base case of the HPCM to allow a direct comparison to be made. Table 7.3 gives base values of the dimensionless parameters. The numerical solution is obtained by a parabolic solver of similar type to that used in Chapter 3. Tables 7.4 to 7.6 show the effects of the design and operating parameters on the dimensionless variables that are used in the numerical simulations.

Variable/group	Value
D	2.8×10^{-9} m^2/s
k	2.5×10^{-3} m/s
L	0.02 m
U	0.01 m/s
Da	33.3
Pe	133.2
R	536.2
δ	37.3×10^{-6} m
μ	4.5×10^{-5} kg/m/s
ρ	1000 kg/m^3

Table 7.3: Table of base parameters and dimensionless groups for the MFFR, note that $Pe/R < 1$.

Mixture Velocity	Pe	R	Da	δ
0.001 m/s	4.22	1694.17	10.54	11.80 μm
0.005 m/s	47.14	757.66	23.57	26.40 μm
0.01 m/s	133.33	535.74	33.33	37.30 μm
0.015 m/s	244.94	437.43	40.82	45.70 μm
0.02 m/s	377.10	378.83	47.14	52.80 μm

Table 7.4: Table of dimensionless groups for the MFFR for varying mixture velocity.

7.5 HPCM and MFFR results

The HPCM model was solved using a commercial CFD code, where the Navier-Stokes equations are solved. From these results the pressure drop was found to vary

Diffusivity	Pe	Da
1×10^{-9} m^2/s	373.31	93.33
3×10^{-9} m^2/s	124.48	31.11
5×10^{-9} m^2/s	74.66	18.66
8×10^{-9} m^2/s	46.66	11.67
10×10^{-9} m^2/s	37.33	9.33

Table 7.5: Table of dimensionless groups for the MFFR for varying diffusivity.

Reaction Rate Constant	Da
0.001 m/s	13.33
0.002 m/s	26.67
0.004 m/s	53.33
0.007 m/s	93.33
0.01 m/s	133.33

Table 7.6: Table of dimensionless groups for the MFFR for varying reaction rate constant.

from 70 to 70,000 Pa. Also, unlike the MFFR model, the results for the full domain can be obtained (not just the averages) and the aniline species field is shown in Figs. 7.5 and 7.6 to give an appreciation of the transverse gradients.

Figure 7.5 is for the base case whilst Fig. 7.6 is for the same case but with decreased reaction mixture velocity. It is observed (as expected) that in the base case the reaction starts significantly further downstream, and a large volume fraction is occupied by unreacted solution. For a lower velocity the reaction starts almost next to the inlet of the reaction channel and transverse gradients of the product are less steep, indicating effective utilisation of the reactor volume.

Figures 7.7 to 7.10 show the effect of different parameters on the conversion of nitrobenzene in the HPCM and MFFR, note that the reactor lengths are equal to allow a direct comparison to be made.

Figure 7.7 shows the effect of channel/film height on reactant conversion. It can be seen that the reactant conversion decreases monotonically with channel/film

Figure 7.5: Mass fraction profile of aniline for the base case simulation (not to scale).

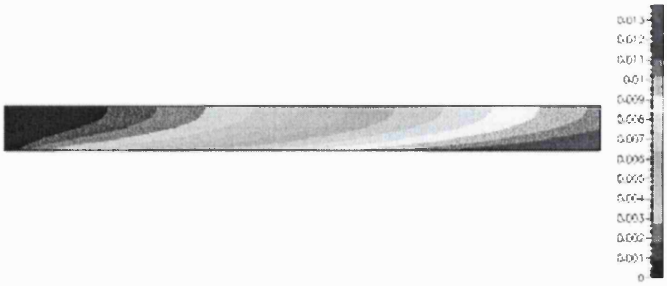

Figure 7.6: Mass fraction profile of aniline for a reaction mixture velocity of 1×10^{-3} m/s (not to scale).

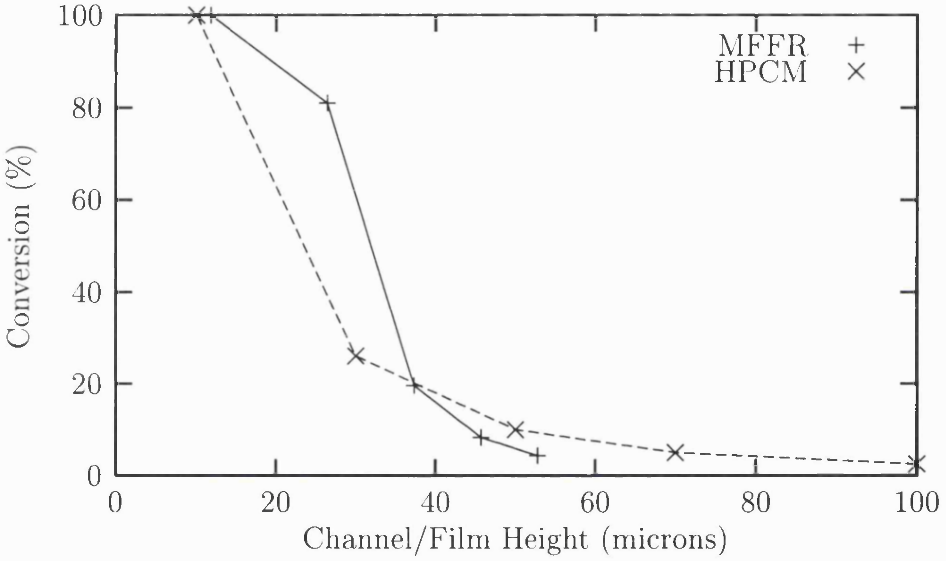

Figure 7.7: Effect of channel height on conversion.

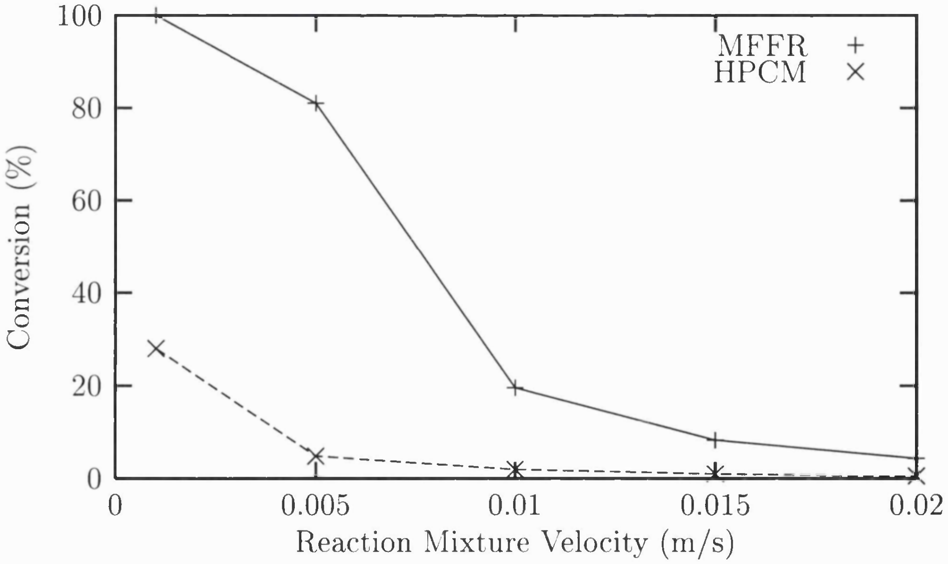

Figure 7.8: Effect of reaction mixture velocity on conversion.

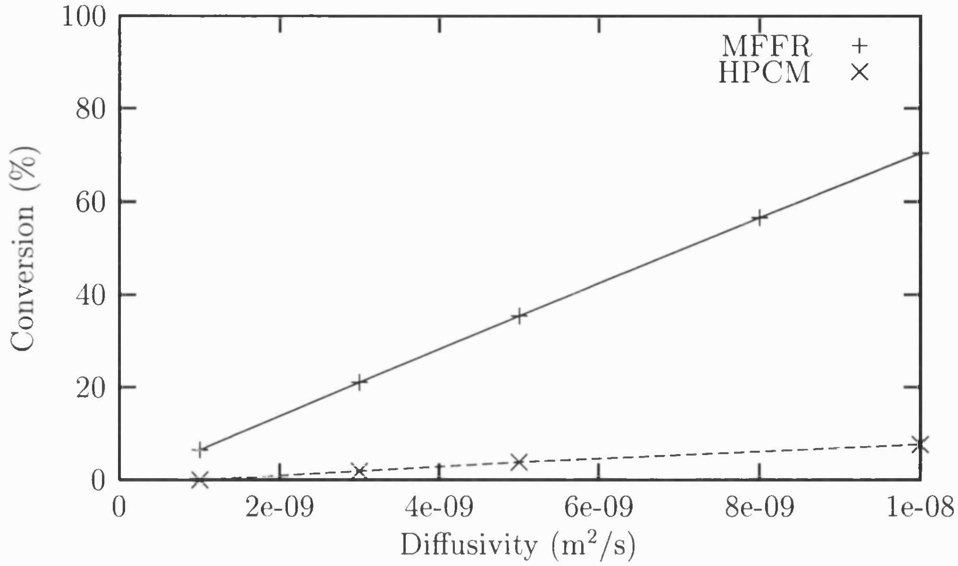

Figure 7.9: Effect of the diffusivity on conversion, phyisically varied by choice of solvent.

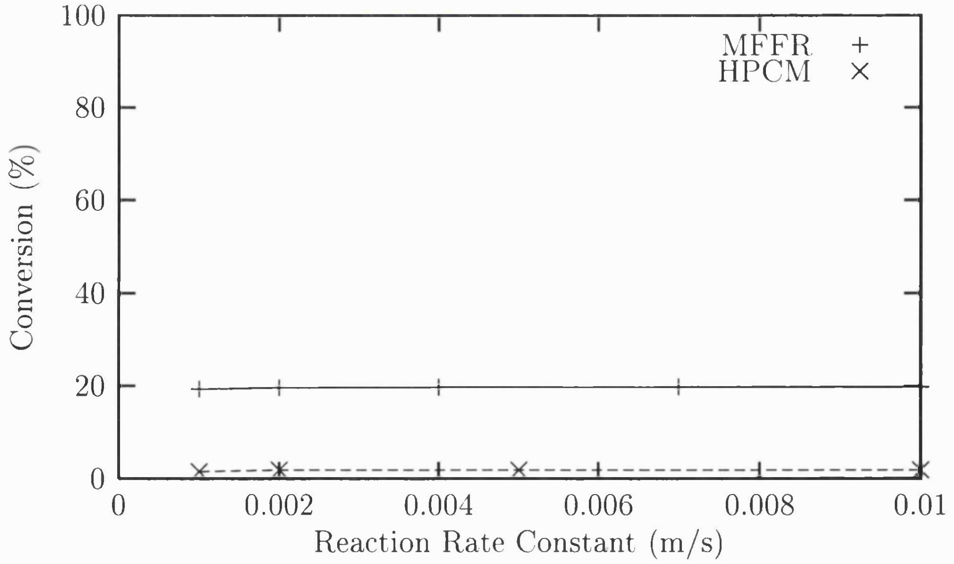

Figure 7.10: Effect of reaction rate constant on conversion.

height. If the results from the HPCM are compared with the MFFR then it can be seen that under identical operating conditions (channel/film height of 37.3 microns and a mixture velocity of 0.01 m/s) the reactant conversions are near identical. Thus, the velocity profiles (corresponding to different reactor types) have little effect on nitrobenzene conversion; an identical observation to the single phase reactor in Chapter 3. In Fig. 7.7 it can be seen that below a channel/film height of roughly 40 microns the MFFR performs better than the HPCM due to a higher residence time. Above 40 microns the conversion in the two reactors becomes similar (as film thickness becomes comparable to channel height), although the MFFR has a shorter residence time (due to the variation of film thickness with velocity) and the choice between the two designs can be made based on desired total flowrate, pressure drop and residence time.

Figure 7.8 shows the effect of reaction mixture velocity on conversion. The conversion decreases monotonically with increasing flowrate for both reactors (corresponding to a decrease in residence time). In the HPCM residence times above 10 s are required to achieve conversion above 20 % (Fig. 7.8). It is worth noting that higher residence times are also accomplished by lower pressure drops. For example, a 4 s residence time (4.5 % conversion) results in a 356 Pa pressure drop, whilst for a 20 s residence time (30 % conversion) the pressure drop was 71 Pa. Unlike the HPCM, the transverse distance for hydrogen to diffuse in the MFFR increases with reaction mixture velocity, and the film thickness ranges from 11.8 to 52.8 microns. Due to the low transverse distance in the MFFR the conversion is higher than the HPCM. The performance of the two reactors becomes comparable at higher velocities as the film thickness in the MFFR approaches the channel height in the HPCM. At relatively low residence times the HPCM will provide a bound of the transverse diffusional distance, in this case 100 microns. The film thickness in the MFFR will rise above this value for velocities greater than 0.072 m/s. Thus, a threshold residence time will exist for the MFFR, where below this value the HPCM will give better performance due to the bounds imposed for the diffusional distance for hydrogen.

Conversion increases almost linearly with the diffusivity (a reduction of the Peclet number), indicating that the mass transfer of dissolved hydrogen is the limiting step (Fig. 7.9). This is corroborated by Fig. 7.10 which shows that at a higher reaction rate constant, which could be physically achieved by a higher catalyst loading, does not have a significant effect on conversion.

From the results shown the differences between the reactors are small, despite differing physical designs. Both reactors have different velocity profiles, but as $Pe/R < 1$ this had negligible impact on reactor performance. The HPCM has a fixed transverse distance, but for a given residence time the MFFR should be made as short as possible to give a low film thickness.

7.6 Conclusions

This chapter has considered two types of multiphase microreactor and the results demonstrate that both the HPCM and MFFR are suitable candidates for nitrobenzene reduction.

A 2D CFD solution was used for the HPCM and a 3D dimensionless solution was used for the MFFR. An explicit form of the velocity profile was used in the MFFR simulations and as a result the CPU time was an order of magnitude lower than the HPCM. The CFD code solved additionally for the axial diffusion term. Under identical operating conditions (for a channel/film height of 37.3 microns) its effect on reactor performance is negligible. This is expected as in all the MFFR simulations $Pe/R < 1$. The effects of interface curvature were also investigated and deemed to have little effect on reactor performance allowing the MFFR to be solved on a Cartesian grid.

Channel/film height was shown to be a dominant design parameter and results from both reactors show that at this scale the reaction is still mass transfer limited. The MFFR has less diffusional distance to the catalyst for lower velocities and a lower pressure drop, due to less shear stress at the phase interface. However, the HPCM may be better suited to operations where the residence time needs to be kept low, as a physical bound is imposed on the transverse distance (film thickness increases with reaction mixture velocity in the MFFR), but with the offset of increased pressure drop.

Both reactors operate in the mass transfer limited regime, and the liquid phase needs to have a high degree of hydrogen saturation for high conversion. Conventional reactors, such as a bubble column or CSTR, could only achieve such saturation in the film around the bubble, resulting in a large unsaturated liquid bulk. The choice between a traditional falling film reactor and multiphase microreactors would be determined by the optimum residence time.

Nomenclature

Symbol	Assignment	Unit
A	cross-sectional liquid area	m^2
Bo	Bond number ($\rho g Y^2/\sigma$)	-
c	concentration	mol/m^3
c_{sat}	saturation concentration of hydrogen	mol/m^3
d	channel height	m
D	molecular diffusivity	m^2/s
Da	Damköhler number (kh/D)	-
g	acceleration due to gravity	m/s^2
h	channel height	m
k	first order rate constant	m/s
k_{la}	liquid film interphase mass transfer coefficient	m/s
L	channel length	m
Pe	Peclet number (Uh/D)	-
r	reaction rate	$mol/m^2/s$
R	aspect ratio (L/h)	-
S	interface arc length	m
S_c	source coefficient	-
U	mean liquid velocity	m/s
X	conversion	-
Y	half width of channel	m
δ	mean film height	m
η	dimensionless transverse coordinate	-
ε	dimensionless transverse coordinate	-
ε_{top}	dimensionless arc length of phase interface	-
ρ	density	kg/m^3
μ	viscosity	kg/m/s
ϕ	liquid contact angle	deg/rad
σ	surface tension	N/m
θ	dimensionless concentration	-

Chapter 8

Conclusions

8.1 Main contributions of this thesis

In this thesis the modelling and design of microengineered reactors (commonly termed microreactors) has been theoretically investigated. At this small scale the transport of energy and mass were investigated in a fundamental manner to yield the dominant design and operating parameters for relatively simple cases through a combination of analytical and numerical techniques.

The understanding and techniques developed were then applied to rigorous simulations of more complex systems. These included a microfluidic T-mixer, a catalytic methanol oxidation reactor and two multiphase microreactors for nitrobenzene reduction.

The aim of the thesis is to develop some design and modelling tools that allow a conceptual insight into the design and rapid prototyping of microreactors, these were the closed form expressions in Chapters 3 and 4, and their application to show high reactor performance. The conclusions of the work can be categorised into two main areas:

Modelling tools for efficient simulation

- The advection-diffusion equation, which describes the transport of energy and mass in a microreactor, reduces to a single eigenvalue problem.
- Concentration profiles are essentially not affected by the velocity profile if $1 \ll Pe \ll R$. This result also applies for reactors with non-linear kinetics, non-isothermal systems and reactors of arbitrary duct shape.
- If $1 \ll Pe \ll R$ the heterogeneous reactor can be modelled as a homogeneous reactor due to small transverse timescales.

- The effect of interface curvature on reactor performance is small in multiphase systems due to the small transverse timescales in microreactors.

Design of mixers and reactors

- The mixing characteristics of T-type micromixers have been shown for gases of different viscosity where the mixing length showed a weak nonmonotonic dependence on aspect ratio of the channel (for a constant channel width). The angle between the inlet channels has little effect on the mixing length or pressure drop. Mixing length could be further reduced by using throttle mixers at the expense of a higher pressure drop.

- The design and operating parameters of a catalytic methanol oxidation reactor were investigated. The inlet temperature had a small impact on reactor performance due to the conducting walls acting as a thermal shunt, maintaining a high degree of isothermality and reducing thermal stress. The most significant design parameter was shown to be the channel height. If the channel height was very low then the reaction mixture would be rapidly quenched due to natural convection, resulting in small conversions due to a low reaction rate. If the channel height was too high there would be depletion of reactants at the catalyst surface and less heat transfer, reducing the amount of desired series intermediate formed.

- Large transverse temperature gradients exist in non-isothermal systems (methanol oxidation), this is in contrast to transverse species gradients. This is due to different energy fluxes on the domain boundaries caused by different thicknesses and conductivities of wall solids, volumetric heat sources and natural convection processes.

- Sharp axial temperature gradients are observed at the inlet of non-isothermal microreactors (methanol oxidation). This is attributed to backward axial heat transmission in the reactor walls. It can be stated that a high degree of isothermality in the reactor has the offset of a sharp temperature gradient at the reactor inlet. Such an operating characteristic must be considered when looking at reactor fabrication materials due to thermal stresses.

- Multiphase microreactors were used for nitrobenzene reduction. Two types of reactor were employed that had different 1D velocity fields. At the same channel/film height and residence time the results of the two reactors were very close. This further corroborated the weak dependence of velocity profiles on reactor performance if $1 \ll Pe \ll R$.

8.2 Suggestions for further work

The thesis has presented analytical tools that allow a conceptual insight into design and operating parameter choice for microreactors, rather than large numbers of parametric simulation studies that may yield a subjective rather than objective interpretation. However the analytical models have their limitations and must be seen to aid in rapid prototyping. More accurate simulation models are needed in microreactors where the flow may not be one dimensional. Such models should be coupled to suitable optimisation algorithms to give an optimum design of the unit operation.

The thesis has concentrated on single unit operations. A wider approach should be developed that allows design rules and models to be developed for the complete plant to aid in an economic study that will allow microreactors to firmly be seen as a viable alternative in industrial process development.

Bibliography

[1] Allen J. A. (1964). The Reaction of Methanol Vapour with Silver Oxide. *Aust. J. Chem.*, 17, 529.

[2] Allen R. (1999). Scale out manufacturing technology. *iAc Foresight Workshop*, June, 1999.

[3] Apelblat A. (1982). Mass transfer with chemical reaction of the first order. Effect of axial diffusion. *Chem. Eng. J.*, 23, 193.

[4] Arkilic E. B. and Breuer K. S. (1994). Gaseous flow in microchannels. *ASME*, 197, 57.

[5] Arkilic E. B., Schmidt M. A. and Breuer K. S. (1997). Gaseous slip flow in long microchannels. *Journal of Micromechanical Systems*, 6, 167.

[6] Atkins P. W. (1986). *Physical Chemistry.* 3rd Ed., Oxford University Press, Oxford.

[7] Bailey D. K., Ameel T. A., Warrington R. O. and Savoie T. I. (1995). IECEC Paper no. ES-396, *ASME*, 301.

[8] Balakotaiah V., Gupta N. and West D. H. (2000). A simplified model for analyzing catalytic reactions in short monoliths. *Chem. Engng. Sci.*, 55, 5367.

[9] Baron T., Manning W. R. and Johnstone H. F. (1952). Reaction kinetics in a tubular reactor. *Chem. Eng. Prog.*, 48, 127.

[10] Batchelor G. K. (1967). *An Introduction to Fluid Mechanics.* Cambridge University Press, Cambridge.

[11] Bennett, C.J., Kolaczkowski, S.T. and Thomas, W.J. (1991). Determination of heterogeneous reaction-kinetics and reaction-rates under mass-transfer controlled conditions for a monolith reactor. *Trans. I.Chem.E.*, 69, Part B, 209.

[12] Benson R.S. and Ponton J. W. (1993). Process miniaturisation - a route to total environmental acceptability. *Chem. Eng. Res. Des.*, 71, 160.

[13] Beskok A. and Karniadakis G. E. (1999). A model for flows in channels, pipes, and ducts at micro and nano scales. *Microscale Thermophysical Engineering*, 3, 43.

[14] Bessoth F. G., deMello A. J. and Manz A. (1999). Microstructure for Efficient Continuous Flow Mixing. *Anal. Commun.*, 36, 213.

[15] Bhattacharyya S. K., Nag N. K. and Ganguly N.D. (1971). Kinetics of Vapor-Phase Oxidation of Methanol on Reduced Silver Catalyst. *Journal of Catalysis*, 23, 158.

[16] Bibby I. P., Harper M. J. and Shaw J. (1998). Design and optimization of microfluidic reactors through CFD and analytical modelling. *Proc. 2nd Int. Conf. Of Microreaction Technology (New Orleans)*, 335.

[17] Bird R. B., Stewart W. E. and Lightfoot E. N. (1960). *Transport Phenomena.* Wiley, New York.

[18] Bökenkamp D., Desai A., Yang X., Tai Y., Marzluff E. M. and Mayo S. L. (1998). Microfabricated Silicon Mixers for SubMillisecond Quench-Flow Analysis. *Anal. Chem.*, 70, 232.

[19] Böhnke F. (1999). Fluid-structure coupling in the inner ear. Design of microchannels for biomedical sensors. *Proc. 2nd Workshop Int. Des. Sim. Tools Micro and Biomedical Fluidic Apps.*

[20] Branebjerg J., Gravesen P., Krog J. P. and Nielsen C. R. (1996). Fast mixing by lamination. *Proc. IEEE-MEMS*, 441.

[21] Burns J. R., Ramshaw C. and Harston P. (1998). *Proc. 2nd Int. Conf. of Microreaction Technology (New Orleans)*, 39.

[22] Burns J. R. and Ramshaw C. (1999). Development of a microreactor for chemical production. *Trans. I.Chem.E.*, 77(A), 206.

[23] Burns J. R. and Ramshaw C. (2000). A microreactor for the nitration of benzene and toluene. *Proc. 4th Int. Conf. Of Microreaction Technology (Atlanta)* 133.

[24] Carnahan B., Luther H. A. and Wilkes J. O. (1969). *Applied Numerical Methods.* Wiley, New York.

[25] CFDRC (1998). CFD-ACE 5 Theory manual.

[26] Chauvel A. R., Courty P. R., Maux R. and Petitpas C. (1973). Select Best Formaldehyde Catalyst. *Hydrocarbon Processing*, 179.

[27] Choi S. B., Barron R. F. and Warrington R. O. (1991). Fluid flow and heat transfer in microtubes. *ASME Microchemical Sensors, Actuators and Systems*, 32, 123.

[28] Chopey N. P., Ondrey G. and Parkinson G. (1998). *Chemical Engineering (March)*, 30.

[29] Christoffel E. G. (1982). Laboratory reactors and heterogeneous catalytic processes. *Catal. rev.*, 24, 159.

[30] Cleland F. A. and Wilhelm R. H. (1956). Diffusion and reaction in viscous-flow tubular reactor. *A.I.Ch.E. J.*, 2, 489.

[31] Colton C. K., Smith K. A., Stroeve P. and Merill E. W. (1971). Laminar flow mass transfer in a flat duct with permeable walls. *A.I.Ch.E. J.*, 17, 773.

[32] Concordia J. J. (1990). Batch catalytic gas/liquid reactions: types and performance characteristics. *Chem. Eng. Prog.*, March, 50.

[33] Cooper C. M., Drew T. B. and McAdams W. H. (1934). Isothermal flow of liquid layers. *Ind. Eng. Chem.*, 26, 428.

[34] Coppage J. E. and London A. L. (1956). Heat transfer and flow friction characteristics of porous media. *Chem. Eng. Prog.*, 52, 57F.

[35] Coulson J. M., Richardson J. F., Backhurst J. R. and Harker J. H. (1993). *Chemical Engineering*, vol. 1, Pergamon, Oxford.

[36] Cybulski, A., Stankiewicz, A., Edvinsson, A. and Moulijn, J.A. (1999). Monolithic Reactors for Fine Chemicals Industries: A Comparative Analysis of a Monolithic Reactor and a Mechanically Agitated Slurry Reactor. *Chem. Engng. Sci.*, 54, 1999, 2351.

[37] Dang V. D. and Steinberg M. (1980). Convective diffusion with homogeneous and heterogeneous reactions in a tube. *J. Phys. Chem.*, 84, 214.

[38] Dang V. D. (1983). Steady-state mass transfer with homogenous and heterogeneous reactions. *A.I.Ch.E. J.*, 29, 19.

[39] Dang V. D. (1984). Diffusive transport with consecutive catalytic wall reactions. *Chem. Engng. Sci.*, 39, 1723.

[40] Daubert T. E. and Danner R. P. (1985). Data compilation tables of properties of pure compounds. *A.I.Ch.E.*, Hemishere Publishing.

[41] Deen W. M. (1998). *Analysis of Transport Phenomena*, 1st Ed., Oxford University Press, Oxford.

[42] Denbigh K. G. (1951). The kinetics of continuous reaction processes: application to polymerization. *J. Appl. Chem.*, 1, 227.

[43] De Wachter D., Eloot S. and Verdonck P. (1999). Artificial kidney modelling. Design of microchannels for biomedical sensors. *Proc. 2nd Workshop Int. Des. Sim. Tools Micro and Biomedical Fluidic Apps.*.

[44] Ehrfeld W., Golbig K., Hessel V., Löwe H. and Richter T. (1999). Characterization of Mixing in Micromixers by a Test Reaction: Single Mixing Units. *Ind. Eng. Chem. Res.*, 38, 1075.

[45] Edvinsson R. K. and Cybulski A. (1995). A comparison between the monolithic reactor and the trickle bed reactor for liquid-phase hydrogenations. *Catalysis Today*, 24, 173.

[46] Dirix C. and van der Wiele K. (1990). Mass transfer in jet loop reactors. *Chem. Engng. Sci.*, 45, 2333.

[47] Ehrfeld W., Hessel V., Löwe, H. (2000). *Microreactors: New technology for modern chemistry.* 17-26, Wiley-VCH, Weinheim.

[48] European Chemist (1999). January, 17.

[49] Ernst H., Jachimowicz A., Jobst G., Moser I. and Urban G. (1999). Design of microchannels for biomedical sensors. *Proc. 2nd Workshop Int. Des. Sim. Tools Micro and Biomedical Fluidic Apps..*

[50] Fogler H. S. (1992). *Elements of Chemical Reaction Engineering.* 2nd Ed., Prentice Hall, London.

[51] Franz A. J., Quiram D., Srinivasan R., Hsing I-M, Firebaugh S. L., Jensen K. F. and Schmidt M. A. (1998). New operating regimes and applications feasible with microreactors. *Proc. 2nd Int. Conf. of Microreaction Technology (New Orleans)*, 33.

[52] Froment G. F. and Bischoff K. B. (1990). *Chemical Reactor Analysis and Design.* Wiley, New York.

[53] Gad-el-Hak M. (1999). The fluid mechanics of microdevices - The Freeman Scholar Lecture. *Journal of Fluids Engineering-Transactions of the ASME*, 121, 5.

[54] Gobina, E., Hou, K. and Hughes, R. (1995). Ethane dehydrogenation in a catalytic membrane reactor coupled with a reactive sweep gas. *Chem. Engng. Sci.*, 50, 2311.

[55] Gravesen P., Branebjerg J. and Jensen O. S. (1993). Microfluidics - a review. *J. Micromech. Microeng.*, 3, 168.

[56] Green A., Johnson B. and John A. (1999). Process intensification magnifies profits. *Chemical Engineer*, December, 66.

[57] Groppi G., Belloli A., Tronconi E. and Forzatti P. (1995). Analysis of Multidimensional Models of Monolith Catalysts for Hybrid Combustors. *A.I.Ch.E. J.*, 41, 2250.

[58] Harley J. C., Huang Y. F., Bau H. H. and Zemel J. N. (1995). Gas flow in micro-channels. *Journal of Fluid Mechanics*, 284, 257.

[59] Harre K. (1998). Microreactors. mpip-mainz.mpg.de/documents/projects98/F6.html.

[60] Haughey D. T. and Beveridge S. G. (1969). *Can. J. Chemeng.*, 47, 130.

[61] Hayes R. E. and Kolackzowski S. T. (1994). Mass and heat transfer effects in catalytic monolith reactors. *Chem. Engng. Sci.*, 49, 3587.

[62] Heck R. H. and Katzer J. R. (1976). Mathematical modeling of monolithic catalysts. *A.I.Ch.E.J.*, 22, 477.

[63] Held T. J. and Dryer F. L. (1998). A Comprehensive Mechanism for Methanol Oxidation. *Int. J. Chem. Kinet.*, 30, 805.

[64] Hessel V., Ehrfeld W., Golbig K., Haverkamp V. Löwe H. and Richter Th. (1998). Gas/liquid dispersion processes in micromixers: the hexagon flow. *Proc. 2nd Int. Conf. of Microreaction Technology*, 259.

[65] Hessel V., Ehrfeld W., Golbig K., Hofmann C., Jungwirth S., Löwe H., Richter T., Storz M., Wolf A., Wörz O., Breysse J. (1999b). High temperature HCN generation in an integrated microreaction system. *Proc. 3rd Int. Conf. of Microreaction Technology*, 151.

[66] Hessel V., Ehrfeld W., Golbig K., Haverkamp V., Löwe H., Storz M., Wille C., Guber A., Jähnisch K. and Baerns M. (2000). Gas/liquid microreactors for direct fluorination of aromatic compounds using elemental fluorine. *Proc. 3rd Int. Conf. of Microreaction Technology*, 526.

[67] Hickman D. A. and Schmidt L. D. (1991). Modeling Catalytic Gauze Reactors: Ammonia Oxidation. *Ind. Eng. Chem. Res.*, 30, 50.

[68] Homsy R. V. and Strohman R. D. (1971). Diffusion and chemical reaction in a tubular reactor with non-newtonian laminar flow. *A.I.Ch.E. J.*, 17, 215.

[69] Hsing I.-M., Srinivasan R., Harold M. P., Jensen K. F. and Schmidt M. A. (2000). Simulation of micromachined chemical reactors for heterogeneous partial oxidation reactions. *Chem. Engng. Sci.*, 55, 3.

[70] Hsu C. (1965). A method of solution for mass transfer with chemical reaction under conditions of viscous flow in a tubular reactor. *A.I.Ch.E. J.*, 11, 938.

[71] Huang D. T. and Varma A. (1980). Yield optimization in a tube-wall reactor. *ACS Symp. Ser.*, 124, 469.

[72] Hudson J. L. (1965). Diffusion with consecutive heterogeneous reactions. *A.I.Ch.E. J.*, 11, 943.

[73] Irandoust S., Andersson B, Bengtsson E. and Silverström (1989). Liquid film in Taylor flow through a capillary. *Ind. Eng. Chem. Res.*, 28, 1684.

[74] Jain S. C., Chen B. H. and McMillan A. F. (1985). Concentration profiles in laminar-flow tubular reactor with wall injection. *Can. J. Chem. Eng.*, 63, 1001.

[75] Jähnisch K., Baerns M., Hessel V., Ehrfeld W., Haverkamp V., Löwe H., Wille Ch. and Guber A. (2000). Direct fluorination of toluene using elemental fluorine in gas/liquid microreactors. *J. Fluorine Chemistry*, 105, 117.

[76] Katz S. (1959). Chemical reactions catalysed on a tube wall. *Chem. Engng. Sci.*, 10, 202.

[77] Kavehpour H. P., Faghri M. and Asako Y. (1997). Effects of Compressibility and Rarefaction on Gaseous Flows in Microchannels. *Numerical Heat Transfer, Part A*, 10, 677.

[78] Kee R. J., Dixon-Lewis J., Warnatz M. E. and Miller J. A. (1986). A FORTRAN Computer Code Package for the Evaluation of Gas Phase Multicomponent Transport Properties. Sandia National Laboratories SAND86-8246.

[79] *Kirk-Othmer Encyclopedia of Chemical Technology* (1999). 4th Ed., Wiley, New York.

[80] Knight J. B., Vishwanath A., Brody J. P. and Austin R. H. (1998). Hydrodynamic focusing on a silicon chip: mixing nanoliters in microseconds. *Phys. rev. Lett.*, 80, 3863.

[81] Kursawe A., Dietzsch E., Kah S., Hönicke D., Fichtner M., Schubert K. and Wie*β*meier G. (1999). Selective reactions in microchannel reactors. *Proc. 3rd Int. Conf. of Microreaction Technology (Berlin)*, 213.

[82] Lauwerier H. A. (1959). A diffusion problem with chemical reaction. *Appl. Sci. Res.*, 8, 366.

[83] Lawal A. (1996). Convective diffusion of power law fluids inside ducts with consecutive homogeneous and catalytic wall reactions. *Chem. Engng. Sci.*, 51, 3427.

[84] Lerou J. J., Harold M. P., Ryley J., Ashmead J., O'Brien T. C., Johnson M., Perrotto J., Blaisdell C. T., Rensi T. A. and Nyquist J. (1996). *Dechema Monographs*, 132, 51.

[85] Levenspiel O. (1999). *Chemical reaction engineering.* 3rd Ed., Wiley, New York.

[86] Levien K. L. and Levenspiel O. (1999). Optimal product distribution from laminar flow reactors: newtonian and other power-law fluids. *Chem. Engng. Sci.*, 54, 2453.

[87] Liu J. and Yu-Chong T. (1995). MEMS for pressure distribution studies of gaseous flows in microchannels. *Proc. IEEE Microelectromechanical Systems.*

[88] Löwe H., Ehrfeld W., Hessel V., Richter T. and Schiewe J. (2000). *Proc. 4th Int. Conf. of Microreaction Technology (Atlanta)*, 31.

[89] Lowenheim F. A. and Moran M. K. (1975). *Faith, Keyes and Clark's Industrial Chemicals.* 4th Ed., Wiley, New York.

[90] Lu X. X., Boyes A. P. and Winterbottom J. M. (1996). Study of Mass Transfer Characteristics of a Cocurrent Downflow Bubble Column Reactor Using Hydrogenation of Itaconic Acid. *Chem. Engng. Sci.*, 51, 2715.

[91] Ludwig, E.E. (1983). *Applied Process Design for Chemical and Petrochemical Plants.* 2nd Ed., Vol. 3, Gulf Publishing Co..

[92] Lupa A. J. and Dranoff J. S. (1966). Chemical reaction on the wall of an annular reactor. *Chem. Engng. Sci.*, 21, 861.

[93] Lyczkowski R. W., Gidaspow D. and Solbrig C. W. (1971). Consecutive surface reactions in fully developed laminar and turbulent flow. *A.I.Ch.E. J.*, 17, 497.

[94] Madou M. (1997). *Fundamentals of Microfabrication.* CRC Press, Florida.

[95] Makihara M. (1993). The flow of liquids in microcapillary tubes - consideration to application of the Navier-Stokes equations. *Journal Japan Prec. Eng.*, 59, 399.

[96] Matsumoto H. and Colgate J. (1990). Preliminary investigation of micropumping based on electrical control of iterfacial tension. *Proc. IEEE MEMS 90.*

[97] McKetta, *Encyclopedia of Chemical Processing and Design*, vol. 23, Dekker, New York, 359.

[98] Mehta K. C. and Sharma M. M. (1970a). *Brit. Chem. Eng.*, 15, 1440.

[99] Mills P. L. and Chaudhari R. V. (1997). Multiphase Catalytic Reactor Engineering and Design for Pharmaceutical and Fine Chemcials. *Catalysis Today*, 37, 367.

[100] Nigam K. M., Srivastava V. K. and Nigam K. D. P. (1982). Homogeneous-heterogeneous reactions in a tubular reactor: an analytical solution. *Chem. Eng. J.*, 25, 147.

[101] Ogren P. J. (1975). Analytical results for first-order kinetics in flow tube reactors with wall reactions. *J. Phys. Chem.*, 79, 1749.

[102] Olim M. (2000). The shape of a gas/liquid interface in a rectangular cavity allowing for an arbitrary direction of the body force. *Microscale Thermophysical Engineering*, 4, 223.

[103] Padmavathi G. and Remananda Rao K. (1991). Hydrodynamic characteristics of reversed flow jet loop reactor as a gas-liquid-solid contactor. *Chem. Engng. Sci.*, 46, 3293.

[104] Patankar S. V. (1980). *Numerical Heat Transfer and Fluid Flow.* 1st Ed., McGraw-Hill, London.

[105] U.S. Patent 3, 711, 253, January 16, 1973 (to Fischer); German Patent 2, 546, 104, April 21, 1977 (to Bayer).

[106] Peng X. F., Peterson G. P. and Wang B. X. (1994). Frictional Flow Characteristics of Water Flowing Through Rectangular Microchannels. *Exp. Heat Transfer*, 7, 249.

[107] Penth B. (2001). New non-clogging micro-reactor. chemweb.com(0101002).

[108] Perry R. H., Green D. W. and Maloney J. O. (1988). *Perry's Chemical Engineers Handbook.* 6th Ed., McGraw Hill, London.

[109] Pfahler J., Harley J., Bau H. and Zemel J. (1990). Liquid transport in micron and submicron channels. *Sensors and Actuators A-Physical*, 22, 431.

[110] Potter A. (1960). *Prog. Energy Combust. Sci.*, 1, 145.

[111] Ramachandran P. A. and Chaudhari R. V. (1983). *Three-Phase Catalytic Reactors.* Gordon and Breach, London.

[112] Rector D. R., Cuta M. and Palmer B. J. (1998). Lattice-Boltzmann simulation code development for micro-fluidic systems. *Proc. 2nd Int. Conf. of Microreaction Technology (New Orleans)*, 272.

[113] Riazi M. R. and Faghri A. (1986). Effect of the interfacial drag on gas adsorption with chemical reaction in a vertical tube. *A.I.Ch.E. J.*, 32, 696.

[114] Robb D. A. and Harriott P. (1974). The Kinetics of Methanol Oxidation on a Supported Silver Catalyst. *Journal of Catalysis*, 35, 176.

[115] Robins I., Shaw J., Miller B., Turner C. and Harper M. (1997). *Proc. 1st Int. Conf. of Microreaction Technology*, 35.

[116] Satterfield C. N. (1969). *Mass Transfer in Heterogeneous Catalysis.* MIT Press, Cambridge (Mass.).

[117] Satterfield C. N. (1980). *Heterogeneous Catalysis in Industrial Practice.* 2nd Ed., McGraw Hill, New York.

[118] Schaaf S. A. and Chambre P. L. (1961). *Flow of Rarefied Gases.* Princeton University Press, Princeton N. J..

[119] Sesterhenn M., Mellmann J., Löhr M., Stierle B., Strobelt T. (1999). Design of microchannels for biomedical sensors. *Proc. 2nd Workshop Int. Des. Sim. Tools Micro and Biomedical Fluidic Apps.*

[120] Shah R. K. and London A. L. (1978). *Laminar Flow Forced Convection in Ducts.* Academic Press, London.

[121] Shah Y. T. (1979). *Gas-Liquid-Solid Reactor Design.* 1st Ed., McGraw Hill, New York.

[122] Shanley A. (1997). *Chemical Engineering (March)*, 30.

[123] Shaw J., Turner C., Miller B. and Harper M. (1998). *Proc. 2nd Int. Conf. of Microreaction Technology (New Orleans)*, 176.

[124] Smith T. G. (1977). An Examination of the Isothermal Pellet Assumption Relative to the Design of Nonadiabatic Fixed Bed Catalytic Reactors. *Chem. Engng. Sci.*, 32, 1023.

[125] Solomon R. L. and Hudson J. L. (1967). Heterogeneous and homogeneous reactions in a tubular reactor. *A.I.Ch.E. J.*, 13, 545.

[126] Srinivasan R., Hsing I. M., Berger P. E., Jensen K. F., Firebaugh S. L., Schmidt M. A., Harold M. P., Lerou J. J. and Ryley J. F. (1997). Micromachined Reactors for Catalytic Partial Oxidation Reactions. *Chem. Engng. Sci.*, 43, 3059.

[127] Stanley R. S., Barron R. F. and Ameel T. A. (1997). Two-phase flow in microchannels, Microelectromechanical Systems, DSC-62/HTD-354, 143.

[128] Stemme G., Kittilsland G. and Norden B. (1990). A sub-micron particle filter in silicon. *Sensors Actuators A*, 21, 904.

[129] Suo M. and Griffith P. (1964). Two phase flow in capillary tubes. *J. Basic Engng.*, 576.

[130] Talens-Alesson, F.I. (1999). The Modelling of Falling Film Chemical Reactors. *Chem Engng. Sci*, 54, 1871.

[131] Taylor G. I. (1953). Dispersion of soluble matter in a solvent flowing slowly through a tube, *Proc. Roy. Soc.*, A219, 186.

[132] Taylor R. and Krishna R. (1993). *Multicomponent Mass Transfer.* Wiley, New York.

[133] Tonkovich A. L. Y., Zilka J. L., Powell M. R. and Call C. J. (1998). *Proc. 2nd Int. Conf. of Microreaction Technology (New Orleans)*, 45.

[134] Triplett K. A., Ghiaasiaan S. M., Abdel-Khalik S. I. and Sadowski D. L. (1999). Gas-liquid two-phase flow in microchannels. Part I: two-phase flow patterns. *Int. J. Multiphase Flow*, 25, 377.

[135] Triplett K. A., Ghiaasiaan S. M., Abdel-Khalik S. I. and Sadowski D. L. (1999b). Gas-liquid two-phase flow in microchannels. Part II: void fraction and pressure drop. *Int. J. Multiphase Flow*, 25, 395.

[136] Tuckerman D. B. and Pease R. F. W. (1981). High-performance heat sinking for VLSI. *Electron Device Letters*, 2, 126.

[137] Turek F., Geike R. and Lange R. (1986). Liquid-Phase Hydrogenation of Nitrobenzene in a Slurry Reactor. *Chem. Eng. Proc.*, 20, 213.

[138] *Ullmans Encyclopedia of Chemical Industry*, (1987).

[139] Varma A. and Morbidelli M. (1997). *Mathematical Methods in Chemical Engineering.* Oxford University Press, Oxford.

[140] Veenstra T. T., Lammerink T. S. J., Elwenspoek M. C. and van den Berg A. (1999). Characterization Method for a New Diffusion Mixer Applicable in Micro Flow Injection Analysis Systems. *J. Micromech. Microeng.*, 9, 199.

[141] Versteeg H. K. and Malalasekera W. (1996). *An Introduction to Computational Fluid Dynamics.* Addison Wesley Longman, Harlow.

[142] Veser G. (2001). Experimental and theoretical investigation of H_2 oxidation in a high temperature catalytic microreactor. *Chem. Engng. Sci.*, 56, 1265.

[143] Wachs I. E. and Madix R. J. (1978). The Selective Oxidation of CH_3OH to H_2CO on a Copper (110) Catalyst, *Journal of Catalysis*, 53, 208.

[144] Walker R. E. (1961). Chemical reaction and diffusion in a catalytic tubular reactor. *Phys. Fluids*, 4, 1211.

[145] Walter S. and Liauw M. (1999). Fast concentration cycling in microchannel reactors. *Proc. 4th Int. Conf. of Microreaction Technology (Atlanta)*, 209.

[146] Wegeng R. S., Call C. J. and Drost M. K. (1996). Chemical system miniaturization. *Spring National Meeting of A.I.Ch.E., New Orleans.*

[147] Weiβmeier G. and Hönicke D. (1998). Strategy for the development of micro channel reactions for heterogeneously catalysed reactions. *Proc. 4th Int. Conf. Of Microreaction Technology (New Orleans)*, 24.

[148] Wisniak J. and Klein M. (1984). Reduction of nitrobenzene to aniline. *Ind. Eng. Chem. Res.*, 23, 44.

[149] Witte J. H. (1968). Mixing shocks in two phase flow. *J. Fluid Mech.*, 36, 639.

[150] Wörz O., Jäckel K.P., Richter Th. and Wolf A. (2001). Microreactors, a new efficient tool for optimum reactor design. *Chem. Engng. Sci.*, 56, 1029.

[151] Wu P. Y. and Little W. A. (1983). Measurement of friction factors for the flow of gases in very fine channels used for microminiature Joule-Thomson refrigerators. *Cryogenics*, 23, 273.

[152] Yu D. (1995). An experimental and theoretical investigation of fluid flow and heat transfer in microtubes. *ASME/JSME Thermal Eng. Joint Conf.*.

Appendix A

FORTRAN 77 Codes

The codes in this Appendix relate to the isothermal microreactor in Chapter 3. All codes have been written in FORTRAN 77 and compiled in IBM AIX XL FORTRAN on an IBM RS6000. There are 5 codes and all are fully described in each section.

A.1 Calculation of decay rate

This code calculates the decay group as a function of *Da* (3.14) as shown in Fig. 3.2(a). The code is looped for different values of *Da* and within each loop values for λ_a are sought (for intermediate *Da* numbers). Upon satisfying the boundary conditons the results are dumped to a file (tan.dat).

```
**==aa0001.spg  processed by SPAG 5.11R  at 11:56 on  8 Feb 2001
      implicit none
! This program is to solve the equation a tan a= da
c
      integer i, j, k, nu
      parameter (nu=10000)
      double precision da, a, x, temp
      double precision astar, diff, diffstar
c
      open (unit=1,file="tan.dat")
c
      do 100 i = 1, 1000
         da = 0.01D0*(i-1)
c
         astar = 1.0D0
         diffstar = 10.0D0
c
         do 50 j = 1, nu
            a = (0.5*3.142)*(j-1.0D0)/(nu-1.0D0)
            diff = abs((a*tan(a))-da)
```

```
c
            if ( diff.lt.diffstar ) then
               astar = a
               diffstar = diff
            endif
 50      continue
c
         write (1,99001) da, (astar**2.0)
c
 100  continue
c
      stop
99001 format (2F16.7)
      end
```

A.2 Calculation of transverse profiles

This code calculates the transverse profiles shown in Fig. 3.2(b). The code is looped for different values of *Da*. Initially a value for λ_a is sought in each loop. Upon finding a value of λ_a that satisfies the boundary conditions the transverse profile can be calulated according to (3.18) which uses finite differencing.

```
**==aa0001.spg  processed by SPAG 5.11R  at 15:15 on  4 Feb 2001
      implicit none
c Calculate variation across the channel
c
      integer i, j, k, nu, mu, p
      parameter (nu=1000,mu=10000)
      double precision deltaeta, da, pe, r, c
      double precision f(nu), eta, psi, finaldfdelta
      double precision alphastar, dfstar, area, v, alpha
c
      da = 1.0D0
      pe = 10.0D0
      r = 10.0D0
c
      open (unit=1,file="f.dat")
      open (unit=2,file="df.dat")
      open (unit=3,file="fstar.dat")
      open (unit=4,file="cstar.dat")
c
      deltaeta = (1/((nu-1)*1.0D0))
      do 200 p = 1, 1
         do 100 k = 1, 30
c
            alphastar = 1.0D0
            dfstar = 10.0D0
c
            psi = (k-1)*10.0D0/29.0
            psi = 0.0D0
c
            da = (k-1)*10.0/29.0D0
c           da=5.0d0
            if ( (deltaeta*da).gt.0.01 ) write (6,*)
     &           "Increment is too large"
c
            do 20 j = 1, mu
c
               alpha = 3.0D0*(j-1)/(mu-1.0D0)
c
               f(1) = 1.0D0
```

```
c
               f(2) = f(1)*(1+(deltaeta*da))
c
               do 10 i = 3, nu
                  eta = (i-1)*deltaeta
c
                  v = ((eta)-(eta**2.0)+psi)/((1.0/6.0)+psi)
c
                  f(i) = (2.0*f(i-1)) - (f(i-2))
     &                   - ((alpha*(deltaeta**2.0))*(v*f(i-1)))
 10            continue
c
               finaldfdelta = abs((f(nu)-f(nu-1))/deltaeta)
c
               write (1,*)
               if ( finaldfdelta.lt.dfstar ) then
                  alphastar = alpha
                  dfstar = finaldfdelta
               endif
c
               write (2,99001) c, finaldfdelta
 20         continue
c
            write (6,*) "Da, alpha :", da, alphastar, psi
c
c        Calculate the profile f
            alpha = alphastar
            do 40 i = 3, nu
               eta = (i-1)*deltaeta
c
               v = ((eta)-(eta**2.0)+psi)/((1.0/6.0)+psi)
c
               f(i) = (2.0*f(i-1)) - (f(i-2))
     &                - ((alpha*(deltaeta**2.0))*(v*f(i-1)))
c
 40         continue
c
c    Calculate integral under f
            area = 0.0D0
c
            do 60 i = 2, nu
               area = area + ((0.5*deltaeta)*(f(i)+f(i-1)))
 60         continue
c
            do 80 i = 1, nu
               write (3,99001) (deltaeta*(i-1)), (f(i)/area)
 80         continue
```

```
            write (3,*)
c   Output the critical value of da and alphastar
            write (4,99002) da, alphastar, psi
c
 100     continue
         write (6,*) "p is ", p
 200  continue
c
      stop
c
99001 format (2F16.7)
99002 format (3F16.7)
      end
```

A.3 Full numerical simulation

This code solves the parabolic advection-diffusion equation for three components. Large number of grid points have been used in the axial direction to ensure stability of the method (Carnahan et al.1961).

```
**==aa0001.spg  processed by SPAG 5.11R  at 13:22 on  8 Feb 2001
      implicit none
c     Explicit method program to solve the advection diffusion equation
c
      integer i, j, nu, mu, g, u, hi
      parameter (nu=50,mu=1000000)
      real*8 thetaa(nu), beta(nu), alpha(nu), f(nu)
      real*8 b(nu), w(nu), kappa, eta, v, thetab(nu), thetac(nu)
      real*8 deltaeta, deltazeta, r, pe, psi, da1, da2, tempa(nu), dfgh
      real*8 averagea, averageb, averagec, profile(nu), tempb(nu),
     &       tempc(nu)
c
      open (unit=1,file="fullsim.dat")
      open (unit=2,file="average.dat")
      open (unit=3,file="similarity.dat")
      open (unit=4,file="decayrate.dat")
      open (unit=5,file="finalconc.dat")
      open (unit=7,file="tranv7.dat")
      open (unit=8,file="tranv8.dat")
      open (unit=9,file="tranv9.dat")
c
c     Define the variables
c
      do 200 hi = 1, 3
c
         do 100 u = 1, 10
            pe = 10.0D0
            r = 10.0D0
            psi = 0.0D0
c
            da1 = 0.005*((100/0.01)**((u-1.0D0)/9.0D0))
            if ( hi.eq.1 ) da2 = 10.0*da1
            if ( hi.eq.2 ) da2 = 1.05D0*da1
            if ( hi.eq.3 ) da2 = 0.1*da1
            if ( hi.eq.5 ) da2 = 0.5/da1
            if ( hi.eq.4 ) da2 = 1.0/da1
            if ( hi.eq.6 ) da2 = 0.05/da1
c
c da1=1.0
c        da2=0.1
```

```
c
            deltaeta = 1.0/((nu*1.0D0)-1.0D0)
            deltazeta = 1.0/(mu-1.0D0)
c
c       Initialise the concentration profile of reactant
c
            do 20 i = 1, nu
               eta = (i-1)*deltaeta
               thetaa(i) = 1.0D0
               thetab(i) = 0.0D0
               thetac(i) = 0.0D0
 20         continue
c
c       Initialise the coefficients in the matrix
c
            do 60 j = 1, mu
c       given theta calculate the value of r and update
c       write (6,*) j*1.0d0
c
               do 30 i = 2, (nu-1)
c
                  eta = (i-1)*deltaeta
                  v = (eta-(eta**2.0)+psi)/(0.16666+psi)
                  dfgh = (deltazeta*(r**1.0)/(v*pe*(deltaeta**2.0)))
c
                  tempa(i) = thetaa(i)
     &                       + (dfgh*(thetaa(i+1)-(2.0*thetaa(i))
     &                       +thetaa(i-1)))
                  tempb(i) = thetab(i)
     &                       + (dfgh*(thetab(i+1)-(2.0*thetab(i))
     &                       +thetab(i-1)))
                  tempc(i) = thetac(i)
     &                       + (dfgh*(thetac(i+1)-(2.0*thetac(i))
     &                       +thetac(i-1)))
c       write (6,*) i*1.0d0
 30            continue
c
               tempa(nu) = thetaa(nu-1)
               tempb(nu) = thetab(nu-1)
               tempc(nu) = thetac(nu-1)
c        Original 1st
               tempa(1) = thetaa(2)/(1.0D0+(da1*deltaeta))
c        Second Order
c        tempa(1)=((((4.0d0*deltaeta*da1*thetaa(2))
c     &+1.d0)**(0.5d0))-1.d0)/(2.0d0*deltaeta*da1)
c        Original 1st
               tempb(1) =
```

```
               &(thetab(2)+(deltaeta*da1*thetaa(2)))
     &            /(1.0D0+(da2*deltaeta))
c        Second Order
c        tempb(1)=(thetab(2)+(deltaeta*Da1*thetaa(2)**2.0d0))
c     &/(1.0d0+(da2*deltaeta))
c        Original 1st
               tempc(1) = (thetac(2)+(deltaeta*da2*thetab(1)))
c
c exchange variables
               do 40 i = 1, nu
                  thetaa(i) = tempa(i)
                  thetab(i) = tempb(i)
                  thetac(i) = tempc(i)
 40            continue
c
c
c calculate the concentration averaged across channel width
c
               if ( mod(j,50000).eq.0 ) then
cc
                  averagea = 0.0D0
                  averageb = 0.0D0
                  averagec = 0.0D0
                  do 45 i = 1, (nu-1)
                     averagea = averagea +
     &                          ((0.5*deltaeta)*(thetaa(i)+thetaa(i+1)))
                     averageb = averageb +
     &                          ((0.5*deltaeta)*(thetab(i)+thetab(i+1)))
                     averagec = averagec +
     &                          ((0.5*deltaeta)*(thetac(i)+thetac(i+1)))
c
c calculate f
c
 45               continue
c
c dump transverse profile
c
                  if ( j.eq.50000 ) then
                     do 46 i = 1, nu
c write(7,*) j
                        write (7,*) (float(i)*deltaeta) - deltaeta,
     &                              thetaa(i)/averagea
 46                  continue
                  endif
c
                  if ( j.eq.100000 ) then
                     do 48 i = 1, nu
```

```
c write(8,*) j
                          write (8,*) (float(i)*deltaeta) - deltaeta,
     &                                 thetaa(i)/averagea
 48                    continue
                    endif
c
                    if ( j.eq.150000 ) then
                       do 50 i = 1, nu
c write(9,*) j
                          write (9,*) (float(i)*deltaeta) - deltaeta,
     &                                 thetaa(i)/averagea
 50                    continue
                    endif
c
c        write (5,995)(1-averagea),  (averageb),  averagec
                 endif
c
 60          continue
c
             do 80 i = 1, nu
                write (1,99001) ((i-1)*deltaeta), thetaa(i)
 80          continue
c
             write (5,99003) (1-averagea), (averageb), averagec
c
             write (6,99003) da1, da2, (1-averagea), (averageb), averagec
c
 100      continue
          write (5,*)
 200   continue
c
       close (1)
       close (2)
       close (3)
       close (4)
       close (5)
       close (7)
       close (8)
       close (9)
c
       stop
99001 format (2F16.7)
99002 format (4F16.7)
99003 format (5F16.7)
       end
```

A.4 Vertically averaged system

This code provides the solution to the vertically averaged formulation for the three component system with series reactions. It is looped with different Da numbers and searches for λ_a and λ_b so that the boundary conditions are satisfied (3.21). Upon satisfying the boundary conditions the plot data is dumped to a file (three.dat).

```
**==aa0001.spg  processed by SPAG 5.11R  at 13:36 on  8 Feb 2001
      implicit none
C*** Start of declarations inserted by SPAG
      real thetaa, thetab
C*** End of declarations inserted by SPAG
c     This program is to plot out predictions for
c     concentration for the three component problem
c
      integer i, j, k, nu, mu, g
c
      parameter (nu=20000)
      double precision a, x, temp, da1, da2
      double precision astar, diff, diffstar, bmaxstar, maxb, maxa
      double precision r, pe, lambdaa, lambdab, dada2, dadastar
      open (unit=1,file="three.dat")
      open (unit=2,file="bmaxversuskb.dat")
c
      pe = 1.0D0
      r = 10.0D0
c
      do 100 g = 1, 3
         dadastar = 100.0D0
         bmaxstar = 0.001D0
c
         do 50 k = 1, 100
c
            da1 = 0.001D0*((2000/0.001)**((k-1.0D0)/99.0D0))
c
            if ( g.eq.1 ) da2 = 10.0*da1
            if ( g.eq.2 ) da2 = 1.05D0*da1
            if ( g.eq.3 ) da2 = 0.1*da1
            if ( g.eq.5 ) da2 = 0.5*da1
c
            if ( g.eq.4 ) da2 = 1.3*da1
            if ( g.eq.6 ) da2 = 0.05*da1
c
c      da2=( 0.08*((200.0/0.08)**((g-1.0d0)/(49.0d0))))*da1
c
c      here we calculate the decay rates for A
```

```
c
            astar = 1.0D0
            diffstar = 10.0D0
c
            do 20 j = 1, nu
               a = (0.5*3.142)*(j-1.0D0)/(nu-1.0D0)
               diff = abs((a*tan(a))-da1)
c
               if ( diff.lt.diffstar ) then
                  astar = a
                  diffstar = diff
               endif
c
 20         continue
c
            lambdaa = (r*(astar**2.0)/pe)
c
c       here we calculate the decay rates for B
c
            astar = 1.0D0
            diffstar = 10.0D0
c
            do 40 j = 1, nu
               a = (0.5*3.142)*(j-1.0D0)/(nu-1.0D0)
               diff = abs((a*tan(a))-da2)
c
               if ( diff.lt.diffstar ) then
                  astar = a
                  diffstar = diff
               endif
c
 40         continue
c
            lambdab = (r*(astar**2.0)/pe)
c
c       end of calculating decay rates

            thetaa = exp(-lambdaa)
            thetab = (da1/(da2-da1))*(exp(-lambdaa)-exp(-lambdab))
c        if (abs((da2/da1)-1.0d0).gt.1.0d-3) then
            write (1,99001) (1-thetaa), thetab
c        endif
c
            if ( thetab.gt.bmaxstar ) then
               bmaxstar = thetab
               dadastar = (da1/da2)
               maxa = thetaa
```

```
            endif
c
 50      continue
         write (1,*)
c
         write (2,99002) dadastar, bmaxstar, (1.0D0-maxa)
 100  continue
c
      stop
c
99001 format (2F16.7)
99002 format (3F16.7)
      end
```

A.5 Vertically averaged system (flow profile)

This code is essentially the same as given in Appendix A.4 except that the effect of velocity profile is included.

```
**==aa0001.spg  processed by SPAG 5.11R  at 11:21 on 12 Feb 2001
      implicit none
c
      real bmaxstar
      integer maxa
c
c       Calculate variation across the channel
c       Flow profile can be altered in this code
c       by use of the variable Psi.
c
      integer i, j, k, nu, mu, p, tu
      parameter (nu=2000,mu=50000)
      double precision deltaeta, da, pe, r, c
      double precision f(nu), eta, psi, finaldfdelta
      double precision alphastar, dfstar, area, v, alpha
      double precision da1, da2, thetaa, thetab
      double precision lambdaa, lambdab, dada2, dadastar
c
      pe = 1.0D0
      r = 10.0D0
      psi = 10.0D0
c
c number of points along each curve is tu
c
      tu = 60
c
      open (unit=1,file="f3b.dat")
      open (unit=2,file="df2a.dat")
      open (unit=3,file="fstar2a.dat")
      open (unit=4,file="cstar.dat")
c
      do 100 p = 1, 3
         dadastar = 100.0D0
         bmaxstar = 0.001D0
c
         deltaeta = (1/((nu-1)*1.0D0))
         do 50 k = 1, tu
c
            da1 = 0.001D0*((2000.0D0/0.001)
     &           **((k-1.0D0)/(tu*1.0D0-1.0D0)))
c
```

```
            if ( p.eq.1 ) da2 = 10.0*da1
            if ( p.eq.2 ) da2 = 1.05D0*da1
            if ( p.eq.3 ) da2 = 0.1*da1
            if ( p.eq.5 ) da2 = 0.5*da1
            if ( p.eq.4 ) da2 = 1.3*da1
            if ( p.eq.6 ) da2 = 0.05*da1
c
c       find value of lambdaa for da1
c
            alphastar = 1.0D0
            dfstar = 10.0D0
c
            da = da1
            do 20 j = 1, mu
c
               alpha = 2.5D0*(j-1)/(mu-1.0D0)
c
               f(1) = 1.0D0
c
               f(2) = f(1)*(1+(deltaeta*da))
c
               do 10 i = 3, nu
                  eta = (i-1)*deltaeta
c
                  v = ((eta)-(eta**2.0)+psi)/((1.0/6.0)+psi)
c
                  f(i) = (2.0*f(i-1)) - (f(i-2))
     &                   - ((alpha*(deltaeta**2.0))*(v*f(i-1)))
c
 10            continue
c
               finaldfdelta = abs((f(nu)-f(nu-1))/deltaeta)
c
               if ( finaldfdelta.lt.dfstar ) then
                  alphastar = alpha
                  dfstar = finaldfdelta
               endif
c
c        write (2,992) c, finaldfdelta
 20         continue
c
            lambdaa = (alphastar)*(r/pe)
c
c       value of lambdab for Da2
c
            alphastar = 1.0D0
            dfstar = 10.0D0
```

```
c
            da = da2
            do 40 j = 1, mu
c
               alpha = 2.5D0*(j-1)/(mu-1.0D0)
c
               f(1) = 1.0D0
c
               f(2) = f(1)*(1+(deltaeta*da))
c
               do 30 i = 3, nu
                  eta = (i-1)*deltaeta
c
                  v = ((eta)-(eta**2.0)+psi)/((1.0/6.0)+psi)
c
                  f(i) = (2.0*f(i-1)) - (f(i-2))
     &                   - ((alpha*(deltaeta**2.0))*(v*f(i-1)))
c
 30            continue
c
               finaldfdelta = abs((f(nu)-f(nu-1))/deltaeta)
c
               if ( finaldfdelta.lt.dfstar ) then
                  alphastar = alpha
                  dfstar = finaldfdelta
               endif
c
 40         continue
c
            lambdab = (alphastar)*(r/pe)
c
            write (6,*) lambdaa, lambdab
c
c       use the values of lambdaa and lambdab to calculate the concentration
c       of a, b
c       end of calculating decay rates
c
            thetaa = exp(-lambdaa)
            thetab = (da1/(da2-da1))*(exp(-lambdaa)-exp(-lambdab))
            write (1,99001) (1.0D0-thetaa), thetab
c
            if ( thetab.gt.bmaxstar ) then
               bmaxstar = thetab
               dadastar = (da1/da2)
               maxa = thetaa
            endif
c
```

```
c       write (1,992) (1.0-thetaa), thetab
c
 50      continue
         write (1,*)
         write (2,99002) dadastar, bmaxstar, (1.0D0-maxa)
c
 100  continue
c
      stop
c
99001 format (2F16.7)
99002 format (3F16.7)
      end
```

Appendix B

Derivation of Dimensionless Energy Boundary Condition

This appendix shows the derivation of the dimensionless energy boundary conditon used in Chapter 4.

$$\begin{aligned}
k\frac{\partial T}{\partial x} &= r\,(-\Delta H) + \lambda_m \left.\frac{\partial T_s}{\partial x}\right|_w, && \text{(B.1)}\\
k\frac{\partial T}{\partial x} &= A\exp\left(\frac{-E_a}{RT}\right) c\,(-\Delta H) + \lambda_m \left.\frac{\partial T_s}{\partial x}\right|_w, && \text{(B.2)}\\
k\frac{T_0}{r_1}\frac{\partial y}{\partial \eta} &= A\exp\left(\frac{-E_a}{RT_0 y}\right) \theta c_0\,(-\Delta H) + \lambda_m \left.\frac{T_0}{\delta}\frac{\partial y_s}{\partial \eta}\right|_w, && \text{(B.3)}\\
\frac{\partial y}{\partial \eta} &= \frac{r_1 c_0}{T_0 k} A\exp\left(\frac{-E_a}{RT_0 y}\right) (-\Delta H)\,\theta + \left.\frac{\lambda_m r_1}{k\delta}\frac{\partial y_s}{\partial \eta}\right|_w. && \text{(B.4)}
\end{aligned}$$

Some further definitions

$$\begin{aligned}
Le &= \frac{k}{\rho c_p D}, && \text{(B.5)}\\
\gamma &= \frac{E_a}{RT_0}, && \text{(B.6)}\\
\beta &= \frac{(-\Delta H)\,c_0}{\rho c_p T_0}. && \text{(B.7)}
\end{aligned}$$

Therefore

$$\begin{aligned}
\frac{\partial y}{\partial \eta} &= \frac{r_1 c_0}{T_0 Le \rho c_p D} A\exp\left(\frac{-E_a}{RT_0 y}\right) (-\Delta H)\,\theta + \left.\frac{\lambda_m r_1}{k\delta}\frac{\partial y_s}{\partial \eta}\right|_w, && \text{(B.8)}\\
\frac{\partial y}{\partial \eta} &= \frac{\beta r_1}{Le D} A\exp\left(\frac{-E_a}{RT_0 y}\right) \theta + \kappa_1 \left.\frac{\partial y_s}{\partial \eta}\right|_w. && \text{(B.9)}
\end{aligned}$$

However

$$\exp\left(\frac{-E_a}{RT_0 y}\right) = \exp\left(\frac{-E_a}{RT_0}\right)\exp\left(\frac{E_a}{RT_0}\left(\frac{y-1}{y}\right)\right) = \exp\left(\frac{-E_a}{RT_0}\right)\exp\left(\frac{E_a}{RT_0}\left(1-\frac{1}{y}\right)\right). \tag{B.10}$$

As the Damkohler number (Da) can be expressed as $Da = \frac{A\exp\left(\frac{-E_a}{RT_0}\right)L}{D}$, then (B.9) becomes

$$\frac{\partial y}{\partial \eta} = \frac{\beta Da}{LeR_1}\exp\left(\gamma\left(\frac{y-1}{y}\right)\right)\theta + \kappa_1 \left.\frac{\partial y_s}{\partial \eta}\right|_w. \tag{B.11}$$

Appendix C

CFD Governing Equations

Mass Conservation is expressed as:

$$\frac{\partial \rho}{\partial t} + \frac{\partial}{\partial x_j}(\rho u_j) = m \tag{C.1}$$

Momentum Equations are derived from the law of conservation of momentum:

$$\frac{\partial}{\partial t}(\rho u_i) + \frac{\partial}{\partial x_i}(\rho u_i u_j) = -\frac{\partial p}{\partial x_i} + \frac{\partial \tau_{ij}}{\partial x_i} + \rho f_i \tag{C.2}$$

For Newtonian fluids the stress tensor can be related to the velocity gradients through:

$$\tau_{ij} = \mu\left(\frac{\partial u_i}{\partial x_j} + \frac{\partial u_j}{\partial x_i}\right) - \frac{2}{3}\mu\left(\frac{\partial u_k}{\partial x_k}\right)\delta_{ij} \tag{C.3}$$

Substitution of C.3 into C.2 results in the Navier Stokes equations:

$$\frac{\partial}{\partial t}(\rho u_i) + \frac{\partial}{\partial x_j}(\rho u_i u_j) = -\frac{\partial p}{\partial x_i} + \frac{\partial}{\partial x_j}\left\{\mu\frac{\partial u_i}{\partial x_i} + \frac{\partial u}{\partial x_i} - \frac{2}{3}\mu\frac{\partial \mu_k}{\partial x_k}\delta_{ij}\right\} + \rho f_i \tag{C.4}$$

For incompressible and low Mach number flows the static enthalpy form of the energy equation can be used, and expressed as:

$$(\rho h) + \frac{\partial}{\partial x_j}(\rho u_j h) = -\frac{\partial q_j}{\partial x_j} + \frac{\partial p}{\partial t} + u_j\frac{\partial p}{\partial x_j} + \tau_{ij}\frac{\partial u_i}{\partial x_j} - \frac{\partial}{\partial x_j}(J_{ij}h_i) + S_a \tag{C.5}$$

J_{ij} is the total (concentration-driven + temperature-driven) diffusive mass flux for species i, and h represents the enthalpy for species i. S_a stands for additional sources due to surface reaction. q_j is the j component of the heat flux; this is modelled by Fourier's Law.

Appendix D

PFR Verification Parameters

Parameter/variable	Value
$\Delta H_{298\mathrm{K}}$	-35.5 kJ/mol
Vol. Flowrate	1.3 m^3/s
ε	0.375
$\Delta \hat{c_p}$	-0.725 J/mol/K
Θ_a	1
Θ_b	0.25
Θ_c	0
Θ_d	0
Θ_e	0.4
Θ_i	0.75
c_{pa}	84.50 J/mol/K
c_{pb}	33.81 J/mol/K
c_{pc}	57.45 J/mol/K
c_{pd}	31.60 J/mol/K
c_{pe}	38.39 J/mol/K
c_{pi}	30.00 J/mol/K
catalyst diameter	1mm
void fraction	0.45
A (k_o)	2.9×10^{13} mol/(s.kg_{cat}.$\mathrm{Pa}^{0.5}$)
A (k_m)	5.0×10^{13} mol/(s.kg_{cat}.Pa)
E_a (k_o)	95×10^3 J/mol
E_a (k_m)	62.7×10^3 J/mol
Inlet temp.	437 K
Conversion	0.85

Appendix E

FORTRAN 90 Codes

The codes in this Appendix relate to the adiabatic PFR in Chapter 6. All codes have been written in FORTRAN 90 and compiled in Digital Visual FORTRAN v6.0a linking to the IMSL FORTRAN 90 MP library v3.0. The main file, driver.f90, calls the IMSL integrator QDAG.

```
program driver
!
use adiabatic_pfr
use dfimsl
use nrtype
!
implicit none
!
integer(i4b), parameter :: irule = 2
real(sp), parameter :: a=0.,b=0.7,errabs=0.0,errrel=0.001
real(sp) errest,res,rr
external rr
!
cao = (inlet_pressure)/(r*to) ! Added steam
delta_h = -71000. ! j/kmol
!
call qdag (rr,a,b,errabs,errrel,irule,res,errest)
!
fao = cao*vf
weight = fao*res
volume = weight/cat_rho
tau = volume/vf
!
print 10
print 20, fao, b, weight, volume, vf, tau
print 30
print 40, tx(b), tx(b)-273., to-273.
!
```

```
open(2, file=’results.dat’, status=’replace’)
!
write (2,10)
write (2,20), fao, b, weight, volume, vf, tau
write (2,30)
write (2,40), tx(b), tx(b)-273., to-273.

write (6,*) ’rr’, rr(0.0)
write (6,*) ’tx’, tx(0.0)
write (6,*) ’pax’, pax(0.0)
write (6,*) ’pbx’, pbx(0.0)
write (6,*) ’km’, km(423.)
write (6,*) ’ko’, ko(423.)
!
close(2)
!
10 format (1x, ’Fm0 (mol/s)’, 5x, ’X’, 5x, ’Cat. (kg)’, 5x,&
 ’V (m3)’, 5x, ’Vol F (m3/s)’, 5x, ’Space-time (s)’ / 1x,&
 11(’-’), 5x, ’-’, 5x, 9(’-’)&
 , 5x, 6(’-’), 5x, 12(’-’), 5x, 14(’-’) /)
20 format (1x, e11.4, t18, f4.2, t23, e11.4, t36,&
 e10.4, t49, e10.4, t66, f7.4 //)
30 format (1x, ’Outlet temp. (K)’, 5x ’Outlet temp. (C)’ &
 5x, ’Inlet temp. (C)’ / 1x, 16(’-’), 5x, 16(’-’), 5x, 15(’-’) /)
40 format (1x, f9.3, t23, f9.3, t44, f9.3 /)
!
end program driver
!
function rr(x) ! mol/(kg.s)
use adiabatic_pfr
use nrtype
implicit none
real(sp) rr,x
!
rr = 1./((1./sall)*sact(ag_r)*(1000./3600.)&
*(2*ko(tx(x))*km(tx(x))*(pbx(x)**(0.5))*pax(x))/&
((km(tx(x))*pax(x))+(2.0*ko(tx(x))*(pbx(x)**(0.5)))))
end function rr
```

```
!
MODULE nrtype
!
INTEGER, PARAMETER :: I4B = SELECTED_INT_KIND(9)
INTEGER, PARAMETER :: I2B = SELECTED_INT_KIND(4)
INTEGER, PARAMETER :: I1B = SELECTED_INT_KIND(2)
!
```

```
INTEGER, PARAMETER :: SP = KIND(1.0)
INTEGER, PARAMETER :: DP = KIND(1.0D0)
!
INTEGER, PARAMETER :: SPC = KIND((1.0,1.0))
INTEGER, PARAMETER :: DPC = KIND((1.0D0,1.0D0))
!
INTEGER, PARAMETER :: LGT = KIND(.true.)
!
! Frequently used mathematical constants
!
REAL(SP), PARAMETER :: PI=3.141592653589793238462643383279502884197_sp
REAL(DP), PARAMETER :: PI_D=3.141592653589793238462643383279502884197_dp
!
END MODULE nrtype
!
module ADIABATIC_PFR
!
use nrtype
!
implicit none
!
real(sp), parameter :: r = 8.314 ! m^3.Pa/(mol.K)
real(sp), parameter :: epsilon = 0.375 ! -
real(sp), parameter :: to = 423. ! K
real(sp), parameter :: tr = 298.15 ! K
real(sp), parameter :: phib = 0.5
real(sp), parameter :: sall = 1670 ! m^2/kg
real(sp), parameter :: ag_r = 5e-04 ! m
real(sp), parameter :: ag_rho = 10.e+03 ! kg/m^3
real(sp), parameter :: cat_rho = 5.5e+03 ! kg/m^3 (bed density)
real(sp), parameter :: inlet_pressure = 0.5e+05 ! Pa (pp methanol)
real(sp), parameter :: vf = 1.29 ! m3/s (methanol @ inlet temp)
!
! parameters for feed conditions
!
real(sp), parameter :: phi_methanol = 1.0 ! basis on methanol
real(sp), parameter :: phi_oxygen = 0.25
real(sp), parameter :: phi_nitrogen = 0.75
real(sp), parameter :: phi_form = 0.0
real(sp), parameter :: phi_water = 0.4
real(sp), parameter :: phi_hydrogen = 0.0
!
real(sp) temp ! K
real(sp) delta_h ! J/mol
real(sp) weight ! kg
real(sp) volume ! m^3
real(sp) tau ! s
```

```
real(sp) fao ! mol/s
real(sp) cao ! mol/m3
!
type species
character(15) name
real hof ! J/mol
real rmm ! kg/mol
real stoich ! -ve for reactants
real cp ! J/mol/K
endtype
!
type(species) :: methanol = species("methanol",-2.0067e+05,32.04e-03,-1.,70.
type(species) :: oxygen = species("oxygen",0.0,32.0e-03,-0.25,30.)
type(species) :: form = species("form",-1.1590e+05,30.03e-03,1.0,50.)
type(species) :: water = species("water",-2.4182e+05,18.02e-03,0.5,36.)
type(species) :: hydrogen = species("hydrogen",0.0,2.0e-03,0.5,30.)
type(species) :: nitrogen = species("nitrogen",0.0,28.0e-03,0.0,30.)
!
contains
!
function sact(radius)
real(sp) sact, radius
!
sact = 3./(radius*ag_rho) ! m^2/kg (actual)
!
end function sact
!
function tx(conv)
real(sp) tx, conv, delta_cp
!
delta_cp = (hydrogen%stoich*hydrogen%cp)+(water%stoich*water%cp)&
+(form%stoich*form%cp) &
+(oxygen%stoich*oxygen%cp)+(methanol%stoich*methanol%cp)
!
tx = ((conv*(-delta_h)) + &
(to*((phi_methanol*methanol%cp)+(phi_oxygen*oxygen%cp)+&
(phi_form*form%cp)+ &
(phi_water*water%cp)+(phi_hydrogen*hydrogen%cp)+&
(phi_nitrogen*nitrogen%cp)))+(conv*delta_cp*tr))/ &
(((phi_methanol*methanol%cp)+(phi_oxygen*oxygen%cp)+&
(phi_form*form%cp)+(phi_water*water%cp)+&
(phi_hydrogen*hydrogen%cp)+(phi_nitrogen*nitrogen%cp))+&
(conv*delta_cp))
!
end function tx
!
function pax(x)
```

```
real(sp) pax, x
!
pax = (cao*(1-x)*r*to)/(1.013e+05*(1+(epsilon*x)))
!
end function pax
!
function pbx(x)
real(sp) pbx, x
!
pbx = (cao*(phi_oxygen-((oxygen%stoich/methanol%stoich)*x))*r*to)&
/(1.013e+05*(1+(epsilon*x)))
!
end function pbx
!
function km(t)
real(sp) km,t
!
km = 2.9e13*exp(-62850./(r*t))
!
end function km
!
function ko(t)
real(sp) ko,t
!
ko = 2.9e13*exp(-95113./(r*t))
!
end function ko
!
end module ADIABATIC_PFR
```

Appendix F

FORTRAN 90 Codes

The codes in this Appendix relate to the finite-difference/volume methanol oxidation reactor in Chapter 6. All codes have been written in FORTRAN 90 and compiled in Digital Visual FORTRAN v6.0a linking to the IMSL FORTRAN 90 MP library v3.0. There are six files that must be compiled and linked to create an executeable binary.

Normally direct solver number 2 is used.

nrtype.f90 Module file that contains specification statements relating to FORTRAN 90 kind types.

driver.f90 Main file that obtains information from input files and calls appropriate solvers during each iteration.

solvers.f90 Contains two external subroutines that are the mass and energy solvers; IMSL routines are called from these.

transfer.f90 Module file that serves as global storage between the two solvers in 'solvers.f90', interface blocks for all external subroutines are also contained in this file.

gmressolver.f90 Subroutine that initialises the GMRES solver, this solver is used only if the solver integer in the input file is set to 3.

amultp.f90 Subroutine that is called by the GMRES solver.

F.1 nrtype.f90

```
**==aa0001.spg  processed by SPAG 5.11R  at 18:12 on  9 Feb 2001
      implicit none
!
      integer kind
      real selected_int_kind
!
      modulenrtype
!
      integer, parameter :: i4b = selected_int_kind(9)
      integer, parameter :: i2b = selected_int_kind(4)
      integer, parameter :: i1b = selected_int_kind(2)
!
      integer, parameter :: sp = kind(1.0)
      integer, parameter :: dp = kind(1.0D0)
!
      integer, parameter :: spc = kind((1.0,1.0))
      integer, parameter :: dpc = kind((1.0D0,1.0D0))
!
      integer, parameter :: lgt = kind(.true.)
!
!   Frequently used mathematical constants
!
      real(sp), parameter :: pi =
     &                       3.14159265358979323846264338327950288419
      real(dp), parameter :: pi_d =
     &                       3.141592653589793238462643383279502884
!
      end modulenrtype
```

F.2 driver.f90

```
**==driver.spg  processed by SPAG 5.11R  at 16:37 on  9 Feb 2001
!
! This is the driver program for the energy (elliptic)
! and mass (parabolic) solvers for the methanol oxidation
! reactor. An input file is first read that contains
! parameters relevent to both solvers. Each solver is then
! called until convergencein mass and energy are achieved.
!
! Each solver is accessed as an external subprogram.
! Temperature varuables are passed between the solves by
! global variables that are declared in the module transfer.
!
! Due to memory requirments caused by the number of nodes
! in the parabolic solver the energy solver is solved on a
! smaller grid. The heat of reaction nodes are not passed
! directly but use interpolation routines.
!
! 1. Mass solver generates mu energy source terms due to
! heat of reaction.
! 2. This is interpolated as a cubic spline.
! 3. Discrete values are returned to the mass solver, which
! is passed directly to
! global storage (these are compared subject to user specified
! tolerance).
! 4. Energy solver accepts interpolated values and solvers.
! 5. Like before temperature on the catalyst boundary is
! interpolated as a cubic
! spline and returned as mu nodes to the mass solver.
!
! Author D. Gobby 11/12/2000
!
      program driver
!
      usenrtype
      usetransfer
!
      implicit none
!
      integer(i4b) counter, i, nu, mu, enu, emu
!
      real(sp) ctime
      real(dp) ar, deltah, height, length, pe_h, utol, initial_temp,
     &         t_zero
```

```
!
      open (9,status='old',file="common.in",action='read')
!
      read (9,*) mu
      read (9,*) nu
      read (9,*) height
      read (9,*) length
      read (9,*) deltah
      read (9,*) pe_h
      read (9,*) emu
      read (9,*) enu
      read (9,*) utol
!
      allocate(add_source(1:mu+2))
      allocate(oldaverage_t(1:emu))
      allocate(xtol(1:emu))
      add_source = 0.0D0
      allocate(rt(1:mu+2))
      read (9,*) initial_temp
      read (9,*) t_zero
      read (9,*) diffusivity
      rt = initial_temp
      close (9)
!
! rt=570.d0 ! This serves as an initial condition
      oldaverage_t = rt
      xtol = rt
!
! Calculate flow channel aspect ratio (ar)
!
      ar = length/height
!
! Start calls to solvers
!
      first = .true.
      write (6,*) 'Solvers started'
!
      counter = 0
      do while ( maxval(xtol).ge.utol )
         write (6,*) 'Maxval ', maxval(xtol)
         counter = counter + 1
         write (6,*) 'Mass solver iteration ', counter
         call masssolver(nu,mu,height,ar,deltah,pe_h,t_zero)
         write (6,*) 'Energy solver iteration (loop) ', counter
         call energysolver(nu,mu,enu,emu,length,ar,height)
         first = .false.
      enddo
```

```
!
      deallocate(add_source)
      deallocate(oldaverage_t)
      deallocate(xtol)
!
      call cpu_time(ctime)
      write (6,*) 'cpu time ', ctime, 's'
!
      stop
!
      end programdriver
```

F.3 solvers.f90

```
!
subroutine masssolver(nu,mu,height,ar,deltah,pe_h,t_zero,deltah_series)
!
use nrtype
use transfer
!
implicit none
!
integer(i4b) nu,mu
integer(i4b) i,j
!
real(dp) theta_a(nu),theta_b(nu),theta_c(nu)
real(dp) theta_d(nu),theta_e(nu),theta_f(nu),theta_g(nu)
real(dp) temp_a(nu),temp_b(nu),temp_c(nu)
real(dp) temp_d(nu),temp_e(nu),temp_f(nu),temp_g(nu)
real(dp) average_a,average_b,average_c
real(dp)        average_d,average_e,average_f,average_g
real(dp) deltaeta,deltazeta
real(dp) dfgh,eta,pe_h,ar,v,rmm_bar,density_bar,height,t_zero
real(dp) conc_methanol,conc_oxygen
        real(dp)        pp_methanol,pp_oxygen,r_flux,deltah
real(dp) r_flux_kc,r_flux_mc_1,r_flux_mc_2
real(dp) r_flux_series,r_flux_series_mc_1,r_flux_series_mc_2
real(dp) a_in,b_in,c_in,d_in,e_in,f_in,g_in,r_flux_s
real(dp) tod,deltah_series
real(dp) xtemp!temporary variables passed to global storage
real(dp), parameter :: r=8.314d0
real(dp), parameter :: rmm_a=0.032d0,rmm_b=0.032d0,rmm_c=0.030d0
real(dp), parameter :: rmm_d=0.018d0,rmm_e=0.002d0,rmm_f=0.044d0
real(dp), parameter :: rmm_g=0.028d0, sall=1670 ! m**2/kg
real(dp), parameter :: pressure=1.013E+05 ! Negligible pressure drop
!
! a - Methanol
! b - Oxygen
! c - Formaldehyde
! d - Water
! e - Hydrogen
! f - Carbon Dioxide
! g - Nitrogen
!
! Explicit method to solve the advection-diffusion equation on a
! mass fraction basis.
!
```

```
open(unit=1,status='replace',file="averagea.dat")
open(unit=2,status='replace',file="averageb.dat")
open(unit=3,status='replace',file="averagec.dat")
open(unit=4,status='replace',file="averaged.dat")
open(unit=5,status='replace',file="averagee.dat")
open(unit=15,status='replace',file="averagef.dat")
open(unit=16,status='replace',file="averageg.dat")
open(unit=30,status='replace',file="mlc.dat")
!
deltaeta=1.0d0/((nu*1.0d0)-1.0d0)
deltazeta=1.0d0/(mu-1.0d0)
!
! Check for convergence and stability
!
! This check is performed by the criteria of Carnahan et al.
!      , (1969). It can be shown
! that the explicit method is both convergent and stable if
!
! deltazeta .le. 0.5*(deltaeta**2)*ar/pe
!
if (first) then
 if (deltazeta.ge.(0.5d0*(deltaeta**2)*ar/pe_h)) then
  write(6,*)'************************************************'
  write(6,*)'       WARNING'
  write(6,*)''
  write(6,*)'Parabolic solver does not satisfy convergence and'
  write(6,*)'stability criteria'
  write(6,*)'************************************************'
 endif
endif
!
open(unit=20,status='old',file="inlet.in")
!
read(20,*) a_in
read(20,*) b_in
read(20,*) c_in
read(20,*) d_in
read(20,*) e_in
read(20,*) f_in
read(20,*) g_in
!
close(20)
!
m_in=a_in
!
! Initialise concentration profile of components
!
```

```
do i=1,nu
theta_a=a_in
theta_b=b_in
theta_c=c_in
theta_d=d_in
theta_e=e_in
theta_f=f_in
theta_g=g_in
enddo
!
write(1,*) 0.0,theta_a(1)
write(2,*) 0.0,theta_b(1)
write(3,*) 0.0,theta_c(1)
write(4,*) 0.0,theta_d(1)
write(5,*) 0.0,theta_e(1)
write(15,*) 0.0,theta_f(1)
write(16,*) 0.0,theta_g(1)
!
do j=1,mu ! Start axial loop
 do i=2,(nu-1) ! Start transverse loop
  eta=(i-1)*deltaeta
  v=(eta-(eta**2.0d0))/(0.16666d0)
  dfgh=(deltazeta*ar)/(v*pe_h*(1.0d0-(deltar* &
  (a_in-theta_a(i))))*((rt(j)/ t_zero)**-0.5d0)* &
  (deltaeta**2.0d0))
  temp_a(i)=theta_a(i)+(dfgh*(theta_a(i+1) &
  -(2.0d0*theta_a(i))+theta_a(i-1)))
  temp_b(i)=theta_b(i)+(dfgh*(theta_b(i+1) &
  -(2.0d0*theta_b(i))+theta_b(i-1)))
  temp_c(i)=theta_c(i)+(dfgh*(theta_c(i+1) &
  -(2.0d0*theta_c(i))+theta_c(i-1)))
  temp_d(i)=theta_d(i)+(dfgh*(theta_d(i+1) &
  -(2.0d0*theta_d(i))+theta_d(i-1)))
  temp_e(i)=theta_e(i)+(dfgh*(theta_e(i+1) &
  -(2.0d0*theta_e(i))+theta_e(i-1)))
  temp_f(i)=theta_f(i)+(dfgh*(theta_f(i+1) &
  -(2.0d0*theta_f(i))+theta_f(i-1)))
  temp_g(i)=theta_g(i)+(dfgh*(theta_g(i+1) &
  -(2.0d0*theta_g(i))+theta_g(i-1)))

 enddo ! End transverse loop
!
  temp_a(nu)=theta_a(nu-1)
  temp_b(nu)=theta_b(nu-1)
  temp_c(nu)=theta_c(nu-1)
  temp_d(nu)=theta_d(nu-1)
  temp_e(nu)=theta_e(nu-1)
```

```
  temp_f(nu)=theta_f(nu-1)
  temp_g(nu)=theta_g(nu-1)
!
! Calculate reaction variables and flux
!
! Average RMM of reaction mixture (kg/mol)
rmm_bar=1.0d0/((theta_a(1)/rmm_a)+ &
(theta_b(1)/rmm_b)+(theta_c(1)/rmm_c)+ &
(theta_d(1)/rmm_d)+(theta_e(1)/rmm_e)+ &
(theta_f(1)/rmm_f)+(theta_g(1)/rmm_g))
! Density of reaction mixture; ideal gas law (kg/m^3)
density_bar=pressure*rmm_bar/(r*rt(j+1))
! Concentration of methanol (mol/m**3)
conc_methanol=density_bar*theta_a(2)/rmm_a
! Concentration of oxygen (mol/m**3)
conc_oxygen=density_bar*theta_b(2)/rmm_b
! Partial pressure of methanol (atm)
pp_methanol=conc_methanol*r*rt(j+1)/1.013e+05
! Partial pressure of oxygen (atm)
pp_oxygen=conc_oxygen*r*rt(j+1)/1.013e+05
! Calculate reaction flux (mol/(m**2.s)
!
r_flux_kc=(1000.0d0/3600.0d0)*(1.d0/sall)* &
(2.0d0*ko(rt(j+1))*km(rt(j+1))*pp_oxygen**(0.5d0)* &
pp_methanol)/ &
((km(rt(j+1))*pp_methanol)+(2.0d0*ko(rt(j+1))* &
pp_oxygen**(0.5d0)))
r_flux_mc_1=temp_a(2)*density_bar*(diffusivity* &
((rt(j)/t_zero)**1.5)) &
/(deltaeta*height*rmm_a)
r_flux_mc_2=temp_b(2)*density_bar*(diffusivity* &
((rt(j)/t_zero)**1.5)) &
/(deltaeta*height*rmm_b)
!
r_flux_series=5.0e+13*(exp((-172.6e3)/(r*rt(j+1))))*
(density_bar*diffusivity*((rt(j)/t_zero)**1.5)*theta_c(2) &
/(height*rmm_c))
r_flux_series_mc_1=temp_b(2)*density_bar*(diffusivity* &
((rt(j)/t_zero)**1.5)) &
/(deltaeta*height*rmm_b)
r_flux_series_mc_2=temp_c(2)*density_bar*(diffusivity* &
((rt(j)/t_zero)**1.5)) &
/(deltaeta*height*rmm_c)
!
! Total oxygen demand based on kinetics (joint reactant)
!
tod=r_flux_kc+r_flux_series
```

```
!
if(tod.gt.r_flux_mc_2)then
 r_flux_mc_2=(r_flux_kc/tod)*r_flux_mc_2
 r_flux_series_mc_1=(r_flux_series/tod)*r_flux_series_mc_1
endif
 r_flux=min(r_flux_kc,(r_flux_mc_1),(4.0d0*r_flux_mc_2))
!       As basis is on methanol
 r_flux_s=min(r_flux_series,r_flux_series_mc_1,r_flux_series_mc_2)
!       Equal stoichiometry
!
if(r_flux.lt.0.0d0) write(6,*) 'Warning: negative flux at ', &
float(j)*deltazeta
!
temp_a(1)=(-height*r_flux*deltaeta*rmm_a/(density_bar* &
(diffusivity*((rt(j)/t_zero)**1.5))))+theta_a(2)
temp_b(1)=(height*((0.25d0*(-1.0d0*r_flux))+(-1.0d0*r_flux_s))* &
deltaeta*rmm_b/ &
(density_bar*(diffusivity*((rt(j)/t_zero)**1.5))))+theta_b(2)
temp_c(1)=(height*(r_flux-r_flux_s)*deltaeta*rmm_c/(density_bar* &
(diffusivity*((rt(j)/t_zero)**1.5))))+theta_c(2)
temp_d(1)=(height*((0.5d0*r_flux)+(r_flux_s))*deltaeta*rmm_d/ &
(density_bar*(diffusivity*((rt(j)/t_zero)**1.5))))+theta_d(2)
temp_e(1)=(height*0.5d0*r_flux*deltaeta*rmm_e/(density_bar* &
(diffusivity*((rt(j)/t_zero)**1.5))))+theta_e(2)
temp_f(1)=(height*r_flux_s*deltaeta*rmm_f/(density_bar* &
(diffusivity*((rt(j)/t_zero)**1.5))))+theta_f(2)
temp_g(1)=theta_g(2)
!
! Calculate additional source term for energy solver due to
!      heat of reaction, this is passed to the energy solver as a
!      volumetric source, hence the term is divided by deltaeta
!
add_source(j)=(-r_flux*deltah)+(-r_flux_s*deltah_series)
mc(j)=temp_a(nu-1)
!
! Exchange variables
!
do i=1,nu
 theta_a(i)=temp_a(i)
 theta_b(i)=temp_b(i)
 theta_c(i)=temp_c(i)
 theta_d(i)=temp_d(i)
 theta_e(i)=temp_e(i)
 theta_f(i)=temp_f(i)
 theta_g(i)=temp_g(i)
enddo
!
```

```
! Calculate average of variables over transverse direction
!
if(mod(j,10).eq.0)then
!
 average_a=0.0d0
 average_b=0.0d0
 average_c=0.0d0
 average_d=0.0d0
 average_e=0.0d0
 average_f=0.0d0
 average_g=0.0d0
!
do i=1,(nu-1)
 average_a=average_a+((0.5d0*deltaeta)*(theta_a(i)+theta_a(i+1)))
 average_b=average_b+((0.5d0*deltaeta)*(theta_b(i)+theta_b(i+1)))
 average_c=average_c+((0.5d0*deltaeta)*(theta_c(i)+theta_c(i+1)))
 average_d=average_d+((0.5d0*deltaeta)*(theta_d(i)+theta_d(i+1)))
 average_e=average_e+((0.5d0*deltaeta)*(theta_e(i)+theta_e(i+1)))
 average_f=average_f+((0.5d0*deltaeta)*(theta_f(i)+theta_f(i+1)))
 average_g=average_g+((0.5d0*deltaeta)*(theta_g(i)+theta_g(i+1)))
enddo
!
write(1,*) float(j)*deltazeta,average_a
write(2,*) float(j)*deltazeta,average_b
write(3,*) float(j)*deltazeta,average_c
write(4,*) float(j)*deltazeta,average_d
write(5,*) float(j)*deltazeta,average_e
write(15,*) float(j)*deltazeta,average_f
write(16,*) float(j)*deltazeta,average_g
write(30,*) float(j)*deltazeta,theta_a(1)
!
select case (j)
case(10)
open(unit=31,status='replace',file="mlc_10.dat")
do i=1,nu
 write(31,*) float(i-1)*deltaeta,theta_a(i)
enddo
close(31)
case(30)
open(unit=32,status='replace',file="mlc_30.dat")
do i=1,nu
 write(32,*) float(i-1)*deltaeta,theta_a(i)
enddo
close(32)
case(50)
open(unit=33,status='replace',file="mlc_50.dat")
do i=1,nu
```

```
 write(33,*) float(i-1)*deltaeta,theta_a(i)
enddo
close(33)
case(70)
open(unit=34,status='replace',file="mlc_70.dat")
do i=1,nu
 write(34,*) float(i-1)*deltaeta,theta_a(i)
enddo
close(34)
case(100)
open(unit=35,status='replace',file="mlc_100.dat")
do i=1,nu
 write(35,*) float(i-1)*deltaeta,theta_a(i)
enddo
close(35)
case(150)
open(unit=36,status='replace',file="mlc_150.dat")
do i=1,nu
 write(36,*) float(i-1)*deltaeta,theta_a(i)
enddo
close(36)
case(200)
open(unit=37,status='replace',file="mlc_200.dat")
do i=1,nu
 write(37,*) float(i-1)*deltaeta,theta_a(i)
enddo
close(37)
case(300)
open(unit=38,status='replace',file="mlc_300.dat")
do i=1,nu
 write(38,*) float(i-1)*deltaeta,theta_a(i)
enddo
close(38)
case(500)
open(unit=39,status='replace',file="mlc_500.dat")
do i=1,nu
 write(39,*) float(i-1)*deltaeta,theta_a(i)
enddo
close(39)
case(1000)
open(unit=40,status='replace',file="mlc_1000.dat")
do i=1,nu
 write(40,*) float(i-1)*deltaeta,theta_a(i)
enddo
close(40)
case default
end select
```

```
!
endif
!
enddo ! End axial loop
!
! write(6,*)average_a,average_b,average_c,average_d,average_e, &
! average_a+average_b+average_c+average_d+average_e
!
close(1)
close(2)
close(3)
close(4)
close(5)
close(15)
close(16)
close(30)
!
contains
!
function km(temp)
!
real(dp), intent(in) :: temp
real(dp) km
!
km=2.9e+13*exp(-95113.0d0/(r*temp))
!
end function km
!
function ko(temp)
!
real(dp), intent(in) :: temp
real(dp) ko
!
ko=2.9e+13*exp(-62850.0d0/(r*temp))
!
end function ko
!
end subroutine masssolver
!
! This subroutine contains the elliptic energy solver
!
subroutine energysolver(enu,emu,nu,mu,length,ar,height)
!
! This subroutine solves a PDE with complex boundary conditions, the finite
! volume method is used to give a dicretised form of the governing equation
!
! Boundary conditions are stored and/or solved as exterior ficticious nodes
```

```
! on the node limits 1,nu, and mu
!
! The algebraic set of equations produces are passed to IMSL solvers
!
! 0. Standard LU solver (dlsarg)
! 1. Sparse solver (dlsxlg)
!      2.     Band sparse solver with iterative refinement (dlsarb)
!      3.     GMRES iterative solver (g2res)
!
! Computational grid is shown below. Active fluid cells are given by 0
! (nu in vertical direaction and mu in horizontal direction). Boundary
! nodes are given by +. Details on the calculation of boundary nodes can
! be found in Patankar (1980)
!
!
! +--+--+--+--+
! |  |  |  |  |
! +--0--0--0--+
! |  |  |  |  |
! +--0--0--0--+
! |  |  |  |  |
! +--0--0--0--+
! |  |  |  |  |
! +--+--+--+--+
!
use nrtype
use dfimsl
use transfer
use avdef
!
implicit none
!
integer(i4b) iparam(6),info(10)
integer(i4b) counter,ido,i,j,k,l,lda,enu,emu,nu,nz,mu,solver,tempk,xi,xj
integer(i4b), parameter :: ipath=2
integer(i4b), dimension(:), allocatable :: irow,jcol
integer(i4b) scounter,itercounter
integer(i4b) status
!
real(dp) ah,ar,av,deltaeta,deltazeta,dh,dv,pe,xgamma
real(dp) rparam(5)
real(dp) aw,ae,an,al,ap,xsp
real(dp) averaget,height
real(dp) theta_inf,bi_bot,bi_top,total,r_top,hss,g,t_0
real(dp) r_glass,r_cat,r_si,r_ss
real(dp) k_glass,k_silver,k_silicon,k_ss,k_fluid
real(dp) length
```

```
!
real(dp), dimension(:), allocatable :: west,east,south,north
real(dp), dimension(:), allocatable :: as,b,tres,ntres,itres
real(dp), dimension(:), allocatable :: emux,mux,muy,imux,mua
real(dp), dimension(:), allocatable :: x,z,work,p,transfer_temp
real(dp), dimension(:), allocatable :: average_t
real(dp), dimension(:,:), allocatable :: a,band_coefficient,theta,ntheta
!
logical av_graphics
!
save av_graphics
!
data av_graphics/.true./
!
type krelation
integer(i4b) i ! icoordinate
integer(i4b) j ! jcoordinate
endtype
!
type(krelation), dimension(:), allocatable :: kij
!
! Open files for input/output
!
open(7,status='old',file="energy.in",action='read')
open(8,status='replace',file="average.dat")
open(9,status='replace',file="irow")
open(10,status='replace',file="jcol")
open(11,status='replace',file="nas")
open(12,status='replace',file="rhs")
open(13,status='replace',file="diagin")
open(unit=17,status='replace',file="tlc.dat")
open(unit=18,status='replace',file="thc.dat")
!
! Obtain data from input file
!
read(7,*) solver
read(7,*) pe
read(7,*) theta_inf
read(7,*) t_0
read(7,*) r_glass
read(7,*) r_cat
read(7,*) r_si
read(7,*) r_ss
read(7,*) g
!
! Calculate and set various parameters
!
```

```
read(7,*) k_fluid
read(7,*) k_glass
read(7,*) k_silver
read(7,*) k_silicon
read(7,*) k_ss
!
r_top=r_glass
total=(((k_silver/k_silver)*r_cat)+((k_silicon/k_silver)*r_si) &
+((k_ss/k_silver)*r_ss))
bi_top=h_top(theta_inf,t_0,length)*length/k_glass
bi_bot=h_bot(theta_inf,t_0,length)*length/k_silver
hss=length*r_ss
!
! Check that lumped solid model is valid
!
if ((h_top(theta_inf,t_0,length)*(length*r_glass)/k_glass).ge.1.0d0) then
print*, 'Top boundary condition violates model validity, check results'
else if ((h_bot(theta_inf,t_0,length)*(length*r_si)/k_silicon).ge.1.0d0) the
print*, 'Bottom boundary condition violates model validity, check results'
endif
!
! Set the leading dimension of the array to be passed to the 77 routine
!
lda=(nu+2)*(mu+2)
!
! Set up BAND solver (if required)
!
! No. of lower codiagonals - nu+2
! No. of upper codiagonals - mu+2
! Total band width - nlca+nuca+1
!
if (solver.eq.2) then
allocate(band_coefficient(1:nu+2+mu+2+1,1:(nu+2)*(mu+2)))
band_coefficient=0.0d0
lda=nu+2+mu+2+1
endif
!
! Size of increment
!
deltaeta=1.0d0/dfloat(nu)
deltazeta=1.0d0/dfloat(mu+1)
xgamma=1.0d0
!
! Size boundary arrays
!
allocate(west(2:nu+1))
!
```

```
! Size right hand vector - B (and r in transfer module)
!
allocate(b(1:(nu+2)*(mu+2)))
allocate(rb(1:(nu+2)*(mu+2)))
b=0.0d0
rb=0.0d0
!
! Size diagin,x and z (if sparse iterative solver used)
!
if(solver.eq.3)allocate(diagin(1:(nu+2)*(mu+2)))
allocate(x(1:(nu+2)*(mu+2)))
allocate(z(1:(nu+2)*(mu+2)))
allocate(work(1:(nu+2)*(mu+2)))
allocate(p(1:(nu+2)*(mu+2)))
diagin=0.0d0
x=0.0d0
z=0.0d0
work=0.0d0
p=0.0d0
!
! Size output vector
!
allocate(tres(1:(nu+2)*(mu+2)))
tres=0.0d0
allocate(ntres(1:(nu+2)*(mu+2)))
ntres=0.0d0
allocate(itres(1:(nu+2)*(mu+2)))
itres=0.0d0
!
! Size coefficient matrix - A
!
if(solver.eq.0)then
allocate(a(1:(nu+2)*(mu+2),1:(nu+2)*(mu+2)))
a=0.0d0
endif
!
! Size k relator
!
allocate(kij(1:(nu+2)*(mu+2)))
!
! Size output array
!
allocate(theta(1:(nu+2),1:(mu+2)))
allocate(ntheta(1:(nu+2),1:(mu+2)))
!
! Size interpolation arrays
!
```

```
allocate(emux(emu))
allocate(mux(mu))
allocate(muy(mu))
allocate(mua(mu+2))
!
! Evaluate matrix parameters
!
ah=1.0d0/dfloat(mu+1)
av=1.0d0/dfloat(nu)
!
dh=0.0d0 !av/(deltazeta*ar**2) !Horizontal diffusion coefficient
dv=ah/deltaeta !Vertical diffusion coefficient
!
! Evaluate boundary conditions
!
! West(inlet)
!
do i=2,nu+1
west(i)=1.0d0
enddo
!
! Obtain information from global 'add_source' variable to use in the
! heat source term. Interpolate the values and return at energy solver
! points.
!
do i=1,emu
emux(i)=dfloat(i)/dfloat(emu)
enddo
!
do i=1,mu
mux(i)=dfloat(i)/dfloat(mu)
enddo
!
call dcsiez(emu,emux,add_source,mu,mux,muy)
call dcsiez(emu,emux,mc,mu,mux,mua)
!
! Set sparse solver parameters
!
call dl4lxg(iparam,rparam)
iparam(5)=1e7
!
! Each row of the coefficient matrix is subscripted (i,j) according to
!     the row number involved; i.e.
!
! row 1 (top row) is (1,1)
! row 2 (next down) is (2,1)
!
```

```
! If necessary the row number can be evaluated from the function knumber
!
! A storage array is created to develop i,j as a function of k
! If k entry in the dynamic vector is called; i and j can be returned
!
do i=1,nu+2
do j=1,mu+2
tempk=knumber(i,j)
kij(tempk)%i=i
kij(tempk)%j=j
enddo
enddo
!
! For each row in the coefficient vector (i,j) is first calculated,
!      from the i,j integers the coefficients from the original equation
!      can be obtained and placed in the knumber(i,j) position in that row.
!      This is repeated for all rows up to nu*mu
! Note that the leading dimension will equal nu*mu in this case as
!      the array is allocated dynamically
!
ncounter=0
scounter=1
!
do k=1,((nu+2)*(mu+2)) ! Start row loop
!
! Determine i,j
!
xi=kij(k)%i
xj=kij(k)%j
!
! Calculate Sp,aw,ae,an,as
!
if((xj.eq.1).and.(xi.eq.1))then
ncounter=ncounter+3
else if((xj.eq.1).and.(xi.gt.1).and.(xi.lt.nu+2))then
ncounter=ncounter+4
else if((xj.eq.1).and.(xi.eq.nu+2))then
ncounter=ncounter+3
else if((xj.gt.1).and.(xj.lt.mu+2).and.(xi.eq.1))then
ncounter=ncounter+4
else if((xj.gt.1).and.(xj.lt.mu+2).and.(xi.eq.nu+2))then
ncounter=ncounter+4
else if((xj.eq.mu+2).and.(xi.eq.1))then
ncounter=ncounter+3
else if((xj.eq.mu+2).and.(xi.gt.1).and.(xi.lt.nu+2))then
ncounter=ncounter+4
else if((xj.eq.mu+2).and.(xi.eq.nu+2))then
```

```
ncounter=ncounter+3
else
ncounter=ncounter+5
endif
!
enddo
!
! Allocate new sparse arrays
!
allocate(nas(1:ncounter))
allocate(nirow(1:ncounter))
allocate(njcol(1:ncounter))
nas=0.0d0
nirow=0.0d0
njcol=0.0d0
!
do k=1,((nu+2)*(mu+2)) ! Start row loop
!
! Determine i,j
!
xi=kij(k)%i
xj=kij(k)%j
!
! Calculate Sp,aw,ae,an,as
!
if((xj.eq.1).and.(xi.eq.1))then
xsp=-bi_bot
aw=0.0d0
ae=dh+(total/deltazeta**2)
an=dv
al=0.0d0
else if((xj.eq.1).and.(xi.gt.1).and.(xi.lt.nu+2))then
xsp=-(f(xi)+dh)
aw=0.0d0
ae=dh
an=dv
al=dv
else if((xj.eq.1).and.(xi.eq.nu+2))then
xsp=-bi_top
aw=0.0d0
ae=dh+((r_top)/deltazeta**2)
an=0.0d0
al=dv
else if((xj.gt.1).and.(xj.lt.mu+2).and.(xi.eq.1))then
xsp=-bi_bot
aw=dh+(total/deltazeta**2)
ae=dh+(total/deltazeta**2)
```

```
an=dv
al=0.0d0
else if((xj.gt.1).and.(xj.lt.mu+2).and.(xi.eq.nu+2))then
xsp=-bi_top
aw=dh+((r_top)/deltazeta**2)
ae=dh+((r_top)/deltazeta**2)
an=0.0d0
al=dv
else if((xj.eq.mu+2).and.(xi.eq.1))then
xsp=-bi_bot
aw=dh+(total/deltazeta**2)
ae=0.0d0
an=dv
al=0.0d0
else if((xj.eq.mu+2).and.(xi.gt.1).and.(xi.lt.nu+2))then
xsp=0.0d0
aw=f(xi)+dh
ae=0.0d0
an=dv
al=dv
else if((xj.eq.mu+2).and.(xi.eq.nu+2))then
xsp=-bi_top
aw=dh+((r_top)/deltazeta**2)
ae=0.0d0
an=0.0d0
al=dv
else
xsp=0.0d0
aw=(f(xi)*(1.0d0-(deltar*(m_in-mua(xj)))))+dh
ae=dh
an=dv
al=dv
endif
!
! Determine coefficients
!
if((xi.eq.nu+2).and.(xj.ge.2).and.(xj.le.mu+1))then ! Section 0
b(k)=b(k)+(bi_top*theta_inf)
else
if((solver.eq.0).and.(an.ne.0.0d0)) a(knumber(xi+1,xj),k)=-an
!
if((solver.eq.2).and.(an.ne.0.0d0))then
! print*, knumber(xi+1,xj)-k+mu+2+1,k
band_coefficient(knumber(xi+1,xj)-k+mu+2+1,k)=-an
endif
if(an.ne.0.0d0)then
nas(scounter)=-an
```

```
nirow(scounter)=knumber(xi+1,xj)
njcol(scounter)=k
scounter=scounter+1
endif
endif
!
if((xi.eq.1).and.(xj.ge.2).and.(xj.le.mu+1))then ! Section 1
!
b(k)=b(k)+(bi_bot*theta_inf)+(g*deltazeta*height*hss &
/(t_0*k_fluid))+(muy(xj-1)*deltazeta*height/ &
(t_0*k_fluid*((rt(xj)/t_0)**0.7)))
else
if((solver.eq.0).and.(al.ne.0.0d0)) a(knumber(xi-1,xj),k)=-al
!
if((solver.eq.2).and.(al.ne.0.0d0))then
! print*, knumber(xi-1,xj)-k+mu+2+1,k
band_coefficient(knumber(xi-1,xj)-k+mu+2+1,k)=-al
endif
if(al.ne.0.0d0)then
nas(scounter)=-al
nirow(scounter)=knumber(xi-1,xj)
njcol(scounter)=k
scounter=scounter+1
endif
endif
!
if((xj.eq.mu+2).and.(xi.ge.2).and.(xi.le.mu+1))then ! Section 2
b(k)=b(k)+0.0d0
else
if((solver.eq.0).and.(ae.ne.0.0d0)) a(knumber(xi,xj+1),k)=-ae
!
if((solver.eq.2).and.(ae.ne.0.0d0))then
! print*, knumber(xi,xj+1)-k+mu+2+1,k
band_coefficient(knumber(xi,xj+1)-k+mu+2+1,k)=-ae
endif
if(ae.ne.0.0d0)then
nas(scounter)=-ae
nirow(scounter)=knumber(xi,xj+1)
njcol(scounter)=k
scounter=scounter+1
endif
endif
!
if((xj.eq.1).and.(xi.ge.2).and.(xi.le.nu+1))then ! Section 3
b(k)=b(k)+((f(xi)+dh)*west(xi))
else
if((solver.eq.0).and.(aw.ne.0.0d0)) a(knumber(xi,xj-1),k)=-aw
```

```
!
if((solver.eq.2).and.(aw.ne.0.0d0))then
! print*, knumber(xi,xj-1)-k+mu+2+1,k
band_coefficient(knumber(xi,xj-1)-k+mu+2+1,k)=-aw
endif
if(aw.ne.0.0d0)then
nas(scounter)=-aw
nirow(scounter)=knumber(xi,xj-1)
njcol(scounter)=k
scounter=scounter+1
endif
endif
!
if((xi.eq.1).and.(xj.eq.1))then ! Section 4
b(k)=(bi_bot*theta_inf)+(g*deltazeta*height*hss/ &
(t_0*k_fluid*((rt(xj)/t_0)**0.7)))
endif
!
if((xi.eq.nu+2).and.(xj.eq.1))then ! Section 5
b(k)=(bi_top*theta_inf)
endif
!
if((xi.eq.1).and.(xj.eq.mu+2))then ! Section 6
b(k)=(bi_bot*theta_inf)+(g*deltazeta*height*hss/ &
(t_0*k_fluid*((rt(xj)/t_0)**0.7)))
endif
!
if((xi.eq.nu+2).and.(xj.eq.mu+2))then ! Section 7
b(k)=(bi_top*theta_inf)
endif
!
! Calculate ap
ap=aw+ae+an+al-xsp
if(solver.eq.0) a(knumber(xi,xj),k)=ap
!
if(solver.eq.2) then
! print*, knumber(xi,xj)-k+mu+2+1,k
band_coefficient(knumber(xi,xj)-k+mu+2+1,k)=ap
elseif(solver.eq.3)then
diagin(knumber(xi,xj))=1.0d0/ap
endif
!
nas(scounter)=ap
nirow(scounter)=knumber(xi,xj)
njcol(scounter)=k
scounter=scounter+1
!
```

```
enddo ! End row loop
!
rb=b
!
! The coefficient matrix A which should be BAND DIAGONAL and
!      the right hand side vector B have now been determined.
!
! This solver uses a sparse method, a varient of Gaussian
!      elimination.
!
nz=0
!
! This section is the old version of obtaining sparse array
!      information, it has been replaced by an earlier do loop.
!
! do i=1,(nu+2)*(mu+2)
! do j=1,(nu+2)*(mu+2)
! if(a(i,j).ne.0.0d0) nz=nz+1
! enddo
! enddo
!
! allocate(as(1:nz))
! allocate(irow(1:nz))
! allocate(jcol(1:nz))
! as=0.0d0
! irow=0.0d0
! jcol=0.0d0
!
! counter=0
!
! do i=1,(nu+2)*(mu+2)
! do j=1,(nu+2)*(mu+2)
! if(a(i,j).ne.0.0d0)then
! counter=counter+1
! as(counter)=a(i,j)
! irow(counter)=i
! jcol(counter)=j
! endif
! enddo
! enddo
!
! write(9,*) nirow
! write(10,*) njcol
! write(11,*) nas
! write(12,*) b
! write(13,*) diagin
!
```

```
if(solver.eq.1)then
!
 if(first) print*, 'solution method is sparse'
 call dlslxg(((nu+2)*(mu+2)),ncounter,nas,nirow,njcol,b,ipath, &
 iparam,rparam,ntres)
!
 elseif(solver.eq.0)then
!
! This solver performs a LU factorisation, checks for
!      condition number
!      and provides an iterative solution
!
if(first) print*,'solution method is LU'
 call dlsarg(((nu+2)*(mu+2)),a,lda,b,ipath,tres)
!
elseif(solver.eq.2)then
!
if(first) print*, 'solution is BAND with iterative refinement'
 call dlsarb(((nu+2)*(mu+2)),band_coefficient,lda,nu+2,mu+2,b,2,itres)
!
elseif(solver.eq.3)then
!
print*, 'solution is full iterative (GMRES)'
 call iterative(mu,nu)
!
endif
!
! Convert vector tres back into array form which follows same
!      indexing as the physical grid
!
if(solver.eq.0)then
!
counter=0
!
do j=1,mu+2
do i=1,nu+2
counter=counter+1
theta(i,j)=tres(counter)
enddo
enddo
!
elseif(solver.eq.1)then
!
counter=0
!
do j=1,mu+2
do i=1,nu+2
```

```
counter=counter+1
ntheta(i,j)=ntres(counter)
enddo
enddo
!
elseif(solver.eq.2)then
!
counter=0
!
do j=1,mu+2
do i=1,nu+2
counter=counter+1
ntheta(i,j)=itres(counter)
enddo
enddo
!
! if(av_graphics)then
!
! Set FAGL routines to point to array ntheta
!
!     print*, 'Starting array viewer......'
! call faglstartwatch(ntheta,status)
! call faglshow(ntheta,status)
! call faglname(ntheta,'Temperature contours',status)
! av_graphics=.false.
! else
! call faglupdate(ntheta,status)
! endif
!
endif
!
! Write catalyst temperature array back to global (transfer) module
! making dimensional at the same time
!
allocate(transfer_temp(0:mu))
!
if(solver.eq.0)then
!
transfer_temp(0)=t_0
!
allocate (imux(0:mu))
!
imux(0)=0.0d0
!
do i=1,mu
imux(i)=mux(i)
enddo
```

```
!
do i=1,mu
transfer_temp=theta(2,i+1)*t_0
enddo
!
call dcsiez(mu,imux,transfer_temp,emu,emux,rt)
!
elseif(solver.eq.1)then
!
transfer_temp(0)=t_0
!
allocate (imux(0:mu))
!
imux(0)=0.0d0
!
do i=1,mu
imux(i)=mux(i)
enddo
!
do i=1,mu
transfer_temp=ntheta(2,i+1)*t_0
enddo
!
call dcsiez(mu,imux,transfer_temp,emu,emux,rt)
!
deallocate(imux)
!
elseif(solver.eq.2)then
!
transfer_temp(0)=t_0
!
allocate (imux(0:mu))
!
imux(0)=0.0d0
!
do i=1,mu
imux(i)=mux(i)
enddo
!
do i=1,mu
transfer_temp(i)=ntheta(2,i)*t_0
enddo
!
call dcsiez(mu,imux,transfer_temp,emu,emux,rt)
!
deallocate(imux)
!
```

```
endif
!
! Output theta array in matrix form
!
! if(solver.eq.0)then
! call dwrrrn('Theta',nu+2,mu+2,theta,nu+2,0)
! elseif(solver.eq.1)then
! call dwrrrn('nTheta',nu+2,mu+2,ntheta,nu+2,0)
! elseif(solver.eq.2)then
! call dwrrrn('iTheta',nu+2,mu+2,ntheta,nu+2,0)
! endif
!
! Perform cross sectional averaging
!
allocate(average_t(1:mu))
!
write(8,*) 0.0,1.0d0
!
do j=1,mu
select case(nu)
case(1)
if(solver.eq.0)then
averaget=theta(2,j)
else
averaget=ntheta(2,j)
endif
case default
averaget=0.0d0
do i=2,nu+1
if(solver.eq.0)then
averaget=averaget+((1.0d0/nu)*theta(i,j))
else
averaget=averaget+((1.0d0/nu)*ntheta(i,j))
endif
enddo
endselect
average_t(j)=averaget
write(8,*) ((0.05d0*deltazeta)+(j*deltazeta)),averaget
write(17,*) ((0.05d0*deltazeta)+(j*deltazeta)),ntheta(2,j)
write(18,*) ((0.05d0*deltazeta)+(j*deltazeta)),ntheta(nu,j)
enddo
!
do i=1,mu
xtol(i)=abs(average_t(i)-oldaverage_t(i))
enddo
!
oldaverage_t=average_t
```

```
!
! Close all files and deallocate all dynamic arrays
!
close(7)
close(8)
close(9)
close(10)
close(11)
close(12)
close(13)
close(17)
close(18)
!
if(solver.eq.0)deallocate(a)
deallocate(b,kij,theta,ntheta,tres,ntres,itres)
deallocate(west)
! deallocate(as,irow,jcol)
deallocate(nas,nirow,njcol)
deallocate(emux,mux,muy,mua)
deallocate(rb)
deallocate(transfer_temp)
deallocate(average_t)
if(solver.eq.2)deallocate(band_coefficient)
if(solver.eq.3)deallocate(diagin)
!
contains
!
function knumber(i,j)
!
integer(i4b) knumber
integer(i4b), intent(in) :: i,j
!
knumber=((nu+2)*(j-1))+i
!
end function knumber
!
function f(xi)
!
integer(i4b), intent(in) :: xi
real(dp) eta,f,v
!
eta=(dfloat(xi)-1.0d0)/(dfloat(nu+1))
v=(eta-(eta**2.0))/(0.1666d0)
f=pe*av*v/(ar*(rt(xj)/t_0)**0.7)
!
end function f
!
```

```
function h_top(theta_inf,t_0,length)
!
real(dp), intent(in) :: theta_inf,t_0,length
real(dp) h_top
!
h_top=1.31d0*((t_0*(1.0d0-theta_inf)/length)**0.25d0)
!
end function h_top
!
function h_bot(theta_inf,t_0,length)
!
real(dp), intent(in) :: theta_inf,t_0,length
real(dp) h_bot
!
h_bot=0.059d0*((t_0*(1.0d0-theta_inf)/length)**0.25d0)
!
end function h_bot
!
end subroutine energysolver
!
```

F.4 transfer.f90

```
module transfer

use nrtype

implicit none

integer(i4b) ncounter
integer(i4b), dimension(:), allocatable :: nirow,njcol

real(dp) diffusivity,m_in
real(dp), dimension(:), allocatable :: add_source,rt,mc
real(sp), dimension(:), allocatable :: diagin,rb
real(dp), dimension(:), allocatable :: nas
real(dp), dimension(:), allocatable :: oldaverage_t,xtol
real(dp), parameter :: deltar=0.75

logical first

interface
subroutine masssolver(nu,mu,height,ar,deltah,pe_h,t_zero,deltah_series)

use nrtype

implicit none

integer(i4b) nu,mu
integer(i4b) i,j

real(dp) theta_a(nu),theta_b(nu),theta_c(nu)
real(dp) theta_d(nu),theta_e(nu),theta_f(nu)
real(dp) temp_a(nu),temp_b(nu),temp_c(nu)
real(dp) temp_d(nu),temp_e(nu),temp_f(nu)
real(dp) average_a,average_b,average_c,average_d,average_e,average_f
real(dp) deltaeta,deltazeta,deltah_series
real(dp) dfgh,eta,pe_h,ar,v,rmm_bar,density_bar,height,t_zero
real(dp) conc_methanol,conc_oxygen,pp_methanol,pp_oxygen,r_flux,deltah
real(dp) xtemp ! temporary variables passed to global storage
real(dp), parameter :: r=8.314d0
real(dp), parameter :: rmm_a=0.032d0,rmm_b=0.032d0,rmm_c=0.030d0
real(dp), parameter :: rmm_d=0.018d0,rmm_e=0.002d0,rmm_f=0.044d0
real(dp), parameter :: sall=1670 ! m**2/kg
real(dp), parameter :: pressure=1.013E+05 ! Negligible pressure drop
```

```
end subroutine masssolver

subroutine energysolver(nu,mu,enu,emu,length,ar,height)

use nrtype
use dfimsl

implicit none

integer(i4b) iparam(6)
integer(i4b) counter,i,j,k,l,lda,enu,emu,nu,nz,mu,solver,tempk,xi,xj
integer(i4b), parameter :: ipath=2
integer(i4b), dimension(:), allocatable :: irow,jcol

real(dp) ah,ar,av,deltaeta,deltazeta,dh,dv,pe,xgamma
real(dp) rparam(5)
real(dp) aw,ae,an,al,ap,xsp
real(dp) averaget,height
real(dp) theta_inf,bi_bot,bi_top,total,r_top,hss,g
real(dp) r_glass,r_cat,r_si,r_ss
real(dp) k_glass,k_silver,k_silicon,k_ss,t_0
real(dp) length

real(dp), dimension(:), allocatable :: west,east,south,north
real(dp), dimension(:), allocatable :: as,b,tres
real(dp), dimension(:,:), allocatable :: a,theta

type krelation
integer(i4b) i ! icoordinate
integer(i4b) j ! jcoordinate
endtype

type(krelation), dimension(:), allocatable :: kij

end subroutine energysolver

subroutine iterative(imu,inu)

use nrtype

implicit none

integer(i4b) counter,imu,inu

integer(i4b) ido,info(10),nout,n
real(sp) p((imu+2)*(inu+2)),tol,work(1000000)
                real(sp) x((imu+2)*(inu+2)),z((imu+2)*(inu+2))
```

```
intrinsic  SQRT
real(dp)   SQRT

external   amultp,g2res,iset,scopy,shprod,sset,umach,wrrrn

external amach,g8res,g9res
real(sp) amach

end subroutine iterative
endinterface

end module transfer
```

F.5 gmressolver.f90

```
subroutine iterative(imu,inu)

use nrtype
use transfer

implicit none

integer(i4b) counter,imu,inu

      integer(i4b) ido,info(10),nout,n
      real(sp) p((imu+2)*(inu+2)),tol,work(1000000)
      real(sp) x((imu+2)*(inu+2)),z((imu+2)*(inu+2))

      intrinsic  SQRT
      real(dp)   SQRT

      external   amultp,g2res,iset,scopy,shprod,sset,umach,wrrrn

      external amach,g8res,g9res
      real(sp) amach

  n=(imu+2)*(inu+2)

      call umach(2,nout)
!                        Initial guess = (1 ... 1)
      call sset(n,1.0,x,1)
!                        Set up the options vector INFO
!                        to use preconditioning
      call iset(10,0,info,1)
      info(4)=1
!                        Set stopping tolerance to
!                        square root of machine epsilon
      tol=sqrt(amach(4))
      ido=0
counter=0
p=0.0
x=0.0
z=0.0

do while(ido.ne.4)
counter=counter+1
write(6,*) 'GMRES Solver iteration number ', counter
call g2res(ido,n,x,p,rb,z,tol,info,g8res,g9res,work)
```

```
if(ido.eq.1)then
!                       Set z = A*p
call amultp(p,z,imu,inu)

elseif(ido.eq.2)then
!
!                       Set z = inv(M)*p
!                       The diagonal of inv(M) is stored
!                       in DIAGIN
!
call shprod(n,diagin,1,p,1,z,1)
elseif(ido.eq.3)then
!
!                       Set z = A*inv(M)*p
!
call shprod(n,diagin,1,p,1,z,1)
call scopy(n,z,1,p,1)
call amultp(p,z,imu,inu)

endif
enddo
!
      call wrrrn('Solution',n,1,x,n,0)
      write(nout,'(a11, e15.5)') 'Residual = ', tol
      end
!
      subroutine amultp(p,z,imu,inu)
use nrtype
use transfer
implicit none

      real(sp)       p(*),z(*)

      integer(i4b) i,imu,inu
      external sset

      call sset((imu+2)*(inu+2),0.0,z,1)
!                       Accumulate the product A*p in z
      do i=1,ncounter
         z(njcol(i))=z(njcol(i))+nas(i)*p(nirow(i))
enddo
      return
      end
```

F.6 amultp.f90

```
subroutine amultp(p,z,iirow,ijcol,inas)

use nrtype
use transfer

integer(i4b), intent(in) :: iirow(:),ijcol(:)
integer(i4b) i,n

real(dp),intent(in) :: inas(:)
real(dp) p(*),z(*)

external sset

n=((nu+2)*(mu+2))

call dset(n,0.0d0,z,1)

do i=1,ncounter
z(iirow(i))=z(iirow(i))+inas(i)*p(ijcol(i))
enddo

end subroutine amultp
```

Appendix G

Calculation of Interface Curvature

This appendix summarises the work by Olim (2000) in formulating a minimisation problem to calculate the interface curvature of a gas-liquid interface in a rectangular microchannel duct.

Olim (2001) states that the potential energy of a liquid contained in a cavity is the sum of the energy due to body forces acting on the bulk of the liquid and the energy due to surface tension acting at the gas liquid interface. In steady-state the shape of the interface is determined by the system achieving a minimum potential energy, subject to the constraint the volume os liquid must be conserved. The shape of the interface can be determined by minimising the following functional (I)

$$I = \mathrm{BE} + \mathrm{SE} + \lambda V, \tag{G.1}$$

where BE abd SE are the body energy and surface enregy components respectively, V is the liquid volume and λ is a Lagrange multiplier to be determined. Olim showed that (G.1) could be formulated as (in dimensionless form)

$$I = \int_{-1}^{1} \left[\left(1 + f'^2\right)^{0.5} + Bof \left(\frac{1}{2} f \cos\alpha - x \sin\alpha \right) + \lambda f \right], \tag{G.2}$$

where Bo is the Bond number, f is the dimensionless height of the interface, α is the angle from the vertical of the channel (in this case 0^o) and x is the dimensionless distance from the centre of the channel. Olim assumed constant physical properties, the minimisation of (G.2) yielded the Euler-Lagrange equation for the interface

$$f'' = \left[Bo \left(f \cos\alpha - x \sin\alpha \right) + \lambda \right] \left(1 + f'^2\right)^{1.5}. \tag{G.3}$$

This is a second order O.D.E. and the contact angles (β) at $x = -1$ and $x = 1$ serve as boundary conditions.

$$f \mid_{x=-1} = 0 \quad f' \mid_{x=-1} = -\cot\beta \quad f' \mid_{x=-1} = \cot\beta. \tag{G.4}$$

Appendix H

Derivation of the Developed 3D Velocity Profile in a Channel

This appendix gives the derivation of a 3D velocity profile for a zero shear stress boundary condition at the flat phase interface. The flow is assumed developed and one-dimensional (in the x direction) hence if the pressure gradient and inertial terms are neglected (creeping flow) the u velocity equation in the x direction becomes

$$\frac{\partial^2 u}{\partial y^2}+\frac{\partial^2 u}{\partial z^2}+\frac{\rho g}{\mu}=0, \tag{H.1}$$

which is a non-homogeneous form of the diffusion equation and can be solved analytically. The boundary conditions are Dirichlet ($u=0$) at all surfaces except $y=0$, where a zero flux (Neumann) condition is applied. The finite Fourier transform (FFT) method has been used to solve the equation due to the ease of use when multiple non-homogeneous forms are present. It is assumed that a solution exists of the form

$$u\left(z,y\right)=\sum_{n=1}^{\infty}u_n\left(z\right)\Phi_n\left(y\right), \tag{H.2}$$

where Φ_n is a basis function, and is defined as

$$\Phi_n\left(y\right)=\sqrt{2}\cos\left(\left(n+\frac{1}{2}\right)\pi y\right), \qquad n=0,1,2,\ldots$$

Applying the FFT to the first term in (H.1) yields

$$\int_0^1 \Phi_n\frac{\partial^2 u}{\partial y^2}\mathrm{d}y=\left(\Phi_n\frac{\partial u}{\partial y}\right)\Bigg|_{y=0}^{y=1}-\left(u\frac{\mathrm{d}\Phi_n}{\mathrm{d}y}\right)\Bigg|_{y=0}^{y=1}+\int_0^1 u\frac{\mathrm{d}^2\Phi_n}{\mathrm{d}y^2}\mathrm{d}y,$$

$$\Phi(0)=1, \qquad \Phi(1)=\sqrt{2},$$

therefore the above can be simplified to

$$\int_0^1 \Phi_n \frac{\partial^2 u}{\partial y^2} \mathrm{d}y = \left(\Phi_n \frac{\partial u}{\partial y} - u \frac{\mathrm{d}\Phi_n}{\mathrm{d}y} \right) \Bigg|_{y=0}^{y=1} + \int_0^1 u \frac{\mathrm{d}^2 \Phi_n}{\mathrm{d}y^2} \mathrm{d}y,$$

the first term on the RHS goes to zero from boundary conditions, therefore

$$\int_0^1 \Phi_n \frac{\partial^2 u}{\partial y^2} \mathrm{d}y = \int_0^1 u \frac{\mathrm{d}^2 \Phi_n}{\mathrm{d}y^2} \mathrm{d}y, = \frac{-\pi^2 (2n+1)^2}{4} \int_0^1 u \Phi_n \mathrm{d}y,$$

the last term is the definition of the FFT, hence

$$\int_0^1 \Phi_n \frac{\partial^2 u}{\partial y^2} \mathrm{d}y = -\pi^2 \left(n + \frac{1}{2} \right)^2 u_n.$$

Integration of other terms is straightforward

$$\int_0^1 \Phi_n \frac{\partial^2 u}{\partial z^2} \mathrm{d}y = \frac{\mathrm{d}^2}{\mathrm{d}z^2} \int_0^1 \Phi_n u \mathrm{d}y = \frac{\mathrm{d}^2}{\mathrm{d}z^2} u_n,$$

$$\int_0^1 \Phi_n \left(\frac{\rho g}{\mu} \right) \mathrm{d}y = \sqrt{2} \int_0^1 \cos \left(\left(n + \frac{1}{2} \right) \pi y \right) K \mathrm{d}y = \sqrt{2} K \int_0^1 \left(\left(n + \frac{1}{2} \right) \pi y \right),$$

where $K = \frac{\rho g}{\mu}$

$$= \frac{\sqrt{2} K \sin \left(n + \frac{1}{2} \right) \pi y}{\left(n + \frac{1}{2} \right) \pi} = \frac{\sqrt{2} K (-1)^n}{\left(n + \frac{1}{2} \right) \pi}.$$

The results are combined to give a non-homogeneous differential equation for $u_n(z)$

$$\frac{\mathrm{d}^2 u_n}{\mathrm{d}z^2} - \pi^2 \left(n + \frac{1}{2} \right)^2 u_n = - \frac{\sqrt{2} K (-1)^n}{\left(n + \frac{1}{2} \right) \pi}, \tag{H.3}$$

with associated boundary conditions

$$u_n(0) = 0,$$
$$u_n(1) = 0.$$

Equation (H.3) has the general solution (where A and B are constants)

$$u_n = A \cosh \left(\left(n + \frac{1}{2} \right) \pi z \right) + B \sinh \left(\left(n + \frac{1}{2} \right) \pi z \right),$$

and a particular solution

$$u_n = \frac{\sqrt{2} K (-1)^n}{\left(n + \frac{1}{2} \right)^3 \pi^3}.$$

Therefore the full solution is

$$u_n = A\cosh\left(\left(n+\frac{1}{2}\right)\pi z\right) + B\sinh\left(\left(n+\frac{1}{2}\right)\pi z\right) + \frac{\sqrt{2}K\left(-1\right)^n}{\left(n+\frac{1}{2}\right)^3\pi^3}.$$

It can be readily be seen that at $z = 0$ the sinh term is zero, therefore

$$A = -\frac{\sqrt{2}K\left(-1\right)^n}{\left(n+\frac{1}{2}\right)^3\pi^3}.$$

B can be evaluated in a similar manner to yield

$$\frac{8\sqrt{2}K\left(-1\right)^n\left(\cosh\left(\frac{\pi}{2}+n\pi\right)-1\right)}{\pi^3\sinh\left(\frac{\pi}{2}+\pi n\right)\left(8n^3+12n^2+6n+1\right)}.$$

Using (H.2) the complete solution can be given as

$$\begin{aligned} u\left(z,y\right) &= \\ \sqrt{2}\sum_{n=1}^{\infty}\left(A\cosh\left(\left(n+\frac{1}{2}\right)\pi z\right)\right. &+ \\ B\sinh\left(\left(n+\frac{1}{2}\right)\pi z\right) &+ \left.\frac{\sqrt{2}K\left(-1\right)^n}{\left(n+\frac{1}{2}\right)^3\pi^3}\cos\left(\left(n+\frac{1}{2}\right)\pi y\right)\right). \end{aligned} \tag{H.5}$$